THESIS FOR THE DEGREE OF DOCTOR OF PHILOSOPHY

Sustainable conversion of strategic industrial wastes and biomass into activated carbons for CO_2 capture: mechanisms, material design, and adsorption performance

BARTOSZ DZIEJARSKI

Department of Environmental and Energy Sciences

Energy Technology Division

CHALMERS UNIVERSITY OF TECHNOLOGY

Faculty of Environmental Engineering

Department of Air Conditioning, Heating, Gas Engineering and Air Protection

WROCŁAW UNIVERSITY OF SCIENCE AND TECHNOLOGY

Gothenburg, Sweden; Wrocław, Poland, 2026

Sustainable conversion of strategic industrial wastes and biomass into activated carbons for CO_2 capture: mechanisms, material design, and adsorption performance

BARTOSZ DZIEJARSKI
ISBN: 978-91-8103-447-9
DOI: https://doi.org/10.63959/chalmers.dt/590

Doktorsavhandlingar vid Chalmers tekniska högskola
Ny serie nr: 5904
ISSN: 0346-718X

Department of Environmental and Energy Sciences
Chalmers University of Technology
SE-412 96 Gothenburg
Sweden
Telephone + 46 (0)31-772 1000

Department of Air Conditioning, Heating, Gas Engineering and Air Protection
Wrocław University of Science and Technology
ul. Norwida 4/6, 50-370 Wrocław
Poland

Cover:
Schematic illustration of the sustainable conversion of waste tires, lithium-ion batteries, and woody biomass into activated carbon as a gas sorbent for flue gas treatment, highlighting circular economy principles, waste valorization, and the adsorption of CO_2.

Printed by Chalmers Reproservice
Gothenburg, Sweden 2026

Abstract

The increasing concentration of atmospheric CO_2 necessitates sustainable sorbent materials for efficient carbon capture . This thesis explores the valorization of carbon-intensive waste streams into porous carbons for CO_2 capture within a circular materials framework. Three structurally distinct precursors were investigated: woody biomass, recovered carbon black from end-of-life tires, and graphite from spent lithium-ion batteries. Potassium-assisted chemical activation served as a unifying synthesis approach to establish structure–property–performance relationships and assess the chosen materials suitability as solid adsorbents.

The effects of precursor structure, activation conditions, and potassium speciation on pore development, carbon framework evolution, and surface chemistry were systematically analyzed. Particular attention was given to adsorption-relevant microporosity and its role in governing CO_2 uptake and CO_2/N_2 selectivity.

The obtained results suggested that activation responsiveness was strongly precursor-dependent. Biomass showed the highest reactivity toward KOH, yielding dense microporous networks with BET surface areas up to 2655 $m^2\ g^{-1}$ and high CO_2 capacities, although excessive activation caused pore widening and performance loss. Recovered carbon black exhibited limited activation due to its compact morphology, leading to mesopore-dominated structures and lower uptake. Recovered graphite was the most resistant, with porosity developing mainly through defect-driven edge etching while preserving graphitic order.

CO_2 adsorption across all systems was governed by the presence of narrow micropores rather than total surface area, highlighting that the key performance factor was pore size matching to the kinetic diameter of CO_2 as. KOH provided the highest activation efficiency, while alternative potassium salts enabled milder pore development with improved yield. Oxygen-containing surface groups formed as a result of the activation contributed to adsorption energetics but remained secondary to textural effects under physisorption-controlled conditions.

Biomass- and recovered carbon black–derived carbons showed stable cyclic operation and favorable CO_2/N_2 selectivity under dilute and flue-gas-relevant conditions.

Beyond adsorption performance, this work demonstrates scalable routes for converting renewable, industrial, and technological carbon residues into high-value porous materials. The results provide design guidelines for precursor selection, activation strategy, and pore engineering in waste-derived carbons for gas separation and related environmental applications.

Keywords: Activated carbon; Waste valorization; Potassium activation; Recovered carbon black; Recovered graphite; Biomass; CO_2 capture; CCU, CCUS.

Acknowledgments

First and foremost, I would like to express my deepest gratitude to my supervisors, Professor Pavleta Knutsson and Professor Klas Andersson at Chalmers University of Technology, as well as Professor Renata Krzyżyńska at Wrocław University of Science and Technology. Their guidance, encouragement, and invaluable expertise have been instrumental throughout my research journey. Their continuous support, insightful advice, and confidence in my abilities have significantly contributed to both the completion of this work and my development as a researcher.

I would also like to extend my sincere appreciation to my colleague and friend, Jarosław Serafin. The many scientific discussions we shared have broadened my perspective, deepened my understanding of the field, and strengthened my enthusiasm for research. His friendship and intellectual support have been greatly valued.

My thanks go to all members of the Unit of Inorganic Environmental Chemistry and the Division of Energy Technology for fostering a collaborative, welcoming, and inspiring research environment. Their support and willingness to share knowledge have made my time in academia both productive and enjoyable.

I am also grateful to my friends at Chalmers, especially Joanna, Elena, Pedram, Kanming, and Hooman, for their friendship, encouragement, and the many memorable moments we shared throughout these years.

A special note of gratitude goes to my friend Maciej and Jason, whose unwavering friendship and support have been a constant source of strength and motivation..

Finally, I would like to thank everyone who has contributed, directly or indirectly, to my academic and personal growth. Your support, encouragement, and belief in me have played an important role in making this achievement possible.

Bartosz Dziejarski, Gothenburg (2026)

List of publications

This thesis is based on the following appended papers, which are referred to in the text by their assigned Roman numerals:

Paper I

Dziejarski, B*., Serafin, J., Hernández-Barreto, D. F., Naumovska, E., Sreńscek-Nazzal, J., Klomkliang, N., Tam, E., Krzyżyńska, R., Andersson, K., & Knutsson, P. (2025). Tailoring highly surface and microporous activated carbons (ACs) from biomass via KOH, $K_2C_2O_4$ and KOH/$K_2C_2O_4$ activation for efficient CO_2 capture and CO_2/N_2 selectivity: characterization, experimental and molecular simulation insights. ***Chemical Engineering Journal***, 169677.

Paper II

Dziejarski, B*., Hernández-Barreto, D. F., Moreno-Piraján, J. C., Giraldo, L., Serafin, J., Knutsson, P., Andersson K., & Krzyżyńska, R. (2024). Upgrading recovered carbon black (rCB) from industrial-scale end-of-life tires (ELTs) pyrolysis to activated carbons: Material characterization and CO_2 capture abilities, ***Environmental Research****, 247, 118169.*

Paper III

Dziejarski, B*., Faust, R., Serafin, J., Krzyżyńska, R., Andersson, K., & Knutsson, P. (2024). Insights into activation pathways of recovered carbon black (rCB) from end-of-life tires (ELTs) by potassium-containing agents, ***ACS Omega****, 9(29), 31814-31831.*

Paper IV

Dziejarski, B*., Fester, J. E. A., Serafin, J., Petranikova, M., Tam, E., Martinelli, A., Krzyżyńska, R., Andersson, K., & Knutsson, P. (2025). Valorization of hazardous graphite from black mass (NMC 111) of lithium-ion battery recycling via KOH activation for functional carbon design. ***Materials & Design****, 254, 114073.*

Related peer-reviewed papers not included in the thesis

Dziejarski, B*., Serafin, J., Andersson, K., & Krzyżyńska, R. CO_2 capture materials: a review of current trends and future challenges (2023), ***Materials Today Sustainability****, 24, 100483.*

Dziejarski, B*., Krzyżyńska, R., & Andersson, K. Current status of carbon capture, utilization, and storage technologies in the global economy: A survey of technical assessment (2023), ***Fuel****, 342, 127776.*

Serafin, J., & **Dziejarski, B.** (2024). Activated carbons—preparation, characterization and their application in CO_2 capture: a review. ***Environmental Science and Pollution Research***, 31(28), 40008-40062.

Serafin, J., & **Dziejarski, B**. (2023). Application of isotherms models and error functions in activated carbon CO_2 sorption processes. ***Microporous and Mesoporous Materials***, 354, 112513.

Serafin, J., **Dziejarski, B**., Junior, O. F. C., & Sreńscek-Nazzal, J. (2023). Design of highly microporous activated carbons based on walnut shell biomass for H_2 and CO_2 storage. ***Carbon***, 201, 633-647.

Fonseca-Bermúdez, Ó. J., Giraldo, L., Sierra-Ramírez, R., Serafin, J., **Dziejarski, B**., Bonillo, M. G., ... & Moreno-Piraján, J. C. (2024). Cashew nut shell biomass: a source for high-performance CO_2/CH_4 adsorption in activated carbon. ***Journal of CO_2 Utilization***, 83, 102799.

Serafin, J., **Dziejarski, B**., Vendrell, X., Kiełbasa, K., & Michalkiewicz, B. (2023). Biomass waste fern leaves as a material for a sustainable method of activated carbon production for CO_2 capture. ***Biomass and Bioenergy***, 175, 106880.

Serafin, J., **Dziejarski, B**., Fonseca-Bermúdez, Ó. J., Giraldo, L., Sierra-Ramirez, R., Bonillo, M. G., ... & Moreno-Piraján, J. C. (2024). Bioorganic activated carbon from cashew nut shells for H2 adsorption and H_2/CO_2, H_2/CH_4, CO_2/CH_4, $H_2/CO_2/CH_4$ selectivity in industrial applications. ***International Journal of Hydrogen Energy***, 86, 662-676.

Serafin, J., **Dziejarski, B**., & Sreńscek-Nazzal, J. (2023). An innovative and environmentally friendly bioorganic synthesis of activated carbon based on olive stones and its potential application for CO_2 capture. ***Sustainable Materials and Technologies***, 38, e00717.

Serafin, J., Vikram, S., **Dziejarski, B**., & Sahoo, S. (2023). An environmentally friendly synthesis method of activated carbons based on subabul (Leucaena leucocephala) sawdust waste for CO_2 adsorption. ***Journal of Cleaner Production***, 412, 137406.

Serafin, J., **Dziejarski, B**., Rodríguez-Estupiñán, P., Fernández, V. B., Giraldo, L., Sreńscek-Nazzal, J., ... & Moreno-Piraján, J. C. (2024). Effective synthesis route of renewable activated biocarbons adsorbent for high CO_2, CH_4, H_2, N_2, C_2H_4 gas storage and CO_2/N_2, CO_2/CH_4, CO_2/H_2, C_2H_4/CH_4 selectivity. ***Fuel***, 374, 132462.

* *Corresponding author*

Contribution report

Paper I Principal author with main responsibility for all the experimental work, conceptualization, methodology, validation, data curation, formal analysis, visualization, project administration, and writing.

Paper II Principal author with main responsibility for all the experimental work, conceptualization, methodology, validation, data curation, formal analysis, modeling, visualization, project administration, and writing.

Paper III Principal author with main responsibility for most of the experimental work, conceptualization, methodology, validation, data curation, formal analysis, visualization, project administration, and writing.

Paper IV Principal author with main responsibility for most of the experimental work, conceptualization, methodology, validation, data curation, formal analysis, modeling, visualization, project administration, and writing.

Table of Contents

Nomenclatures

List of abbreviations

AC	Activated carbon
ACs	Activated carbons
BET	Brunauer–Emmett–Teller
BM	Black mass
CBp	Pyrolytic carbon black
CCUS	Carbon capture, utilization, and storage
CH_3COOK	Potassium acetate
CLC	Chemical looping combustion
CO_2	Carbon dioxide
CO_2/N_2	Carbon dioxide/nitrogen selectivity
COFs	Covalent organic frameworks
DAC	Direct air capture
DFT	Density functional theory
EDS	Energy-dispersive X-ray spectroscopy
ELTs	End-of-life tires
EV	Electric vehicle
FT-IR	Fourier-transform infrared spectroscopy
GHG	Greenhouse gas
IAST	Ideal adsorbed solution theory
IPCC	Intergovernmental Panel on Climate Change
K_2CO_3	Potassium carbonate
$K_2C_2O_4$	Potassium oxalate
KCl	Potassium chloride
KOH	Potassium hydroxide
LiBs	Lithium-ion batteries
LFP	Lithium iron phosphate
LMO	Lithium manganese oxide
MOFs	Metal–organic frameworks

MSW	Municipal solid waste
N_2	Nitrogen
NCA	Lithium nickel cobalt aluminum oxide
NMC	Lithium nickel manganese cobalt oxide
PSD	Pore size distribution
PVDF	Polyvinylidene fluoride
rCB	Recovered carbon black
SEM	Scanning electron microscopy
SEM–EDS	Scanning electron microscopy with energy-dispersive X-ray spectroscopy
TCD	Thermal conductivity detector
TGA	Thermogravimetric analysis
vCB	Virgin carbon black
V_{MIC}	Micropore volume
V_{TOT}	Total pore volume
XPS	X-ray photoelectron spectroscopy
XRD	X-ray diffraction

List of symbols

C	Carbon content (wt.%)
H	Hydrogen content (wt.%)
I_D/I_G	Intensity ratio of D and G Raman bands (–)
N	Nitrogen content (wt.%)
O	Oxygen content (wt.%)
P	Pressure (bar)
P_0	Saturation pressure (bar)
P/P_0	Relative pressure (–)
R^2	Coefficient of determination (–)
S	Sulfur content (wt.%)
S_{BET}	Specific surface area ($m^2\ g^{-1}$)
V_{TOT}	Total pore volume ($cm^3\ g^{-1}$)

V_{MIC}	Micropore volume ($cm^3\ g^{-1}$)
$V_{MIC(N_2)}$	Micropore volume determined from N_2 adsorption at −196 °C ($cm^3\ g^{-1}$)
θ	Diffraction angle (°)

1. Introduction

1.1 The CO_2 challenge and the role of carbon capture, utilization, and storage (CCUS)

The accelerating increase in atmospheric carbon dioxide (CO_2) concentration remains one of the most critical environmental challenges of the twenty-first century. CO_2 is the predominant anthropogenic greenhouse gas, and its accumulation is the principal driver of global warming and climate instability [1]. In 2024, total energy-related CO_2 emissions increased by 0.8%, reaching an all-time high of 37.8 Gt CO_2. This rise contributed to record atmospheric CO_2 concentrations of 422.5 ppm, approximately 3 ppm higher than in 2023 and about 50% above pre-industrial levels. During the same year, CO_2 emissions from fuel combustion grew by around 1% (357 Mt CO_2), while those from industrial processes declined by 2.3% (62 Mt CO_2). Emissions growth remained below the global GDP increase of 3.2%, indicating a partial decoupling between economic expansion and emissions [2].

According to the Intergovernmental Panel on Climate Change (IPCC, 2022), immediate and coordinated mitigation actions are essential to limit global warming to 1.5 °C above pre-industrial levels. The IPCC projects that global greenhouse gas (GHG) emissions must peak by 2025 at the latest and decline by at least 43% by 2030 to achieve this target [3]. Meeting these ambitious goals requires a rapid transition to low-carbon technologies across all sectors, including power generation, transportation, and materials production, complemented by efficient, scalable, and sustainable methods for CO_2 capture and management.

Among the available strategies for CO_2 mitigation, carbon capture, utilization, and storage (CCUS) has emerged as a key enabling technology for deep decarbonization [4]. The schematic methodology for reducing both capturable and uncapturable CO_2 emissions through the CCUS framework is illustrated in **Figure 1**. In this system, CO_2 is primarily captured from major point sources such as power plants, cement and steel industries, and chemical manufacturing facilities, or directly from ambient air using Direct Air Capture (DAC) technologies. The captured CO_2 is then compressed and transported, typically via pipelines, ships, or trucks, to storage or utilization sites, where it can be permanently stored in geological formations such as depleted reservoirs and saline aquifers, or converted into valuable products including fuels, chemicals, and construction materials [5].

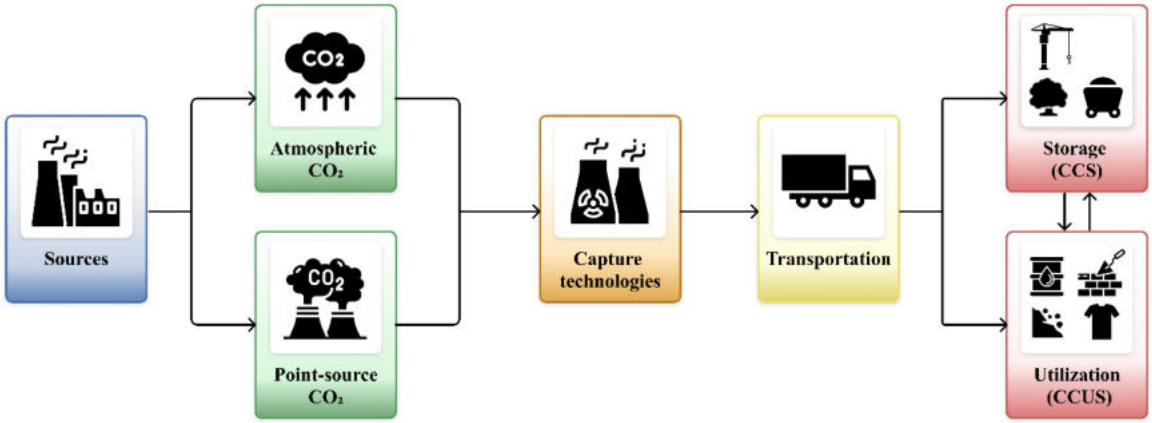

Figure 1. Schematic methodology for reducing CO_2 emissions through CCUS.

Carbon capture represents a critical limitation in CO_2 mitigation, as the separation step strongly influences both energy demand and overall process viability. In CCUS systems, CO_2 can be captured via pre-combustion, post-combustion, or oxy-fuel combustion configurations. To enable separation within these approaches, several technologies have been developed, including absorption (e.g., conventional amine scrubbing), adsorption, membrane separation, cryogenic methods, chemical looping combustion (CLC), and calcium looping (CaL). Within these approaches, adsorption-based CO_2 capture has gained increasing attention as an energy-efficient and environmentally sustainable alternative to amine-based absorption [6]. Adsorption processes operate under moderate conditions and allow repeated CO_2 uptake and release with low regeneration energy. In practical applications, this approach relies mainly on solid sorbents, valued for their high thermal stability, chemical robustness, and adjustable surface characteristics. Among the various materials investigated for gas sorption applications, including metal–organic frameworks (MOFs), covalent organic frameworks (COFs), zeolites, amine-functionalized solids, and carbon-based sorbents, considerable attention has been devoted to materials offering low cost, wide availability, low density, and well-developed porosity. These attributes support their use under diverse conditions. Activated carbons form a major and technologically mature subgroup within carbon-based sorbents and remain widely explored in CO_2 capture research [7].

1.2 Activated carbons development from waste-derived carbon resources

Activated carbon, one of the most extensively studied carbon-based adsorbents, play a crucial role in addressing environmental challenges. In their production, carbon-rich materials are used as precursors, which undergo physical or chemical activation to develop the desired porosity and surface characteristics. Ideally, suitable precursors are expected to possess high

carbon content, low ash levels, minimal volatile matter, and limited thermal degradation to maintain the desired physicochemical properties [8]. Traditionally, materials such as brown, bituminous, and anthracite coals, and peat have been employed in large-scale AC production due to their abundance, high carbon yield, and well-established processing technologies [9]. However, these conventional raw materials are finite, and not all are renewable, which has driven increasing research interest toward sustainable alternatives. With the growing emphasis on sustainability, attention has shifted toward renewable and waste-derived precursors with biological origin, such as agricultural residues, municipal wastes, animal by-products, forestry residues, and food industry wastes (**Figure 2**). These feedstocks, rich in lignocellulosic components (cellulose, hemicellulose, and lignin), offer significant potential for conversion into ACs with well-developed porous structures and large surface areas after carbonization and activation [10, 11].

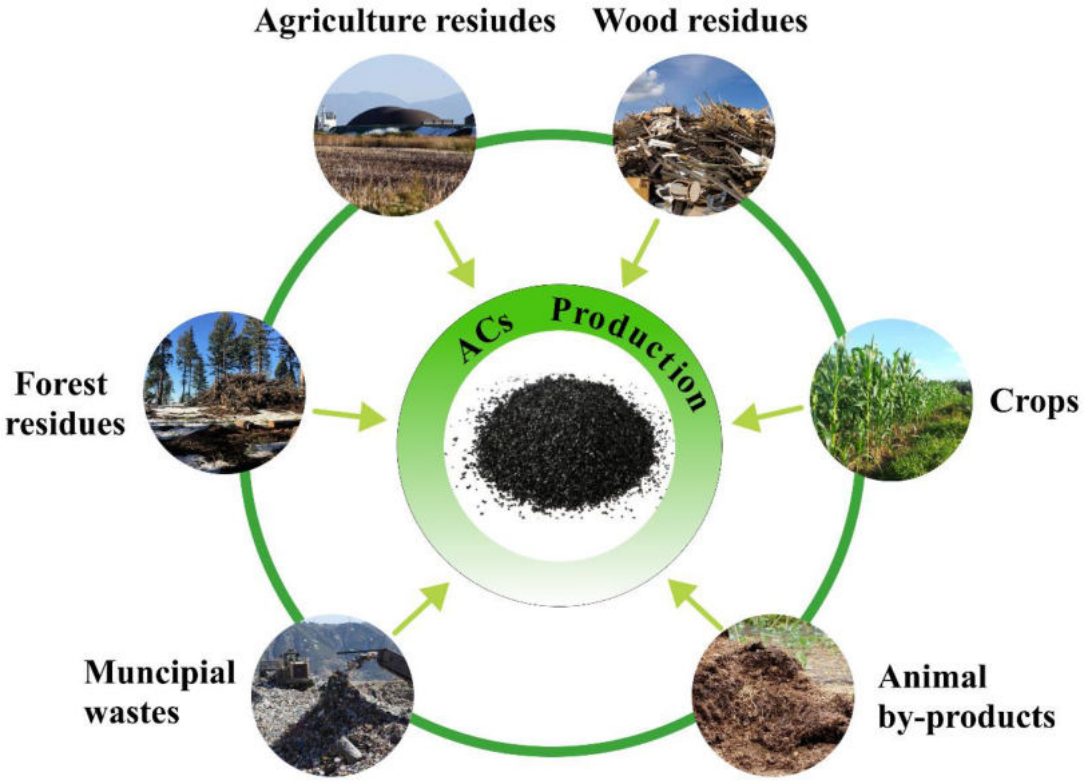

Figure 2. Available and suitable materials for the production of activated carbons.

Beyond biological products, with time and increasing demand for renewable technologies, it has become equally important to consider carbon-rich waste streams originating from industrial processes, which remain largely underutilized despite their high recovery potential. End-of-life tires (ELTs), for instance, represent a persistent environmental concern, continuously generated as by-products of the transportation sector [12]. In contrast, lithium-ion batteries (LiBs) are linked to emerging waste flows that are expected to grow considerably as

their use expands in sustainable energy systems [13]. Although battery wastes large-scale disposal is not yet critical, future projections indicate a substantial increase in waste volumes in the coming decades. Both recovered carbon black (rCB) obtained from ELT pyrolysis and graphite recovered from the black mass of spent batteries exhibit high carbon intensity, making them attractive precursors for the synthesis of functional porous materials. Even though available as streams and presenting potential for AC production, the industrial residue materials present complex composition and presence of inorganic and metallic impurities, which pose additional production challenges that require advanced processing and purification strategies [14, 15]. Integrating these industrial waste streams with biomass-derived precursors supports a comprehensive approach to waste valorization, enabling the transformation of diverse carbon sources into high-performance materials. In addition to the potential for CO_2 capture, the utilization of such feedstocks reinforces circular economy principles by minimizing environmental impact, enhancing resource efficiency, and contributing to carbon neutrality goals. A comparative overview of major carbon-rich feedstocks discussed in this thesis, including their global availability, distribution, future outlook, and associated challenges, is presented in **Table 1**.

Table 1. Comparison of major carbon-rich feedstocks, including their global availability, distribution, future outlook, challenges.

Stock	Availability	Geographical occurrence	Future outlook	Key challenges	References
Biomass residues	~3–5 Gt/year globally	Widespread but uneven; high in Asia, Europe, and USA	Rising demand toward 2050	Stock variability (moisture, ash) and seasonal availability	[16]
End-of-life tires	~1.5 Mt/year	Clustered in China, USA, EU with big vehicle fleets	Expected growth with transport sector expansion	Stock variability and processing challenges due to steel, ZnO, and additives	[17]
Lithium-ion batteries	~1.6-2 Mt/yr by 2030	Present in China, EU and USA (70% recycling in China; 10% EU/USA each.)	Strong rise post-2030 with EV market growth	Processing challenges arising from persistent metal impurities	[18]

2. Thesis overview

2.1 Aim and scope

The overall aim of this thesis is to develop routes for the synthesis of functional carbon materials from waste-derived precursors and to evaluate their potential for gas sorption applications, with particular emphasis on CO_2 capture (**Figure 3**). The work addresses the increasing need for circular and resource-efficient approaches to carbon material production by utilizing waste streams of biological, industrial, and technological origin. These include woody biomass, rCB from end-of-life tires, and graphite recovered from the black mass of spent LiBs. The focus is placed on establishing a mechanistic understanding of activation and conversion processes, optimizing synthesis parameters, and linking structural evolution to sorption performance.

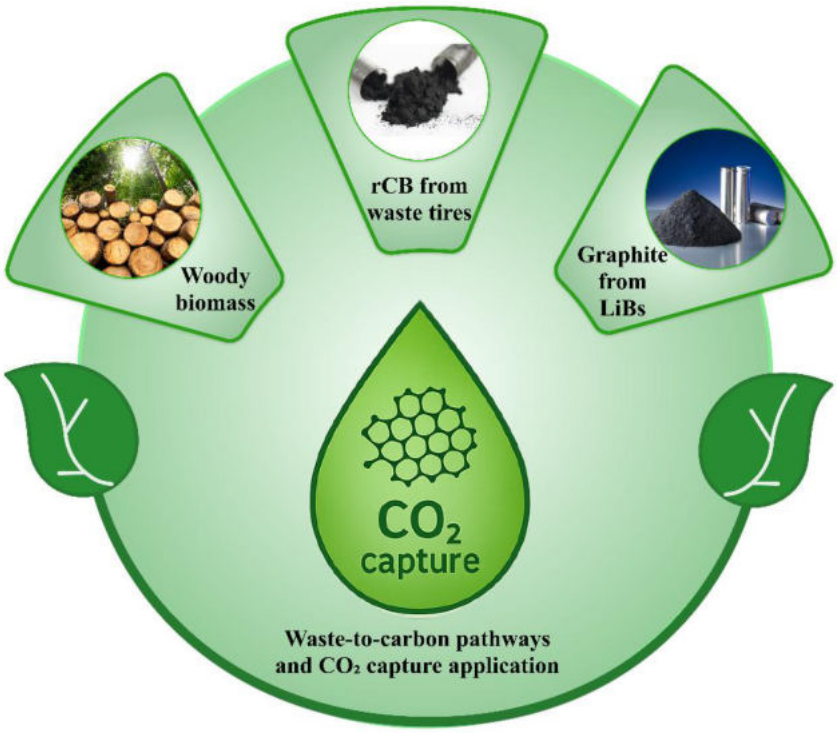

Figure 3. Illustration of the materials and the end-goal application within the framework of the current thesis.

More specifically, the research has been conducted to meet the following objectives:

- Follow the activation mechanisms of waste-derived precursors under potassium-based activation (KOH, K_2CO_3, CH_3COOK, $K_2C_2O_4$, KCl) and their impact on pore development and surface chemistry.

- Link structure and performance by combining textural, structural, and surface analyses to track how activation conditions shape micro- and mesoporosity and functional groups.
- Compare biomass, recovered carbon black, and recovered graphite to determine how precursor origin governs transformations, advantages, and limitations.
- Quantify CO_2 capture, emphasizing adsorption capacity, CO_2/N_2 selectivity, and cyclic stability.
- Outline scalable routes that convert waste carbons into high-value sorbents to advance circular economy goals and industrial decarbonization.

2.2 Outline

This thesis comprises the main findings from four appended papers (**Papers I-IV**) that investigate the activation of biomass- and waste-derived precursors into porous carbon materials for potential CO_2 capture applications. The work combines experimental studies to understand how the type of precursor, the type of potassium-based activator, and processing conditions affect pore development, surface chemistry, and structural properties of the obtained carbons. The development of the research work and its relation to the research papers are schematized in **Figure 4**.

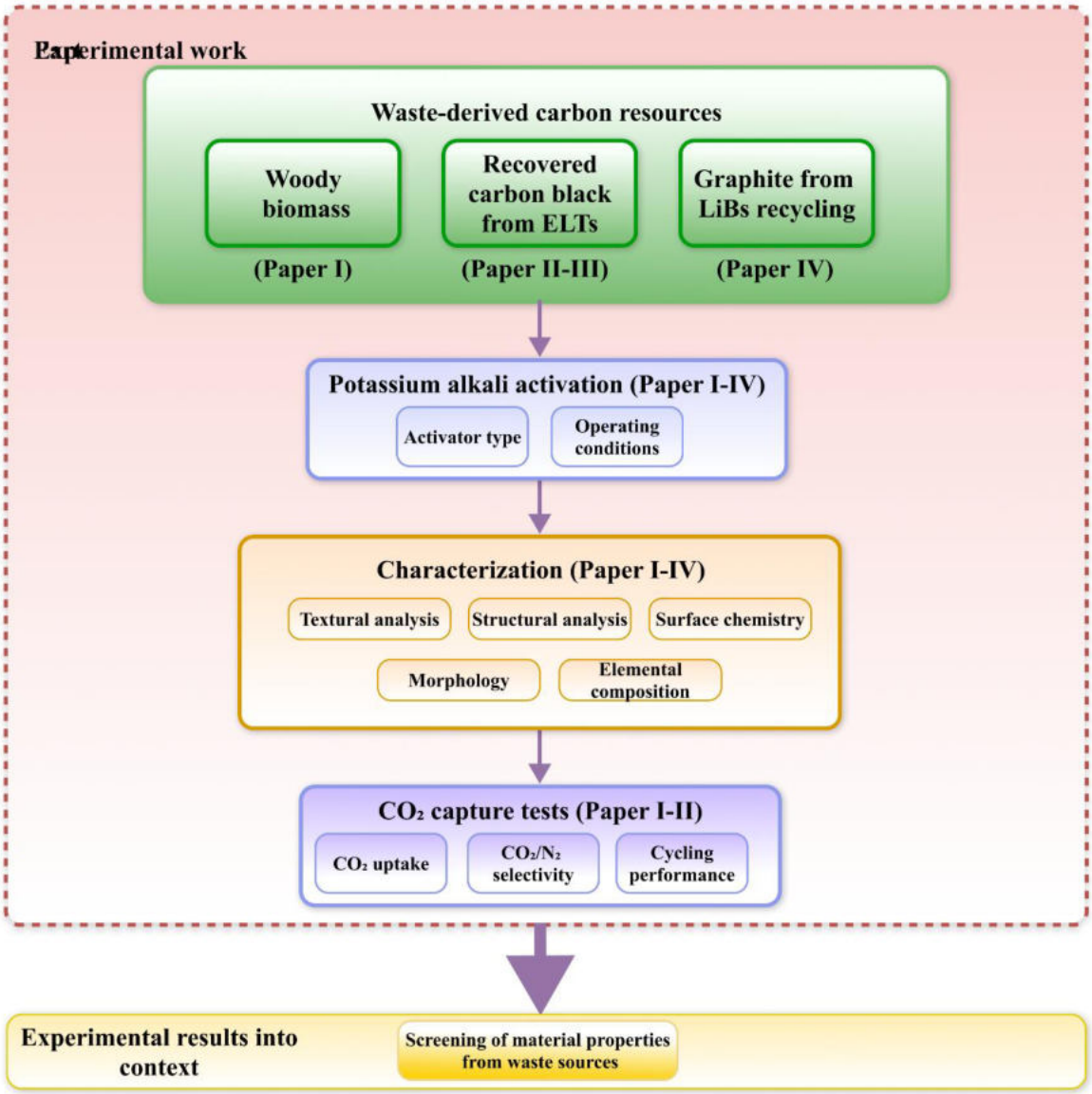

Figure 4. Overview of the research pathways and their connections to the papers included in this thesis.

Paper I focuses on the preparation of activated carbons from woody biomass using KOH, $K_2C_2O_4$, and their mixture as activating agents. The study compares the influence of these activators on pore formation, surface features, and CO_2 adsorption behavior, emphasizing the potential of $K_2C_2O_4$ as a more environmentally friendly alternative to conventional KOH activation. The work provides a foundation for understanding how activation conditions control the textural and CO_2 adsorption characteristics of highly surface and microporous biomass-derived carbons.

Paper II introduces the use of rCB from industrial-scale end-of-life tire pyrolysis as a carbon precursor. KOH was used as the activating agent to develop porous structures suitable for gas adsorption. The study includes characterization of the produced materials and evaluates their CO_2 capture performance in terms of adsorption capacity, selectivity, and cyclic stability. The work demonstrates the potential of rCB as a reliable and scalable raw material for activated carbon production and highlights its suitability for environmental applications.

Paper III continues the investigation of recovered carbon black by testing different potassium salts, such as KCl, K_2CO_3, CH_3COOK, and $K_2C_2O_4$, as activating agents. The work compares the effectiveness of the different salts and examines how temperature, activation time, and activator ratio affect the development of porosity and surface properties. The study helps identify the most suitable conditions and activators for improving the quality of carbon materials produced from industrial residues.

Paper IV extends the research to high-technology waste by converting graphite recovered from the black mass (NMC 111) of spent lithium-ion batteries into activated carbons using KOH. The study focuses on structural and surface changes during activation and demonstrates a sustainable route for transforming hazardous graphite waste into functional porous carbons with potential use in environmental and energy-related applications.

Together, the four papers present a consistent research path that connects the production of porous carbons from renewable, industrial, and technological waste sources. The thesis contributes to developing sustainable methods for converting carbon-rich residues into useful materials, supporting circular economy goals and potential CO_2 capture applications.

2.3 Scientific contribution

This thesis contributes to the development of sustainable ACs from biomass and industrial waste streams for potential CO_2 capture applications. The work also deepens the understanding of how potassium-based activation influences pore development, surface chemistry, and structure across different precursors. A unifying motivation behind the research is the close link between CO_2 emissions and the generation of carbon-rich byproducts in energy- and transport-intensive sectors. Both sectors are major CO_2 emitters and simultaneously produce substantial waste streams that require responsible management. Connecting these two challenges through the valorization of waste materials into functional adsorbents offers a pathway toward more sustainable industrial practices. Designing activation routes that are

energy efficient, rely on accessible salts, and can be broadly applied to diverse carbon-rich residues is therefore a crucial step in aligning CO_2 capture with circular economy principles.

The main contributions of this thesis are:

- Establishing activation strategies for biomass using KOH, $K_2C_2O_4$, and their mixture, highlighting the more environmentally friendly character of potassium oxalate.
- Extending KOH activation to rCB from end-of-life tires, including detailed characterization and CO_2 adsorption assessment.
- Comparing different potassium salts (KCl, K_2CO_3, CH_3COOK, and $K_2C_2O_4$) to determine their influence on porosity and surface properties of rCB.
- Demonstrating the valorization of graphite from lithium-ion battery black mass into functional porous carbons using KOH activation.
- Providing a unified understanding of potassium-assisted activation across renewable, industrial, and technological carbon sources.

Together, these studies demonstrate how coupling CO_2 capture with waste-stream valorization can support the transition toward circular economy principles and guide the development of more sustainable processes within carbon-intensive industrial sectors.

3. Theoretical background

3.1 Precursors for ACs production

The diversity of waste-derived precursors available for activated carbon production reflects the significant differences in chemical composition, structural characteristics, and practical processing constraints among the different precursors. To provide a structured comparison, **Table 2** summarizes representative feedstock categories explored in this thesis, highlighting their carbon content, compositional features, industrial handling limitations, and current recycling levels.

Table 2. Comparison of waste-derived feedstocks for activated carbon production.

Feedstock	Chemical and structural content	Restrictions for material use	Carbon intensity (C content, %)	Activated carbon production scale from this source
Biomass waste	Predominantly cellulose (35–50%), hemicellulose (20–35%), lignin (10–30%); minor ash, extractives, alkali and alkaline earth metals	Seasonal variability, heterogeneous composition, high moisture content, ash-related fouling, transport logistics, land-use competition	45–55% (dry basis)	Strong growth expected due to low-cost feedstock availability
End-of-life tires	Crosslinked elastomers, carbon black (30–35%), steel (~10–15%), additives (ZnO, sulfur, oils)	Hazardous classification, heavy metal residues, strict emissions regulations for pyrolysis, product quality standardization	70–85% (pyrolytic carbon black fraction)	Expected increase with rCB upgrading technologies
Lithium-ion batteries	Graphite (12–21%), cathode oxides, Cu/Al residues, PVDF binder, electrolyte salts	Hazardous waste classification, fluorinated binders, metal contamination, purification complexity, safety regulations	Graphite fraction: 90–99% C (purified); black mass overall: 20–30% C	Mostly pilot and demonstration scale

3.1.1 Biomass waste - a growing constraint and a carbon feedstock opportunity

Biomass is abundant in terrestrial and aquatic ecosystems and is also produced as industrial waste. The World Bioenergy Association estimates global standing biomass resources at approximately 1.804 trillion tonnes [19]. Annual biomass generation fluctuates strongly across seasons and regions due to climate, land management, and the distribution of cropland and forest, particularly in Europe and North America, but overall has increased over the past 22 years [20]. In 2022, EU biomass supply totaled ~1.2 billion tons of dry matter (tdm), dominated by primary biomass (directly harvested plant matter and residues) at 82%, followed by secondary biomass (processing by-products) at 7% and recovered or tertiary biomass (post-consumer waste streams) at 11% [21]. Within the primary fraction, agricultural crops, residues, and grazed biomass represented 67%, wood 33%, and fisheries and aquaculture <0.3% (dry matter). Beyond these primary inputs, additional residual streams arise from agro-industrial processing, livestock and industrial activities, sewage treatment, and municipal solid waste (MSW), which generate additional recoverable biomass residues. The recovery and use of biomass waste can partly displace fossil-based inputs, support rural development, and alleviate resource constraints. This recovery, however, is often limited by geographic dispersion, feedstock heterogeneity, and seasonal availability, which collectively increase the cost and emissions connected to collection, storage, and transport requirements and frequently result in material underutilization. On a global scale, wood-based biomass wastes are generated at ~4.6 Gt per year, with ~20% attributed to losses during production and processing, underscoring both the magnitude of the stream and the inefficiencies embedded in current value chains (**Figure 5**) [22].

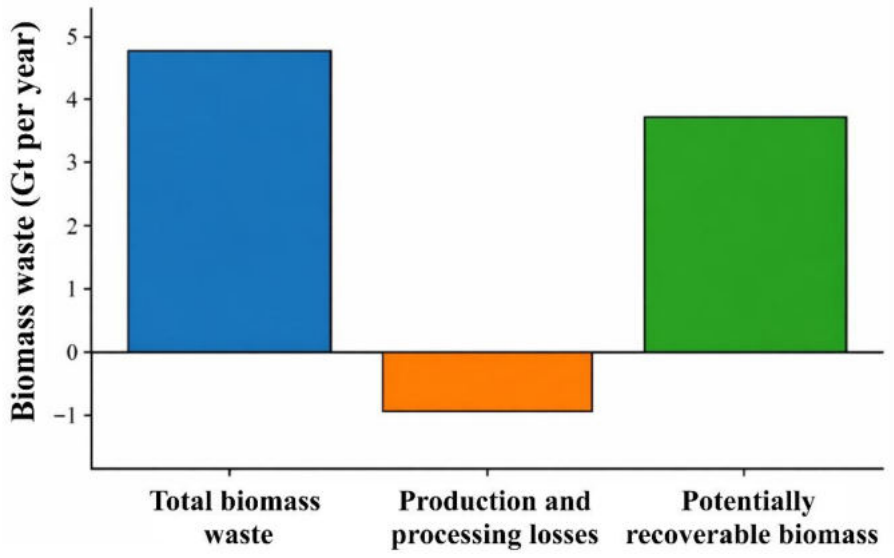

Figure 5. Mass balance of global wood biomass waste: total generation, losses, and potentially recoverable fraction.

The use of biomass-derived carbons and char-containing materials is gaining momentum across industries, as environmental compliance and sustainability targets increasingly prioritize lower emissions and cleaner production. Since wood represents a substantial fraction of primary biomass resources, forestry operations inherently generate large quantities of residual materials, including branches, treetops, bark, and low-grade roundwood [23], which are well suited for thermochemical conversion processes such as combustion, gasification, pyrolysis, and hydrothermal treatment [24]. In parallel, industrial processing produces significant volumes of secondary biomass, including sawdust and process-derived bark, forming carbon-rich by-products suitable for valorization. These streams represent particularly relevant feedstocks for the production of biochar and activated carbon, offering a pathway to partially substitute fossil-derived carbon materials.

3.1.2 End-of-life waste tires - valorization as a secondary carbon source

It is estimated that over 1 billion tires are manufactured and discarded worldwide each year, accounting for approximately 2% of total global solid waste generation [25]. The rapidly increasing accumulation of ELTs represents a persistent management challenge due to their durability, complex composition, and resistance to natural degradation, necessitating resource-efficient recovery strategies aligned with circular economy objectives. Effective ELT management requires coordinated action across the tire value chain, including manufacturers, recyclers, and regulatory bodies, to enable scalable material valorization pathways [26]. The ELT management challenge is further intensified by the global shift toward electric vehicles (EVs), which, due to their higher torque and vehicle weight, experience accelerated tire wear. Consequently, EV adoption is expected to increase the total volume of ELTs generated annually. For instance, in the United States, approximately 315 million ELTs are generated each year, and this figure is projected to rise by 12% to around 352 million by 2030 due to the growing EV market [27].

Globally, the management of ELTs follows several established pathways, including recycling (40–50%), energy recovery (30–40%), reuse (10–20%), and landfilling (5–10%), with exact shares depending on local regulations, technological maturity, and economic conditions (5–10%) [28, 29]. Despite progress in recycling, significant regional disparities remain. Developed countries operate advanced recycling and recovery systems, whereas many emerging economies still depend on landfilling and open dumping due to limited infrastructure

and weak policy enforcement. These practices pose serious environmental and health risks, as tires are chemically stable and degrade extremely slowly (releasing hazardous constituents such as heavy metals, polycyclic aromatic hydrocarbons, and organic additives), leading to soil and groundwater contamination. Uncontrolled burning releases toxic gases such as carbon monoxide, dioxins, and furans [30], while large stockpiles increase fire hazards and create breeding sites for disease-carrying insects.

Among existing treatment methods, pyrolysis has emerged as one of the most promising options for sustainable ELT management. During pyrolysis tires are decomposed in an oxygen-deficient environment to produce three main products: liquid oil, gas, and a solid carbonaceous residue known as pyrolytic carbon black (CBp) [31]. The solid fraction accounts for approximately 35–40% of the total output and is a critical factor determining the overall economic viability of the process. To obtain higher-value carbon materials, the solid pyrolysis residue must undergo further purification and refinement, yielding recovered carbon black. This material possesses properties comparable to those of virgin carbon black (vCB), which is conventionally produced through the partial combustion of petroleum-derived hydrocarbons [32]. Since vCB production is energy-intensive and emits substantial amounts of CO_2, substituting it with rCB provides both environmental and economic benefits. ELTs therefore represent a valuable secondary carbon resource capable of reducing dependence on fossil-based raw materials and supporting low-carbon manufacturing.

The quality of rCB depends strongly on tire composition, process parameters, and post-treatment efficiency. CBp typically contains additivies (1-3%), inorganic impurities (10-15%) such as zinc oxide (ZnO), silica (SiO_2), and sulfur compounds (e.g., FeS, ZnS), which can limit its performance compared with vCB, as shown in **Figure 6**. Achieving consistent and high-purity rCB requires optimization of the entire process chain, encompassing feedstock selection, pyrolysis control, and purification techniques [33]. Supportive policy measures and market incentives are essential to encourage the large-scale utilization of rCB and to establish standards for its industrial application.

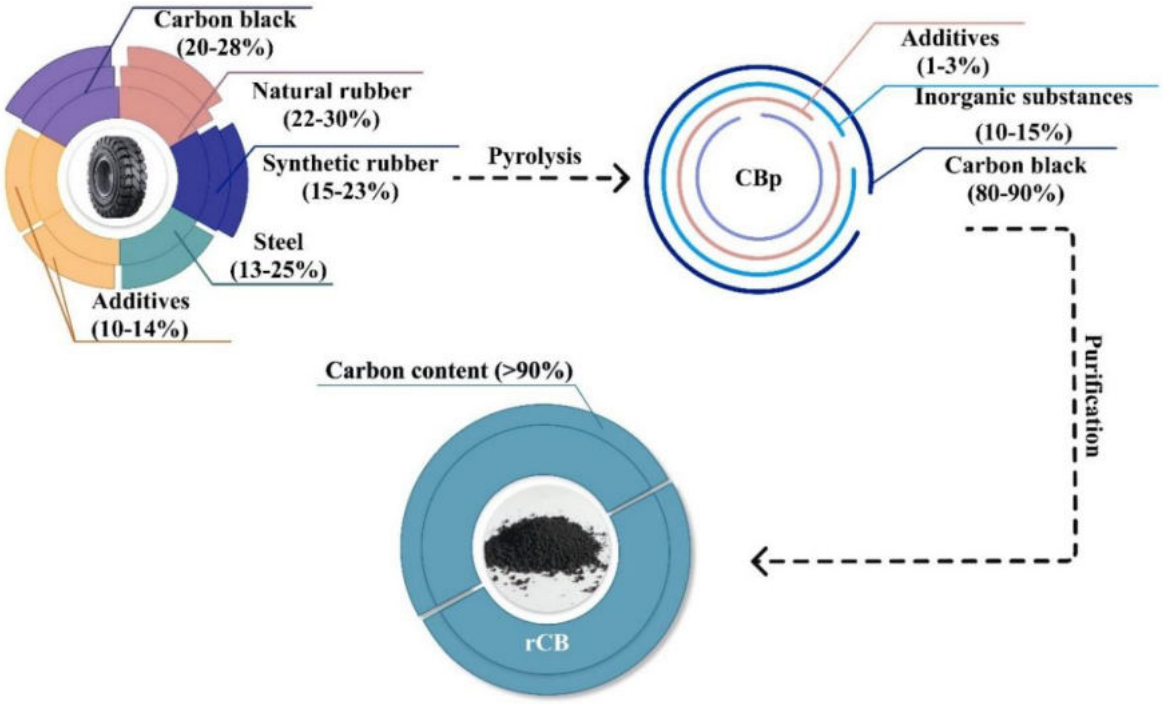

Figure 6. Schematic representation of the recycling pathway for end-of-life tires and the purification of pyrolytic carbon black into recovered carbon black, highlighting the transformation in material composition.

3.1.3 Lithium-ion batteries - graphite recovery and carbon feedstock utilization

The extensive integration of LiBs in electric vehicles and stationary storage systems has established them as a central technology in the transition toward sustainable, low-carbon energy systems. This expansion is reflected in global electric cars sales, which exceeded 17 million units in 2024, accounting for more than 20% of total car sales worldwide. This momentum continued into 2025, when global EV sales surpassed 20 million units, representing over one quarter of all vehicles sold globally and highlighting the accelerating electrification of the automotive sector [34]. Although only a limited number of EV batteries have reached end-of-life (EoL) so far, recycling facilities already process substantial quantities of production scrap, and forecasts suggest that more than 1.2 million EV batteries will be retired annually by 2030, increasing to over 14 million per year by 2040 [35]. In view of this, the heterogeneous architecture of LIBs, containing critical metals, reactive electrolytes, and polymeric components, complicates safe end-of-life handling and recycling, creating material recovery and environmental control challenges [36].

LiBs typically consist of metallic casings, cathode and anode materials, electrolytes, separators, and polymeric binders [37]. Among the broad range of cathode formulations used

in lithium-ion batteries, the dominant ones are lithium iron phosphate (LFP), lithium nickel manganese cobalt oxide (NMC), lithium nickel cobalt aluminum oxide (NCA), and spinel lithium manganese oxide (LMO) [38]. Among the enumerated cathode types, NMC ($LiNi_xMn_yCo_{1-x-y}O_2$) continues to dominate the automotive sector, largely due to their high specific energy, which typically reaches 100-265 Wh/kg [39]. Their development has progressed toward increasingly nickel-rich compositions, exemplified by the transition from NMC 111 to NMC 622 and NMC 811, where nickel content rises while manganese and particularly cobalt fractions are reduced [40].

In response to these material recovery challenges, the European Battery Regulation aims to close the material loop by enforcing ambitious recovery targets of up to 95% for Co, Ni, and Cu and 80% for Li by 2031 [41]. The current recovery process comprises pretreatment activities (sorting, discharging, disassembly, and crushing), pyrometallurgical steps such as smelting and roasting, and hydrometallurgical processes based on leaching and selective extraction [42]. The shredding or crushing of spent cells produces black mass (BM), a mixed fraction of cathode (Li, Ni, Mn, and Co) and anode materials, together with Cu and Al collectors, and polyvinylidene fluoride (PVDF) binders (**Figure 7**) [43]. Despite accounting for roughly 20% of the battery mass, the graphite anode receives considerably less attention [44].

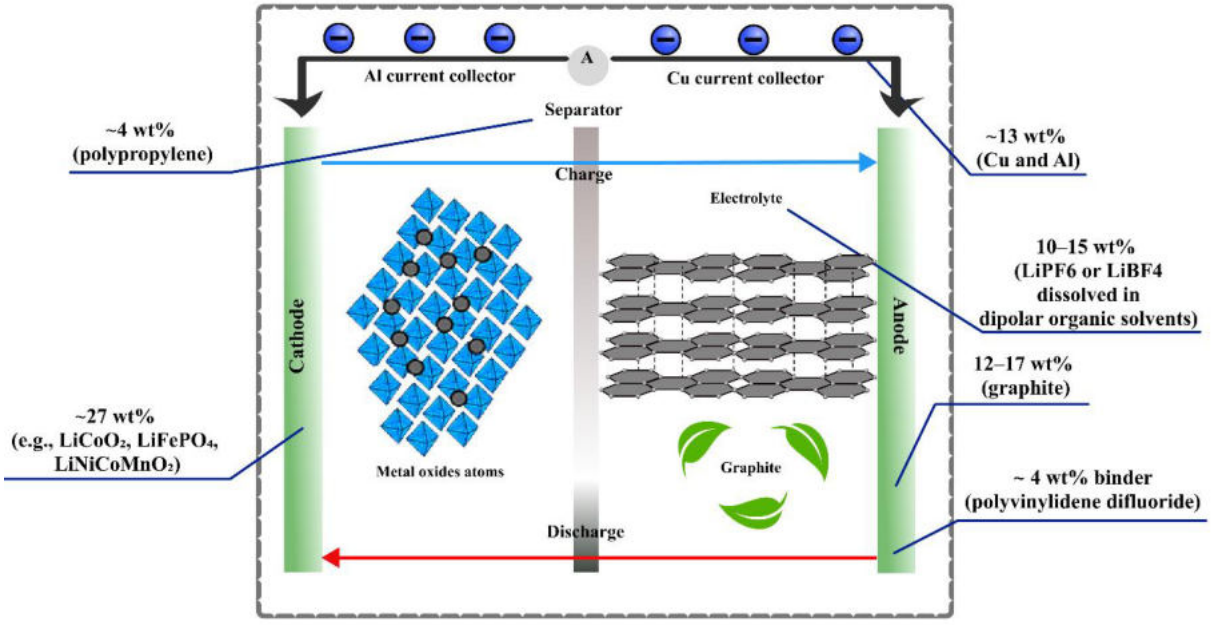

Figure 7. Structural overview of lithium-ion batteries in electric vehicles with specified material composition

Although graphite becomes the predominant component of black mass once metallic foils and polymers are removed, its recovery is often deprioritized due to the difficulty of

eliminating residual impurities left in the graphitic structure. Yet spent graphite remains a valuable and underutilized resource. Commercial anode graphite typically costs 8–13 USD kg^{-1}, accounting for 10–15% of the material cost in conventional LIBs, and spent batteries contain approximately 12–21 wt% graphite. These figures underscore the need for more comprehensive and resource-efficient recycling approaches [45]. The need for recovery is further amplified by projections from the World Bank, which estimate that by 2050 approximately 4.5 million tonnes of graphite will be required for low-carbon energy technologies, primarily LIBs, implying substantial growth in graphite consumption and corresponding waste generation [46]. Valorizing recovered graphite therefore represents a critical opportunity within a circular battery economy, as integrating its recovery into existing recycling infrastructure would reduce the environmental burden of black mass disposal while providing high-purity carbon precursors for advanced applications [47].

3.2 Activation of carbon materials

Carbon materials obtained after carbonization generally exhibit limited surface area and insufficient porosity for adsorption applications. Activation is therefore required to restructure the carbon framework and generate accessible pore networks [48]. Depending on the nature of the activating medium, activation is commonly classified into physical and chemical approaches, which differ significantly in their mechanisms, processing conditions, and degree of control over pore development.

3.2.1 Physical activation

Physical activation relies on the controlled gasification of carbon in the presence of oxidizing gases such as steam, CO_2, air or limited oxygen-containing mixtures. This process is typically conducted at high temperatures, generally in the range of 750–1000 °C, where porosity develops through gradual carbon burn-off [49]. Two principal routes can be distinguished, depending on whether activation is coupled with thermochemical conversion or conducted as a separate stage, corresponding to the direct and two-step strategies (**Figure 8**). While physical activation can effectively increase total porosity, the process is largely governed by reaction time and burn-off extent, which limits the possibility for precise control over pore size and distribution. Moreover, the high thermal demand and prolonged activation times associated with gas-phase routes impose substantial energy penalties, making physical activation less attractive for applications requiring finely tuned porosity.

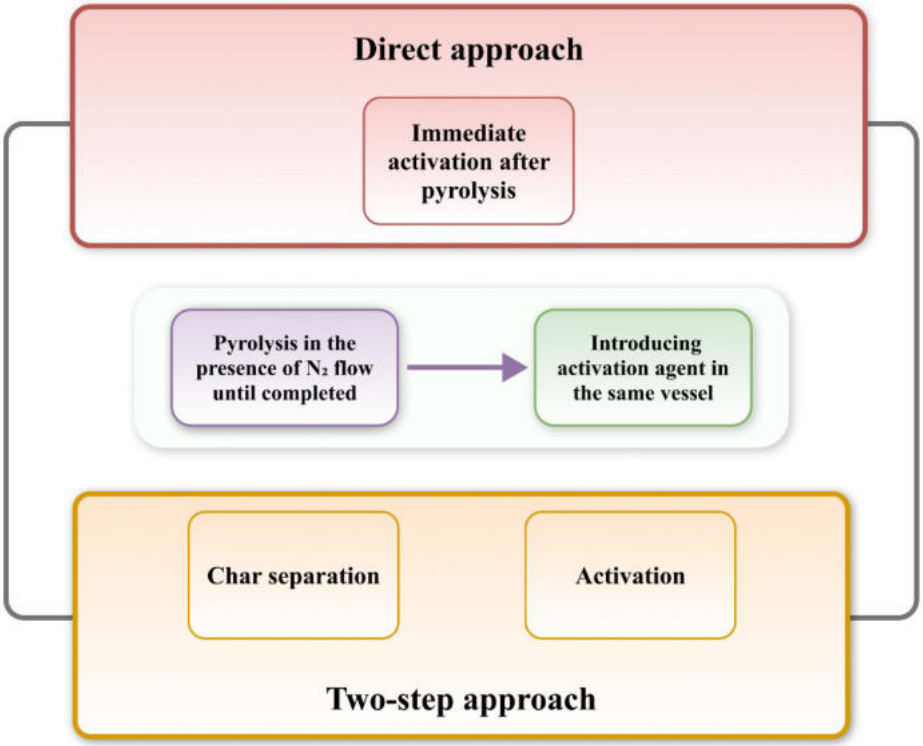

Figure 8. Schematic representation of the two physical activation routes distinguished by the mode of thermal conversion: direct and two-step approaches.

3.2.2 Chemical activation

Chemical activation is based on the interaction between a carbon precursor and a chemical agent, followed by heat treatment under an inert atmosphere. During this process, porosity develops through reactions whose nature depends on both the precursor and the activating agent. These include dehydration and cross-linking reactions, as well as redox driven carbon etching and lattice expansion, which collectively restructure the carbon framework. The extent and nature of pore development depend on several parameters, including precursor composition (C, H, O, N content), activation temperature (450–900 °C), residence time (1-4 h), heating rate (5-10 °C/min), impregnation conditions (dry mixing or wet impregnation), the precursor-to-activator ratio (1:1 to 1:6), and the activating agent employed (**Figure 9**). Compared with physical activation, chemical activation offers several advantages, including lower activation temperatures and shorter processing times, increased carbon yield, enhanced pore development, reduced energy and operational demands, and more effective generation of microporosity [50].

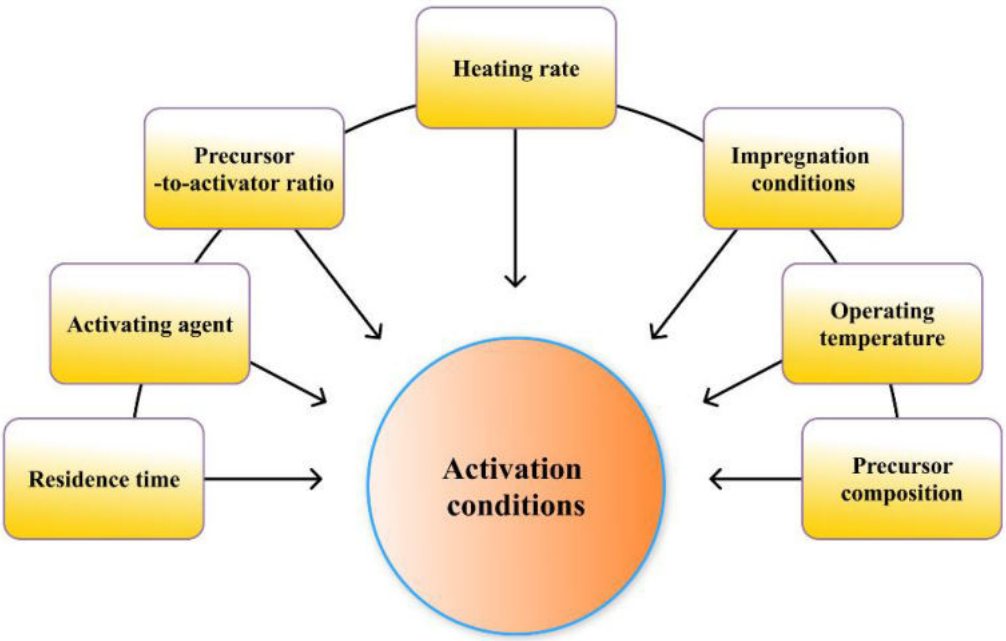

Figure 9. Key parameters in chemical activation affecting the properties of ACs.

Chemical activating agents are generally classified as alkaline agents (KOH, NaOH, K_2CO_3, Na_2CO_3, K_3PO_4), acidic agents (H_3PO_4, H_2SO_4, HNO_3), or Lewis-acid salts ($FeCl_3$, $ZnCl_2$,). These classes differ in their activation mechanisms and consequently in the pore structures they generate. Alkaline activators exhibit stronger chemical interaction with carbon matrices and are therefore more effective in producing microporous structures. In particular, KOH is considered to be highly efficient because it induces lattice expansion and carbon etching, as elemental potassium formed in situ intercalates into the carbon lattice and promotes structural expansion [51], but it can potentially cause excessive burn-off and reduced yield at high loadings [52]. This has led to increasing interest in alternative potassium salts, such as $KHCO_3$, K_2CO_3 and $K_2C_2O_4$, which typically operate at lower temperatures and provide improved yield retention and reduced environmental impact.

3.3 ACs applications

Activated carbons are versatile adsorbents widely used in water treatment to remove color, odor, taste, and diverse organic and inorganic contaminants, with additional applications in wastewater remediation (dyes [53-55], heavy metals [56-58], and phenolic compounds [59-61]), gas purification (CO_2 [62, 63], H_2S [64-66], SO_2 [67-69], NO_x [70-72], and volatile organic compounds [73-75]), and chemical, food, and pharmaceutical processing. Effective AC performance requires carefully tailored properties that satisfy application-specific technical and economic criteria. The key performance determinants can be grouped as follows [76, 77]:

- Adsorption capacity: determining the maximum uptake of target species.
- Selectivity toward specific adsorbates: enabling preferential removal in multicomponent systems.
- Pore characteristics, including pore size distribution and accessibility: mass transfer control and effective surface utilization.
- Surface chemical nature: influencing adsorbate–adsorbent interactions.
- Adsorption–desorption kinetics: governing uptake rates and process reversibility.
- Mechanical properties: ensuring resistance to attrition and structural degradation during operation.
- Chemical and thermal stability: allowing operation under aggressive chemical environments and elevated temperatures.
- Regenerability: reflecting the ability to restore adsorption performance after use.
- Stability over multiple adsorption–desorption cycles: indicating long-term durability.
- Production costs: affecting economic feasibility and large-scale deployment.

These requirements can be addressed through controlled material design, primarily by selecting appropriate activation strategies, including physical and chemical activation.

4. Experimental section

This research focuses on the production of high-performance activated carbons from diverse carbonaceous waste streams, including biomass, recovered carbon black from end-of-life tires, and graphite derived from lithium-ion battery recycling. Emphasis is placed on chemical activation strategies using potassium-based agents and their role in tailoring pore structure, surface chemistry, and adsorption behavior.

This section describes the complete experimental workflow, from raw material recovery and activation to comprehensive physicochemical characterization and adsorption performance evaluation. Each subsection provides a structured overview of the methodologies used to link material design with functional performance in gas separation. References to the corresponding publications are introduced within the relevant material-specific sections.

4.1 Materials

This thesis is based on three distinct carbonaceous waste streams: biomass, recovered carbon black from end-of-life tires, and graphite derived from lithium-ion battery recycling. **Figure 10** outlines the processing routes applied to the carbonaceous waste streams considered

in this thesis, illustrating their conversion into activated carbons for CO_2 capture. In this context, **Table 3** summarizes the main elemental composition of the examined waste streams. The values reported are normalized elemental contents, with the oxygen content calculated based on mass balance.

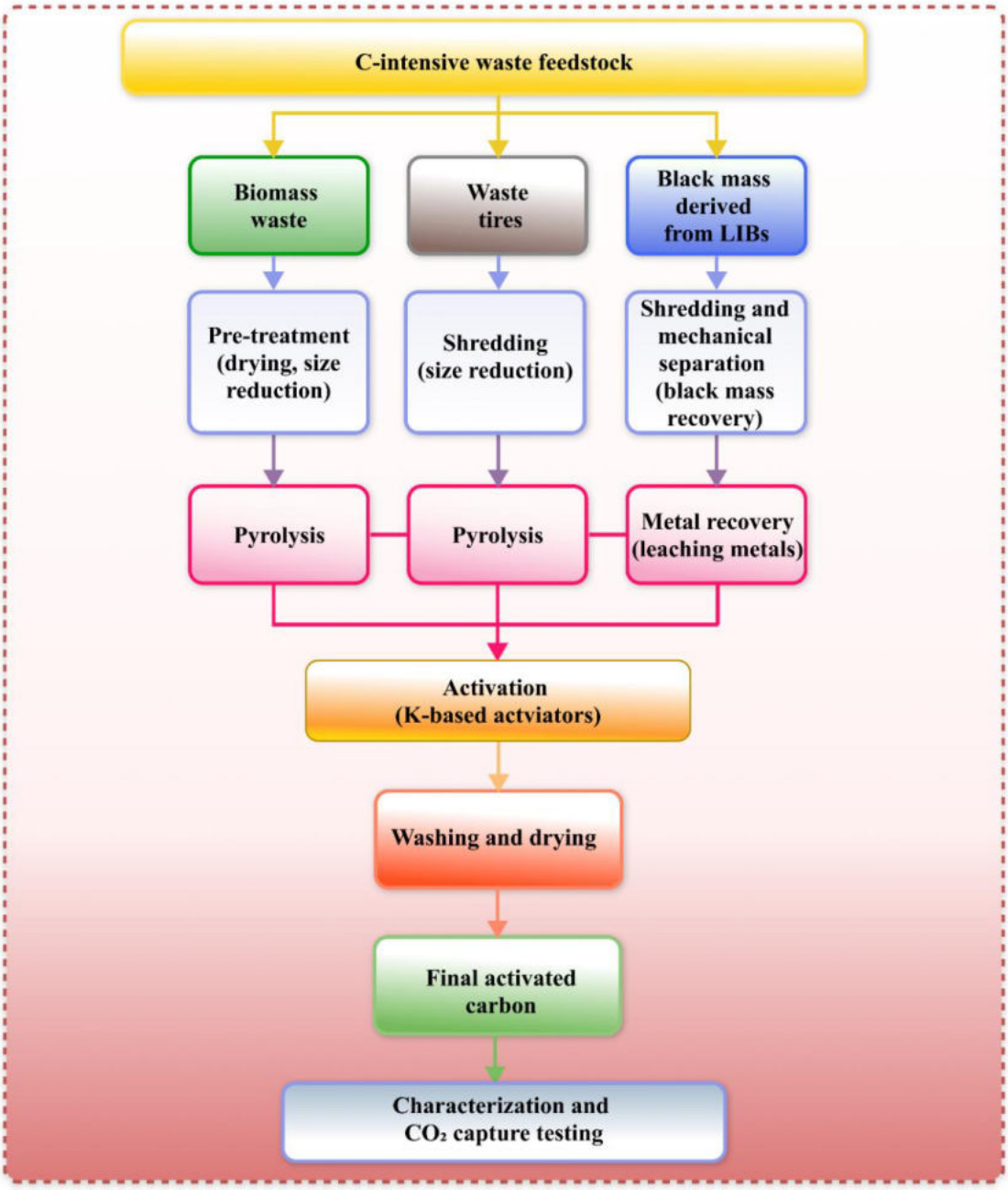

Figure 10. Integrated pathway for valorization of C-intensive waste feedstocks into activated carbons.

Table 3. Elemental composition of the carbonaceous waste streams considered in this thesis

Element	Composition (wt.%)		
	Woody biomass	Recovered carbon black	Recovered graphite
C	50.00	92.53	72.18
H	6.00	1.16	-
N	0.11	0.42	-
S	0.89	0.71	-
O	43.00	5.18	9.13

4.1.1 Woody biomass

Pine wood was used as the biomass precursor in Paper I and was obtained as residual wood fractions originating from conventionally harvested coniferous trees processed for energy applications. The material was collected during routine fuel handling at the plant facility of Chalmers University of Technology (Sweden), following standard forestry processing and mechanical pre-conditioning procedures, listed below and presented in **Figure 11**.

- **Forestry processing and wood preparation**

Following tree felling, the wood was sectioned and processed into fuel-grade pieces through standard forestry and wood-handling operations.

- **Mechanical pre-conditioning of biomass**

Pine wood was mechanically processed to reduce particle size and improve uniformity prior to activation. Milling produced a fine powder (<0.5 mm), facilitating consistent dry mixing and subsequent thermal treatment.

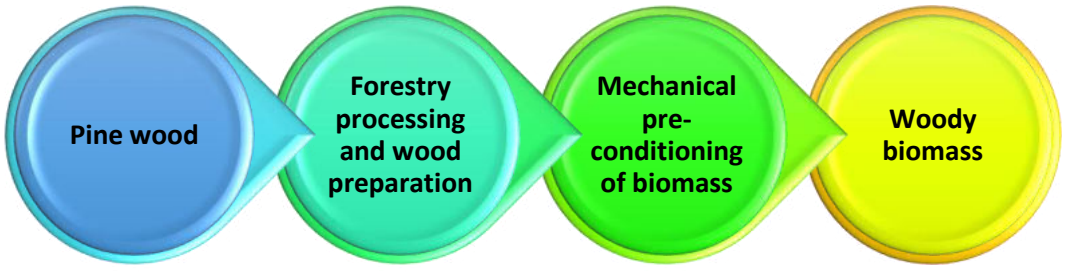

Figure 11. Schematic overview of the main steps involved in woody biomass pretreatment prior to activation.

It should be noted that the biomass had not been subjected to any chemical treatments, preservation processes, or surface modifications prior to use, ensuring that it remained a raw and unaltered lignocellulosic feedstock.

4.1.2 Recovered carbon black (rCB)

The recovered carbon black used in this work was derived from ELTs and served as the primary precursor material in **Paper II** and **Paper III**. The rCB was produced via industrial-scale pyrolysis of ELTs, followed by a sequence of post-treatment and purification steps designed to enhance its physicochemical quality, as illustrated in **Figure 12.** As a result of these processing steps, the obtained rCB exhibited an average particle size of approximately 30 μm, with particle sizes ranging from 15 to 100 μm and a dominant fraction between 73 and 80 μm.

- **Pyrolysis for pyrolytic char production**

Pyrolysis is the chosen thermochemical process in which ELTs were decomposed at temperatures exceeding 500 °C under an oxygen-free atmosphere. This inert environment prevented combustion and promoted the controlled breakdown of polymeric components, including natural and synthetic rubbers composed of long-chain macromolecules. The process yielded three main fractions: a solid carbonaceous char, a condensable liquid oil, and a non-condensable gaseous phase.

- **Post-pyrolysis processing**

Following pyrolysis, the resulting material contained various contaminants, including residual ash, organic residues, inorganic compounds, and partially reacted or unreacted hydrocarbons, as well as elements such as Zn, Si, Ca, S, and Al. Therefore, additional post-pyrolysis processing steps based on chemical or physical treatments were required to reduce these impurities. The removal of inorganic species enhanced the quality and applicability of the char by increasing the elemental carbon content and improving porosity.

- **Purification steps**

To convert pyrolytic char into commercially viable recovered carbon black, a series of purification and post-treatment steps was applied. These processes included concentrated pickling, devolatilization, milling and pulverization and, when required, pelleting, to further remove residual impurities, control particle size distribution, and reduce variability in material quality.

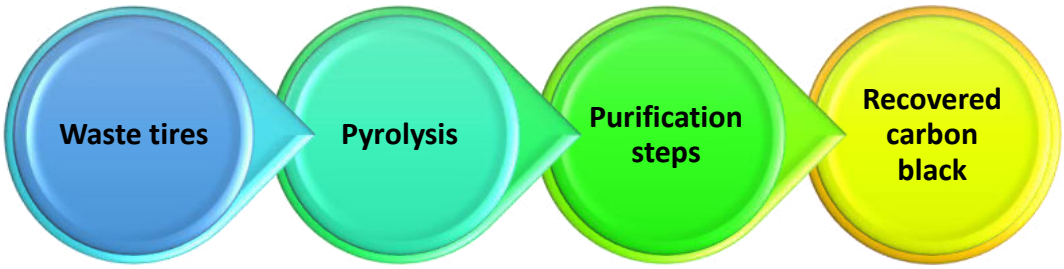

Figure 12. Overview of the general steps in rCB production from waste tires.

4.1.3 Graphite derived from LiBs recycling

The graphite used in this work was derived from end-of-life lithium-ion battery packs with NMC 111 chemistry and served as the primary precursor material in **Paper IV**. The material originated from industrial battery recycling streams and was obtained following battery discharge, disassembly, and mechanical processing carried out by industrial partners. A subsequent pre-treatment route was applied to upgrade the black mass and enable graphite recovery, as illustrated in **Figure 13**.

➢ **Industrial processing of lithium-ion batteries**

As part of the industrial recycling workflow, NMC 111 battery packs underwent controlled discharge, dismantling, and mechanical separation to isolate a fine particulate fraction known as black mass. This intermediate product represents a mixed stream containing electrode materials and served as the starting point for the subsequent graphite recovery and purification steps.

➢ **Post-processing of black mass**

The obtained black mass was further sieved to particle sizes below 500 µm to improve homogeneity and concentrate the carbonaceous fraction. After this treatment, the material remained a complex mixture of graphite, residual active materials, other inorganic species, and polymeric binders.

➢ **Purification and conditioning steps of black mass via acid leaching**

A purification and conditioning route based on acid leaching using H_2SO_4 in the presence of H_2O_2 was applied to reduce impurity content and enable the recovery of a graphite-rich precursor suitable for subsequent activation.

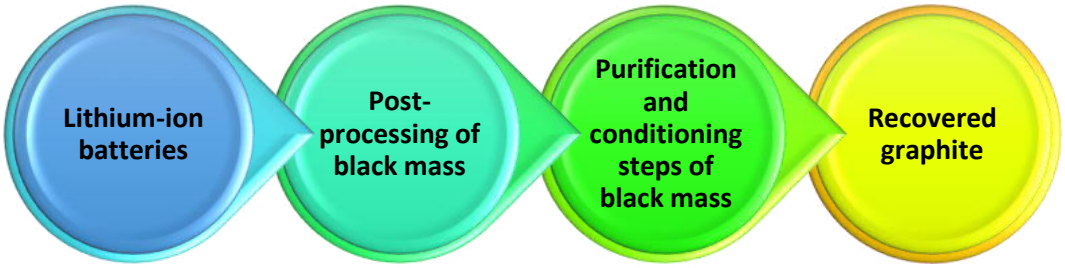

Figure 13. Process chain for graphite recovery from LiBs.

4.2 Analytical techniques

In this thesis, complementary analytical techniques were used. **Table 4** provides an overview of these techniques including their underlying principles, analytical outputs, and position within the characterization workflow.

Table 4. Summary of analytical techniques used in this thesis.

Technique	Theoretical basis	Information obtained	Role in workflow
Ultimate analysis	Combustion-based elemental quantification	C, H, N, S, O composition	Initial precursor and final material characterization
Proximate analysis	Thermogravimetric mass-loss analysis	Moisture, volatile matter, fixed carbon, ash	Thermal behavior and material classification
N_2 adsorption–desorption	Physisorption and multilayer adsorption	Surface area, pore volume, mesopore distribution	Post-activation structural evaluation
CO_2 adsorption	Micropore filling at controlled temperature	Micropore volume and pore size distribution	Detailed microporosity assessment
FT-IR spectroscopy	Infrared vibrational absorption	Surface functional groups	Chemical surface characterization
Raman spectroscopy	Inelastic photon scattering (Raman effect)	Structural order, defect density, graphitization	Carbon framework evaluation
SEM–EDS	Electron–matter interaction and X-ray emission	Morphology and elemental distribution	Microstructural and compositional analysis
XRD	X-ray diffraction from crystalline planes	Phase composition and crystallinity	Structural evolution assessment
XPS	Photoelectron emission from surface atoms	Surface elemental states and bonding	Surface chemistry evaluation

4.2.1 Ultimate and proximate analysis

Ultimate analysis is employed to determine the elemental composition of materials, typically quantifying carbon, hydrogen, nitrogen, sulfur, and oxygen calculated by difference [78]. The analysis is commonly based on the Dumas combustion principle, in which the sample undergoes rapid and complete oxidation through flash combustion. The resulting gaseous products are separated chromatographically and quantified using a thermal conductivity detector (TCD), generating signals proportional to the concentration of each element. Ultimate analysis provides fundamental insight into chemical composition.

Proximate analysis, in contrast, assesses the bulk physical composition by determining moisture content, volatile matter, fixed carbon, and ash. This analysis is frequently conducted using thermogravimetric methods, where mass changes are monitored as a function of temperature, allowing evaluation of thermal behavior and compositional fractions. Proximate analysis is particularly informative for assessing thermal stability, combustion behavior, and handling characteristics of carbonaceous materials.

In this thesis, ultimate and proximate analyses were applied in **Papers I–IV** to both precursor wastes and the resulting activated carbons. Together, these techniques provided complementary information on elemental composition and physical structure, supporting optimization of activated carbons.

4.2.2 N_2 and CO_2 adsorption-desorption isotherm analysis

Gas adsorption is a widely applied technique for characterizing the textural properties of porous materials, including specific surface area, pore volume, and pore size distribution (PSD). The method is based on controlled adsorption of a probe gas using dedicated instrumentation comprising a sample cell, precise pressure regulation, and gas dosing systems. Incremental amounts of adsorbate are introduced, and equilibrium uptake at each pressure step is used to define discrete points along the adsorption isotherm. During measurement, gas molecules physisorb onto the solid surface and interact with the pore walls through physisorption mechanisms that depend on pore size and adsorbate–adsorbent interactions at pressures below the saturation pressure (P_0) [79]. At low relative pressures (P/P_0), adsorption proceeds through micropore filling in microporous materials and monolayer formation on external and nonporous surfaces.. With increasing pressure, multilayer adsorption develops on open surfaces, while capillary condensation may occur in mesopores, producing a characteristic plateau in the isotherm [80]. Upon pressure reduction, desorption often follows a different path,

particularly in mesoporous materials, resulting in hysteresis due to delayed evaporation of condensed adsorbate. This hysteresis loop closes once condensed adsorbate is removed and equilibrium surface coverage is restored.

According to the IUPAC classification, six fundamental types of adsorption isotherms are distinguished, as presented in **Figure 14**. Type I isotherms describe adsorption in microporous materials and are characterized by rapid uptake at low pressures followed by saturation, consistent with the Langmuir model. Type II isotherms represent reversible multilayer adsorption on nonporous or macroporous solids, featuring a distinct inflection point that marks completion of monolayer coverage and the onset of multilayer adsorption. Type III isotherms arise from weak adsorbent–adsorbate interactions and show enhanced adsorption at higher relative pressures due to adsorbate–adsorbate interactions. Type IV and V isotherms are associated with mesoporous materials and exhibit hysteresis caused by capillary condensation; Type IV follows Brunauer–Emmett–Teller (BET) behavior at low pressures, while Type V reflects weaker surface interactions. Type VI isotherms, typical of uniform nonporous surfaces, display stepwise multilayer adsorption.

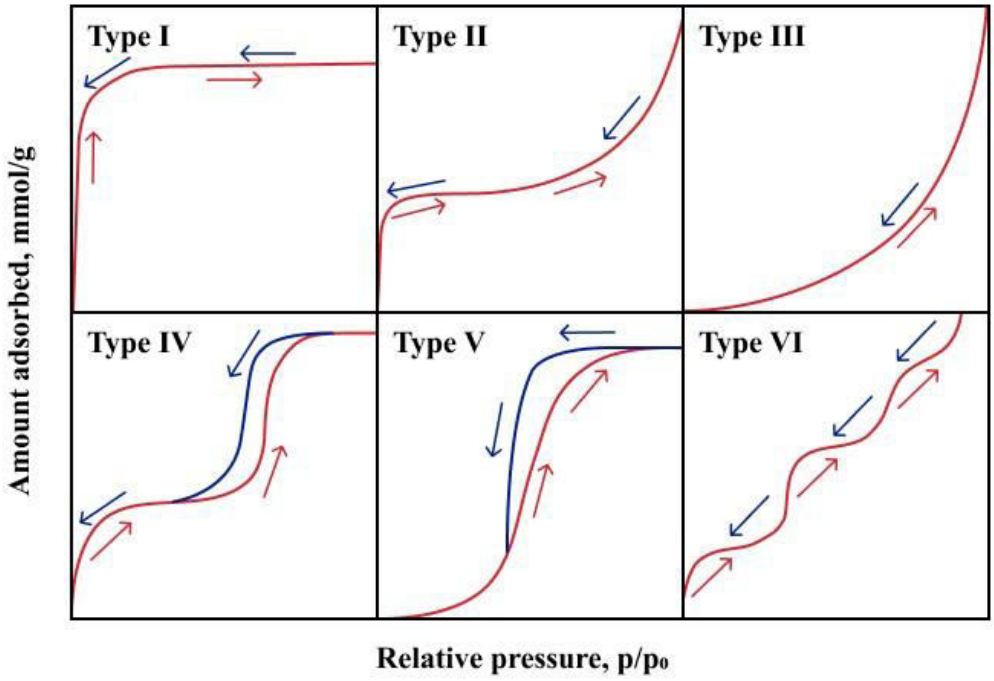

Figure 14. Classification of adsorption-desorption isotherms (red arrows: adsorption course; blue arrows: desorption course) [49].

Textural parameters are commonly derived from N_2 adsorption measurements at −196 °C. The total pore volume is estimated from the adsorbed N_2 quantity at a relative pressure close to saturation ($P/P_0 \approx 0.99$), where pores are commonly assumed to be filled by condensed

adsorbate[81]. The specific surface area is calculated using the BET equation, typically applied within the relative pressure range of 0.05–0.35, based on the formation of a complete monolayer followed by multilayer adsorption and selected according to established consistency criteria [82]. Since N_2 diffusion into ultramicropores may be kinetically limited at cryogenic temperatures due to kinetic restrictions arising from its molecular size(0.364 nm), quadrupole moment and low measurement temparature, CO_2 adsorption at 0 °C is frequently employed as a complementary technique to probe micropores below approximately 1 nm. Combined N_2 and CO_2 adsorption data enable PSD analysis across different pore size regimes, typically 2–50 nm for N_2 and 0.3–1.4 nm for CO_2. These distributions are calculated using density functional theory (DFT), which accounts for pore geometry and adsorption thermodynamics to provide a detailed description of pore structure and volume contributions [83].

In this thesis, N_2 adsorption–desorption measurements were systematically applied in **Papers I–IV** to determine BET surface area, total pore volume, mesopore volume, micropore volume (<2 nm), and PSD of activated carbons. Additionally, CO_2 adsorption experiments were performed in **Papers I** and **II** to further quantify micropore volume (0.3–1.4 nm) and refine PSD analysis.

4.2.3 Fourier-transform infrared spectroscopy (FT-IR)

Fourier-transform infrared spectroscopy (FT-IR) is a vibrational spectroscopic technique that combines infrared radiation with Fourier transformation to obtain high-resolution spectral information. The method enables identification of chemical functional groups in organic, polymeric, and selected inorganic materials through characteristic absorption features observed in FT-IR spectra. An FT-IR spectrometer operates based on an interferometer, which constitutes its central component. Infrared radiation is divided into two beams: one reflected by a fixed mirror and the other by a moving mirror. The recombination of these beams generates an interference pattern that varies with mirror displacement and is recorded as an interferogram. This interferogram contains contributions from all infrared frequencies interacting with the sample and is mathematically converted into an absorption spectrum through Fourier transformation [84].

For activated carbons, FT-IR spectroscopy is particularly valuable for examining surface functional groups, which significantly influence adsorption behavior toward organic compounds, contaminants, and gaseous species in both aqueous and gas-phase environments. The presence and nature of oxygen-containing and other surface functional groups provide insight into surface chemistry and potential adsorption mechanisms.

In this thesis, FT-IR spectroscopy was used to analyze the surface chemistry of activated carbons in **Papers I-II**.

4.2.4 Raman spectroscopy

Raman spectroscopy is a non-destructive analytical technique that provides information on molecular structure, chemical bonding, and lattice vibrations of materials. The technique is based on the Raman effect, which arises from the inelastic scattering of incident photons by molecular vibrations, leading to an energy shift relative to the excitation light [85]. While most photons undergo elastic (Rayleigh) scattering without energy change, a very small fraction experiences inelastic scattering, producing characteristic energy shifts that correspond to specific vibrational modes of the material.

A Raman spectrometer primarily consists of a monochromatic laser source, which illuminates the sample. The scattered light is collected, spectrally filtered using a monochromator, and detected by a charge-coupled device (CCD) detector [86]. The resulting Raman spectrum presents signal intensity as a function of Raman shift, typically expressed in wavenumbers (cm^{-1}), and serves as a molecular fingerprint of the analyzed material. Raman spectroscopy is particularly well suited for carbon-based materials, including activated carbons, graphene derivatives, carbon nanotubes, and related structures, due to its sensitivity to carbon bonding environments and structural disorder.

In this thesis, Raman spectroscopy was employed to evaluate the structural features of activated carbons. The technique provided insight into the degree of graphitization and defect density of the carbon framework, as discussed in **Paper II** and **Paper IV**.

4.2.5 Scanning electron microscopy (SEM) coupled with energy-dispersive X-ray spectroscopy (EDS) analysis

Scanning electron microscopy (SEM) is a powerful imaging technique used to examine surface morphology and microstructural features of materials. An SEM system comprises three main components: an electron gun, which generates and accelerates the electron beam; an electron column, where electromagnetic lenses and apertures shape and focus the beam; and a sample chamber, in which interactions between the electron beam and the specimen occur [87].

High-quality imaging requires focusing of the electron beam to achieve a small probe size while maintaining sufficient beam current. This is accomplished through a combination of condenser and objective lenses, which control beam convergence and focus it at the specimen surface. When the electron beam interacts with the sample, several signals are generated,

including secondary electrons (SE), backscattered electrons (BSE), and characteristic X-rays. These signals originate from different interaction volumes and provide complementary information.

In this thesis, SEM–EDS was employed in **Papers I–IV** to examine the morphological features of activated carbons and to identify elemental composition and spatial distribution after activation. Particular attention was given to evaluating the distribution of potassium following chemical activation.

4.2.6 X-ray diffraction (XRD) analysis

X-ray diffraction (XRD) is a widely used analytical technique for qualitative and quantitative assessment of material structure, providing information on crystalline phases and degree of crystallinity. The technique is based on the constructive interference of X-rays scattered elastically by periodic lattice planes within a crystalline material [88]. In a typical XRD setup, polychromatic X-rays generated in an X-ray tube (commonly using Cu or Mo radiation) are monochromatized and directed toward the sample. Interaction of the incident beam with crystal lattice planes produces diffraction when the Bragg condition is satisfied, resulting in a characteristic diffractogram.

In this thesis, XRD was applied in **Paper I, Paper III,** and **Paper IV** to identify changes in the relative contributions of amorphous and graphitic-like crystalline structures during chemical activation using potassium-based activating agents. The technique provided insight into the influence of potassium compounds on the structural evolution of ACs. XRD patterns were interpreted through qualitative comparison with reference data from the ICDD PDF-4+ 2025 database.

4.2.7 X-ray photoelectron spectroscopy (XPS) analysis

X-ray photoelectron spectroscopy (XPS), also known as electron spectroscopy for chemical analysis (ESCA), is a surface-sensitive technique used to determine elemental composition and chemical bonding states within the outermost surface (few nanometers) of a material. The method is based on the emission of core-level electrons induced by X-ray irradiation, with the kinetic energy of the emitted photoelectrons measured by an electron energy analyzer [89].

Because binding energies are characteristic of both the element and its chemical environment, XPS enables identification of surface elements and analysis of both their chemical bonding and oxidation states. Survey scans provide rapid elemental detection, while high-

resolution spectra yield detailed chemical state information. When combined with Ar^+ ion sputtering, XPS can also be used for depth profiling, making it a powerful tool for surface and interface analysis in materials science.

In this thesis, XPS was applied in **Paper I** and **Paper IV** to investigate surface elemental composition and chemical states of activated carbons, providing insight into the influence of activation conditions on surface chemistry and functional group evolution.

4.3 Methods

In this thesis, this section presents the methodologies used for the synthesis of ACs and for evaluating their CO_2 adsorption performance. The section is organized into two main subsections covering AC preparation and CO_2 adsorption studies, with detailed descriptions of the used experimental procedures, setups, and operating conditions.

4.3.1 Preparation of ACs

The conversion of the three investigated waste-derived precursors into activated carbons was performed via potassium-mediated chemical activation using a dry mixing approach. KOH was applied as the activating agent in all studies, as the most established activator in the literature (**Papers I–IV**). In addition, alternative potassium-based compounds, including K_2CO_3, KCl, CH_3COOK, and $K_2C_2O_4$, were investigated in **Paper III** as activating agents or reference additives to assess their impact on pore formation and structural evolution of rCB. **Paper I** further examined mixed activating systems based on combined KOH and $K_2C_2O_4$ formulations to identify potential synergistic effects during the chemical activation of biomass, with additional emphasis on improving the environmental friendliness of the activation process.

Prior to activation, the waste-derived precursors were subjected to appropriate conditioning and mechanical size reduction to obtain homogeneous powdered materials. The activation route involved solid–solid blending of the precursors with the selected potassium-containing reagents, carried out by manual grinding in a mortar to ensure uniform dispersion. The resulting mixtures were placed in alumina crucibles and thermally treated in a horizontal tubular furnace operated under a continuous N_2 flow to maintain inert conditions. A schematic representation of the preparation of the ACs workflow is provided in **Figure 15**.

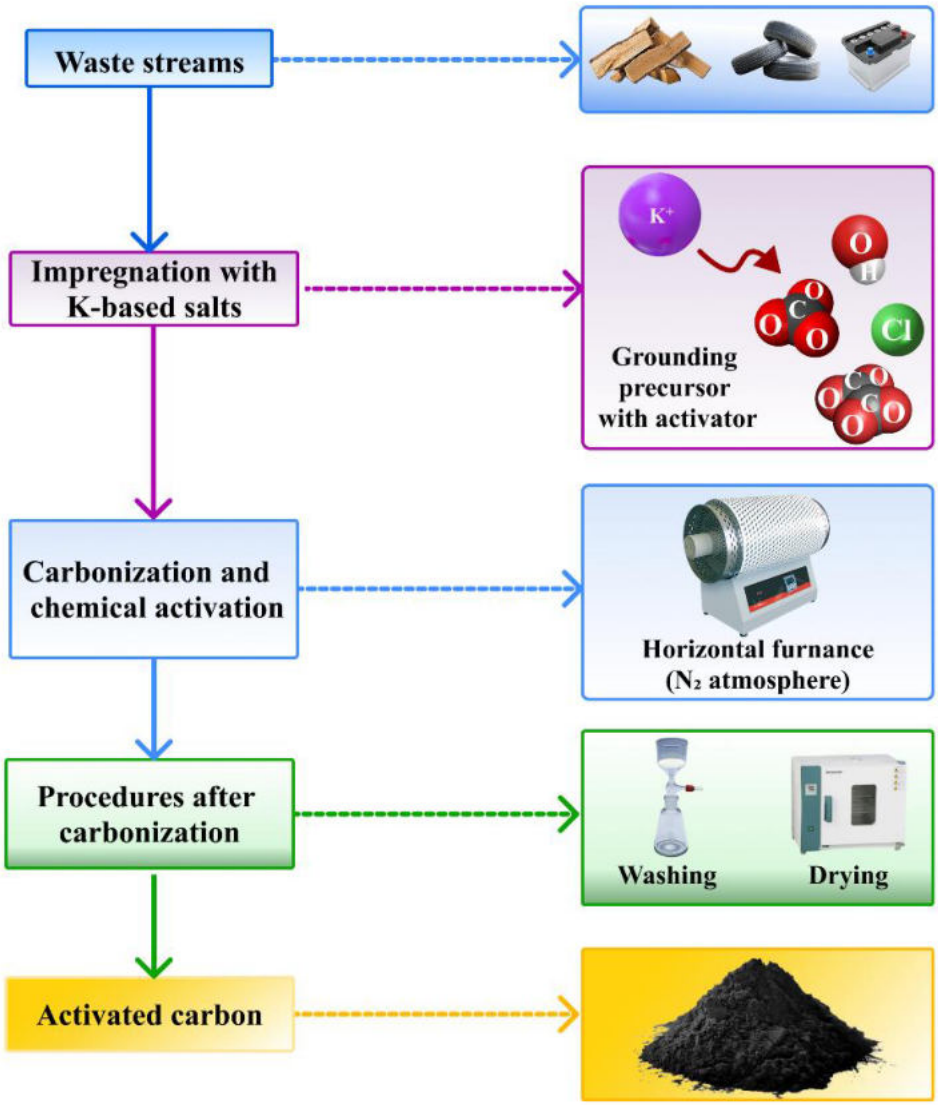

Figure 15. Schematic illustration of the different stages in the preparation of activated carbon from waste streams via K-based chemical activation.

Thermal activation was performed using parameters selected to promote effective carbonization and controlled development of porosity. The activation temperature profiles, residence times, heating rates, and precursor-to-activator mass ratios were established through systematic optimization based on preliminary experiments and literature reviews. Following thermal treatment, the activated materials were thoroughly washed with deionized water until neutral pH was reached to remove residual inorganic species and subsequently dried to constant mass. The final activation conditions applied in the individual studies are summarized in **Table 5**.

Paper	Heating rate [°C/min]	Temperature [°C]	Activation time [h]	Flow rate of N_2 [cm^3/min]	Activator	Precursor: activator ratio
Biomass						
I	5	800	3	250	KOH, $K_2C_2O_4$, KOH/$K_2C_2O_4$,	1:1-1:4
Recovered carbon black from ELTs						
II	7	800-900	2	150	KOH	1:1
III	5-13	700-900	1-4	200	KOH, K_2CO_3, KCl, CH_3COOK, $K_2C_2O_4$	1:3-1:6
Recovered graphite from LiBs						
IV	5	700-900	3	250	KOH	1:5-1:7

4.3.1.1 Obtaining ACs from woody biomass

ACs were produced from biomass via chemical activation followed by thermal treatment under inert conditions. Potassium-based activating agents, including KOH, $K_2C_2O_4$, and mixed KOH/$K_2C_2O_4$ systems, were employed.

The precursor-to-activator mass ratio was systematically varied in the range of 1:1–1:4 and constituted the key manipulated parameter. Thermal activation was conducted in a tubular furnace under a constant nitrogen flow of 250 cm^3/min. A fixed heating rate of 5 °C/min, an activation temperature of 800 °C, and a residence time of 3 h were applied for all samples. These thermal parameters were kept constant, while the type of activating agent and the precursor-to-activator mass ratio were intentionally adjusted to evaluate their effect on the properties of the resulting ACs. The applied activation conditions correspond to those summarized in **Paper I**.

4.3.1.2 Obtaining ACs from recovered carbon black

Recovered carbon black derived from end-of-life tires was converted into activated carbons under potassium-assisted activation conditions using differentiated thermal protocols.

For **Paper II**, chemical activation was carried out exclusively with KOH at a fixed precursor:activator mass ratio of 1:1. Thermal treatment was performed under a nitrogen flow of 150 cm^3/min, applying a heating rate of 7 °C/min. The process temperature was varied within the range of 800–900 °C, while the activation time was maintained at 2 h. Under these conditions, the activation temperature represented the principal variable, whereas the remaining parameters were held constant.

In **Paper III**, a wider parameter space was explored. Activation was conducted using different potassium-containing reagents (KOH, K_2CO_3, KCl, CH_3COOK, and $K_2C_2O_4$), and the precursor:activator mass ratio was adjusted between 1:3 and 1:6. Thermal treatment was carried out under a nitrogen flow of 200 cm^3/min, with heating rates varied from 5 to 13 °C/min, activation temperatures between 700 and 900 °C, and residence times ranging from 1 to 4 h. In this study, the type of activating agent, thermal regime, and precursor-to-activator ratio were intentionally modified to evaluate their impact on the activation outcome and material characteristics.

4.3.1.3 Obtaining activated carbons using graphite recovered from LiBs

Recovered graphite obtained from lithium-ion batteries was converted into activated carbons through potassium-assisted chemical activation. KOH was employed as the activating agent.

Thermal activation was conducted under a continuous nitrogen flow of 250 cm^3/min, using a fixed heating rate of 5 °C/min. The activation temperature varied between 700 and 900 °C, while the residence time was maintained at 3 h for all samples. The graphite-to-activator mass ratio constituted a key manipulated parameter and was adjusted within the range of 1:5–1:7 to assess its influence on the activation outcome. Under these conditions, the activation temperature and precursor-to-activator ratio were systematically varied, whereas the remaining process parameters were kept constant. The applied activation conditions correspond to those summarized in **Paper IV**.

4.3.2 CO_2 adsorption studies

4.3.2.1 CO_2 capture performance

In **Papers I** and **II**, the ability of biomass- and recovered carbon black–derived activated carbons to adsorb CO_2 was examined. Gas uptake measurements were carried out at specific temperatures ranging from 0 to 30 °C, with pressure reaching up to 1 bar. Before analysis, the samples were conditioned by evacuation under high vacuum to eliminate residual moisture and adsorbed gases.

4.3.2.2 CO_2/N_2 selectivity

In **Papers I** and **II**, the ideal adsorption solution theory (IAST) was utilized to calculate the selectivity for CO_2/N_2 adsorption of the ACs, which is considered a critical parameter for CO_2 capture with reference to N_2 sorption data at 25 °C.

In **Paper I**, selectivity trends were examined as a function of total pressure under a fixed CO_2 molar fraction of 0.05, representing a particularly demanding scenario for sorbent-based systems, as well as across varying CO_2 concentrations. In **Paper II**, the IAST-based evaluation was further applied to equimolar CO_2/N_2 mixtures and gas compositions relevant to post-combustion capture conditions (15% CO_2 and 85% N_2).

4.3.2.3 Cyclic performance

Cyclic regeneration stability was investigated in both **Paper I** and **Paper II** to evaluate the durability and reusability of the adsorbents under repeated operation. In **Paper I**, regeneration performance was assessed over 1–20 consecutive adsorption–desorption cycles, whereas in **Paper II** the evaluation was conducted over 1–10 cycles, reflecting sustained performance under cyclic working conditions.

5. Results and discussion

The present chapter is organized according to a cause–effect framework that links material design to adsorption performance. The discussion follows the sequence: selection of precursor and activating agent → activation pathway and evolution of the carbon microstructure → development of porosity and surface accessibility → changes in surface chemistry → adsorption response (capacity, selectivity, cyclic stability).

The chosen approach is necessary because, in carbon-based materials, CO_2 capture efficiency is not a simple function of high BET surface area. Instead, adsorption performance arises from the matching of pore size and adsorption energetics to the CO_2 molecule, as well as from the balance between microporosity and mass transport resistance. At the same time, the waste streams investigated in this work (biomass, rCB from waste tires, and graphite from LiBs) differ substantially in structural ordering of carbon atoms, heteroatom content, and mineral impurities. Consequently, the same activating agent may lead to different structural reconstruction pathways and pore development mechanisms.

Based on these considerations the present chapter is structured around three main parts: (I) activation-driven pore development and carbon framework evolution; (II) surface chemistry and potassium-assisted activation mechanisms; and (III) adsorption performance evaluation for CO_2 capture (where applicable). The investigation of textural and structural properties constitutes the first level of material screening, since pore size distribution, microporosity, and carbon framework ordering govern surface accessibility and adsorption energetics under post-combustion conditions. In parallel, surface chemical characteristics are analyzed to clarify how potassium-based activation modifies functional groups and regulates gas–solid interactions. Finally, CO_2 uptake, CO_2/N_2 selectivity, and cyclic stability are discussed for systems where adsorption measurements were performed (**Papers I–II**), whereas the remaining studies **(Papers III–IV**) are interpreted in terms of their contribution to scalable production routes and structure–property relationships.

This structure directly reflects the sequential precursor-to-performance pathway adopted in this dissertation. **Figure 16** summarizes how each part contributes to material screening and application-oriented assessment.

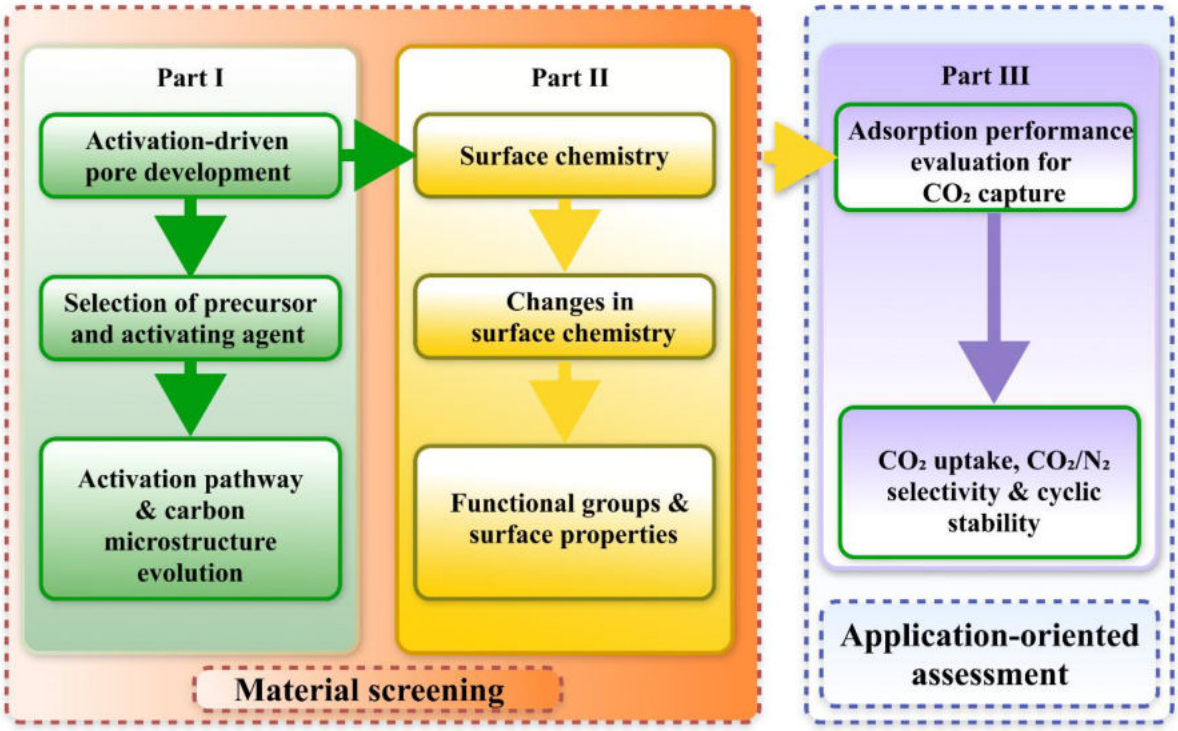

Figure 16. Framework illustrating material design, and performance connect to application-oriented assessment.

5.1 Activation and the development of porosity and carbon framework structure

This section analyzes activation-driven pore development and carbon framework reconstruction using KOH as a common reference activating agent (**Papers I–IV**). The discussion focuses on how precursor origin and activation parameters, particularly temperature and precursor-to-KOH mass ratio, influence porosity evolution and structural transformations, thereby enabling direct comparison of reactivity and pore formation pathways in waste-derived carbon materials.

5.1.1 Precursor as a determinant of reactivity

Biomass-derived carbon (**Paper I**) exhibited the highest activation responsiveness among the studied waste streams. Increasing the biomass-to-KOH ratio from 1:1 to 1:4 led to a systematic increase in BET surface area and total pore volume from approximately 1956 to

2655 $m^2\ g^{-1}$ (~36%) and from 0.943 to 1.339 $cm^3\ g^{-1}$ (~42%), respectively, with micropore volumes (< 2 nm) exceeding 1.0 $cm^3\ g^{-1}$ at moderate activation severities (1:2–1:3). At higher KOH loading, further surface area growth was accompanied by pore widening and a pronounced decrease in material yield, indicating the onset of over-etching. XRD analysis corroborated this trend by revealing progressive broadening and attenuation of the (002) basal plane reflection (2θ = 19.3–22.7°) and the overlapping (100)/(101) in-plane reflections (2θ = 43–44°), which indicated increasing turbostratic disorder and fragmentation of graphene layers.

Recovered carbon black, investigated in **Paper II** and **Paper III**, exhibited substantially lower reactivity toward KOH activation. Even under aggressive conditions used in **Paper III** (rCB:KOH ratios up to 1:6 and temperatures up to 900 °C), micropore volumes remained limited (≤ 0.332 $cm^3\ g^{-1}$), while mesoporosity dominated the pore structure, with total pore volumes approaching ~0.9 $cm^3\ g^{-1}$ and BET surface areas reaching approximately 1000 $m^2\ g^{-1}$. Furthermore, Raman analysis revealed high defect densities (I_D/I_G = 1.04–1.07), indicating a strongly disordered structure; however, extensive micropore network formation remained restricted. This behavior reflected the structurally compact nature of rCB, which limited effective structural reconstruction and favored pore widening over dense micropore formation.

Recovered graphite from LiBs (**Paper IV**) represented the most structurally resistant precursor among the investigated systems. Measurable porosity developed only under high activation severity (graphite:KOH ratios of 1:4–1:6 and temperatures of 700–900 °C), yielding BET surface areas in the range of approximately 531–678 $m^2\ g^{-1}$ and total pore volumes between 0.286 and 0.442 $cm^3\ g^{-1}$. XRD patterns indicated preservation of graphitic ordering after activation, while Raman spectroscopy revealed a pronounced increase in defect density, with the I_D/I_G ratio rising from 0.251 to 1.053. This combination suggests that KOH activation primarily induced localized defect formation and edge disorder rather than complete lattice collapse.

Comparison of the three materials showed that KOH activation produced distinct pore development pathways governed by precursor characteristics. Biomass formed dense microporous networks but became susceptible to over-etching at high activation severity, recovered carbon black underwent moderate transformation dominated by mesopore formation, and recovered graphite exhibited the greatest structural resistance, requiring aggressive conditions to initiate framework reconstruction. Consequently, precursor selection emerged as a key factor controlling porosity evolution and structural stability in waste-derived activated carbons. A comparative summary of textural properties and activation response is provided in **Table 6**.

Table 6. Activation and structural response of investigated waste-derived carbon precursors under KOH treatment.

Precursor (Paper)	**Activation conditions (precursor: KOH ratio, temperature)**	**BET surface area ($m^2\ g^{-1}$)**	**Total pore volume ($cm^3\ g^{-1}$)**	**Micropore volume ($cm^3\ g^{-1}$)**	**Dominant pore regime**	**XRD response**	**Raman response (I_D/I_G)**	**Structural implication**
Biomass (Paper I)	1:1–1:4, 800 °C	1956–2655	0.943–1.339	0.836-1.021	Microporous	Broadening and attenuation of (002) and (100)/(101)	Not measured	Turbostratic disorder and layer fragmentation
rCB (Papers II–III)	1:1–1:6, 700–900 °C	131–1025	0.275–0.901	0.036-0.327	Mesoporous -dominated	Limited framework reconstruction	1.04–1.07	Defective but compact carbon matrix
Recovered graphite (Paper IV)	1:4–1:6, 700-800 °C	531–678	0.286–0.442	~0.20	Mixed micro/mesoporous	Preservation of graphitic peaks	0.251 → 1.053	Defect generation with retained long-range order

5.1.2 Relevance of porosity beyond BET surface area

Across the investigated materials, pore size distribution analysis highlighted that the development of narrow micropores (0.3 to 1.0 nm), specifically ultramicropores (<0.7 nm), was a key structural feature influencing CO_2 adsorption in the systems where adsorption measurements were performed.

In biomass-derived ACs (**Paper I**), KOH activation generated a dense population of micropores below 1.25 nm based on N_2-derived PSD and a pronounced fraction of ultramicropores and supermicropores (0.7–2 nm) based on CO_2-derived PSD, with dominant peaks in the 0.3–1.0 nm range. According to widely reported adsorption mechanisms in porous carbons, these pore dimensions closely match the kinetic diameter of CO_2 (~0.33 nm**)** and maximize adsorption potential at low partial pressures, providing a structural basis for the high uptake observed in this system.

rCB-derived ACs evaluated for CO_2 adsorption (**Paper II**) exhibited broader N_2-derived PSD profiles dominated by mesopores, with micropores concentrated in the 1.05–1.54 nm range and mesopores spanning 2.30–34.05 nm. CO_2-derived PSD confirmed ultramicropores at 0.37–0.59 nm with additional contributions at 0.61–0.91 nm; however, their limited volumetric fraction relative to mesoporosity was consistent with the lower CO_2 adsorption performance compared to biomass-derived carbons, in agreement with trends reported for mesopore-rich ACs. A similar structural pattern was observed in rCB samples optimized for KOH activation (**Paper III**), where micropores accounted for ~30–40% of the total pore volume, with dominant populations centered at 0.99–1.63 nm and mesopores distributed between 2.0 and 13.49 nm. Despite increased micropore contribution, pore widening remained significant, providing structural context for the CO_2 adsorption limitations observed in rCB-based systems.

For the remaining system, recovered graphite (**Paper IV**), PSD analysis primarily served as a structural screening tool because CO_2 uptake measurements were not performed. KOH activation induced partial formation of micropores below 2 nm, with pronounced PSD peaks between 1.2 and 2.0 nm, while mesopores remained predominantly in the 2.2–4.0 nm range. These results reinforce that the presence and distribution of narrow micropores constitute a critical structural descriptor for CO_2 adsorption performance where measured, whereas PSD analysis in non-tested systems provides guidance for identifying promising activation pathways requiring further experimental validation (**Table 7**).

Table 7. Pore size distribution characteristics and CO_2 adsorption relevance.

Precursor (Paper)	PSD method	Dominant micropore range (nm)	Narrow micropore range (<0.7 nm)	Dominant mesopore range (nm)	Structural implication	CO_2 adsorption measured
Biomass (Paper I)	N_2 + CO_2 DFT	<1.25 (N_2)	High: 0.3–1.0 (CO_2)	2.1–4.0	Dense microporous network	Yes
rCB (Paper II)	N_2 + CO_2 DFT	1.05–1.54 (N_2)	Limited: 0.37–0.59; 0.61–0.91 (CO_2)	2.3–35	Mesoporosity dominates, limited effective micropore fraction	Yes
rCB optimized (Paper III)	N_2 DFT	0.99–1.63 (N_2)	Not resolved separately	2.0–13.5	Moderate micropore enhancement, pore widening dominates	No
Recovered graphite (Paper IV)	N_2 DFT	1.2–2.0 (N_2)	Present (cumulative volume evidence)	2.2–4.0	Micropore-dominant structure with persistent mesoporosity	No

5.1.3 Morphology and activator diffusion as mechanistic factors

Beyond chemical reactivity and lattice-level reconstruction, particle morphology and activator transport were identified as additional controlling factors governing pore development during potassium-assisted activation. SEM analysis enabled direct visualization of precursor-dependent differences in terms of particle shape, aggregation state, and surface accessibility, which are widely recognized in the literature as key parameters affecting alkali metal diffusion and spatial activation uniformity [51].

Biomass-derived carbons (**Paper I**) exhibited highly open and interconnected porous morphologies after KOH activation, characterized by thin pore walls and extensive framework etching. Such open architectures facilitated rapid potassium penetration and promoted relatively homogeneous activation throughout the carbon matrix, in agreement with previous reports on lignocellulosic precursors [90]. At higher activation severity, however, the same efficient transport pathways accelerated carbon consumption, leading to framework thinning and the onset of over-etching.

rCB-derived carbons (**Papers II and III**) consisted of rigid, spherical primary particles forming compact aggregates. SEM analysis revealed a closed and clustered morphology that restricted potassium diffusion into particle interiors and promoted surface-localized reactions. As a consequence, activation proceeded in a spatially heterogeneous manner, favoring pore widening and mesopore formation rather than the development of dense, interconnected microporous networks.

Recovered graphite (**Paper IV**) displayed plate-like, highly ordered particles prior to activation. Following KOH treatment, SEM micrographs revealed pronounced surface roughening, defect formation, and partial fragmentation, while remnants of the layered graphitic structure remained visible. This morphological evolution indicated selective etching dominated by reactions at edges, grain boundaries, and defect sites rather than uniform bulk restructuring.

Taken together, these observations demonstrated that precursor morphology directly influenced activator accessibility and diffusion efficiency, thereby regulating the balance between homogeneous pore generation, localized surface etching, and framework preservation during KOH activation (**Table 8**). Consequently, effective pore engineering in waste-derived carbons required simultaneous consideration of activation chemistry and morphology-induced mass transport limitations.

Table 8. Morphological features and potassium diffusion behavior.

Precursor (Paper)	Morphological features (SEM)	KOH accessibility	Activation uniformity	Mechanistic implication	Morphology
Biomass (Paper I)	Open interconnected porous framework	High	Homogeneous	Rapid micropore generation, prone to over-etching	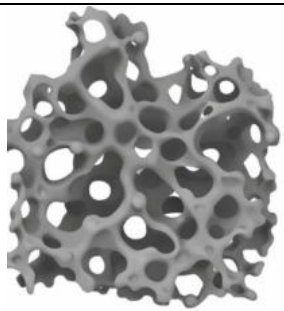
rCB (Papers II–III)	Rigid spherical particles, compact aggregates	Limited	Heterogeneous	Surface-localized reactions, mesopore formation dominates	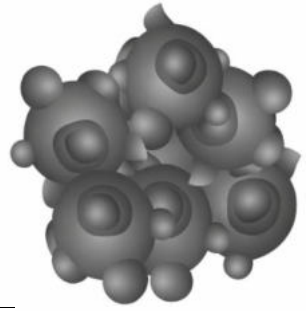
Recovered graphite (Paper IV)	Plate-like layered particles	Moderate (edge sites)	Localized	Selective etching and carbon framework preservation	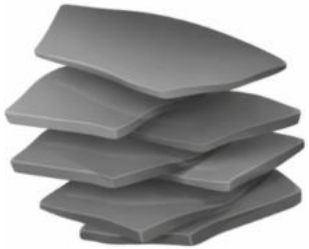

5.2 Variability of activation mechanisms and CO_2-specific surface chemistry among potassium-based activators

This section examines the variability of activation mechanisms among potassium-based activating agents by comparing their roles in pore development and carbon framework modification (**Papers I and III**), as well as the associated evolution of surface chemistry in systems where adsorption performance was evaluated (**Papers I and II**). The analysis focuses on how potassium precursor speciation, thermal decomposition behavior, and in situ potassium migration controlled etching efficiency, pore formation, structural expansion, and functional group development.

Within the current framework, differences between KOH and potassium salts were evaluated for biomass-derived carbons in **Paper I** (comparison between KOH and $K_2C_2O_4$) and for rCB-derived carbons in **Paper III** (comparison between KOH, K_2CO_3, CH_3COOK, $K_2C_2O_4$, and KCl), and were attributed to distinct reaction pathways and pore generation efficiencies.

For systems with available CO_2 adsorption data (**Paper I and Paper II**), the surface chemistry of KOH-activated carbons and $K_2C_2O_4$-activated biomass carbons (**Paper I**) was evaluated in relation to adsorption behavior, where surface functional groups were treated as secondary modifiers of gas–solid interactions acting in combination with micropore structure rather than as primary performance drivers. For recovered graphite (**Paper IV**), surface chemical characterization was used to interpret activation-induced structural modification instead of adsorption performance due to the absence of CO_2 uptake measurements.

5.2.1 KOH vs. K-based salts: reactivity and transport related limitations in activation efficiency

The comparison between KOH and $K_2C_2O_4$ in **Paper I** demonstrated clear differences in activation behavior arising from differences in potassium reactivity and transport properties in biomass-derived ACs. Under identical activation conditions (mass ratio biomass:activator = 1:4, 800 °C), KOH produced substantially higher overall porosity, with a BET surface area of 2655 $m^2\ g^{-1}$ and total pore volume of 1.339 $cm^3\ g^{-1}$, whereas $K_2C_2O_4$ yielded lower values (1709 $m^2\ g^{-1}$ and 0.885 $cm^3\ g^{-1}$, respectively). Despite this difference, both activators generated comparable CO_2 accessible narrow micropore volumes relevant for CO_2 adsorption (0.133 $cm^3\ g^{-1}$ for KOH and 0.150 $cm^3\ g^{-1}$ for $K_2C_2O_4$), indicating that KOH primarily enhanced bulk pore expansion, while $K_2C_2O_4$ promoted more selective formation of narrow micropores. This distinction was further reflected in pore structure distribution and material yield. KOH

activation generated a larger mesopore contribution (0.318 $cm^3\ g^{-1}$) and resulted in significant carbon burn-off (7.8%), whereas $K_2C_2O_4$ produced a more micropore-focused structure with limited mesoporosity (0.091 $cm^3\ g^{-1}$) and higher yield (18.5%). SEM observations supported these trends by revealing uniformly etched, highly open frameworks for KOH-activated carbon and localized cracking with compact granular regions for $K_2C_2O_4$-activated sample, indicating restricted potassium mobility.

Furthermore, XRD analysis of unwashed samples showed that $K_2C_2O_4$ activation favored the formation of crystalline carbonate-rich potassium phases ($K_2CO_3 \cdot 1.5H_2O$, $K_4H_2(CO_3)_3 \cdot 1.5H_2O$, K_2CO_3, K_2O), which is in agreement with literature reports on $K_2C_2O_4$ decomposition behavior [91]. KOH-activated samples exhibited broader and less intense potassium-related reflections, indicating the presence of ess crystalline and weakly bound potassium species. This difference reflects higher potassium mobility and reactivity during KOH activation, enabling homogeneous framework etching and efficient pore generation, whereas oxalate-based activation remains governed by diffusion-limited and structurally conservative mechanisms (**Table 9**).

Table 9. Comparison of KOH and $K_2C_2O_4$ activation for biomass-derived carbons (**Paper I**).

Parameter	**KOH activation**	**$K_2C_2O_4$ activation**
Potassium reactivity	Intensive carbon etching	Lower reactivity with carbonate-dominated decomposition products
Potassium transport	Homogeneous penetration	Restricted transport with localized activation zones
Pore development pathway	Strong bulk pore expansion and framework thinning	Selective formation of narrow micropores with limited pore widening
Carbon yield	Low	Higher
Structural implication	Efficient but aggressive activation	Milder, transport-limited activation

The screening of potassium-based activators in **Paper III** demonstrated that pore development in rCB-derived carbons was strongly influenced by potassium speciation and transport behavior. KOH exhibited the highest activation efficiency, reaching S_{BET} = 945 m² g⁻¹, V_{TOT} = 0.743 cm³ g⁻¹, and $V_{MIC(N_2)}$ = 0.303 cm³ g⁻¹. Among the potassium salts, $K_2C_2O_4$ showed the strongest performance, with S_{BET} = 299 m² g⁻¹, V_{TOT} = 0.369 cm³ g⁻¹, and $V_{MIC(N_2)}$ = 0.093 cm³ g⁻¹, while CH_3COOK (S_{BET} = 217 m² g⁻¹, V_{TOT} = 0.240 cm³ g⁻¹, $V_{MIC(N_2)}$ = 0.071 cm³ g⁻¹) and K_2CO_3 (S_{BET} = 146 m² g⁻¹, V_{TOT} = 0.207 cm³ g⁻¹, $V_{MIC(N_2)}$ = 0.043 cm³ g⁻¹) produced lower values. KCl exhibited negligible textural properties development, resulting in the overall activation efficiency trend: KOH > $K_2C_2O_4$ > CH_3COOK > K_2CO_3 > KCl. Furthermore, SEM–EDS analysis in **Paper III** revealed systematic differences in potassium distribution among the activators. KOH produced the highest potassium loading (~29.5 wt%) with a relatively homogeneous spatial distribution, consistent with efficient potassium transport and uniform activation. $K_2C_2O_4$ exhibited high potassium content (~27.5 wt%) accompanied by patchy spatial distribution, whereas CH_3COOK (~20.9 wt%) and K_2CO_3 (~13.1 wt%) showed increasingly heterogeneous potassium dispersion and localized potassium-rich regions. This behavior directly correlated with the resulting textural properties, as activators with more uniform potassium distribution generated higher surface area and micropore volume. Overall, these results demonstrate that effective activation of rCB requires not only sufficient potassium availability but also homogeneous potassium transport within the carbon matrix, conditions most efficiently fulfilled by KOH and only partially achieved by potassium salts, as summarized in **Table 10**.

Table 10. Summary of potassium-speciation-controlled activation behavior in rCB-derived carbons (**Paper III**).

Activator	Potassium transport behavior	Spatial K distribution	Pore formation tendency	Overall activation effectiveness
KOH	High mobility	Homogeneous	Strong	Highest
$K_2C_2O_4$	Moderate mobility	Patchy	Moderate	Intermediate
CH_3COOK	Limited mobility	Heterogeneous	Weak	Low
K_2CO_3	Low mobility	Strongly heterogeneous	Very weak	Very low
KCl	Minimal chemical interaction	Poor penetration	Negligible	Ineffective

A central outcome of the K-based activator comparison in **Paper I** and **Paper III** is that effective activation requires chemically reactive potassium species, sufficient potassium mobility with homogeneous distribution during heating, and controlled pore development without excessive burn-off. In this context, the differences observed between KOH and potassium salts (K_2CO_3, CH_3COOK, $K_2C_2O_4$, KCl) reflect distinct reaction pathways and potassium transport efficiencies. KOH consistently exhibited the highest activation efficiency in both biomass- and rCB-derived systems due to its strong interaction with the carbon matrix, while simultaneously introducing a process-level trade-off associated with increased carbon consumption at high activation severity. Consequently, for KOH activation, the identification of an optimal activation window that balances overall porosity development, BET surface area, and structural stability emerges as a key design criterion for the development of practical adsorption-oriented sorbents.

5.2.2 Surface chemistry evolution during K-based activation and its role in CO_2 adsorption

Surface chemistry analysis across the investigated systems indicates that potassium-based activation introduces a broadly similar set of oxygen-containing functional groups; however the relative abundance and chemical environment of these groups depend on the activating agent and precursor type.

In biomass-derived carbons (**Paper I**), both KOH and $K_2C_2O_4$ produced comparable FT-IR spectra with bands assigned to –C–H, –O–H, –C=O, –C–O, –C=C, and –C≡C functionalities, indicating that the same types of surface functional groups are present irrespective of the activator, although their relative abundance may differ. However, XPS analysis revealed that KOH exerted a stronger influence on surface reconstruction, promoting higher concentrations of oxygen functionalities (–C=O, –C–O) and defect-rich aromatic domains, whereas $K_2C_2O_4$ favored partial retention of carbonate-related species (CO_3^{2-}), in agreement with the XRD detection of potassium carbonate phases ($K_2CO_3 \cdot 1.5H_2O$, $K_4H_2(CO_3)_3 \cdot 1.5H_2O$, and K_2CO_3). In mixed activation systems (KOH/$K_2C_2O_4$), KOH dominated the resulting surface chemistry, confirming its stronger chemical interaction with the carbon matrix.

For rCB-derived carbons activated with KOH (**Paper II**), FT-IR analysis similarly confirmed the presence of –O–H, and –C–O functionalities, which are known to enhance CO_2 adsorption through increased quadrupole–dipole interactions. In these systems, oxygen-

containing surface functionalities were therefore treated as secondary contributors, with textural properties considered the primary factor controlling CO_2 adsorption capacity.

In recovered graphite activated with KOH (**Paper IV**), XPS results showed an increase in the graphitic carbon contribution accompanied by partial redistribution of surface oxygen species, including –C–O, –O–H, and –C=O groups. This behavior reflects K intercalation and high-temperature redox reactions, which restructure the carbon framework while modifying the population and distribution of oxygen-containing functionalities. Although CO_2 adsorption was not evaluated for this system, the increase in graphitic ordering together with the reorganization of surface oxygen species suggests that the CO_2 adsorption performance would be primarily determined by the developed microporosity and could therefore be expected to follow trends similar to those observed for other KOH-activated carbons with comparable textural properties.

These results demonstrate that potassium-based activation generates broadly similar functional group families across different precursors and KOH induces the most pronounced surface chemical restructuring. In systems relevant to CO_2 capture (**Paper I** and **Paper II**), surface chemistry acts primarily as a supporting factor that enhances adsorption energetics in combination with appropriate pore architecture, rather than serving as the dominant performance-controlling parameter. A consolidated overview of the surface chemical transformations induced by the different potassium activators is presented in **Table 11**.

Table 11. Comparison of surface chemistry evolution with different potassium-based activation.

System (Paper)	Activator	Dominant surface features	Activator influence on surface chemistry	CO_2 relevance
Biomass-derived ACs (Paper I)	KOH	–C=O, –C–O, –O–H groups, defect-rich aromatic domains	Strong surface reconstruction and enhanced defect formation	Contributing factor alongside pore development
Biomass-derived ACs (Paper I)	$K_2C_2O_4$	Similar to KOH functional group types, partial carbonate retention	Milder chemical modification and carbonate stabilization	Supporting role; less pronounced than structural effects
rCB-derived ACs (Paper II)	KOH	O–H, and –C–O groups	Moderate surface oxidation coupled with pore development	Limited direct contribution
Recovered graphite (Paper IV)	KOH	Increased graphitic carbon fraction, C–O, –O–H, and –C=O groups	Framework restructuring via K intercalation and redox reactions	Mechanistic relevance only

5.3 CO_2 adsorption performance and CO_2/N_2 separation behavior

This section analyzes the CO_2 capture performance and selectivity behavior of waste-derived activated carbons by integrating adsorption capacity, selectivity, and cyclic stability results obtained in **Paper I** and **Paper II**. The discussion focuses on how precursor type, activation strategy, and resulting pore structure influence adsorption behavior under low-pressure conditions (≤1 bar) relevant to post-combustion CO_2 capture. Within this framework, biomass-derived carbons (**Paper I**) and recovered carbon black–derived carbons (**Paper II**) are chosen to compare structure–performance relationships controlling CO_2 uptake and CO_2/N_2 selectivity.

5.3.1 CO_2 adsorption capacity and temperature-dependent performance

In **Paper I**, biomass-derived activated carbons exhibited steep low-pressure CO_2 uptake, confirming adsorption dominated by narrow micropores. The highest capacity was obtained for KOH-activated material at low KOH loading (biomass:KOH = 1:1), reaching 5.95 mmol g^{-1} at 25 °C and 9.65 mmol g^{-1} at 0 °C. Increasing the KOH ratio reduced CO_2 uptake despite higher BET surface area and total pore volume, as the CO_2-accessible micropore volume decreased from 0.164 to 0.133 cm^3 g^{-1}, indicating pore widening and partial loss of micropores below 1.4 nm. $K_2C_2O_4$-activated biomass (biomass:$K_2C_2O_4$ = 1:4) achieved comparable uptake (5.52 mmol g^{-1} at 25 °C and 8.79 mmol g^{-1} at 0 °C) at lower S_{BET}, V_{TOT}, and $V_{MIC(N2)}$, demonstrating that selective formation of narrow micropores is more critical for CO_2 capture than maximizing total porosity.

In **Paper II**, rCB-derived carbons showed pronounced temperature-dependent adsorption behavior characteristic of physisorption. KOH-activated rCB exhibited a CO_2 uptake, reaching 30.9 cm^3 g^{-1} (1.38 mmol g^{-1}) at 0 °C and 20.5 cm^3 g^{-1} (0.84 mmol g^{-1}) at 25 °C under 1 bar. Textural analysis in **Paper II** further supports the interpretation of the activation process. Increasing the KOH activation temperature from 800 to 900 °C resulted in systematic enhancement of pore development, with BET surface area increasing from 131 to 328 m^2 g^{-1} and total pore volume from 0.275 to 0.448 cm^3 g^{-1}. This evolution was driven mainly by micropore formation, with micropore volume increasing from 0.036 to 0.100 cm^3 g^{-1}. Importantly, both supermicropores and ultramicropores increased with temperature (0.021 → 0.069 cm^3 g^{-1} and 0.015 → 0.031 cm^3 g^{-1}, respectively), indicating improved development of CO_2-relevant narrow porosity. It should be noted that CO_2 adsorption measurements were performed only for the 900 °C-activated sample; therefore, the textural trends at lower

temperatures are interpreted as indicators of adsorption potential rather than direct performance metrics.

Cyclic stability tests in both studies demonstrated excellent regenerability of the surfaces. In **Paper I**, KOH- and $K_2C_2O_4$-activated biomass carbons maintained constant CO_2 uptake over 20 adsorption–desorption cycles at 25 °C, with a maximum deviation of approximately 0.09 mmol g^{-1}. Similarly, in **Paper II**, KOH-activated rCB showed no measurable capacity loss over 10 cycles at 0 °C. The preserved performance confirms reversible physisorption within structurally stable micropores and indicates the absence of irreversible surface reactions during repeated operation.

These results show that high CO_2 uptake combined with long-term cyclic stability is achieved when the activation conditions promote the formation of stable narrow microporosity as the key structural parameter controlling adsorption performance in waste-derived activated carbons.

Table 12. Structural and functional comparison of the performance of waste-derived adsorbents (**Paper I** and **Paper II**).

Precursor type (Paper)	**Activator (precursor:KOH ratio, and temperature)**	**Key pore feature**	**Structural characteristics of precursor**	**Performance implication**
Biomass (Paper I)	KOH (biomass:KOH = 1:1, 800 °C)	High narrow micropore density	Highly disordered lignocellulosic carbon framework	Strong low-pressure CO_2 adsorption driven by narrow micropores
Biomass (Paper I)	$K_2C_2O_4$ (biomass:KOH = 1:4, 800 °C)	Similar but less developed narrow micropore region compared to KOH	Moderately preserved carbon framework	Efficient CO_2 uptake despite lower S_{BET}, V_{TOT}, and $V_{MIC(N2)}$
Recovered carbon black (Paper II)	KOH (rCB:KOH = 1:1, 900 °C)	Mixed micro/mesoporous structure	Compact, thermally pre-processed aggregated particles	Low CO_2 uptake because of structural limitations

5.3.2 CO_2/N_2 selectivity and separation performance

CO_2/N_2 selectivity was evaluated using IAST calculations for biomass-derived carbons (**Paper I**) and rCB-derived carbons (**Paper II**) under dilute and post-combustion–relevant conditions. In **Paper I**, all investigated materials exhibited selectivity values above 12 at low CO_2 mole fraction (0.05) and at 1 bar, confirming effective separation performance under these selected conditions. The highest selectivity was obtained for the $K_2C_2O_4$-activated carbon (20.5–21.7), whereas the KOH-activated sample (biomass:KOH = 1:1) exhibited slightly lower values (19.13–21.29). Increasing the KOH loading (biomass:KOH = 1:4) reduced the selectivity (12.8–13.8) due to the partial loss of ultramicropores. In addition, the $K_2C_2O_4$-derived carbon demonstrated robust performance under variable feed compositions, maintaining selectivity above 20 across the entire range of CO_2 concentrations and operating pressures. These trends indicate that CO_2/N_2 separation efficiency is based on primarily by the availability of ultramicropore formation that preferentially accommodate CO_2 molecules while restricting N_2 adsorption due to size exclusion and enhanced adsorption potential at low pressure.

In **Paper II**, KOH-activated rCB exhibited exceptionally high selectivity for an equimolar CO_2/N_2 mixture at low pressure (>300 at 0.001 bar) and maintained favorable performance under flue-gas conditions (~60 at 1 bar, 15% CO_2). This behavior, evaluated from the coefficient of determination (R^2) as a function of the cumulative micropore volume within defined pore width ranges, is mainly associated with submicropores and ultramicropores. The preferential filling of these narrow pores at low pressure leads to outstanding separation, while their progressive occupation at higher pressure results in a decrease in selectivity, although the values remain competitive for practical applications.

Taken together, the findings indicate that CO_2/N_2 selectivity is primarily determined by the ultramicropore size matching, providing the strongest structural contribution to separation performance across both precursor systems, as summarized in **Table 13**.

Table 13. Comparison of CO_2/N_2 selectivity behavior for waste-derived activated carbons (**Paper** I and **Paper II**).

Precursor type	**Activator (biomass:KOH ratio/temperature)**	**Process conditions**	**Dominant selectivity driver**	**Selectivity behavior**	**Separation implication**
Biomass (Paper I)	KOH (biomass:KOH = 1:1)	Low CO_2 fraction (0.05), ≤1 bar	High ultramicropore density	High selectivity	Favorable for dilute CO_2 separation
Biomass (Paper I)	$K_2C_2O_4$ (biomass: $K_2C_2O_4$ = 1:4)	Low CO_2 fraction (0.05), ≤1 bar	Refined ultramicropores	The highest selectivity	Robust performance under variable feed compositions
Biomass (Paper I)	KOH (biomass: KOH = 1:4)	Low CO_2 fraction (0.05), ≤1 bar	Partial ultramicropore loss	Reduced selectivity	Over-activation limits separation efficiency
rCB (Paper II)	KOH (900 °C)	Low pressure and flue-gas composition	Strong CO_2 confinement in submicropores and ultramicropores	Very high selectivity at low pressure and high values at flue gas conditions	Suitable for post-combustion capture conditions

6. Conclusions

This thesis investigates the transformation of carbon-intensive waste streams into functional porous materials for CO_2 capture within a circular materials framework. The work aims to establish a methodology for the valorization of structurally diverse carbon residues into high-performance sorbents through chemically controlled activation. Potassium-assisted activation was applied to three waste-derived carbon precursors, namely woody biomass, recovered carbon black from end-of-life tires, and graphite from spent lithium-ion batteries, and the resulting materials were evaluated for their gas sorption performance under physisorption dominated conditions where adsorption data were available. The major conclusions are summarized as follows:

- **Waste-stream valorization into functional sorbents**

The work shows that precursor origin governs activation response, attainable pore architecture, and structural stability (**Papers I–IV**).

Woody biomass, rCB, and recovered graphite were demonstrated as viable precursors for producing activated carbons through potassium-mediated chemical activation, establishing a unified waste-to-sorbent framework aligned with circular economy principles and carbon intensive waste management strategies.

- **Precursor-dependent activation responsiveness controls pore development**

The results revealed a precursor-dependent activation behavior, indicating that a universal response could not be assumed for structurally diverse waste-derived carbons. Each material exhibited a different degree of responsiveness under identical potassium-based activation conditions. This variation was attributed to differences in the structural organization of the carbon framework and the resulting accessibility of reactive carbon domains.

Biomass exhibited the highest reactivity toward KOH activation, enabling dense microporous networks and very high surface areas, but also susceptibility to over-etching at high activation severity (**Paper I**). rCB showed moderate activation responsiveness, with mesopore-dominated structures resulting from diffusion-limited activation within compact aggregates (**Papers II–III**). Recovered graphite showed the greatest structural resistance,

with porosity forming mainly through defect-driven edge etching rather than uniform framework reconstruction (**Paper IV**).

- **Microporosity governs CO_2 capture more strongly than total surface area**

The present study demonstrated that pore size distribution, rather than overall surface area, is the dominant structural descriptor influencing CO_2 capture efficiency. Specifically, narrow micropores emerged as the critical structural parameter governing selective low-pressure adsorption.

In the evaluated systems where adsorption was measured, CO_2 uptake and CO_2/N_2 selectivity correlated with the availability of narrow micropores, particularly ultramicropores, rather than with BET surface area alone.

Biomass-derived carbons achieved the highest low-pressure CO_2 capacities due to dense sub-nanometer pores (**Paper I**), whereas rCB-derived carbons showed lower uptake consistent with a smaller fraction of CO_2-relevant microporosity (**Paper II**).

- **Potassium activator chemical speciation determines activation efficiency**

The present study demonstrated that activation efficiency is not solely dictated by potassium content but by its chemical form. Variations in potassium speciation resulted in distinct activation pathways, ranging from aggressive pore expansion (KOH) to selective micropore development with improved yield retention ($K_2C_2O_4$).

KOH consistently delivered the strongest activation effect due to high potassium reactivity and relatively uniform migration within the carbon matrix, enabling efficient pore generation (**Papers I–III**). Alternative potassium salts produced milder activation, with $K_2C_2O_4$ demonstrating selective narrow micropore formation and improved yield retention in biomass-derived systems, highlighting a trade-off between aggressive pore expansion and structural conservation (**Paper I**).

- **Morphology and diffusion limitations regulate activation pathways**

This work demonstrates that precursor morphology governs activation pathways by controlling potassium transport within the carbon matrix. Structural organization and

particle compactness dictate the balance between homogeneous pore development and localized over-etching.

SEM analysis revealed that open biomass-derived structures promoted homogeneous activation but accelerated burn-off at high severity (**Paper I**). Aggregated rCB particles restricted potassium transport, favoring localized reactions and mesopore formation (**Papers II–III**). Plate-like graphite structures underwent selective edge etching with partial retention of graphitic ordering (**Paper IV**). These findings confirm that morphology-induced transport limitations are critical factors in pore engineering.

- **Surface chemistry plays a secondary but supportive role in adsorption**

The results indicate that, under physisorption-controlled conditions, adsorption performance is primarily associated with the developed micropore architecture, while surface chemistry provides a secondary contribution by modifying gas–solid interactions. Oxygen-containing functional groups therefore act as supportive modifiers rather than dominant performance-determining features.

A common feature across all materials is the potassium-driven introduction of oxygen-containing functionalities, indicating a shared activation mechanism (**Paper I** and **Paper II**). In graphite-based systems, the evolution of surface chemistry reflects potassium-induced restructuring of the carbon framework (**Paper IV**).

- **CO_2/N_2 selectivity and cyclic stability confirm separation potential**

The overall performance evaluation demonstrates that selective and stable CO_2 capture can be achieved within these structurally engineered carbon systems.

Biomass- and rCB-derived activated carbons exhibited favorable CO_2/N_2 selectivity under dilute and post-combustion conditions and maintained stable performance during repeated adsorption–desorption cycles, confirming reversible physisorption (**Papers I–II**).

7. Future outlook

Future research directions emerging from this work can be grouped into material innovation, process optimization, and application expansion, with an overarching emphasis on scalability and sustainability.

I. Material innovation

• Environmentally balanced activation strategies

Current practices for producing activated carbons through chemical activation typically require high potassium loadings and severe conditions, which lead to extensive burn-off, low material yields, and the generation of secondary waste streams. These factors reduce resource efficiency and limit the environmental sustainability of sorbent production. The development of more environmentally balanced activation strategies therefore requires approaches that enable precise pore formation while reducing chemical consumption and carbon loss. The use of alternative potassium salts, mixed-activator systems, and staged activation protocols represents a promising pathway toward the selective formation of porosity under milder conditions. In this context, the $K_2C_2O_4$-based activation of biomass-derived carbons provides an important conceptual basis for such process design (**Paper I**).

• Controlled surface functionalization

Surface chemistry in activated carbons is largely determined by the activation process itself, which limits independent control over the type, density, and spatial distribution of functional groups. Post-synthetic modification often leads to partial blockage of pores or deterioration of structural stability, resulting in reduced adsorption efficiency and poorer cyclic performance. The development of post-activation treatments that introduce tailored polar functionalities while preserving pore accessibility could therefore enhance adsorption energetics under realistic gas compositions without compromising stability. Such strategies should enable the decoupling of textural and chemical properties and provide improved performance under practical operating conditions (**Papers I–II**).

• Hybrid and composite sorbents

Waste-derived carbons in the present thesis were primarily evaluated as standalone sorbents, where adsorption performance was tuned through pore structure development and surface chemistry modification. The absence of integrated high-affinity phases limits the extent to which adsorption energetics and selectivity can be independently tailored beyond what is achievable by textural optimization alone. The development of hybrid and composite sorbents, in which waste-derived carbons are combined with high-affinity porous frameworks or functional coatings, offers a pathway to synergistic adsorption behavior by coupling the

structural robustness and conductivity of the carbon matrix with enhanced affinity toward CO_2 and other target gases (**Papers I–IV**).

II. Process optimization

- ### Mitigating diffusion limitations in compact precursors

Current activation approaches applied to compact and aggregated precursors such as rCB and graphite are limited by restricted potassium transport within dense particle structures. This results in heterogeneous activation, localized over-etching, and non-uniform micropore development, as evidenced by the spatially uneven potassium distribution and textural evolution observed in **Paper II** and **Paper IV**. Pre-conditioning strategies, including controlled particle engineering and morphology tuning prior to activation, could improve potassium accessibility and promote more homogeneous pore formation. Such approaches would enable more efficient utilization of the carbon matrix, reduce burn-off, and open pathways toward the controlled design of adsorption-relevant porosity in otherwise diffusion-limited precursors.

- ### Mechanistic refinement of potassium-assisted activation

Although potassium-assisted activation is widely applied, the mechanisms governing potassium speciation, migration, and carbon framework reconstruction remain insufficiently resolved. This limits predictive control over pore development and increases the risk of over-etching and structural degradation under severe activation conditions. Time-resolved and in situ characterization techniques could elucidate the evolution of potassium species and their interaction with the carbon matrix, enabling the rational design of activation protocols with controlled pore formation (**Papers I–III**).

- ### Dynamic and process-relevant adsorption evaluation

Most adsorption evaluations are conducted under ideal equilibrium conditions that do not adequately represent industrial gas separation environments. As a result, performance under dynamic flow, multicomponent gas mixtures, and humidity remains insufficiently understood, which limits reliable scale-up assessment. Extending the current studies toward breakthrough experiments, kinetic analysis, and humidity-influenced adsorption would bridge the gap between laboratory characterization and realistic process conditions and enable more accurate evaluation of sorbent applicability (**Papers I–II**).

III. Application expansion

- **Broadening environmental sorption applications**

Current research on waste-derived activated carbons has primarily focused on CO_2 capture, while their broader potential for environmental remediation remains largely unexplored. The tunable pore structures and adjustable surface functionalities demonstrated in this work provide a basis for extending these materials toward the removal of other gaseous pollutants and aqueous contaminants. Such expansion would enable the utilization of the same structure–property relationships identified here for a wider range of separation and purification applications (**Papers I–IV**).

- **Integration into scalable capture systems**

Most studies remain at the level of laboratory-scale evaluation of powder materials, with limited translation into reactor-relevant configurations. This gap between material synthesis and process-scale implementation prevents realistic assessment of pressure drop, mechanical stability, heat and mass transfer, and long-term operational performance. The development of shaped sorbents together with reactor-scale validation would enable the evaluation of these parameters under practical conditions and support the transfer of the most promising materials into applicable separation technologies (**Papers I–II**).

- **Sustainability and techno-economic assessment**

While the results of this thesis demonstrate the circularity potential of waste-derived sorbents, comprehensive life-cycle and techno-economic assessments are still missing. Without such analyses, the overall environmental impact and economic feasibility of large-scale implementation remain uncertain, particularly for processes integrated with tire and battery recycling infrastructure. The incorporation of life-cycle and techno-economic evaluation alongside scale-up studies would enable identification of the most resource-efficient activation strategies, optimization of material yields, and verification of the practical sustainability of the proposed value chains (**Papers II–IV**).

8. References

[1] Diejarski, B., Krzyżyńska, R., & Andersson, K. (2023). Current status of carbon capture, utilization, and storage technologies in the global economy: A survey of technical assessment. Fuel, 342, 127776. https://doi.org/10.1016/j.fuel.2023.127776

[2] IEA (2025), Global Energy Review 2025, IEA, Paris https://www.iea.org/reports/global-energy-review-2025, Licence: CC BY 4.0

[3] IEA (2019). Transforming Industry through CCUS, IEA, Paris. https://www.iea.org/reports/transforming-industry-through-ccus

[4] Hanson, E., Nwakile, C., & Hammed, V. O. (2025). Carbon capture, utilization, and storage (CCUS) technologies: Evaluating the effectiveness of advanced CCUS solutions for reducing CO_2 emissions. Results in Surfaces and Interfaces, 18, 100381. https://doi.org/10.1016/j.rsurfi.2024.100381

[5] Leonzio, G., & Shah, N. (2024). Recent advancements and challenges in carbon capture, utilization and storage. Current Opinion in Green and Sustainable Chemistry, 46, 100895. https://doi.org/10.1016/j.cogsc.2024.100895

[6] Raganati, F., & Ammendola, P. (2024). CO_2 post-combustion capture: a critical review of current technologies and future directions. Energy & Fuels, 38(15), 13858-13905. https://doi.org/10.1021/acs.energyfuels.4c02513

[7] Deng, H., Li, T., Li, H., Dang, A., & Han, Y. (2025). Carbon-based adsorbents for CO_2 capture: A systematic review. Journal of Industrial and Engineering Chemistry, 147, 39-55. https://doi.org/10.1016/j.jiec.2024.12.026

[8] Tang, S. H., Rashidi, N. A., & Lim, H. Y. (2025). Advancing biomass-based activated carbon production: challenges, techniques, and opportunities with focus on Malaysia. Environment, Development and Sustainability, 1-25. https://doi.org/10.1007/s10668-025-05998-8

[9] Ali, I., Asim, M., & Khan, T. A. (2012). Low cost adsorbents for the removal of organic pollutants from wastewater. Journal of Environmental Management, 113, 170-183. https://doi.org/10.1016/j.jenvman.2012.08.028

[10] Kundu, S., Khandaker, T., Anik, M. A. A. M., Hasan, M. K., Dhar, P. K., Dutta, S. K., ... & Hossain, M. S. (2024). A comprehensive review of enhanced CO_2 capture using activated carbon derived from biomass feedstock. RSC Advances, 14(40), 29693-29736. DOI: 10.1039/D4RA04537H

[11] Mishra, R. K., Singh, B., & Acharya, B. (2024). A comprehensive review on activated carbon from pyrolysis of lignocellulosic biomass: An application for energy and the environment. Carbon Resources Conversion, 7(4), 100228. https://doi.org/10.1016/j.crcon.2024.100228

[12] Briones-Hidrovo, A., Costa, S. M., Maganinho, C., Silva, C. M., Rocha, J., Dias, A. C., ... & Silva, C. M. (2025). Recovering carbon black from end-of-life tires: A consequential life cycle assessment. Environmental Impact Assessment Review, 115, 108044. https://doi.org/10.1016/j.eiar.2025.108044

[13] Wei, X., Guo, Z., Zhao, Y., Sun, Y., Hankin, A., & Titirici, M. (2025). Recovery of graphite from industrial lithium-ion battery black mass. RSC Sustainability, 3(1), 264-274. DOI: 10.1039/D4SU00427B

[14] Jiang, G., Pan, J., Deng, W., Sun, Y., Guo, J., Che, K., ... & Zhang, T. (2022). Recovery of high pure pyrolytic carbon black from waste tires by dual acid treatment. Journal of Cleaner Production, 374, 133893. https://doi.org/10.1016/j.jclepro.2022.133893

[15] Bhar, M., Ghosh, S., Krishnamurthy, S., Kaliprasad, Y., & Martha, S. K. (2023). A review on spent lithium-ion battery recycling: from collection to black mass recovery. RSC sustainability, 1(5), 1150-1167. https://doi.org/10.1039/d3su00086a

[16] Searle, S., & Malins, C. (2015). A reassessment of global bioenergy potential in 2050. GCB Bioenergy, 7(2), 328-336. https://doi.org/10.1111/gcbb.12141

[17] Khan, W., Shyamal, D. S., & Kazmi, A. A. (2024). Management of end-of-life tyres in India: current practices, regulatory framework, challenges, and opportunities. Journal of Material Cycles and Waste Management, 26(3), 1310-1325. https://doi.org/10.1007/s10163-024-01937-3

[18] Tian, H., Graczyk-Zajac, M., Kessler, A., Weidenkaff, A., & Riedel, R. (2024). Recycling and reusing of graphite from retired lithium-ion batteries: a review. Advanced Materials, 36(13), 2308494. https://doi.org/10.1002/adma.202308494

[19] World Bioenergy Association. WBA Global Bioenergy Statistics 2018, Summary Report. Available online: https://www.worldbioenergy.org/ (accessed on 10 January 2026).

[20] Mubareka, S. B., Renner, A. (2025). EU Biomass supply, uses, governance and regenerative actions. Publications Office of the European Union. https://data.europa.eu/doi/10.2760/6511190

[21] Camia, A., Cazzaniga, N., Tandetzki, J., Magnolfi, V., & Gurria, P. (2025). Biomass supply and demand in the EU 2012-2022. European Commission, Ispra, JRC143910. Available online: https://publications.jrc.ec.europa.eu/repository/handle/JRC143910 (accessed on 15 January 2026).

[22] Tripathi, N., Hills, C. D., Singh, R. S., & Atkinson, C. J. (2019). Biomass waste utilisation in low-carbon products: harnessing a major potential resource. npj Climate and Atmospheric Science, 2(1), 35. https://doi.org/10.1038/s41612-019-0093-5

[23] Braghiroli, F. L., & Passarini, L. (2020). Valorization of Biomass Residues from Forest Operations and Wood Manufacturing Presents a Wide Range of Sustainable and Innovative Possibilities. Current Forestry Reports, 6(2), 172-183. https://doi.org/10.1007/s40725-020-00112-9

[24] Wang, K., & Tester, J. W. (2023). Sustainable management of unavoidable biomass wastes. Green Energy and Resources, 1(1), 100005. https://doi.org/10.1016/j.gerr.2023.100005

[25] Goldstein Research. (2020). Global Tire Recycling Market Analysis 2025: Opportunity, Demand, Growth and Forecast 2017–2025. https://www.goldsteinresearch.com/report/global-tire-recycling-industry-market-trends-analysis [Accessed 1 May 2026].

[26] Mmereki, D., Machola, B., & Mokokwe, K. (2019). Status of waste tires and management practice in Botswana. Journal of the Air & Waste Management Association, 69(10), 1230-1246. https://doi.org/10.1080/10962247.2017.1279696

[27] Recycled Rubber Coalition. (2024). AN UNEXPECTED ELECTRIC VEHICLE ENVIRONMENTAL PROBLEM WITH COMMON SENSE SOLUTIONS. https://static1.squarespace.com/static/60e7217fc5b6e37824b94aea/t/65afd6639ecc9728992e23ae/1706022503819/EV+White+Paper+Final.pdf [Accessed 4 May 2026].

[28] Czarna-Juszkiewicz, D., Kunecki, P., Cader, J., & Wdowin, M. (2023). Review in Waste Tire Management—Potential Applications in Mitigating Environmental Pollution. Materials, 16(17), 5771. https://doi.org/10.3390/ma16175771

[29] Landi, D., Marconi, M., Gianvincenzi, M., & Mosconi, E. M. (2023). Technical and environmental assessment of a circular economy scenario for end of life tires fibers used as reinforcement in plastic compounds. International Journal on Interactive Design and Manufacturing (IJIDeM), 1-12. https://doi.org/10.1007/s12008-023-01249-0

[30] Czajczyńska, D., Czajka, K., Krzyżyńska, R., & Jouhara, H. (2020). Waste tyre pyrolysis–Impact of the process and its products on the environment. Thermal Science and Engineering Progress, 20, 100690. https://doi.org/10.1016/j.tsep.2020.100690

[31] Paul, S., Rahaman, M., Ghosh, S. K., Katheria, A., Das, T. K., Patel, S., & Das, N. C. (2023). Recycling of waste tire by pyrolysis to recover carbon black: an alternative reinforcing filler. Journal of Material Cycles and Waste Management, 25(3), 1470-1481. https://doi.org/10.1007/s10163-023-01635-6

[32] Urrego-Yepes, W., Cardona-Uribe, N., Vargas-Isaza, C. A., & Martínez, J. D. (2021). Incorporating the recovered carbon black produced in an industrial-scale waste tire pyrolysis plant into a natural rubber formulation. Journal of Environmental Management, 287, 112292. https://doi.org/10.1016/j.jenvman.2021.112292

[33] Paul, S., Rahaman, M., Ghosh, S. K., Katheria, A., Das, T. K., Patel, S., & Das, N. C. (2023). Recycling of waste tire by pyrolysis to recover carbon black: an alternative reinforcing filler. Journal of Material Cycles and Waste Management, 25(3), 1470-1481. https://doi.org/10.1007/s10163-023-01635-6

[34] IEA (2025). Global EV Outlook 2025. IEA. Paris. https://www.iea.org/reports/global-ev-outlook-2025, Licence: CC BY 4.0

[35] Tankou, A., Bieker, G., & Hall, D. (2023). Scaling up reuse and recycling of electric vehicle batteries: Assessing challenges and policy approaches. International Council on Clean Transportation (ICCT). (1-138). https://theicct.org/publication/recycling-electric-vehicle-batteries-feb-23/ [Accessed 5 May 2026]

[36] Biswal, B. K., Zhang, B., Tran, P. T. M., Zhang, J., & Balasubramanian, R. (2024). Recycling of spent lithium-ion batteries for a sustainable future: recent advancements. Chemical Society Reviews, 53(11), 5552-5592. https://doi.org/10.1039/D3CS00898C

[37] Zheng, S., Chen, T., Fang, Y., He, C., Duan, H., Ren, S., & Xu, C. C. (2024). A review of cathode and electrolyte recovery from spent lithium-ion batteries: recent technologies, processes and policies. Resources Chemicals and Materials, 3(3), 188-229. https://doi.org/10.1016/j.recm.2024.01.003

[38] Patnaik, S. (2024). Overview of electrode advances in commercial Li-ion batteries. Ionics, 30(6), 3069-3090. https://doi.org/10.1007/s11581-024-05579-1

[39] Koech, A. K., Mwandila, G., Mulolani, F., & Mwaanga, P. (2024). Lithium-ion battery fundamentals and exploration of cathode materials: A review. South African Journal of Chemical Engineering, 50(1), 321-339. https://doi.org/10.1016/j.sajce.2024.09.008

[40] Chang, L., Yang, W., Cai, K., Bi, X., Wei, A., Yang, R., & Liu, J. (2023). A review on nickel-rich nickel–cobalt–manganese ternary cathode materials LiNi 0.6 Co 0.2 Mn 0.2 O 2 for lithium-ion batteries: performance enhancement by modification. Materials Horizons, 10(11), 4776-4826. https://doi.org/10.1039/D3MH01151H

[41] Zou, Y., Chernyaev, A., Ossama, M., Seisko, S., & Lundström, M. (2024). Leaching of NMC industrial black mass in the presence of LFP. Scientific Reports, 14(1), 10818. https://doi.org/10.1038/s41598-024-61569-3

[42] Tong, Z., Wang, M., Bai, Z., Li, H., & Wang, N. (2025). Advances in lithium-ion battery recycling: Strategies, pathways, and technologies. ChemPhysMater, 4(1), 30-47. https://doi.org/10.1016/j.chphma.2024.05.005

[43] Amalia, D., Singh, P., Zhang, W., & Nikoloski, A. N. (2025). A review of pretreatment methods for spent lithium-ion batteries to produce black mass–comparison of processes of Asia Pacific recyclers. Mineral Processing and Extractive Metallurgy Review, 46(5), 626-643. https://doi.org/10.1080/08827508.2024.2367420

[44] Wei, X., Guo, Z., Zhao, Y., Sun, Y., Hankin, A., & Titirici, M. (2025). Recovery of graphite from industrial lithium-ion battery black mass. RSC Sustainability, 3(1), 264-274. https://doi.org/10.1039/D4SU00427B

[45] Natarajan, S., & Aravindan, V. (2020). An urgent call to spent LIB recycling: whys and wherefores for graphite recovery. Advanced Energy Materials, 10(37), 2002238.

[46] Pajootan, E., Perrin-Sarazin, F., Mateevici, G., Toupin, M., Mihai, O., Methven, B., ... & Chenitz, R. (2025). Second-Life Evaluation of Li-Ion Battery Graphite after Separation and

Pre-and Postpurification Treatments of Black Mass. ACS Sustainable Resource Management, 2(4), 632-641. https://doi.org/10.1021/acssusresmgt.5c00010

[47] Fahad Halim, A. F. M., Poinern, G. E. J., Fawcett, D., Sharma, R., Surendran, S., & R, R. (2025). Biomass-Derived Carbon Nanomaterials: Synthesis and Applications in Textile Wastewater Treatment, Sensors, Energy Storage, and Conversion Technologies. CleanMat, 2(1), 4-58. https://doi.org/10.1002/clem.15

[48] Tian, J., Wang, P., Deng, Z., Wei, D., Chen, H., Zhou, C., ... & Li, L. (2025). Synergistic Dual Heteroatom-Engineered Superactivated Carbon Unlocks Record-High Hydrogen Storage via Mg─F Orbital Hybridization. Advanced Materials, 38(5), e09511. https://doi.org/10.1002/adma.202509511

[49] Serafin, J., & Dziejarski, B. (2024). Activated carbons—preparation, characterization and their application in CO_2 capture: a review. Environmental Science and Pollution Research, 31(28), 40008-40062. https://doi.org/10.1007/s11356-023-28023-9

[50] Dziejarski, B., Serafin, J., Andersson, K., & Krzyżyńska, R. (2023). CO_2 capture materials: a review of current trends and future challenges. Materials Today Sustainability, 24, 100483. https://doi.org/10.1016/j.mtsust.2023.100483

[51] Wang, J., & Kaskel, S. (2012). KOH activation of carbon-based materials for energy storage. Journal of Materials Chemistry, 22(45), 23710-23725. https://doi.org/10.1039/C2JM34066F

[52] Heidarinejad, Z., Dehghani, M. H., Heidari, M., Javedan, G., Ali, I., & Sillanpää, M. (2020). Methods for preparation and activation of activated carbon: a review. Environmental Chemistry Letters, 18, 393-415. https://doi.org/10.1007/s10311-019-00955-0

[53] Azam, K., Shezad, N., Shafiq, I., Akhter, P., Akhtar, F., Jamil, F., Shafigue, S,. Park, Y, K,. & Hussain, M. (2022). A review on activated carbon modifications for the treatment of wastewater containing anionic dyes. Chemosphere, 306, 135566. https://doi.org/10.1016/j.chemosphere.2022.135566

[54] Neolaka, Y. A., Riwu, A. A., Aigbe, U. O., Ukhurebor, K. E., Onyancha, R. B., Darmokoesoemo, H., & Kusuma, H. S. (2023). Potential of activated carbon from various sources as a low-cost adsorbent to remove heavy metals and synthetic dyes. Results in Chemistry, 5, 100711. https://doi.org/10.1016/j.rechem.2022.100711

[55] Nizam, N. U. M., Hanafiah, M. M., Mahmoudi, E., Halim, A. A., & Mohammad, A. W. (2021). The removal of anionic and cationic dyes from an aqueous solution using biomass-based activated carbon. Scientific Reports, 11(1), 1-17. https://doi.org/10.1038/s41598-021-88084-z

[56] Sultana, M., Rownok, M. H., Sabrin, M., Rahaman, M. H., & Alam, S. N. (2022). A review on experimental chemically modified activated carbon to enhance dye and heavy metals adsorption. Cleaner Engineering and Technology, 6, 100382. https://doi.org/10.1016/j.clet.2021.100382

[57] Mariana, M., HPS, A. K., Mistar, E. M., Yahya, E. B., Alfatah, T., Danish, M., & Amayreh, M. (2021). Recent advances in activated carbon modification techniques for enhanced heavy metal adsorption. Journal of Water Process Engineering, 43, 102221. https://doi.org/10.1016/j.jwpe.2021.102221

[58] Shahrokhi-Shahraki, R., Benally, C., El-Din, M. G., & Park, J. (2021). High efficiency removal of heavy metals using tire-derived activated carbon vs commercial activated carbon: Insights into the adsorption mechanisms. Chemosphere, 264, 128455. https://doi.org/10.1016/j.chemosphere.2020.128455

[59] Xie, B., Qin, J., Wang, S., Li, X., Sun, H., & Chen, W. (2020). Adsorption of phenol on commercial activated carbons: modelling and interpretation. International Journal of Environmental Research and Public Health, 17(3), 789. https://doi.org/10.3390/ijerph17030789

[60] Reza, M. S., Yun, C. S., Afroze, S., Radenahmad, N., Bakar, M. S. A., Saidur, R., Taweekun, J., & Azad, A. K. (2020). Preparation of activated carbon from biomass and its' applications in water and gas purification, a review. Arab Journal of Basic and Applied Sciences, 27(1), 208-238. https://doi.org/10.1080/25765299.2020.1766799

[61] El-Bery, H. M., Saleh, M., El-Gendy, R. A., Saleh, M. R., & Thabet, S. M. (2022). High adsorption capacity of phenol and methylene blue using activated carbon derived from lignocellulosic agriculture wastes. Scientific Reports, 12(1), 5499. https://doi.org/10.1038/s41598-022-09475-4

[62] Sathishkumar, R., & Prakash, R. (2026). A review on activated carbons (AC) for CO_2 capture applications: preparation, characterization and surface modification methods. Fuel, 405, 136521. https://doi.org/10.1016/j.fuel.2025.136521

[63] Umar, M., Yusuf, B. O., Aliyu, M., Hussain, I., Alhassan, A. M., Awad, M. M., ... & Ganiyu, S. A. (2025). Advancing frontiers in CO_2 capture: The renaissance of biomass-derived carbon materials. Coordination Chemistry Reviews, 526, 216380. https://doi.org/10.1016/j.ccr.2024.216380

[64] Sawalha, H., Maghalseh, M., Qutaina, J., Junaidi, K., & Rene, E. R. (2020). Removal of hydrogen sulfide from biogas using activated carbon synthesized from different locally available biomass wastes-a case study from Palestine. Bioengineered, 11(1), 607-618. https://doi.org/10.1080/21655979.2020.1768736

[65] Wang, S., Nam, H., & Nam, H. (2020). Preparation of activated carbon from peanut shell with KOH activation and its application for H2S adsorption in confined space. Journal of Environmental Chemical Engineering, 8(2), 103683. https://doi.org/10.1016/j.jece.2020.103683

[66] Chan, Y. H., Lock, S. S. M., Wong, M. K., Yiin, C. L., Loy, A. C. M., Cheah, K. W., Chai, S. Y. W., Li, C., How, B. S., Chin, B. L. F., Chan, Z. P., & Lam, S. S. (2022). A state-of-the-art review on capture and separation of hazardous hydrogen sulfide (H2S): Recent advances, challenges and outlook. Environmental Pollution, 314, 120219. https://doi.org/10.1016/j.envpol.2022.120219

[67] Hanif, M. A., Ibrahim, N., & Abdul Jalil, A. (2020). Sulfur dioxide removal: An overview of regenerative flue gas desulfurization and factors affecting desulfurization capacity and sorbent regeneration. Environmental Science and Pollution Research, 27(22), 27515-27540. https://doi.org/10.1007/s11356-020-09191-4

[68] Wang, L., Sha, L., Zhang, S., Cao, F., Ren, X., & Levendis, Y. A. (2022). Preparation of activated coke by carbonization, activation, ammonization and thermal treatment of sewage sludge and waste biomass for SO_2 absorption applications. Fuel Processing Technology, 231, 107233. https://doi.org/10.1016/j.fuproc.2022.107233

[69] Jacobs, J. H., Chou, N., Lesage, K. L., Xiao, Y., Hill, J. M., & Marriott, R. A. (2023). Investigating activated carbons for SO_2 adsorption in wet flue gas. Fuel, 353, 129239. https://doi.org/10.1016/j.fuel.2023.129239

[70] Li, Q., Hou, Y., Xiang, N., Liu, Y., & Huang, Z. (2020). A new insight into the promotional effect of nitrogen-doping in activated carbon for selective catalytic reduction of NO_x with NH_3.

Science of the Total Environment, 740, 140158. https://doi.org/10.1016/j.scitotenv.2020.140158

[71] Niu, J., Zhang, H., Li, L., & Guo, Y. (2021). Cost-effective activated carbon (AC) production from partial substitution of coal with red mud (RM) as additive for SO_2 and NO_x abatement at low temperature. Fuel, 293, 120448. https://doi.org/10.1016/j.fuel.2021.120448

[72] Park, B., & Choi, Y. C. (2022). Evaluation of NO_x removal performance of foam composites with titanium dioxide and active carbon. Construction and Building Materials, 348, 128646. https://doi.org/10.1016/j.conbuildmat.2022.128646

[73] Ma, X., Yang, L., & Wu, H. (2021). Removal of volatile organic compounds from the coal-fired flue gas by adsorption on activated carbon. Journal of Cleaner Production, 302, 126925. https://doi.org/10.1016/j.jclepro.2021.126925

[74] Li, X., Zhang, L., Yang, Z., Wang, P., Yan, Y., & Ran, J. (2020). Adsorption materials for volatile organic compounds (VOCs) and the key factors for VOCs adsorption process: A review. Separation and Purification Technology, 235, 116213. https://doi.org/10.1016/j.seppur.2019.116213

[75] Isinkaralar, K. (2024). Multi-component volatile organic compounds (VOCs) treatment nexus: High-performance of activated carbon derived from residual agroforestry biomass. International Journal of Environmental Science and Technology, 21(1), 925-938. https://doi.org/10.1007/s13762-023-05202-2

[76] Rouquerol, J., Rouquerol, F., Llewellyn, P., Maurin, G., & Sing, K. (2012). Adsorption by Powders and Porous Solids: Principles, Methodology and Applications. Academic Press. https://doi.org/10.1016/C2010-0-66232-8.

[77] Yang, R. T. (1997). Gas Separation by Adsorption Processes, Series on Chemical Engineering, (Vol. 1). Imperial College Press. https://doi.org/10.1142/p037.

[78] García–Nieto, P. J., García–Gonzalo, E., & Paredes–Sánchez, J. P. (2024). Estimation of the coal higher heating value for energy systems relied on ultimate analysis with machine learning techniques. Fuel, 357, 130037. https://doi.org/10.1016/j.fuel.2023.130037

[79] Cychosz, K. A., & Thommes, M. (2018). Progress in the physisorption characterization of nanoporous gas storage materials. Engineering, 4(4), 559-566. https://doi.org/10.1016/j.eng.2018.06.001

[80] Thommes, M., Morlay, C., Ahmad, R., & Joly, J. P. (2011). Assessing surface chemistry and pore structure of active carbons by a combination of physisorption (H_2O, Ar, N_2, CO_2), XPS and TPD-MS. Adsorption, 17(3), 653-661. https://doi.org/10.1007/s10450-011-9360-4

[81] Wang, Y., Hu, X., Guo, T., Hao, J., Si, C., & Guo, Q. (2021). Efficient CO_2 adsorption and mechanism on nitrogen-doped porous carbons. Frontiers of Chemical Science and Engineering, 15, 493-504. https://doi.org/10.1007/s11705-020-1967-0

[82] Dombrowski, R. J., Hyduke, D. R., & Lastoskie, C. M. (2000). Pore size analysis of activated carbons from argon and nitrogen porosimetry using density functional theory. Langmuir, 16(11), 5041-5050. https://doi.org/10.1021/la990827a

[83] Song, Z. Z., Abula, A., Zhao, J. Y., Liu, G. D., Li, M. R., Yang, D. L., & Wang, Y. L. (2022). A novel hybrid thermodynamic model for pore size distribution characterisation for shale. Petroleum Science, 19(3), 963-978. https://doi.org/10.1016/j.petsci.2021.12.015

[84] Bhargava, R., & Levin, I. W. (2005). Fourier Transform Mid-infrared Spectroscopic Imaging: Microspectroscopy with Multichannel Detectors. Spectrochemical Analysis Using Infrared Multichannel Detectors, 1-24. DOI:10.1002/9780470988541

[85] Peticolas, W. L. (1972). Inelastic light scattering and the Raman effect. Annual Review of Physical Chemistry, 23(1), 93-116. https://doi.org/10.1146/annurev.pc.23.100172.000521

[86] Smith, E., & Dent, G. (2019). Modern Raman spectroscopy: a practical approach. John Wiley & Sons. DOI:10.1002/0470011831

[87] Zhou, W., Apkarian, R., Wang, Z. L., & Joy, D. (2007). Fundamentals of scanning electron microscopy (SEM). Scanning microscopy for nanotechnology: techniques and applications, 1-40. https://doi.org/10.1007/978-0-387-39620-0

[88] Bunaciu, A. A., UdriŞTioiu, E. G., & Aboul-Enein, H. Y. (2015). X-ray diffraction: instrumentation and applications. Critical Reviews in Analytical Chemistry, 45(4), 289-299. https://doi.org/10.1080/10408347.2014.949616

[89] Bubert, H., Rivière, J. C., & Werner, W. S. (2011). X-Ray Photoelectron Spectroscopy (XPS). Surface and Thin Film Analysis: A Compendium of Principles, Instrumentation, and Applications, 7-41. DOI:10.1002/9783527636921

[90] Zheng, Y., Wang, J., Li, D., Liu, C., Lu, Y., Lin, X., & Zheng, Z. (2021). Insight into the KOH/$KMnO_4$ activation mechanism of oxygen-enriched hierarchical porous biochar derived

from biomass waste by in-situ pyrolysis for methylene blue enhanced adsorption. Journal of Analytical and Applied Pyrolysis, 158, 105269. https://doi.org/10.1016/j.jaap.2021.105269

[91] Chen, Y. D., Chen, W. Q., Huang, B., & Huang, M. J. (2013). Process optimization of $K_2C_2O_4$-activated carbon from kenaf core using Box–Behnken design. Chemical Engineering Research and Design, 91(9), 1783-1789. https://doi.org/10.1016/j.cherd.2013.02.024

Paper I

Chemical Engineering Journal 524 (2025) 169677

Contents lists available at ScienceDirect

Chemical Engineering Journal

journal homepage: www.elsevier.com/locate/cej

Tailoring highly surface and microporous activated carbons (ACs) from biomass via KOH, $K_2C_2O_4$ and KOH/$K_2C_2O_4$ activation for efficient CO_2 capture and CO_2/N_2 selectivity: characterization, experimental and molecular simulation insights

Bartosz Dziejarski [a,b,c,*], Jarosław Serafin [d,e,**], Diego Felipe Hernández-Barreto [f], Elena Naumovska [a], Joanna Sreńscek-Nazzal [g], Nikom Klomkliang [h], Eric Tam [i], Renata Krzyżyńska [c], Klas Andersson [b], Pavleta Knutsson [a]

[a] Department of Chemistry and Chemical Engineering, Division of Energy and Materials, Chalmers University of Technology, SE-412 96 Gothenburg, Sweden
[b] Department of Space, Earth and Environment, Division of Energy Technology, Chalmers University of Technology, SE-412 96 Gothenburg, Sweden
[c] Faculty of Environmental Engineering, Wroclaw University of Science and Technology, 50-370 Wroclaw, Poland
[d] Department of Inorganic and Organic Chemistry, University of Barcelona, Martí i Franquès, 1-11, 08028, Barcelona, Spain
[e] ENPHOCAMAT Group, Institute of Nanoscience and Nanotechnology (IN2UB), University of Barcelona, C/ Martí i Franquès, 1, 08028, Barcelona, Catalunya, Spain
[f] Departamento de Química, Facultad de Ciencias, Grupo de Investigación en Sólidos Porosos y Calorimetría, Universidad de Los Andes, Cra. 1a No. 18A-10, Bogotá D.C., 11711, Colombia
[g] West Pomeranian University of Technology in Szczecin, Faculty of Chemical Technology and Engineering, Department of Catalytic and Sorbent Materials Engineering, Piastów Ave. 42, 71-065, Szczecin, Poland
[h] School of Chemical Engineering, Suranaree University of Technology, Nakhon Ratchasima, 30000, Thailand
[i] Department of Industrial and Materials Science, Division of Materials and Manufacture, Chalmers University of Technology, SE-412 96, Gothenburg, Sweden

ARTICLE INFO

Keywords:
Lignocellulosic biomass
Chemical activation
Ultramicroporosity
Gas adsorption and separation
Molecular simulation

ABSTRACT

The environmental impact of wood waste disposal and limitations of conventional chemical activation underscore the need for sustainable strategies to convert lignocellulosic biomass into efficient CO_2 sorbents. In this study, pine wood was activated at 800 °C using KOH, $K_2C_2O_4$, and their mixtures (mass ratios 1:1 to 1:4) to tailor porosity and surface chemistry for selective CO_2 capture. Co-activation at a 1:2:2 ratio (biomass:KOH:$K_2C_2O_4$) delivered optimal textural features, including a BET surface area of 2029 m^2/g, total pore volume of 1.028 cm^3/g, and micropore volumes of 0.923 cm^3/g (N_2) and 0.156 cm^3/g (CO_2). The KOH-activated carbon (1:1) achieved the highest CO_2 uptake 9.65 mmol/g at 0 °C and 5.95 mmol/g at 25 °C due to extensive ultramicropore development. In contrast, the $K_2C_2O_4$-derived sample (1:4) exhibited lower uptake (8.79 mmol/g at 0 °C) but superior CO_2/N_2 selectivity (>21 at 5 % CO_2, 1 bar), linked to narrower pores and higher surface polarity. Structural and surface analyses (XRD, FTIR, XPS, XRF, SEM, TGA) confirmed turbostratic carbon, abundant oxygenated groups (C—O, C═O), and sponge-like morphology with residual inorganic species. Isosteric heats of CO_2 adsorption (26–36 kJ/mol) indicated strong physisorption, and isotherm modeling identified Radke–Prausnitz as the best-fit model. Grand canonical Monte Carlo simulations supported the experimental results, revealing that sub-nanometer pores and carbonyl-rich surfaces enhance CO_2 affinity. This work presents a comprehensive comparison of K-based activation strategies and demonstrates that co-activation offers a scalable, less harsh route to high performance porous carbons for CO_2 capture.

* Correspondence to: B. Dziejarski, Department of Chemistry and Chemical Engineering, Division of Energy and Materials, Chalmers University of Technology, SE-412 96, Gothenburg, Sweden.
** Correspondence to: J. Serafin, Department of Inorganic and Organic Chemistry, University of Barcelona, Martí i Franquès, 1-11, 08028, Barcelona, Spain.
E-mail addresses: bartoszd@chalmers.se (B. Dziejarski), jaroslaw.serafin@ub.edu (J. Serafin).

https://doi.org/10.1016/j.cej.2025.169677
Received 26 August 2025; Received in revised form 7 October 2025; Accepted 13 October 2025
Available online 15 October 2025

1. Introduction

The increasing demand for sustainable resource management has intensified the search for efficient strategies to valorize biomass waste from industrial sectors. As the most abundant renewable feedstock, biomass transformation into value-added materials aligns with circular economy and carbon neutrality goals [1–4]. Among various waste streams, forest industry residues are particularly impactful [5]. According to the Food and Agriculture Organization, global wood production exceeded 4 billion m^3/year in 2022, with nearly 2.04 billion m^3 of roundwood harvested about half used as fuel [6]. This generates vast amounts of underutilized wood waste, such as sawdust, bark, and offcuts, often discarded via burning or landfilling [7]. These practices waste carbon-rich materials and contribute to pollution and greenhouse gas emissions. Consequently, environmentally sound and cost-effective valorization of lignocellulosic residues into functional materials is urgently needed [8].

One promising approach is the conversion of biomass into activated carbons (ACs), a highly porous carbonaceous materials with outstanding adsorption properties [9,10]. While traditionally derived from coal or polymers, biomass-based ACs are increasingly attractive due to their low cost and renewability [11]. Rich in carbon, residues like wood, nutshells, and agro-waste can be thermochemically converted into high surface area, microporous sorbents [12]. ACs possesses a set of key properties that make it particularly effective as an adsorbent: high surface area, extensive microporosity, fast adsorption kinetics, chemical and thermal stability, and ease of regeneration [13]. Typically amorphous, they contain ~90 wt% carbon and heteroatoms like O, N, S, and H [14]. Their porosity is categorized into micropores (<2 nm), mesopores (2–50 nm), and macropores (>50 nm) [15,16], each contributing differently depending on the application. Macropores and mesopores support the transport and separation of bulky molecules, while micropores provide primary adsorption sites. Therefore, optimal adsorption performance relies on a balanced pore structure [17]. Because of these advantageous properties, ACs have found broad utility in water purification [18], environmental remediation [19], energy storage [20], and gas separation [21].

Recently, microporous ACs have shown great potential for CO_2 capture in post-combustion and direct air capture (DAC) scenarios, due to their tunable porosity and cycling stability [22,23]. Compared to alternatives like zeolites or MOFs, biomass-derived ACs offer lower cost, greater processability, and enhanced resilience under operating conditions [24,25].

To produce ACs, activation is crucial for tuning pore architecture and surface chemistry. Chemical activation, performed at 400–900 °C, effectively produces high surface area materials with rich microporosity [26,27,28]. In this process, a chemical activating agent, commonly an acid, base, or salt, is intimately mixed with the biomass to facilitate pore development during thermal treatment. Common activators include alkaline agents (KOH, NaOH, K_2CO_3), oxidizing acids (H_3PO_4, HNO_3), and neutral salts ($ZnCl_2$) [14,29]. Two main methods are used: dry mixing, in which the biomass and activator are blended as solids, and wet impregnation, where the biomass is soaked in an activating solution [30]. The resulting mixture is then pyrolyzed under an inert atmosphere, yielding activated carbon. Among these activators, KOH remains the most effective and widely studied [31]. KOH initially converts to K_2O, which is then reduced to metallic potassium. The potassium intercalates into the carbon lattice, penetrating graphene layers and causing structural expansion. Simultaneously, carbon oxidation to CO, CO_2, and K_2CO_3 promotes pore formation [32]. Recent studies have applied KOH activation to various biomass precursors, such as walnut shell, cashew nut shells [33], banana peels [34], olive stones [35], and argan press cake [36], demonstrating that the activation temperature (500–800 °C) and the mass ratio between precursor and activator (1:1–1:4) are critical for optimizing porosity, surface chemistry, and adsorption capacity [37,38].

However, KOH poses drawbacks: it is corrosive, hazardous, and produces alkaline wastewater [32]. This has led to interest in safer alternatives like potassium oxalate ($K_2C_2O_4$), which decomposes into K_2CO_3 while avoiding caustic residues [39,40]. It induces pore formation through thermal cracking, and offers lower toxicity, easier handling, and reduced environmental impact [41].

Notably, activation mechanisms vary with both the K-based chemical agent and the biomass source, resulting in distinct textural and surface chemical properties in the resulting activated carbons. Even closely related activators such as KOH and $K_2C_2O_4$ can lead to different pore architectures and surface functionalities depending on the biomass type [42]. In this context, combining the strong etching effect of KOH with the gas-releasing decomposition of $K_2C_2O_4$ offers a promising mixed-activation strategy. Such an approach could synergistically fine-tune micro- and mesopore volumes, enhance surface heterogeneity, and improve CO_2 capture performance, while reducing the reliance on harsh chemicals. However, to date, there is no comprehensive study that compares these activation routes under identical conditions and explores their impact on CO_2 uptake, selectivity, and isosteric adsorption thermodynamics. Here, we present a first-of-its-kind investigation into the use of KOH/$K_2C_2O_4$ co-activation to engineer ultramicroporous carbons from woody biomass, offering a scalable and more eco-friendly route to high-performance CO_2 sorbents.

Herein, this gap was investigated by activating woody biomass with KOH, $K_2C_2O_4$, and their mixtures at 800 °C, using a range of mass ratios (biomass:activator = 1:1 to 1:4). The same mass ratios were applied for both individual K-based activators and their combinations to allow a systematic comparison. The aims were to (1) evaluate the activation behavior of KOH across different mass ratios, (2) investigate the potential of $K_2C_2O_4$ as a standalone alternative, (3) explore possible synergistic effects of the KOH/$K_2C_2O_4$ combination, and (4) assess the resulting materials for effective CO_2 capture performance. The ACs were characterized by their textural, structural, chemical, morphological, and thermal properties. CO_2 uptake and CO_2/N_2 selectivity were measured to assess application potential. Molecular dynamics simulations supported the experimental findings and helped relate structure to performance. The co-activation strategy proved effective in tuning porosity, enhancing surface heterogeneity, and improving CO_2 capture, while minimizing the use of harsh chemicals. Dynamics simulations were also employed to support experimental observations and provide insight into structure–performance relationships. The results demonstrated that the co-activation strategy enabled effective tuning of micro- and mesopore volumes, improved surface heterogeneity, and enhanced CO_2 capture performance, while reducing dependence on harsh chemicals. This work not only delivers a benchmark in more green chemical activation but also provides molecular-level insight into how activation route governs ultramicropore formation, CO_2 affinity, and multicomponent selectivity.

2. Materials and methods

2.1. Source of woody biomass

The biomass used as a precursor for activated carbon synthesis consisted of untreated pine wood, sourced from pieces utilized as a renewable fuel in the boiler facility at Chalmers University of Technology (Sweden). The wood was free from any chemical treatments, coatings, or additives, ensuring its suitability to produce high-purity carbonaceous materials. The biomass corresponded to a softwood lignocellulosic substrate, dominated by cellulose and hemicellulose, with moderate lignin content typical of coniferous species. The physicochemical composition of pine wood is shown in Table 1. The material exhibits a high carbon content (50 wt%) and oxygen content (43 wt%), a moderate hydrogen content (6.0 wt%), and a low nitrogen content (0.11 wt%). Additionally, the ash content remains minimal (0.4 wt%), and the moisture level is relatively low (6 wt%), confirming its suitability as a clean and renewable precursor for AC synthesis.

Table 1
Textural properties of activated carbons synthesized using KOH, $K_2C_2O_4$, and their mixtures.

Sample	S_{BET}[a], [m^2/g]	V_{TOT}[b], [cm^3/g]	$V_{MIC\ (N2)}$[c], [cm^3/g]	V_{MES}[c], [cm^3/g]	$V_{MIC\ (CO2)}$[c], [cm^3/g]	Yield, [%]
WP-KOH-1:1	1956	0.943	0.836	0.107	0.164	12.6
WP-KOH-1:2	2293	1.146	1.017	0.129	0.158	10.5
WP-KOH-1:3	2371	1.321	1.159	0.162	0.148	9.0
WP-KOH-1:4	2655	1.339	1.021	0.318	0.133	7.8
WP-$K_2C_2O_4$–1:4	1709	0.885	0.794	0.091	0.150	18.5
WP-KOH-$K_2C_2O_4$–1:1:3	1885	0.935	0.726	0.209	0.146	16.2
WP-KOH-$K_2C_2O_4$–1:2:2	2029	1.028	0.923	0.105	0.156	13.5
WP-KOH-$K_2C_2O_4$–1:3:1	1905	0.965	0.757	0.208	0.142	11.2

[a] BET method using the Rouquerol criteria.
[b] Determined from the N_2 adsorption isotherm at a high relative pressure (~0.98–0.99).
[c] DFT method by the NLDFT model.

2.2. Biomass pre-treatment

Prior to chemical activation, the untreated pine wood was subjected to a two-step size reduction process. Initially, the material was coarsely crushed using a Wiley mill to break it into smaller fragments. To enhance the reactivity with chemical activating agents, the pre-crushed wood was subsequently ground using a Retsch ZM 1 centrifugal mill equipped with a single sieve, producing a fine powder with reduced particle diameter. The target particle size was below 0.5 mm to ensure homogeneous impregnation and effective thermal penetration. This approach ensured uniformity in particle size and improved the efficiency of subsequent activation steps.

2.3. Chemical activation with KOH and $K_2C_2O_4$ for ACs production

Chemical activation via the dry-mixing method was employed to produce ACs. As shown in Fig. S1, pre-treated pine wood was thoroughly mixed with the selected chemical activating agents at specific mass ratios. Three types of activators were investigated: KOH, $K_2C_2O_4$, and a combination of both, to assess their individual and synergistic effects on the properties of ACs. The samples are labeled based on the type and ratio of K-based activators. WP-KOH-X or WP-$K_2C_2O_4$-X denote activation with KOH or $K_2C_2O_4$ at biomass-to-KOH mass ratios of 1:1 to 1:4. Combined activations are labeled as WP-KOH-$K_2C_2O_4$-X:Y:Z, indicating the mass ratios of biomass, KOH, and $K_2C_2O_4$, respectively (e.g., 1:1:3, 1:2:2, 1:3:1).

The biomass–activator mixtures were manually ground in a mortar to ensure homogeneous distribution. A grinding time of 10–15 min was applied for each batch to maximize interfacial contact and minimize agglomeration. The prepared mixtures were then placed in alumina crucibles and subjected to thermal activation in a tubular furnace. The activation was conducted at 800 °C for 3 h under a continuous nitrogen flow (250 mL/min) to maintain an inert atmosphere throughout the process, with the temperature and duration selected based on preliminary studies and reported literature confirming their adequacy. The heating rate was controlled at 5 °C/min to allow gradual thermal decomposition and promote uniform pore development. After activation, the samples were washed extensively with deionized water (~6 L) on a paper filter until the pH of the filtrate reached neutral, effectively removing any residual inorganic compounds. Finally, the activated carbon samples were oven-dried at 80 °C for 12 h to ensure complete moisture removal. The resulting powdered materials were stored in airtight, light-protected glass containers under dry argon atmosphere to prevent moisture uptake and surface oxidation prior to characterization.

2.4. Carbon-based material characterization

2.4.1. Textural characterization

The textural characteristics of the synthesized activated carbons were evaluated through gas adsorption analysis. Nitrogen adsorption–desorption isotherms were measured at −196 °C using an automated volumetric sorption analyzer (Quadrasorb Evo™, Quantachrome Instruments). Prior to analysis, all samples were degassed under vacuum at 250 °C for 16 h to remove adsorbed contaminants and moisture.

The specific surface area (S_{BET}) was determined using the Brunauer–Emmett–Teller (BET) method, with the adsorption data fitted in the relative pressure (p/p_o) range of 0.05 to 0.35. The selection of this range was guided by the Rouquerol criteria, ensuring the BET "C" constant remained positive; data points slightly outside this interval were included when they contributed to improved linearity. The total pore volume (V_{TOT}) was calculated from the volume of N_2 adsorbed at a relative pressure of $p/p_o \approx 0.99$. Micropore volume ($V_{MIC(N2)}$) and mesopore volume (V_{MES}), corresponding to pores larger than approximately 1.4 nm and within the 2–50 nm range, as well as the pore size distribution (PSD), were determined using the non-local density functional theory (NLDFT) model applied to the N_2 adsorption isotherms.

Additionally, micropore volume ($V_{MIC(CO2)}$) in the 0.3–1.4 nm range was obtained from CO_2 adsorption isotherms measured at 0 °C and evaluated using the NLDFT model as well, providing complementary insight into the microporous structure.

2.4.2. Structural and morphological characterization

The crystalline structure of the activated carbons was investigated using X-ray diffraction (XRD) on a Bruker D8 Discover diffractometer. Samples were finely ground to ensure homogeneity prior to analysis. Cu Kα radiation ($\lambda = 0.15418$ nm) was used as the X-ray source, and diffraction patterns were recorded over a 2θ range from 10° to 105° with uniform step intervals. Phase identification was performed using the DIFFRAC.EVA software, with reference to the ICDD PDF-4+ 2025 database to determine the phases formed during activation.

The morphological properties of the ACs were examined using a field emission environmental scanning electron microscope (FEI ESEM Quanta 200) integrated with an energy-dispersive X-ray spectroscopy (EDS) system for elemental analysis. Image acquisition was performed utilizing the backscattered electron (BSE) mode to enhance compositional contrast. To minimize surface charging effects, the analysis was conducted under low vacuum conditions at a chamber pressure of 20 Pa. The accelerating voltage of the electron beam was set to 10 kV during all observations.

2.4.3. Surface characterization

To identify the surface functional groups present on the activated carbons, Fourier transform infrared (FTIR) spectroscopy was carried out using a Nicolet 380 spectrometer (Thermo Scientific). The spectra were recorded over a wavenumber range of 400–4000 cm^{-1}. Before each measurement, a background spectrum was collected and automatically subtracted from the sample spectra to ensure accurate baseline correction.

To determine the surface chemical composition and the chemical states of elements present, X-ray photoelectron spectroscopy (XPS) analysis was performed using a PHI 5000 VersaProbe III Scanning XPS Microprobe™. Dual charge compensation, combining an argon ion gun (positive) and an electron neutralizer (negative), was applied during measurements to accommodate the non-conductive nature of the samples. A survey scan was first conducted over the energy range of 0–1300 eV with a step size of 1.0 eV to identify the elemental composition. Based on the detected elements, high-resolution narrow scans were subsequently performed with a step size of 0.1 eV to analyze the chemical states in greater detail. The spectral energy resolution, determined by the full width at half maximum (FWHM) of the Ag $3d_{5/2}$ peak from a sputter-cleaned silver foil, was 0.673 eV. Energy scale calibration was

performed according to ISO 15472 standards, using reference peaks from sputter-cleaned gold (Au $4f_{7/2}$ at 83.96 eV), silver (Ag $3d_{5/2}$ at 368.21 eV), and copper (Cu $2p_{3/2}$ at 932.62 eV).

2.4.4. Thermal and elemental characterization

The thermal behavior of the ACs was analyzed using a TGA-DSC 3+ system from Mettler Toledo. Each sample was subjected to a programmed heating cycle, increasing the temperature from 30 °C to 900 °C at a linear rate of 10 K per minute, while maintaining an inert nitrogen environment throughout the experiment. The resulting mass change data provided insights into the materials' decomposition pathways and overall thermal resistance under non-oxidizing conditions.

Elemental composition (CHNS) was determined according to the CEN/TS 15104 method, with oxygen content calculated by difference. Ash and moisture contents were measured following SS-EN 14775 and SS-EN 14774–2, respectively.

To complement the structural and thermal assessments, the residual inorganic content of the produced ACs was examined to evaluate the influence of activation agents on the retention of elemental species. The elemental composition of the biomass-derived activated carbons was analyzed using an energy-dispersive X-ray fluorescence (EDXRF) spectrometer (Epsilon 3, PANalytical B.*V.*). This analysis was conducted to identify the presence and of inorganic elements originating from the raw material and after activation process.

2.5. CO_2/N_2 adsorption experimental investigation

The equilibrium adsorption of CO_2 and N_2, as well as the long-term CO_2 capture performance of the ACs, was measured using a QUADRASORB evo™ volumetric analyzer (Quantachrome Instruments). Experiments were conducted at two different temperatures, 0 °C (maintained with an ice–water mixture) and 25 °C (regulated by a circulating bath), with pressures reaching up to 1 bar. Pure CO_2 and N_2 gases were used for all measurements. Prior to adsorption testing, each sample underwent thermal pretreatment by heating under vacuum at 200 °C for 16 h to eliminate residual moisture and volatile compounds. After degassing, the samples were cooled to the desired measurement temperature, and ultrahigh-purity gas was introduced into the system for isotherm acquisition.

To gain deeper insight into the CO_2 adsorption process, six isotherm models (Toth, Combined Freundlich–Langmuir, Sips, Redlich–Peterson, Radke–Prausnitz, and Dual-Site Langmuir) were employed to interpret the experimental data. Model fitting was conducted by minimizing the absolute error (EABS), enabling quantitative comparison of the models performance. The equation for EABS is expressed as follows:

$$EABS = \sum_{i=1}^{n} \left| q_{e,\exp} - q_{e,mod} \right| \tag{1}$$

Where: $qe_{,mod}$ represents the predicted adsorption capacity at equilibrium [mmol/g], $qe_{,exp}$ denotes the experimentally measured adsorption capacity at equilibrium [mmol/g].

To assess the CO_2/N_2 separation performance of the materials, selectivity was evaluated using the ideal adsorbed solution theory (IAST). IAST was selected as it provides a reliable theoretical framework to predict multicomponent adsorption equilibrium based on pure-component isotherms. All IAST calculations were performed using the GraphIAST graphical interface, which evaluates selectivity as a function of total pressure and bulk-phase gas composition. To ensure consistency with the experimental isotherm data, the Dual-Site Langmuir (DSL) model was used to fit both CO_2 and N_2 isotherms, as its parameterization is directly compatible with the GraphIAST platform. Once the DSL isotherm functions are defined and the total pressure (P_t) along with the bulk-phase mole fractions (y_i) are specified, GraphIAST numerically solves the coupled non-linear equations to determine the adsorbed-phase compositions (x_i), spreading pressures (π_i), and pure-component equilibrium pressures in the adsorbed phase (p_i^0) [43,44]. The IAST selectivity (S_{IAST}), is then computed via:

$$S_{IAST} = \frac{x_1}{x_2} \bullet \frac{y_2}{y_1} \tag{2}$$

where x_1 and x_2 represent the molar compositions of CO_2 and N_2, respectively, in the adsorbed phase, while y_1 and y_2 denote their corresponding molar fractions in the bulk gas phase.

The isosteric heat of adsorption (Q_{st}) was calculated to evaluate the interaction strength between CO_2 molecules and the adsorbent surface. It is defined as the difference between the partial molar enthalpy of the adsorbed phase and that of the bulk phase at a constant adsorbed amount [45]. As a fundamental thermodynamic parameter, Q_{st} quantifies the strength of interactions between adsorbate molecules and the adsorbent surface. An indirect determination of Q_{st} involves measuring adsorption isotherms at multiple temperatures and applying the Clausius–Clapeyron relation:

$$Q_{st} = -R \left(\frac{\partial(\ln P)}{\partial\left(T^{-1}\right)} \right)_q \tag{3}$$

In this equation, Q_{st} is the isosteric heat of adsorption (kJ/mol), R is the universal gas constant (8.314 × 10^{-3} kJ/mol K^{-1}), P is the equilibrium pressure (bar), T is the absolute temperature (K), and q is the adsorbed amount (mmol/g).

To determine the equilibrium pressure corresponding to specific values of q at each temperature, the fitted Radke–Prausnitz isotherm model was employed. Fractional loading (θ) was defined as the ratio between the adsorbed amount (q) and the maximum experimental adsorbed amount (q at P ≈ 1 bar).

2.6. Molecular simulation of CO_2 adsorption

CO_2 adsorption simulations were carried out using the grand canonical Monte Carlo (GCMC) technique [46]. In GCMC, the temperature (T), volume, and bulk pressure (chemical potential) are constant and specified. Three types of trial moves are used: particle translation and rotation, insertion, and deletion, with microscopic reversibility ensuring that equal numbers of insertions and deletions occur. The other Monte Carlo (MC) parameters used in this work are as follows: (i) 100,000 cycles for the equilibration step and an additional 100,000 cycles for data collection, with each cycle consisting of 1000 attempted trial moves; (ii) periodic boundary conditions applied in all three directions; and (iii) the cut-off radius set to half the box length.

The excess adsorption amount (N_{ex}) is calculated from equation:

$$N_{ex} = N_{ab} - \rho_b V_{free} \tag{4}$$

where N_{ab}, ρ_b, and V_{free} represent the absolute amount adsorbed, the bulk adsorbate density calculated using the Johnson equation of state [47], and the pore volume, respectively.

The simulation-derived total isosteric heat of adsorption (Q_{SIM}) was calculated as the difference between the enthalpy of the adsorbate in the gas phase (approximated as k_BT) and the partial molar energy of the adsorbed phase, which includes the sum of fluid–fluid (F—F) and fluid–solid (F—S) interaction energies. The F—S contribution accounts for interactions between the adsorbate and all atom types within the graphene layers and surface functional groups, as detailed below.

$$Q_{SIM} = k_B T - Q_{F-F} - Q_{F-S} \tag{5}$$

$$Q_{F-S} = Q_{F-G} + Q_{F-Fn} \tag{6}$$

The contribution of each term in Eqs. (5) and (6) was individually calculated using fluctuation theory [48], as follows:

$$Q_{a-b} = \frac{\langle U_{a-b} N \rangle - \langle U_{a-b} \rangle \langle N \rangle}{\langle N^2 \rangle - \langle N \rangle \langle N \rangle} \tag{7}$$

where U_{a-b} is the configuration energy of interaction between *a* and *b* entities, ⟨ ⟩ indicates the ensemble average and *N* is the number of adsorbed molecules.

The GCMC models were built based on the experimental textural and surface chemistry data.

3. Results and discussion

3.1. Effect of K-based activation agent (KOH vs. $K_2C_2O_4$) on porous structure development of ACs

Fig. 1 presents the N_2 adsorption–desorption isotherms at −196 °C for ACs synthesized using KOH, $K_2C_2O_4$, and KOH/$K_2C_2O_4$ mixtures. All samples exhibit Type I isotherms, characteristic of microporous materials, with a steep nitrogen uptake at low relative pressures ($P/P_0 < 0.01$) [49]. This behavior reflects rapid micropore filling due to the high adsorption potential in narrow pores. In such cases, the overall uptake is primarily determined by the accessible micropore volume rather than the total internal surface area [50]. Although the isotherms display similar overall shapes, distinct differences in adsorption capacity and hysteresis behavior can be observed. KOH-activated carbons (Fig. 1a) show the highest N_2 uptake and the steepest initial slope, indicating a well-developed microporous structure. Additionally, a minor H4-type hysteresis loop is present at $P/P_0 > 0.4$, suggesting the occurrence of narrow slit-like pores or partially filled mesopores [51]. In Fig. 1b, the sample activated solely with $K_2C_2O_4$ shows significantly lower adsorption and a more gradual increase in N_2 uptake, which points to limited micropore formation. A broader H4-type hysteresis loop is visible, indicating the presence of wider micropores and narrow mesopores, consistent with the less aggressive activation process of $K_2C_2O_4$ [52]. The other ACs in Fig. 1b, prepared using KOH/$K_2C_2O_4$ mixtures, exhibit intermediate adsorption behavior. Their N_2 uptake is higher than that of WP-$K_2C_2O_4$-1:4 but lower than that of the KOH-activated carbons. The ACs derived from these mixed K-based salts are characterized by more pronounced hysteresis, indicating a more complex pore network with contributions from both micro- and mesopores.

The PSD profiles obtained from N_2 and CO_2 adsorption are presented in Fig. S2, offering valuable insight into the pore structure variations induced by KOH and $K_2C_2O_4$ activation. In Fig. S2a, derived from N_2 sorption, KOH-based ACs exhibit a pronounced micropore peak below 1.25 nm, alongside smaller features in the 1.25–1.75 nm and 1.75–2.0 nm regions. Additionally, a slight increase between 2.1 and 4.0 nm suggests the presence of minor mesoporosity. The corresponding CO_2-derived PSD (Fig. S2b) confirms a high concentration of ultramicropores (<0.7 nm) and supermicropores (0.7–2 nm) [53], with distinct peaks in the 0.3–0.4 nm, 0.4–0.6 nm, and 0.6–1.0 nm ranges. In contrast, biomass treated with $K_2C_2O_4$ and KOH/$K_2C_2O_4$ mixtures (Fig. S2c) shows a similar N_2-based distribution but with lower intensity, indicating reduced total pore volume between 1 nm and 4 nm, while the CO_2-based PSD (Fig. S2d) reveals comparable ultra- and supermicroporosity to that observed earlier. Fig. 2 further demonstrates how pore-width distributions evolve with changes in K-based activator type and biomass-to-activator mass ratio. KOH-based systems exhibit pronounced microporosity below 1.25 nm (N_2) and 0.46 nm (CO_2), while the $K_2C_2O_4$ and $K_2C_2O_4$/KOH systems display weaker pore development yet retain dominant ultramicroporosity, particularly in the 0.23–0.28 nm, 0.29–0.36 nm, and 0.37–0.47 nm ranges.

Moreover, a detailed analysis of the CO_2 adsorption isotherms at low relative pressures (Fig. 3) reveals that $K_2C_2O_4$ promotes ultramicropore formation more effectively than KOH, despite the latter being a well-established micropore-forming agent [32]. Increasing the WP-to-KOH ratio leads to a noticeable decline in ultramicroporosity. When both activators are used simultaneously in balanced proportions (WP-KOH-$K_2C_2O_4$-1:2:2), no synergistic effect is observed in the low-pressure region of the CO_2 isotherms at 0 °C. Nevertheless, the combined use of KOH and $K_2C_2O_4$ still enables the development of a broader microporous network, resulting in a PSD similar to those produced by the individual activators.

The textural parameters of ACs are summarized in Table 1. For the KOH-activated carbons, increasing the KOH ratio leads to a clear enhancement in BET surface area and pore development. The S_{BET} increases from 1956 m^2/g (WP-KOH-1:1) to 2655 m^2/g (WP-KOH-1:4), while the V_{TOT} reaches a maximum of 1.339 cm^3/g for WP-KOH-1:4. However, the highest $V_{MIC(CO2)}$ (0.164 cm^3/g) is found for WP-KOH-1:1, indicating that higher KOH loadings promote the formation of mesopores or larger micropores, without significantly improving porosity between 0.3 nm and 1.4 nm [54]. In contrast, biomass activated with $K_2C_2O_4$ (WP-$K_2C_2O_4$-1:4) exhibits the lowest S_{BET} (1709 m^2/g) and V_{TOT} (0.885 cm^3/g) yet maintains a comparable $V_{MIC(CO2)}$ (0.150 cm^3/g). This suggests that the porosity developed is more selectively concentrated in the ultramicropore range, rather than being distributed across larger pores, as evidenced in Fig. 3. In addition, WP-$K_2C_2O_4$-1:4 also exhibits the highest carbon yield (18.5 %), further supporting the milder and more conservative nature of $K_2C_2O_4$ activation. Within the KOH/$K_2C_2O_4$ mixed systems, the AC with a balanced mass ratio (WP-KOH-$K_2C_2O_4$-1:2:2) demonstrates the most favorable textural properties. It combines a high S_{BET} (2029 m^2/g), well-developed $V_{MIC(N2)}$ and $V_{MIC(CO2)}$ (0.923 cm^3/g and 0.156 cm^3/g), with a low V_{MES} (0.105 cm^3/g),

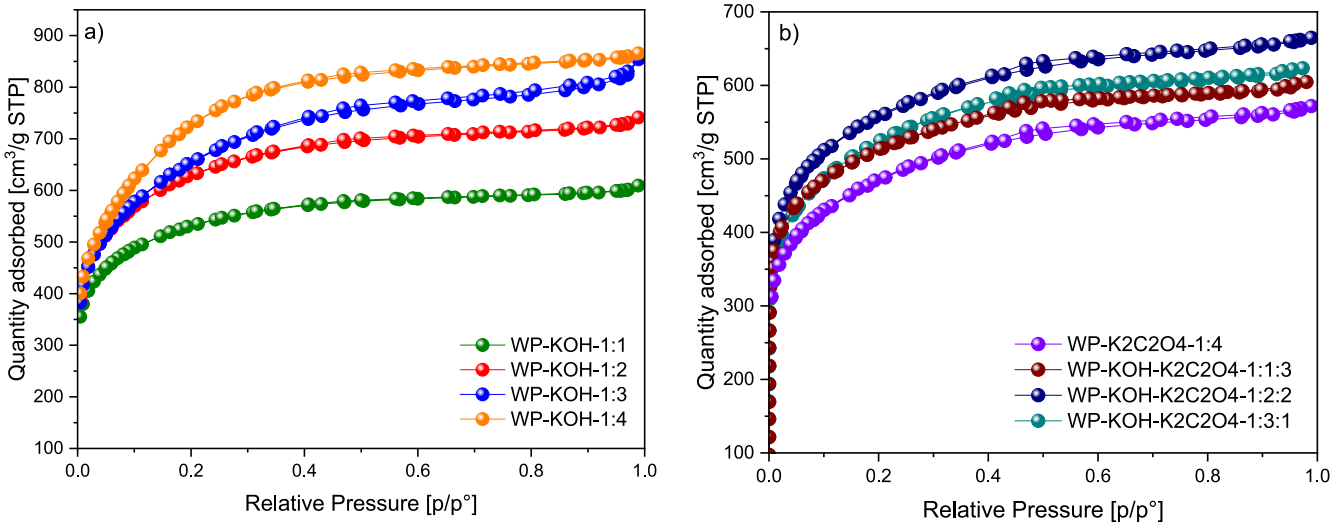

Fig. 1. N_2 adsorption–desorption isotherms at −196 °C of ACs prepared with varying ratios of (a) KOH and (b) and $K_2C_2O_4$ or KOH/$K_2C_2O_4$ mixtures.

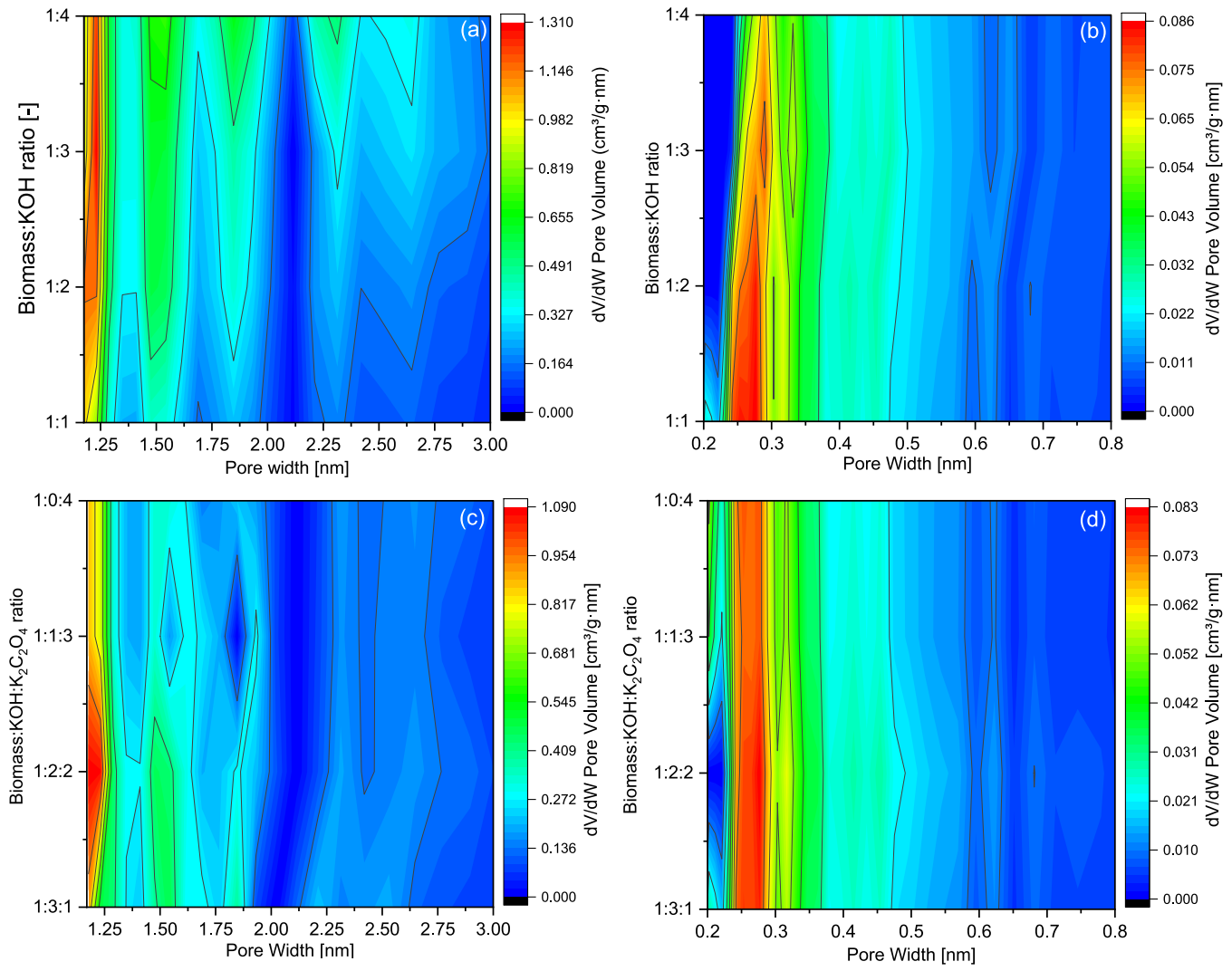

Fig. 2. Two-dimensional contour plots of PSDs based on N_2 and CO_2 adsorption at −196 °C and 0 °C, respectively, for ACs prepared with (a, b) KOH and (c, d) $K_2C_2O_4$ and $K_2C_2O_4$/KOH mixtures.

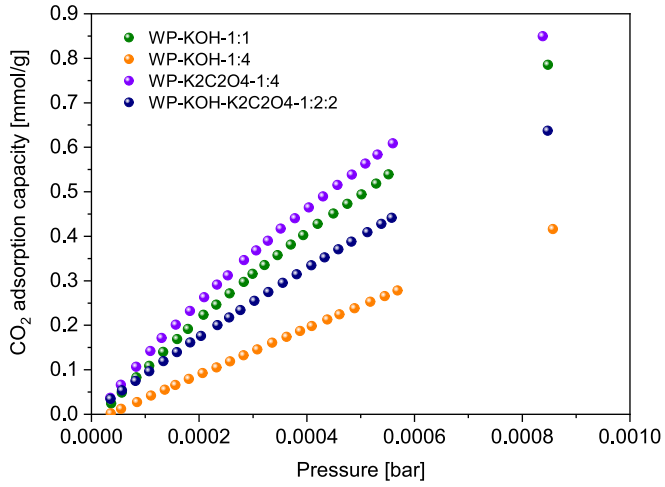

Fig. 3. CO_2 adsorption isotherms at 0 °C at the low relative pressure range (<0.001), corresponding to the region of ultramicropore formation.

indicating efficient micropore generation. This ratio appears to strike the optimal balance between KOH's aggressive activation and the moderating effect of $K_2C_2O_4$. However, increasing the KOH proportion beyond this point (WP-KOH-$K_2C_2O_4$-1:3:1) leads to a slight decline in BET surface area (1905 m^2/g), total pore volume (0.965 cm^3/g), and CO_2-accessible microporosity (0.142 cm^3/g), likely due to over-etching or partial structural collapse [55]. Overall, the data indicate that balanced KOH/$K_2C_2O_4$ activation (WP-KOH-$K_2C_2O_4$-1:2:2) provides optimal pore development, whereas an excessive amount of KOH relative to $K_2C_2O_4$, despite increasing total pore volume, can compromise structural carbon integrity and reduce micropore content.

3.2. *Structural characteristics of ACs and phase formation during KOH, $K_2C_2O_4$ and KOH/$K_2C_2O_4$ activation*

Fig. 4 presents the XRD patterns of as-prepared carbon materials prepared using KOH (Fig. 4a–b), $K_2C_2O_4$, and KOH/$K_2C_2O_4$ mixtures (Fig. 4c–d), all exhibiting diffraction peaks corresponding to a graphitic structure, including the (002), (100)/(101), (103), and (110) planes (JCPDS 41–1487). All ACs can be classified as non-graphitizable, as evidenced by their broad, poorly resolved peaks.

In Fig. 4a, the first peak, located within the angle range of $2\theta \approx 19.3–22.7°$, corresponds to the (002) plane. This low-intensity reflection indicates disordered stacking of graphene-like layers, signifying the

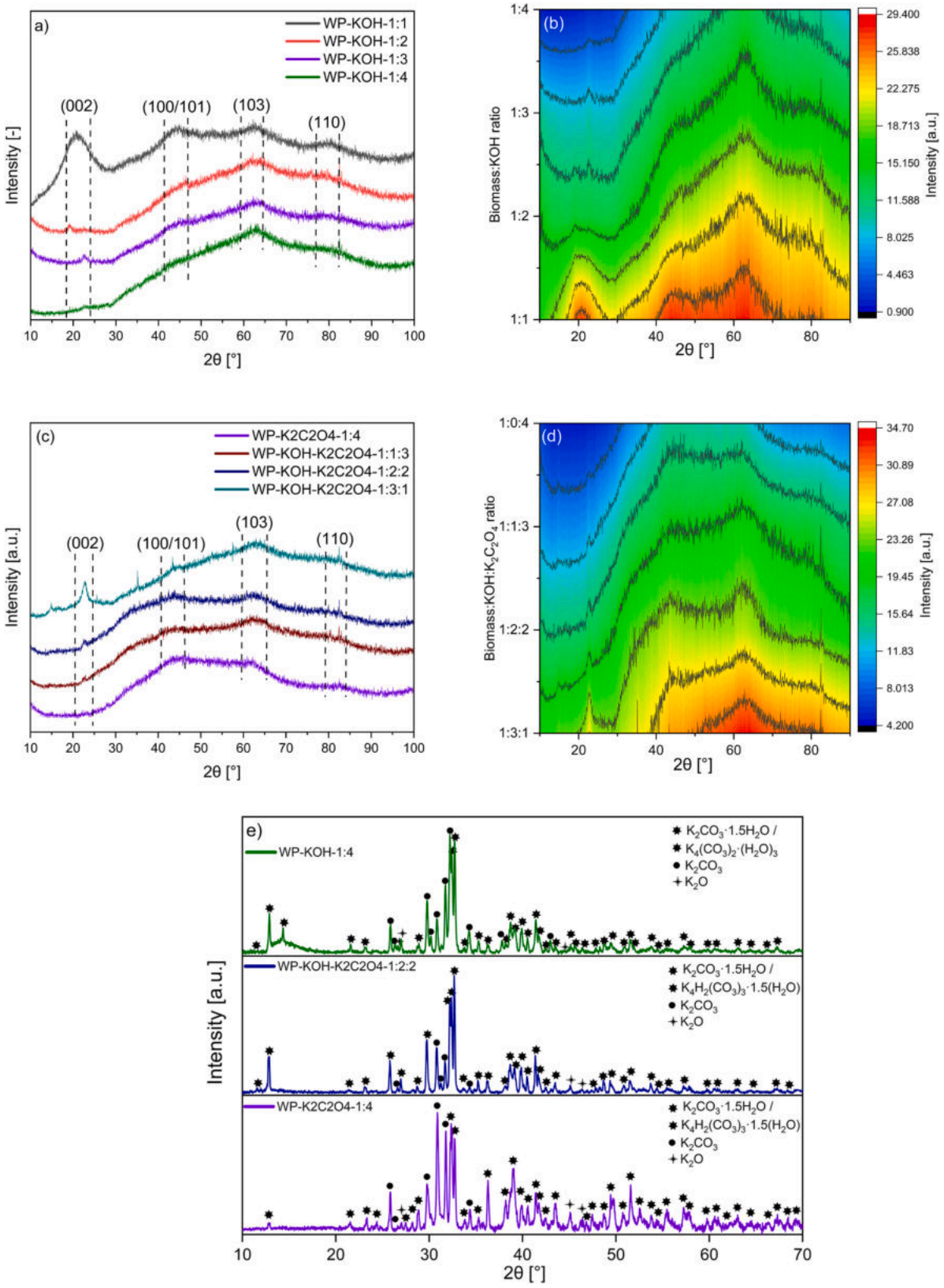

Fig. 4. XRD patterns of ACs prepared using (a) varying KOH mass ratios, (b) 2-D contour plots of KOH mass ratios, (c) $K_2C_2O_4$ and KOH/$K_2C_2O_4$ mixtures, (d) 2-D contour plots of $K_2C_2O_4$ and KOH/$K_2C_2O_4$ mixtures, and (e) unwashed AC samples: WP KOH 1:4, WP $K_2C_2O_4$ 1:4, and WP KOH/$K_2C_2O_4$ 1:2:2.

absence of well-ordered graphitic domains [56]. The second peak, centered around $2\theta \approx 43.8^{\circ}$, arises from the overlapping (100) and (101) in-plane reflections, which are associated with the lateral arrangement of carbon layers in turbostratic structures [57]. Additionally, at higher angles, diffuse reflections are observed, particularly the (103) near 62.4° and the (110) around 79.9°, further confirming the limited structural ordering typical of amorphous carbon [58]. As shown in Fig. 4b, increasing KOH ratios lead to attenuation and broadening of all XRD peaks, with decreasing intensity across the 2θ range. This effect, most evident in WP-KOH-1:4, suggests greater lattice disruption due to more severe activation, which fragments graphene layers and increases porosity, reducing structural coherence.

In Fig. 4c, the XRD profiles of carbons activated with $K_2C_2O_4$ and its mixtures with KOH also reflect a turbostratic arrangement. However, variations in peak shape and intensity indicate differences in local structure. WP-$K_2C_2O_4$-1:4 stands out by exhibiting the most diffuse pattern, indicating extensive disruption of graphene-layer stacking and a high level of structural disorder. With the introduction of KOH into the $K_2C_2O_4$ mixture, WP-KOH-$K_2C_2O_4$-1:2:2 exhibits noticeably sharper (002), (103), and (110) peaks, indicating better retention of basal-plane alignment [59]. As the KOH content increases further, particularly in WP-KOH-$K_2C_2O_4$-1:3:1, the (002) reflection becomes the sharpest of all ACs, reflecting enhanced short-range carbon ordering due to progressively stronger hydroxide etching, opening new micropores, and partial reassembly of graphene fragments [60]. Fig. 4d quantifies this trend, showing a gradual increase in peak intensities and a narrowing of full-width at half-maximum (FWHM) of the XRD peaks as the KOH/$K_2C_2O_4$ ratio increases, while the overall broadness remains consistent with hard-carbon characteristics.

To evaluate the nature of inorganic residues formed during KOH, $K_2C_2O_4$ and KOH/$K_2C_2O_4$ activation and assess the impact of specific K-based activators on phase composition, XRD analysis was performed on the unwashed ACs, such as WP-KOH-1:4, WP-$K_2C_2O_4$-1:4, and WP-KOH-$K_2C_2O_4$-1:2:2 (Fig. 4e). The predominant K-based crystalline phases identified include potassium carbonate hydrate ($K_2CO_3{\cdot}1.5H_2O$, $K_4H_2(CO_3)_3{\cdot}1.5H_2O$), potassium carbonate ($K_2CO_3$), and potassium oxide ($K_2O$), consistent with previous reported studies [61]. Peaks intensity and width vary systematically with the choice of K-based activator. The WP-$K_2C_2O_4$-1:4 exhibits the sharpest and most intense reflections, particularly in the 2θ region of 28–32°, indicating a higher degree of crystallinity and a larger accumulation of K-containing residues, this corresponds with literature that thermal decomposition of $K_2C_2O_4$ promotes the formation of stable carbonate-rich phases within the carbon matrix [62,63]. On the other hand, WP-KOH-1:4 presents weaker, broader reflections, indicating a lower residual load or the presence of less crystalline K-species that can be more easily removed by post-washing. In the case of the mixed K-based salt-AC, WP-KOH-$K_2C_2O_4$-1:2:2 displays reduced peak sharpness and intensity compared to KOH alone, suggesting that KOH/$K_2C_2O_4$ co-activation suppresses carbonate crystallization and partially limits the formation of residual crystalline phases typically induced by KOH.

To present a potential mechanism consistent with the K-based residues identified in the XRD patterns of unwashed ACs (Fig. 4e), the thermal behavior and chemical transformations of KOH and $K_2C_2O_4$ are considered based on previously reported activation pathways. The observed crystalline phases, including K_2CO_3, its hydrated derivatives, and K_2O, indicate that multiple overlapping decomposition and redox reactions occurred during carbon activation at 800 °C.

1) In the case of KOH, activation is often described by the overall reaction:

$$6KOH + 2C \rightarrow 2K + 3H_2 + 2K_2CO_3 \quad (8)$$

This reaction proceeds through several steps, including the dehydration of KOH, formation of K_2O, and steam-assisted gasification of carbon. Metallic K and CO evolve during the high-temperature stages, contributing to the expansion of the carbon framework and formation of microporosity. Detailed mechanistic pathways for KOH activation can be found in numerous prior studies [64–66].

2) For $K_2C_2O_4$, the mechanism is less investigated and involves specific temperature-dependent transitions, as described below [67–69].

- Water desorption from $K_2C_2O_4$ between 110 and 150 °C

$$\text{Dehydratation} : K_2C_2O_4{\cdot}xH_2O \rightarrow K_2C_2O_4 + xH_2O \quad (9)$$

- Initially, below 600 °C (typically between 500 and 580 °C), $K_2C_2O_4$ decomposes to form K_2CO_3 and CO

$$\text{Decarbonylation} : K_2C_2O_4 \rightarrow K_2CO_3 + CO \quad (10)$$

- At 700 °C, any unreacted K_2CO_3 may partially and slowly decompose thermally into K_2O and CO_2

$$\text{Partial carbonate decomposition} \geq 700^{\circ}C : K_2CO_3 \rightarrow K_2O + CO_2 \quad (11)$$

- At 700–800 °C, K_2CO_3 and K_2O can also undergo a redox reaction with carbon, producing metallic K and additional CO

$$\textit{Redox reaction with carbon} : K_2CO_3 + 2C \rightarrow 2K + 3CO \quad (12)$$

$$K_2O + C \rightarrow 2K + CO \quad (13)$$

- Furthermore, at above 800 °C, CO_2 can react with carbon to form additional CO during partial carbon gasification

$$\textit{Gas phase interaction} : CO_2 + C + \rightarrow 2CO \quad (14)$$

3) When combined, KOH and $K_2C_2O_4$ appear to act synergistically. KOH provides strong etching capacity and facilitates rapid pore opening, while $K_2C_2O_4$ promotes more extensive formation of crystalline carbonate phases. Their combination enables a controlled activation process, balancing porosity development with structural preservation. A generalized reaction summarizing the KOH/$K_2C_2O_4$ co-activation process can be represented as:

$$2KOH + K_2C_2O_4 + C \rightarrow K_2CO_3 + K_2O + 2CO + H_2 + porosity \quad (15)$$

3.3. Thermal stability of ACs in inert and oxidative conditions

Fig. 5 presents the TGA curves of ACs under nitrogen (a) and air (b) atmospheres up to 900 °C. In the N_2 atmosphere (Fig. 5a), the decomposition follows a characteristic three-step profile typical of biomass-derived carbons [70]. The first stage, occurring below 200 °C, is attributed to the evaporation of physisorbed moisture located within the pore network and on the external surface of the ACs [71]. The weight loss in this region ranges from 7.5 to 17.5 wt%, with the lowest value observed for WP-$K_2C_2O_4$-1:4, indicating a less polar and more thermally stable surface. The second stage, between 200 and 380 °C, corresponds to the decomposition of volatile matter originating from thermally labile components and oxygen-containing surface functional groups (OCFGs) [72]. This phase shows a sharper mass loss, particularly in ACs with higher KOH content (4.5–10.7 %) or KOH/$K_2C_2O_4$ mixtures (9.2–16.6 %), reflecting the decomposition of reactive fragments derived from the lignocellulosic biomass. These fragments decompose at distinct temperature ranges: hemicellulose (~220–315 °C), cellulose (~300–400 °C), and lignin (~150–900 °C), releasing OCFGs including hydroxyls, carbonyls, carboxyls, ethers, and phenolics [73,74]. In the third stage (above 380 °C), degradation proceeds more slowly and gradually, involving the breakdown of stable carbon structures and decomposition of residual mineral species. The samples WP-KOH-1:4 and WP-$K_2C_2O_4$-

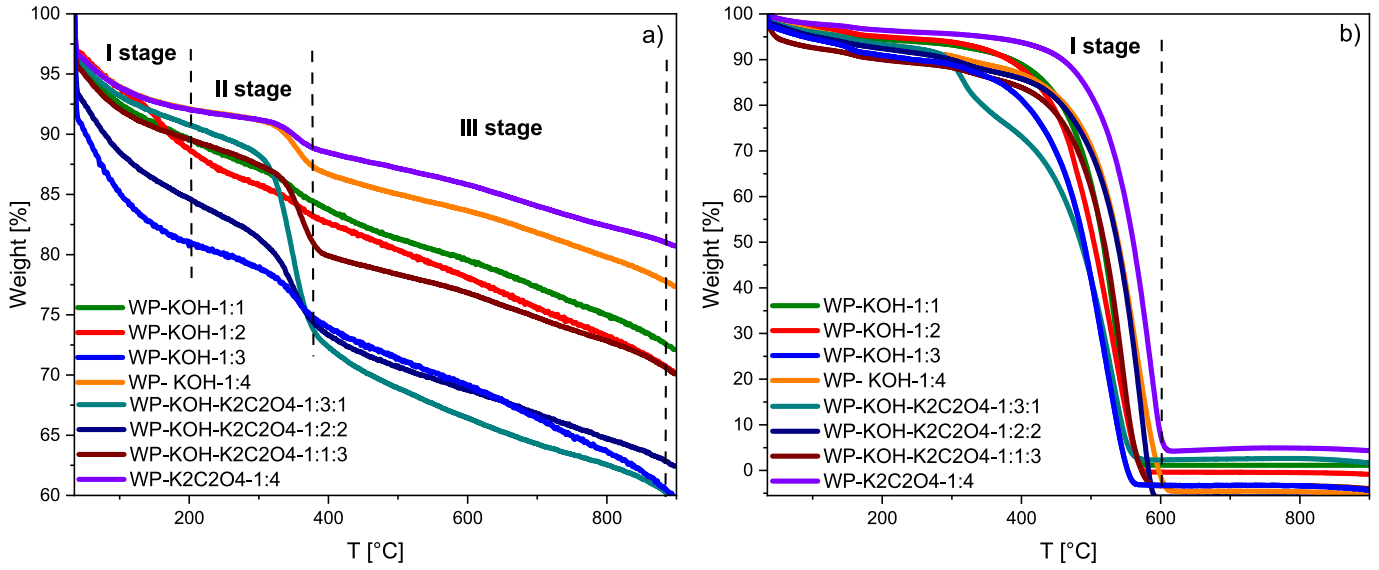

Fig. 5. TGA curves of ACs heated from 30 to 900 °C at 10 K/min: (a) in a nitrogen atmosphere; (b) in an air atmosphere.

1:4 retain the highest final mass (~77.5 % and ~80.8 %, respectively), demonstrating enhanced thermal resistance compared to other treatments [75].

The TGA curves recorded in the air atmosphere (Fig. 5b) exhibit a single, sharp weight loss between 300 and 600 °C, primarily due to oxidative combustion of the carbon structure [76]. While all ACs follow a similar degradation trend, the onset temperature and residual mass at 800 °C vary depending on the activation approach. ACs prepared with lower KOH ratios (e.g., WP-KOH-1:1) begin to degrade around 300 °C and retain only 1–2 wt% at the end of the run, indicating limited thermal stability. Increasing the KOH ratio shifts the onset to ~350 °C, though the remaining mass does not significantly differ. Additionally, ACs produced using KOH/$K_2C_2O_4$ start to decompose between 320 and 360 °C and final residues of 0–2 wt%. WP-$K_2C_2O_4$-1:4 exhibits the highest resistance to oxidation, with degradation initiating around 380 °C and a final residue of 4.9 wt%. These observations highlight the key role of both the type and proportion of KOH and $K_2C_2O_4$ in determining the oxidative stability of the carbon materials.

3.4. Elemental composition of inorganic residues in ACs

Table S2 summarizes the concentrations of silicon (Si), sulfur (S), and potassium (K) remaining in ACs after the washing process.

The K content varies depending on the K-based agent and its ratio. In KOH-ACs, K levels increase gradually with higher KOH loadings, peaking at 0.594 wt% in WP-KOH-1:3, followed by a slight decrease in WP-KOH-1:4. This decline may be attributed to partial volatilization of K-species or pore structure collapse at excessive reagent concentrations, both of which are common during high-temperature activation with strong alkalis. In contrast, biomass samples activated with $K_2C_2O_4$ or KOH/$K_2C_2O_4$ mixtures retain relatively high potassium contents, reaching up to 0.787 wt%. This is consistent with XRD evidence revealing the presence of residual K-based crystalline phases that are embedded within the carbon matrix (Fig. 4e), making them more resistant to removal by post-synthesis washing. These phases likely include K_2CO_3, K_2O, and mixed carbonates formed during the thermal decomposition of the activators. Additionally, at elevated temperatures, metallic K can intercalate into the carbon lattice, further contributing to the persistence of K-species in the final material [77]. Importantly, part of the residual K may originate from the wood biomass itself, which naturally contains K (~0.1–2.2 wt%) in the form of soluble K^+ ions involved in key physiological processes such as osmoregulation [78].

S content is significantly higher in the $K_2C_2O_4$ and KOH/ $K_2C_2O_4$-ACs, reaching up to 3.27 wt%, which is attributed to the stabilization of sulfur-containing species. This likely originates from inherent sulfur in the wood biomass, typically present at low levels (<0.07 wt%) in both organic forms (such as sulfides, thiols, and sulfates) and inorganic forms [79]. Under milder activation with $K_2C_2O_4$, these S-species are less likely to volatilize as gaseous compounds like SO_2, H_2S and can become chemically retained within the AC structure, facilitating their preservation and resulting in higher sulfur content in the final material. The retained sulfur groups may also modify the surface polarity and electron density, potentially enhancing CO_2 binding via acid–base or electrostatic interactions [80].

Si content stays below 0.73 wt% in all ACs and shows no clear dependence on the activation route, suggesting it originates from inherent mineral impurities in the woody biomass precursor, mainly from soil contamination or silica in bark and cell walls.

3.5. Effect of KOH and $K_2C_2O_4$ activation route on morphology of ACs

The morphology of ACs, as revealed by SEM (Fig. 6) for WP-KOH-1:4, WP-$K_2C_2O_4$-1:4, and WP-KOH-$K_2C_2O_4$-1:2:2, shows distinct structural differences depending on whether KOH, $K_2C_2O_4$, or their combination was used. In WP-KOH-1:4 (Fig. 6a–c), the structure is highly porous and open, presenting a uniform, interconnected macroporous framework with thin, extensively etched pore walls and well-developed cavities. This honeycomb-like texture reflects the well-known aggressive activation behavior of KOH, which involves deep etching and gasification reactions that generate extensive micro- and mesoporosity, resulting in some of the highest BET surface areas reported (up to ~3000 m^2/g) [70,81]. Conversely, WP-$K_2C_2O_4$-1:4 (Fig. 6d–f) exhibits a markedly different morphology compared to the KOH-AC. The surface topography is non-uniform, featuring extensive cracking accompanied by dense, compact granular zones [82]. These fractured zones and aggregates indicate a localized activation mechanism, where $K_2C_2O_4$ acts as a solid-phase template that induces pore formation while preserving wall thickness. Despite being less open than the KOH-derived structure, the cracks and surface roughness increase external area, enhancing adsorption. Finally, WP-KOH–$K_2C_2O_4$-1:2:2 (Fig. 6g–i) presents a balanced, sponge-like structure with a continuous yet less pronounced pore network; its walls are thicker and the pore boundaries less defined compared to WP-KOH-1:4. This morphology suggests a synergistic activation mechanism, where KOH promotes aggressive pore

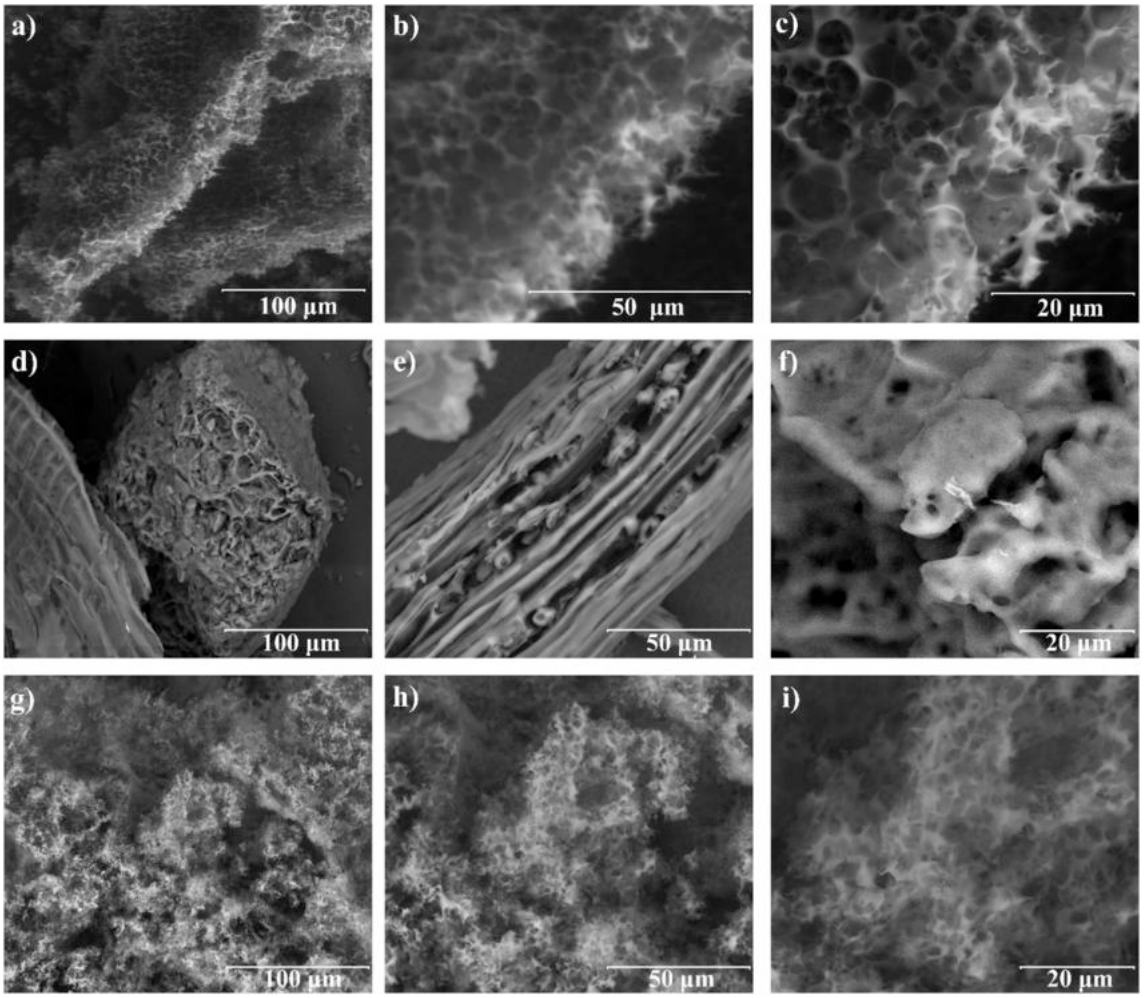

Fig. 6. SEM images of (a–c) WP–KOH–1:4, (d–f) WP–$K_2C_2O_4$–1:4, and (g–i) WP–KOH–$K_2C_2O_4$–1:2:2 at increasing magnifications (100 µm, 50 µm, 20 µm). Micrographs were selected from multiple regions of each sample to provide statistically representative views of the morphology.

development while $K_2C_2O_4$ tempers the process to maintain structural integrity, resulting in a hierarchical porous architecture.

This combination of aggressive etching and controlled preservation produces a structure that integrates high porosity with enhanced mechanical stability, as supported by textural data in Section 3.1. The morphological diversity achieved through activator tuning offers potential benefits for diffusion-limited processes such as CO_2 capture and selectivity.

3.6. Influence of KOH and $K_2C_2O_4$ activation chemistry on the evolution of surface functional groups

FT-IR spectra (Fig. 7) for all ACs display nearly identical profiles, indicating that both KOH and $K_2C_2O_4$ activation consistently introduced a similar suite of oxygenated and conjugated functional groups. Key absorption bands include [83–85]:

- 3328 cm^{-1}: broad O—H stretching, attributed to surface hydroxyls or adsorbed moisture.
- 2340 and 2362 cm^{-1}: asymmetric and symmetric CO_2 stretching, indicative of physically adsorbed CO_2.
- 2155 cm^{-1}: C≡C stretching, suggesting the formation of sp-hybridized carbon domains or alkyne-like structures during activation.
- 1653 cm^{-1}: C═O stretching, likely from conjugated carbonyl groups.

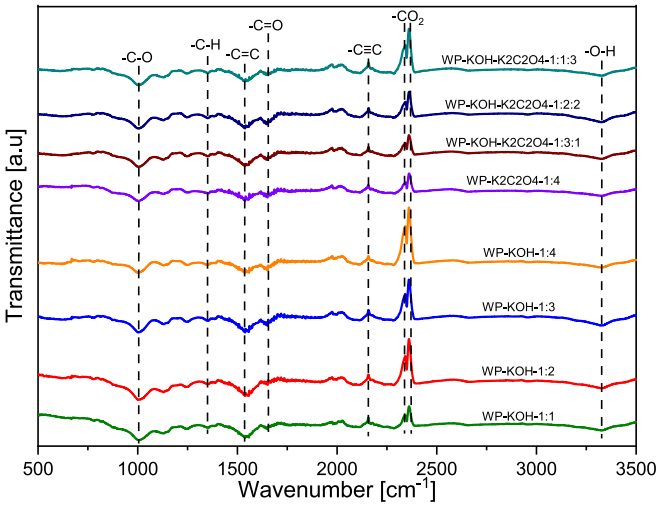

Fig. 7. FT-IR spectra of ACs with KOH, $K_2C_2O_4$, and mixtures of both. The spectra have been baseline-subtracted and vertically shifted for clarity.

- 1538 cm^{-1}: aromatic C═C stretching, signifying the development of conjugated aromatic domains and partial graphitization.
- 1353 cm^{-1}: C—H bending vibration, from aliphatic or aromatic in-plane deformations.

- 1008 cm^{-1}: C—O stretching, associated with alcohol, ether, phenolic groups, or epoxy functionalities.

While the overall FT-IR spectral patterns remain consistent across all ACs, the most pronounced differences appear in the CO_2-related doublet (2340–2362 cm^{-1}), which shows the greatest variation. In the KOH-ACs, the intensity of this band increases with higher KOH ratios (from 1:1 to 1:4), indicating enhanced surface area and porosity, as presented in Table 1. This structural development may lead to the formation of high-energy adsorption sites and promotes stronger interactions with CO_2 molecules. Such interactions are likely facilitated by oxygen-containing surface functionalities, including O—H, C—O, and C═O groups, which engage CO_2 through electrostatic forces, dipole–induced dipole interactions, and hydrogen bonding [86], playing a crucial role in

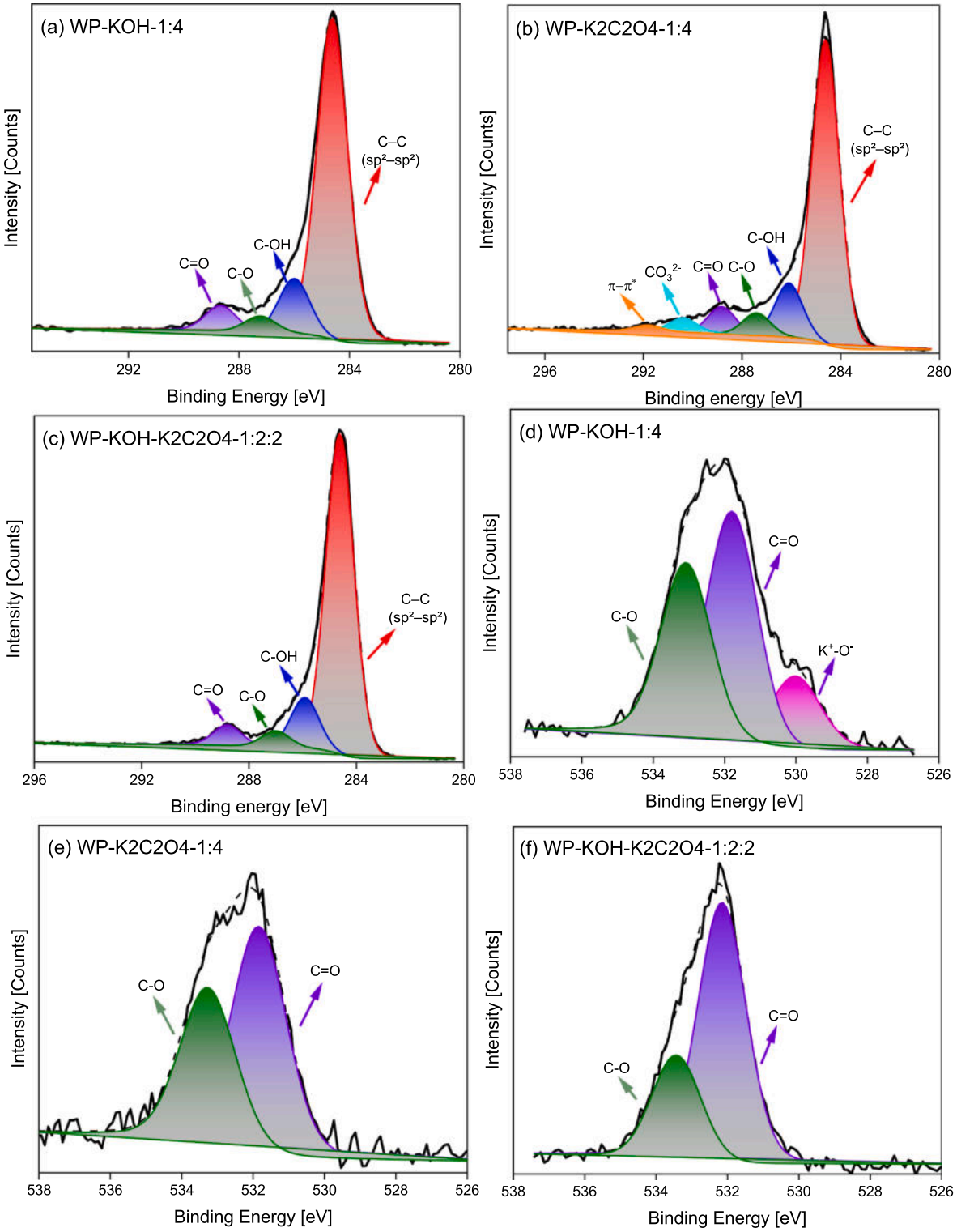

Fig. 8. XPS spectra of the activated carbons: WP-KOH-1:4 (a, d), WP-$K_2C_2O_4$-1:4 (b, e), and WP-KOH-$K_2C_2O_4$-1:2:2 (c, f). Panels (a–c) show the C1s region, while panels (d–f) represent the O1s region.

physisorption. In contrast, increasing the $K_2C_2O_4$ content in the KOH/$K_2C_2O_4$ co-activation systems leads to a gradual increase in CO_2 band intensity, reaching a maximum for WP-KOH-$K_2C_2O_4$-1:1:3, likely reflecting a greater contribution of OCFGs that enhance CO_2 interaction. The WP-$K_2C_2O_4$-1:4 shows the lowest intensity, indicating that a small amount of KOH can be needed to develop a more accessible and reactive surface. However, since the best textural properties were found for WP-KOH-$K_2C_2O_4$-1:2:2 (Table 1), the lack of a direct correlation between CO_2 band intensity and porosity.

XPS was performed in the C1s, O1s, and K2p regions to complement FT-IR data and provide detailed insights into surface carbon bonding and elemental composition following activation with KOH (WP–KOH–1:4), $K_2C_2O_4$ (WP–$K_2C_2O_4$–1:4), and a KOH/$K_2C_2O_4$ mixture (WP–KOH–$K_2C_2O_4$–1:2:2). Table S3 summarizes the possible functional groups, their associated peak assignments, and corresponding contributions.

XPS spectra in the C1s region, as shown in Fig. 8a-c, reveal a series of well-defined peaks associated with distinct carbon environments. A dominant signal corresponds to C—C, sp^2–sp^2 (284.6 eV), indicating the presence of graphitic or aromatic domains and partial structural ordering. Other oxidized states are also evident, including C–OH (286.0 eV), C—O (287.5 eV), and C═O (288.5 eV) [87]. For all ACs, the relative signal contributions from the deconvolution show overall similarity across the analyzed C1s region, as follows: C–OH (10.5–11 at.%), C—O (3–5 at.%), and C═O (4.5–5 % at.%). This uniform distribution of polar functionalities across the series suggests that the activation chemistry, regardless of the K-based activator, preserves a comparable degree of surface oxygenation. Additionally, signals corresponding to CO_3^{2-} (290.5 eV), related to carbonate structures, and a distinct π-π* shake-up satellite (292.0 eV) are observed in WP–$K_2C_2O_4$–1:4. The presence of the π–π* feature is characteristic of graphene-type structures, as it reflects electron delocalization within extended aromatic systems and indicates a higher degree of graphitization [88]. The detection of CO_3^{2-} species aligns with the XRD results (Fig. 5) and confirms the partial retention of carbonate residues after activation and washing. In the mixed KOH/$K_2C_2O_4$-AC (WP–KOH–$K_2C_2O_4$–1:2:2), the C1s profile resembles that of WP–KOH–1:4, implying that KOH wields a stronger influence on the surface chemistry under KOH/$K_2C_2O_4$ activation conditions. This suggests that even in co-activation modes, KOH dominates the chemical reconstruction of the carbon surface, favoring the development of defect-rich, aromatic domains over carbonate retention.

The O1s spectra (Fig. 8d-f) display distinct signals for C═O (~531.5

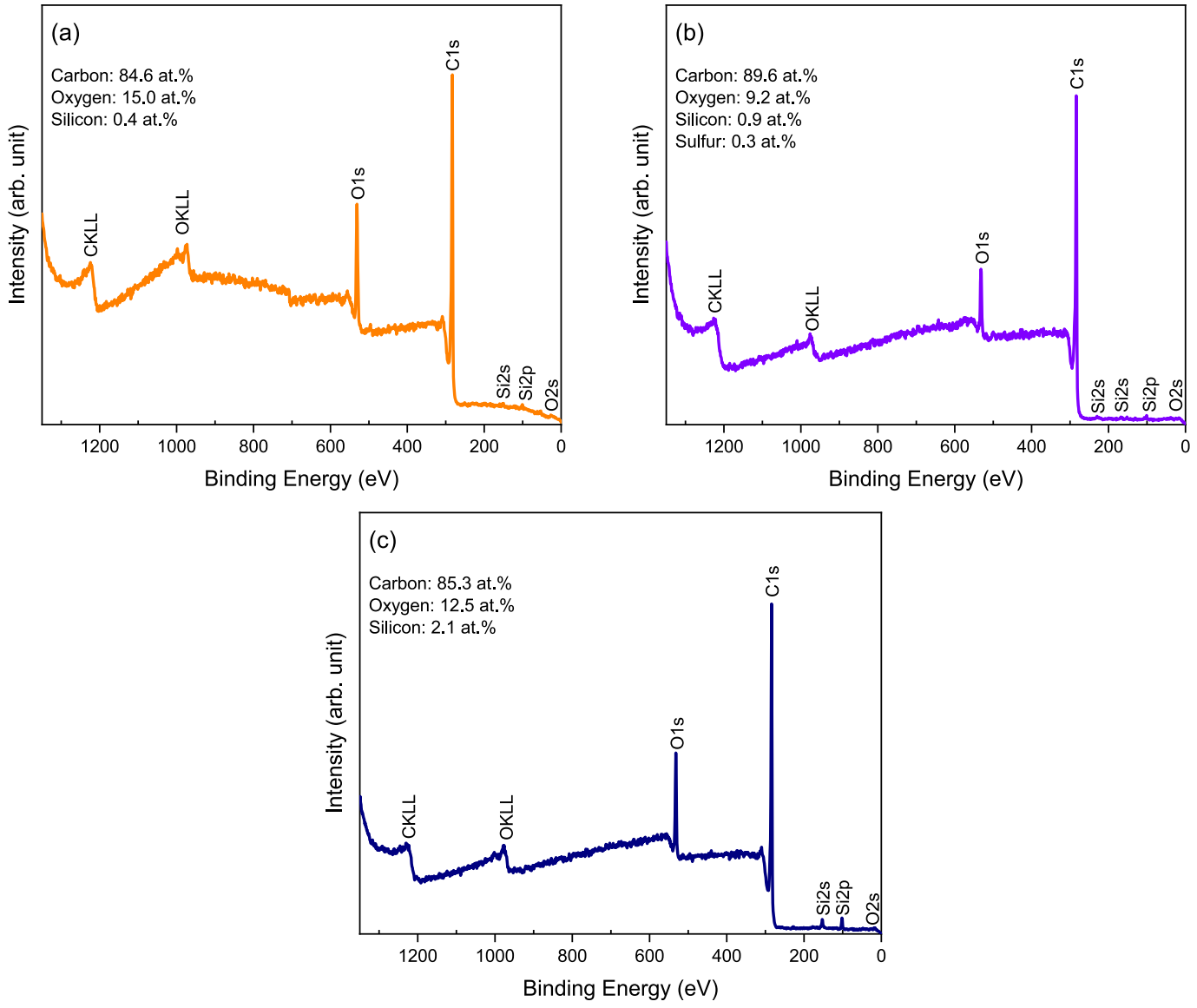

Fig. 9. Survey spectra of (a) WP-KOH-1:4, (b) WP-$K_2C_2O_4$-1:4, and (c) WP-KOH-$K_2C_2O_4$-1:2:2.

eV), C—O (~533 eV), and, uniquely in WP–KOH–1:4, a low-binding-energy signal assigned to K^+–O^- interactions (~530 eV). Although this peak is often attributed to K—O species, the absence of a corresponding K2p signal suggests that it does not originate from residual K-based compounds. Instead, it is likely due to K^+ intercalation, where potassium ions interact electrostatically with surface oxygen groups, causing a shift in the binding energy of nearby oxygen atoms [89].This K^+–O^- signal is absent in both the $K_2C_2O_4$ and KOH/$K_2C_2O_4$-ACs, indicating a distinct surface chemistry under pure KOH activation. Quantitatively, WP–KOH–1:4 favors higher and more uniform oxygen functionalities, with C═O (7.0 at.%) and C—O (5.5 at.%), whereas WP–$K_2C_2O_4$–1:4 shows lower values, with C═O (5.5 at.%) and C—O

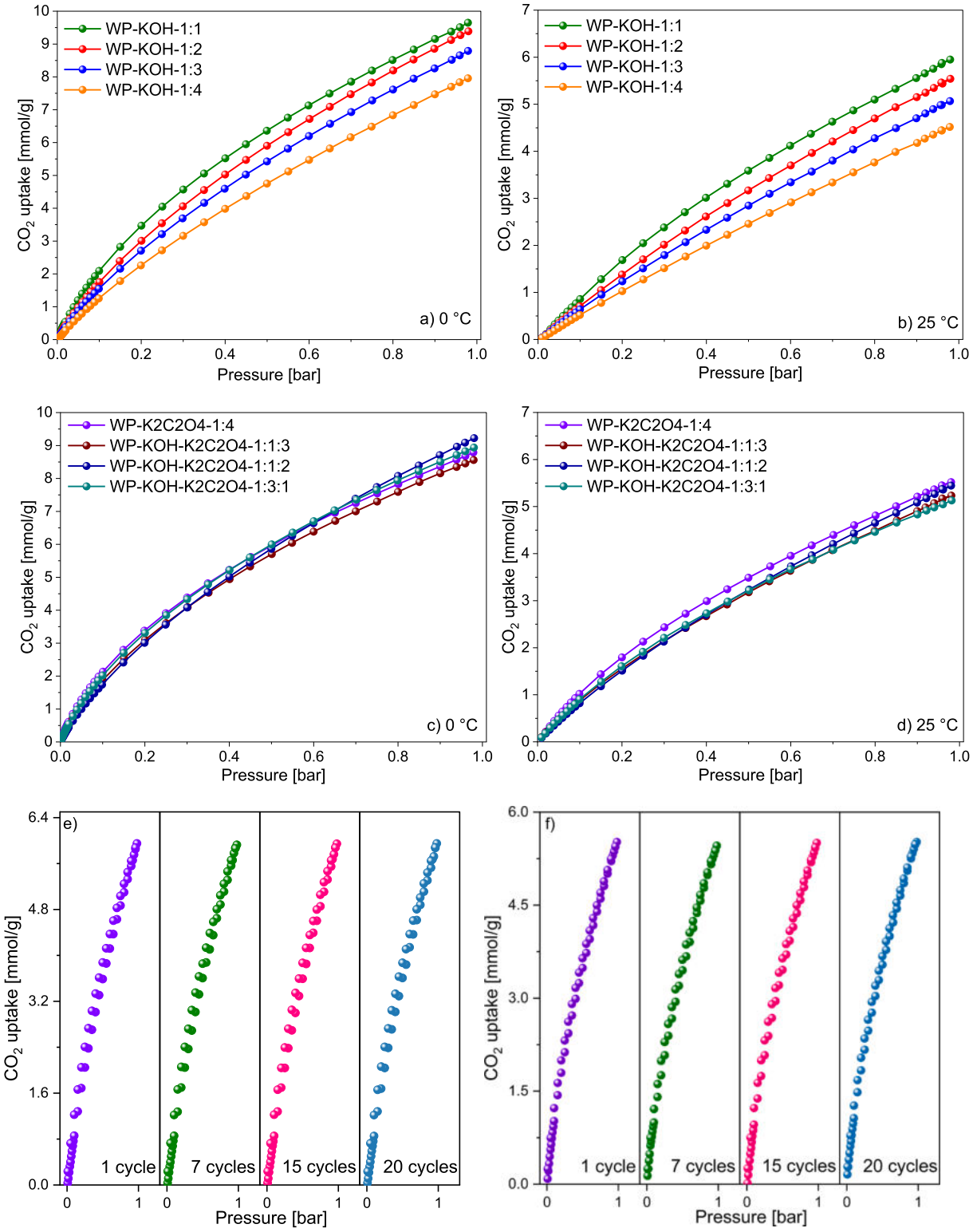

Fig. 10. CO_2 adsorption isotherms of ACs prepared using different (a, b) biomass:KOH mass ratios, and (c, d) $K_2C_2O_4$ or combined KOH/$K_2C_2O_4$ activators, measured at 0 °C and 25 °C. Adsorption–desorption cycling performance of (e) WP–KOH–1:1 and (f) WP–$K_2C_2O_4$–1:4 at 25 °C.

(4.0 at.%), consistent with a lower degree of surface oxidation. Interestingly, WP–KOH–$K_2C_2O_4$–1:2:2 deviates from this trend by presenting the highest proportion of C═O (9.0 at.%) and the lowest C—O content (3.5 at.%), suggesting a preferential development of carbonyl-rich surfaces. Such enrichment in C═O groups may contribute to stronger dipole–quadrupole interactions with CO_2, thus improving adsorption energetics, especially at low pressures.

According to the XPS survey spectra (Fig. 9), WP–$K_2C_2O_4$–1:4 exhibits 89.6 at.% carbon and 9.2 at.% oxygen, representing the most favorable C/O ratio and indicating limited gasification and oxidation during activation. In comparison, WP–KOH–1:4 possesses 84.6 at.% C and 15.0 at.% O, which aligns with the stronger etching effect of KOH. Meanwhile, the dual-activated sample (WP–KOH–$K_2C_2O_4$–1:2:2) presents C and O contents of 85.3 and 12.5 at.%, respectively, with values intermediate between those of the single-activator materials. Overall, the carbon content remains high across all samples, confirming that the carbonaceous framework was largely preserved throughout activation. Furthermore, trace amounts of Si (0.4–2.1 at.%) and S (<0.3 at.%) were detected, originating from residual inorganic species in the biomass precursor, as verified by XRF analysis.

To support the experimental results, the combined C1s and K2p XPS spectra of the unwashed ACs are presented in Fig. S3 and discussed in *Supplementary Information* to provide additional insights into the surface speciation of potassium and associated carbon environments.

3.7. CO_2 capture performance of produced ACs

3.7.1. CO_2 adsorption tests

The CO_2 adsorption isotherms of ACs, measured at 0 and 25 °C under pressures up to 1 bar, are given in Fig. 10. The isotherms show a steep uptake at low pressures (<0.05 bar), indicating strong physisorption and the dominance of a microporous structure. The Type I profile, according to the Brunauer classification, confirms that adsorption primarily occurs within narrow pores, which are critical for efficient CO_2 capture under low-pressure conditions [90]. WP-KOH-1:1 shows the highest CO_2 uptake, approximately 5.95 mmol/g at 25 °C and 9.65 mmol/g at 0 °C, surpassing many comparable materials reported in the literature [14]. Increasing the biomass:KOH activation ratio from 1:1 to 1:4 reduces CO_2 adsorption at both temperatures. This outcome suggests that excessive KOH activation compromises the microporous framework through pore narrowing, which limits CO_2 accessibility ($V_{MIC(CO_2)}$: 0.164 → 0.133 cm^3/g), thereby reducing sorption efficiency (Table 1). This degradation of microporosity at high activator ratios likely results from pore wall collapse or excessive gasification, both of which reduce the effective volume of CO_2-accessible pores. Building on this, WP-$K_2C_2O_4$-1:4 achieves CO_2 uptakes of 5.52 mmol/g at 25 °C and 8.79 mmol/g at 0 °C, values that are closely aligned with those of WP-KOH-1:1. Within the mixed-activator series, WP-KOH-$K_2C_2O_4$-1:2:2 reaches the highest CO_2 uptake in its group, 5.44 mmol/g at 25 °C and 9.22 mmol/g at 0 °C, though its performance at 25 °C remains slightly lower than that of WP-$K_2C_2O_4$-1:4. Despite this, WP-KOH-$K_2C_2O_4$-1:2:2 possesses more favorable textural properties than WP-$K_2C_2O_4$-1:4 (Table 1), indicating that increased S_{BET} and $V_{MIC(N_2)}$ and $V_{MIC(CO_2)}$ do not necessarily translate into improved CO_2 sorption efficiency. These observations reflect an additive interaction between KOH and $K_2C_2O_4$, with no evident synergistic enhancement in CO_2 uptake. Although no clear synergistic effect on CO_2 uptake is observed, co-activation balances pore development and surface chemistry. KOH enhances microporosity through etching, while $K_2C_2O_4$ supports structural integrity and introduces carbonyl groups. Together, they create hierarchical porosity with stable adsorption sites, enabling high CO_2 capacity along with potentially improved kinetics, durability, and regenerability.

The long-term CO_2 capture performance of ACs depends on both initial uptake and stability during repeated use. Adsorption–desorption cycling of WP-KOH-1:1 and WP-$K_2C_2O_4$-1:4 at 25 °C for 20 cycles (Fig. 10e-f) showed no measurable capacity loss, with a maximum standard deviation of only ~0.09 mmol/g. The consistent uptake confirms physisorption within stable ultramicropores that enable full regeneration under mild conditions. The preserved capacity indicates intact pore networks and the absence of irreversible chemical reactions during cycling. Interestingly, WP-$K_2C_2O_4$-1:4 maintains the same stability as the WP-KOH-1:1, suggesting that oxalate activation forms a robust, degradation-resistant pore structure suitable for durable CO_2 sorbents.

3.7.2. N_2 adsorption tests

The N_2 adsorption isotherms of ACs, measured at 25 °C, are presented in Fig. 11. As anticipated, N_2 uptake is considerably lower than that of CO_2, primarily due to weaker intermolecular interactions associated with the lower polarizability and quadrupole moment of the N_2 molecule, both of which constrain its physisorption [91]. In Fig. 11a, the highest N_2 adsorption capacities at 1 bar (~0.40 mmol/g) are recorded for WP-KOH-1:1 and WP-KOH-1:2. Nevertheless, further increases in the KOH ratio result in a slight decline in adsorption, with WP-KOH-1:3 and WP-KOH-1:4 reaching 0.36 mmol/g. By contrast, Fig. 11b indicates that activation using $K_2C_2O_4$, whether alone or combined with KOH, yields a modest improvement in N_2 adsorption performance. The maximum N_2 uptake (0.43 mmol/g) corresponds to WP-$K_2C_2O_4$-1:4, whereas co-activated samples such as WP-KOH-$K_2C_2O_4$-1:1:2 and 1:1:3 reach similar values (0.42 mmol/g). Overall, these minor differences are likely attributed to subtle variations in pore size distribution and surface functionalities introduced by the differing KOH/$K_2C_2O_4$ activation conditions. In particular, wider pore openings and reduced surface polarity may enhance N_2 diffusivity and retention to a limited extent, without substantially altering the overall microporous character of the materials. Despite low uptake, N_2 isotherms are essential for reliable IAST-based CO_2/N_2 selectivity. Limited N_2 adsorption enhances selectivity by minimizing site competition, driven by CO_2's higher affinity for oxygenated groups and size exclusion within ultramicropores.

3.7.3. CO_2/N_2 adsorption isotherm modeling

Fig. 12 presents the isotherm modeling results, where both the Redlich–Peterson and Radke–Prausnitz equations consistently yield the lowest EABS values for CO_2 and N_2 adsorption at 25 °C across all ACs. The corresponding numerical data are listed in Table S4. Particularly, the Radke–Prausnitz model provides the best overall agreement with the experimental data, reflecting its robustness in describing sorption behavior (Fig. S4). For CO_2, low EABS values are observed for ACs such as WP-KOH-1:4 (0.212), WP-KOH-1:3 (0.234), and WP-KOH-1:2 (0.357). Furthermore, similarly low and consistent discrepancies are obtained for N_2, with WP-KOH-1:1 (0.019) and WP-KOH-$K_2C_2O_4$-1:3:1 (0.023). In view of this, the modeling results confirm the applicability of the Radke–Prausnitz equation for describing adsorption over a broad concentration range. Moreover, its ability to capture both low- and high-pressure regimes, along with surface heterogeneity, makes it suitable for porous carbons with diverse structures [92]. Although slightly less precise, the Redlich–Peterson model remains a valid alternative, offering comparable accuracy through its hybrid Langmuir–Freundlich formulation, which accounts for surface heterogeneity and potential multilayer adsorption.

Further support for the suitability of the Radke–Prausnitz equation is provided by the model parameters (Table S5). The maximum adsorption capacities (q_{mRad}) for CO_2 vary between 6.176 and 6.833 mmol/g and closely match the experimental uptake. A similar trend is observed for N_2. The affinity constant (K_{Rad}), which reflects the strength of interaction between the adsorbate and the surface, reaches its highest value for WP-KOH-$K_2C_2O_4$-1:1:3 (2.317 bar^{-1}). For CO_2, K_{Rad} spans from 0.736 to 2.317 bar^{-1}, indicating strong interactions with surface adsorption sites. Meanwhile, in the case of N_2, values are significantly lower (0.019–0.104 bar^{-1}), consistent with weaker interactions with the surface and porous framework. The heterogeneity parameter (m_{Rad}), representing the distribution of adsorption energies, remains below 1 for all

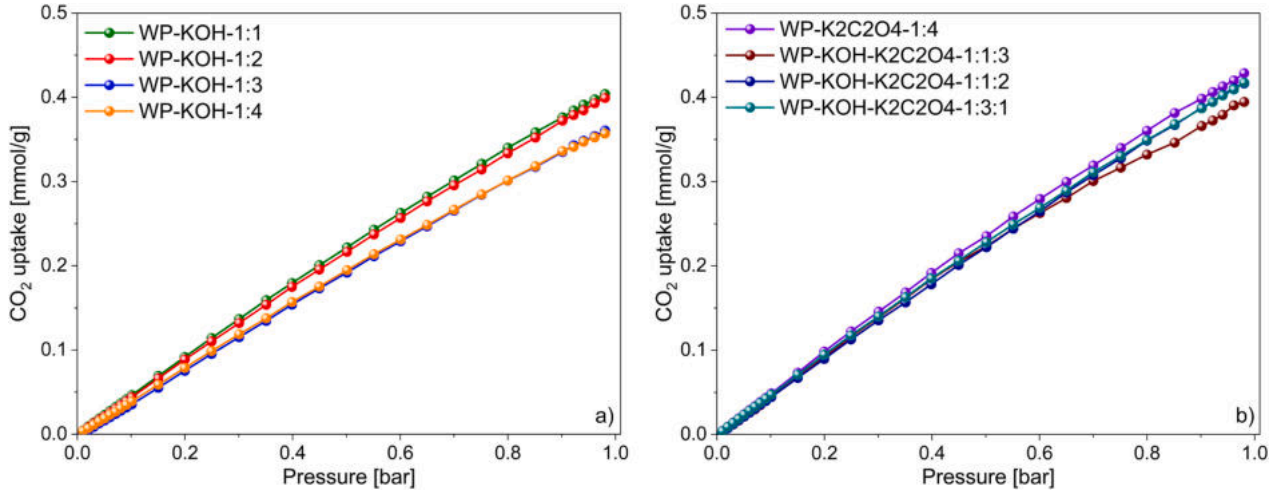

Fig. 11. N_2 adsorption isotherms of ACs prepared using (a) different biomass:KOH mass ratios and (b) $K_2C_2O_4$ or KOH/$K_2C_2O_4$ mixtures, measured at 25 °C.

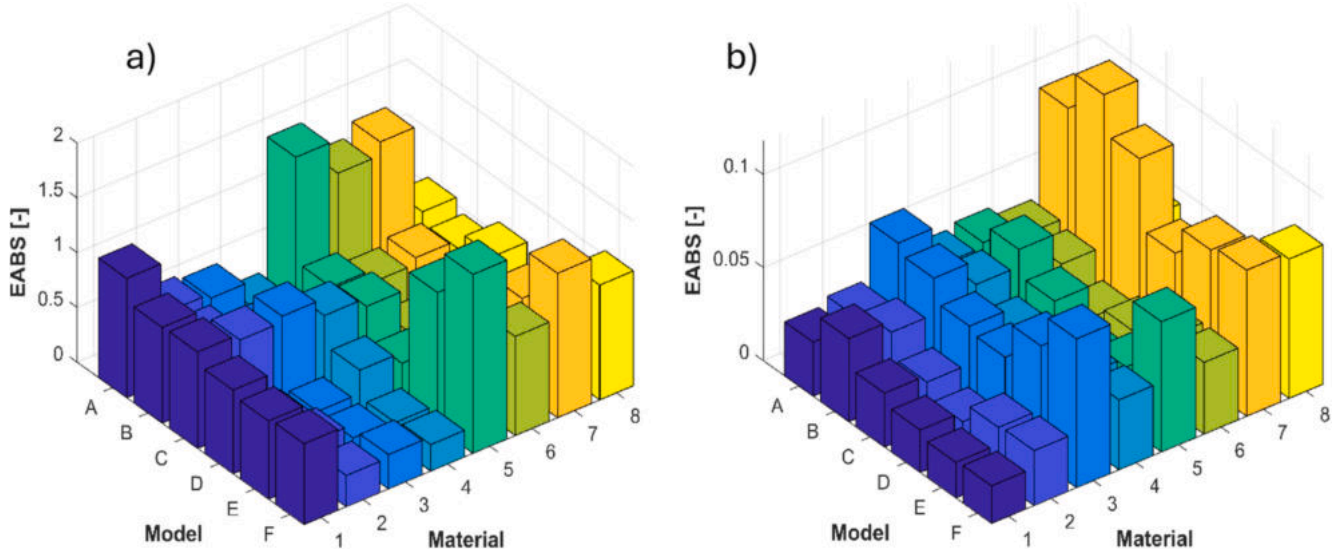

Fig. 12. Error function minimized values (EABS) for each isotherm model (A–F) and AC sample (1–8) based on (a) CO_2 and (b) N_2 adsorption isotherms. Models: A) Toth, B) Freundlich–Langmuir, C) Sips, D) Redlich–Peterson, E) Radke–Prausnitz, and F) Dual-Site Langmuir. ACs: 1) WP-KOH-1:1, 2) WP-KOH-1:2, 3) WP-KOH-1:3, 4) WP-KOH-1:4, 5) WP-$K_2C_2O_4$-1:4, 6) WP-KOH-$K_2C_2O_4$-1:2:2, 7) WP-KOH-$K_2C_2O_4$-1:1:3, 8) WP-KOH-$K_2C_2O_4$-1:3:1).

CO_2 isotherms, falling between 0.234 and 0.633. This confirms the presence of energetically non-uniform sites. For N_2, m_{Rad} lies between 1.202 and 2.385, pointing to more uniform and less selective interactions, in line with its lower adsorption capacity.

3.7.4. *CO_2/N_2 selectivity tests*

S_{IAST} was calculated at a bulk CO_2 mole fraction of 0.05 to reflect separation performance under dilute conditions, which are particularly challenging for sorbent-based systems. Fig. 13a presents the S_{IAST}-predicted CO_2/N_2 selectivity as a function of total pressure for WP-KOH-1:1, WP-KOH-1:4, WP-$K_2C_2O_4$-1:4, and WP-KOH-$K_2C_2O_4$-1:2:2. These samples were chosen to represent different activation approaches and adsorption characteristics. At the tested composition and pressure range, all four ACs display theoretical selectivity values above 12, which is considered satisfactory for low-concentration CO_2 capture relative to other carbon materials reported in the literature [93].

The CO_2/N_2 selectivity trends reveal distinct adsorption behaviors despite only a mild dependence on total pressure. For WP-KOH-1:1, WP-KOH-1:4, and WP-$K_2C_2O_4$-1:4, a steady increase in S_{IAST} with pressure reflects a progressive enhancement in preferential pore filling by CO_2 over N_2. A different adsorption behavior is observed for WP-KOH-$K_2C_2O_4$-1:2:2, where selectivity peaks around 0.5 bar and then declines at higher pressure (16.35–17.12). This deviation may be linked to competitive adsorption or structural heterogeneity, as co-activation with KOH and $K_2C_2O_4$ likely interferes with the individual pore-forming mechanisms of each activator, resulting in a less uniform carbon structure. While high KOH loadings significantly increase S_{BET} (Table 1), excessive amounts such as in WP-KOH-1:4 lead to the lowest S_{IAST} values among the tested carbons (12.8–13.8), likely due to the widening and collapse of ultramicropores (<0.7 nm). WP-KOH-1:1, prepared with a lower KOH ratio, develops a more favorable pore structure and achieves the highest CO_2 uptake at 25 °C (5.95 mmol/g), as previously mentioned, along with noticeably higher CO_2/N_2 separation efficiency (19.13–21.29). However, the performance of WP-KOH-1:1 is still surpassed by WP-$K_2C_2O_4$-1:4, which consistently maintains high S_{IAST} (20.5–21.7). Such behavior is driven by the presence of more refined ultramicropores formed during activation with $K_2C_2O_4$, which favor CO_2 adsorption due to its smaller kinetic diameter (~0.330 nm) compared to N_2 (~0.364 nm) [94], as evidenced in the low-pressure region of the CO_2 isotherms (Fig. 3).

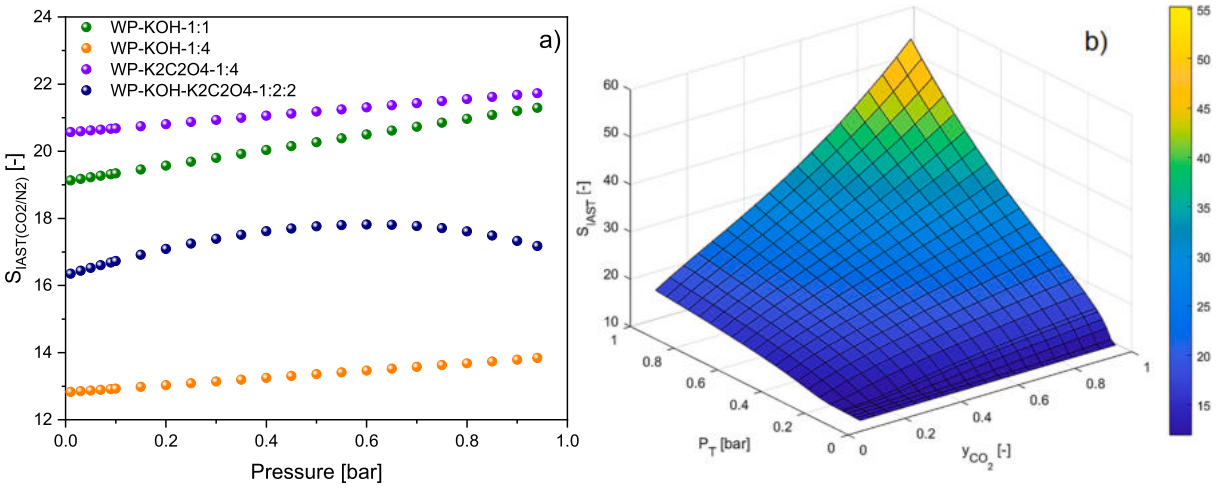

Fig. 13. S_{IAST} as a function of total pressure (a) at a fixed CO_2 molar concentration of 0.05 for selected ACs, and (b) as a function of total pressure and CO_2 molar fraction for WP-$K_2C_2O_4$-1:4 AC.

To further explore a wide range of industrially relevant conditions, S_{IAST} was evaluated for WP-$K_2C_2O_4$-1:4 as a function of total pressure (P_T) and CO_2 mole fraction (yCO_2), as given in Fig. 13b. CO_2/N_2 selectivity remains above 20 across the entire range of y_{CO_2} and P_T, demonstrating strong CO_2 affinity even under highly dilute conditions. As yCO_2 increases, S_{IAST} rises steadily, reaching up to even 54 due to intensified interactions between CO_2 molecules. Furthermore, the 3D surface plot enables extrapolation to various industrial scenarios [95]. For instance, in post-combustion CO_2 capture from coal-fired power plants (7–15 % CO_2), S_{IAST} reaches between 32 and 37. In natural gas flue streams (5–10 % CO_2), it ranges from 28 to 35. Under more challenging conditions, such as biogas upgrading (0.5–3 % CO_2) or direct air capture (≤0.04 % CO_2), SIAST remains within 22 to 26, which reflects the resilience of the AC at low CO_2 concentrations. At higher levels, typical of pre-combustion or syngas applications (30–60 % CO_2), S_{IAST} exceeds 45, highlighting the suitability of WP-$K_2C_2O_4$-1:4 for diverse CO_2 separation scenarios.

The observed higher CO_2/N_2 selectivity of the $K_2C_2O_4$-based ACs can be attributed to the synergistic action of pore size and surface polarity. CO_2-derived NLDFT analysis reveals a dominant fraction of ultra-micropores in the 0.35–0.55 nm range, which generate strong adsorption potentials for CO_2 while sterically limiting N_2. In addition, XPS indicates an enrichment of C═O and O–C═O functionalities, providing polar sites that couple strongly with the quadrupole of CO_2 but only weakly with N_2. These structural and chemical features together rationalize the experimentally observed IAST selectivity values.

Finally, compared to previously reported biomass-based ACs (Table 2), the wooden biomass-derived ACs activated with KOH and $K_2C_2O_4$ in this study exhibit a strong combination of high CO_2 uptake and favorable CO_2/N_2 selectivity.

3.7.5. *Calculation of isosteric heat of CO_2 adsorption*

As shown in Fig. 14a, the isosteric heat of adsorption decreases progressively as fractional loading approaches unity, a trend characteristic of heterogeneous surfaces. At low θ, adsorption is dominated by high-affinity sites, resulting in stronger CO_2–surface interactions. With increasing θ, interactions between adjacent adsorbed CO_2–CO_2 molecules and competition for fewer available sites reduce Q_{st} values [108]. This characteristic appears uniformly across the ACs, suggesting irregular energy distributions over their surfaces.

Quantifying Q_{st} is essential for designing energy-efficient adsorption systems, as it captures the strength of adsorbate–adsorbent interactions and indicates the energy required for desorption. Optimal performance requires a balance: Q_{st} should be high enough to ensure strong uptake, yet low enough to permit easy regeneration. The maximum Q_{st} values observed in this study (26–36 kJ/mol) fall within the physisorption range (<40 kJ/mol) (Fig. 14b), confirming that CO_2 uptake proceeds via physical rather than chemical adsorption, thereby supporting adsorbent

Table 2
Comparison of textural properties, CO_2 uptake, and CO_2/N_2 selectivity of the synthesized ACs with those of biomass-derived carbon materials reported in the literature.

Carbon source	Activator-mass ratio (biomass:activator)-temperature	S_{BET}, [m^2/g]	V_{mic}, [cm^3/g]	CO_2 uptake at 1 bar and 25 °C, [mmol/g]	S_{IAST} (y_{CO2} = 0.05 and 0.15) at 1 bar, [−]	Reference
Pomegranate peel	KOH-1:1–800 °C	2144	0.46	3.64	-; 17	[96]
Biomass tar	KOH-1:3–300 °C	1829	0.49	3.13	-; 20	[97]
Chestnut shell	KOH-1:0.9–600 °C	1296	0.57	3.61	-; 16	[98]
Caltrop shell	KOH-1:2–550 °C	1535	0.67	4.22	-; 19	[99]
Hazelnut shell	KOH-1:2–550 °C	1696	0.78	4.23	-; 19	[100]
Walnut shell	KOH-1:1–800 °C	1868	0.55	5.17	-, 163	[101]
Benzimidazole	KOH-1:1–600 °C	1156	0.49	4.75	-; 27	[102]
Commercial	–	1100	0.38	1.56	-; 11	[103]
Glucose	KOH-1:2–700 °C	1527	0.58	4.71	-; 31	[104]
Coconut shell	KOH-1:2–700 °C	1315	0.66	4.38	-; 17	[105]
Lotus petiole	K_3PO_4–1:3–800 °C	472	0.28	2.57	-; 19	[106]
Common polypody	KOH-1:1–800 °C	1801	0.92	5.67	-; 60	[107]
Wooden pellets	KOH-1:1–800 °C	1956	0.84	5.95	20; 22	This work
Wooden pellets	$K_2C_2O_4$–1:4–800 °C	1709	0.79	5.52	21; 23	This work

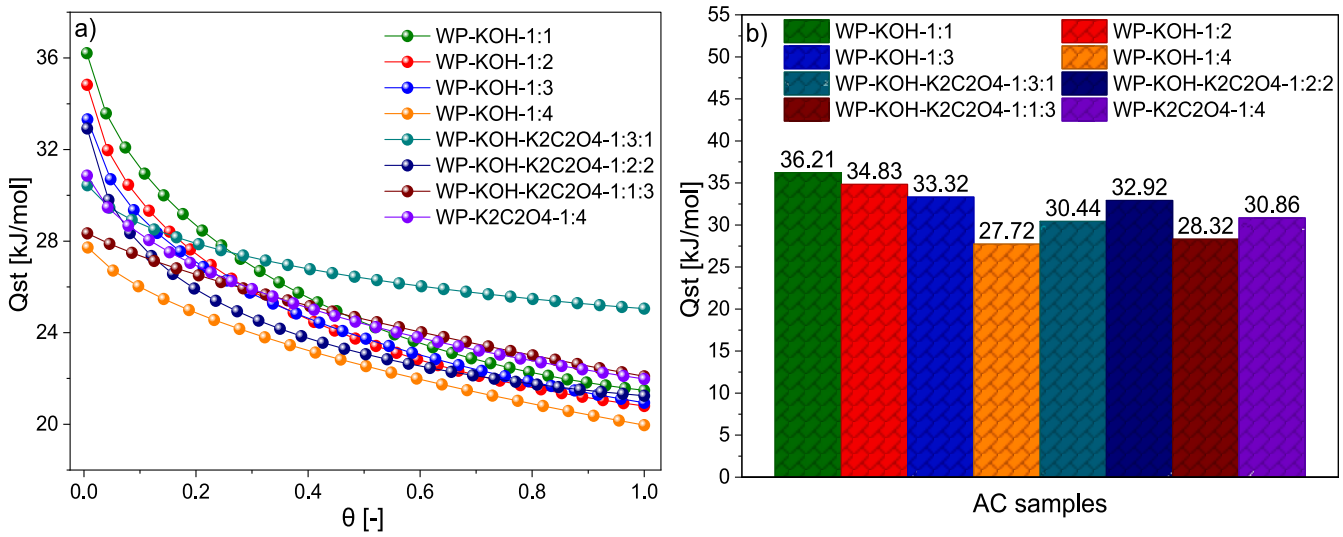

Fig. 14. Q_{st} of CO_2 adsorption as (a) a function of fractional loading, (b) maximum Q_{st} values for ACs.

reusability [109]. Comparable Q_{st} magnitudes and loading-dependent profiles have been reported for CO_2 adsorption on ACs [110] and other porous sorbents, such as MOFs, silicas and zeolites [111,112].

3.7.6. Computational evaluation of CO_2 adsorption via grand canonical Monte Carlo (GCMC) simulation

To support the experimental results, particularly the differences in CO_2 uptake between the best-performing (WP-KOH-1:1) and the least effective (WP-KOH-1:4) samples, these two were modeled as representative systems, denoted as Solid 1 and Solid 2, respectively. Accordingly, solid models were constructed consisting of three graphitic slit-like connected pores of varying widths, as illustrated in Fig. S5. Solid 1 features pore sizes of 1 nm, 1.679 nm, and 2.358 nm, while Solid 2 includes larger pores at 1.2 nm, 2.558 nm, and 3.237 nm. This configuration gives Solid 1 a higher micropore volume content and a lower concentration of surface functional group, whereas Solid 2, with broader pores, exhibits higher S_{BET} and V_{TOT}. The characteristic properties of both solids are summarized in Table S6. The molecular parameters for carbon atoms in the graphene layers and surface functional groups were taken from literature [113], while CO_2 was modeled using the TraPPE model [114], which reliably captures vapor–liquid equilibrium behavior. All atomic parameters are summarized in Table S7. Theoretical insight into their molecular CO_2 adsorption behavior was obtained via GCMC simulations performed at 0 °C, as described in Section 2.5.

The simulations confirmed that the AC with higher S_{BET} and larger V_{TOT} (Solid 2) may lead to lower CO_2 adsorption capacity at low pressure (up to 1 bar) compared to the material with less developed porosity (Solid 1), as illustrated in Fig. 15a. The fluid–functional group interactions (F–Fn) energy for both solids is initially ~40 kJ/mol, gradually decreasing with pressure (Fig. 15b). Saturation of Fn occurs at approximately 0.15 bar for Solid 1 and 0.25 bar for Solid 2, as the F–Fn heat approaches zero. The optimal pore size was found to be pressure-dependent, with the 1 nm pores present in Solid 1 being most effective at 1 bar [107]. Within this confined space, fluid–graphene layer interactions (F–G) are strengthened by the enhanced confinement and the influence of opposing walls.

This observation can be explained by the key influence of pore architecture and surface functional groups on CO_2 adsorption at low pressures, whereas surface area and total pore volume become more relevant at higher pressures [115]. At low pressures, adsorbate molecules preferentially occupy the strongest active sites, either surface functionalities or optimal micropore dimensions, as visualized in the

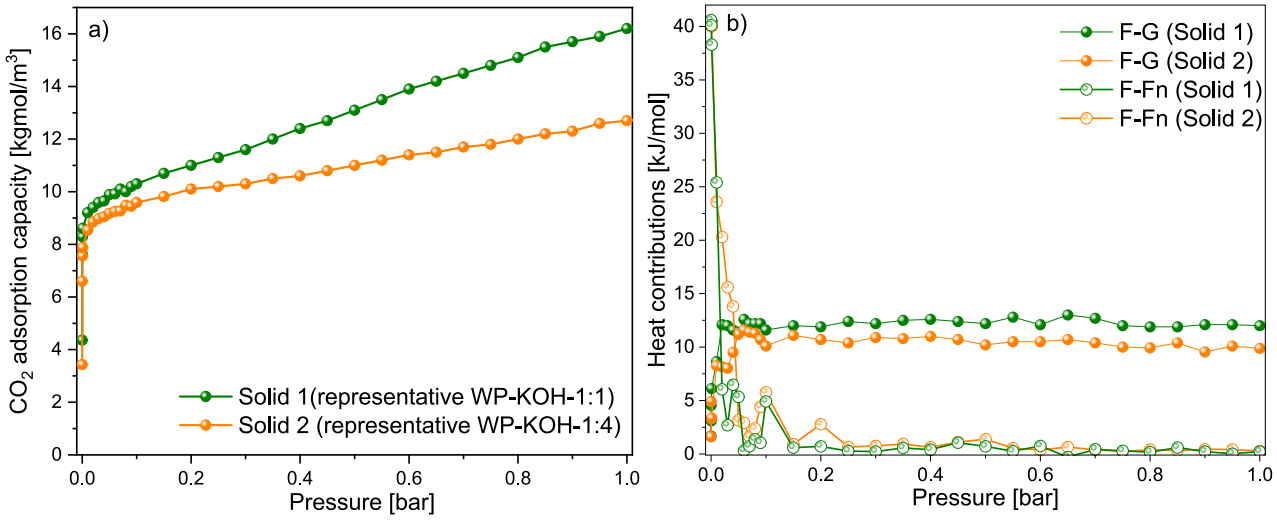

Fig. 15. CO_2 adsorption capacity (a) and heat contributions (b) of Solid 1 and Solid 2 at 0 °C, obtained from GCMC simulations. F–G refers to fluid–graphene layer interactions, F–Fn to fluid–functional group interactions, and the fluid represents CO_2.

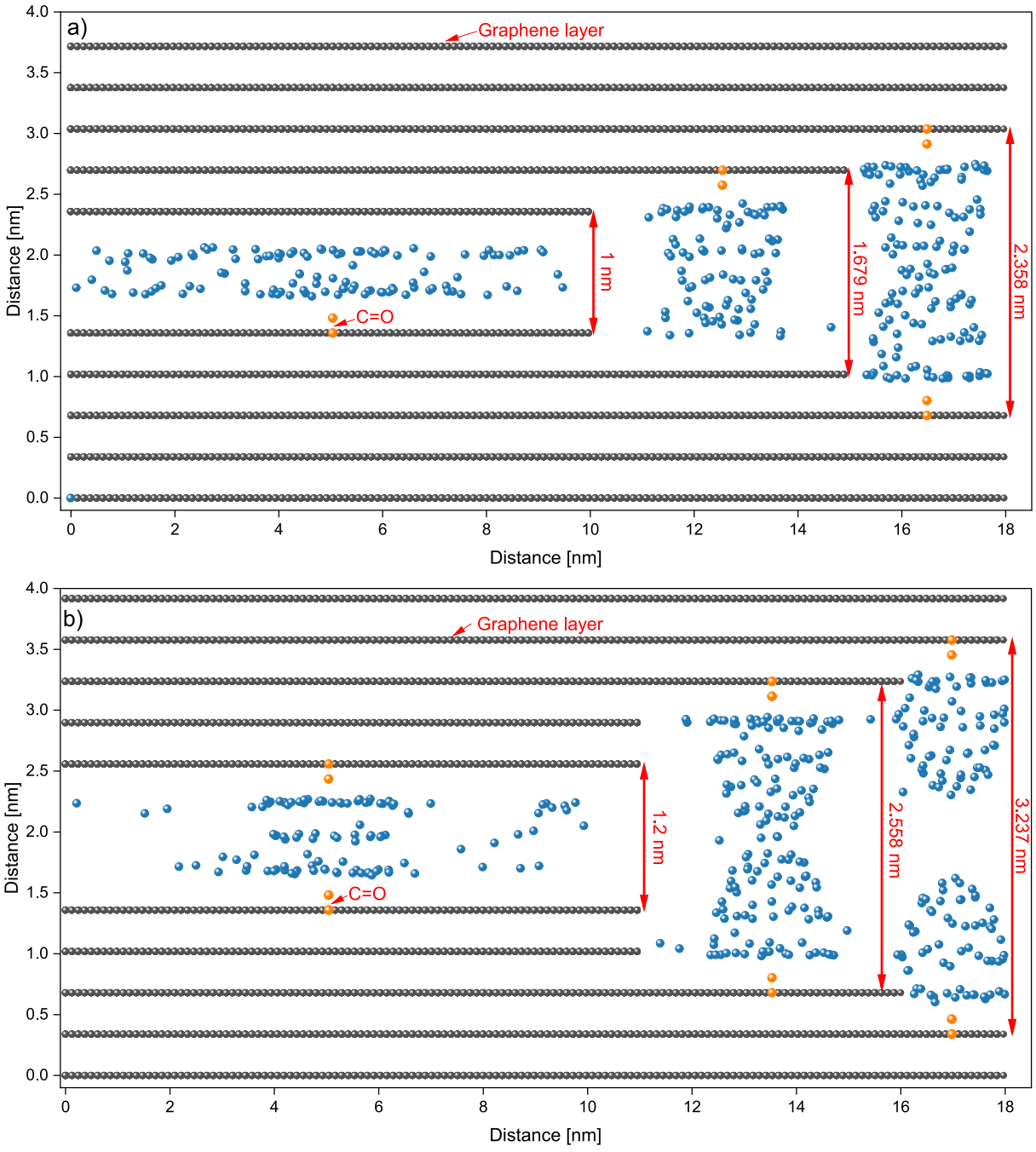

Fig. 16. Snapshots of CO_2 adsorption (center of mass of CO_2) in solid models at 0 °C and 1 bar, obtained via GCMC simulations: (a) Solid 1, (b) Solid 2.

GCMC snapshots (Fig. 16).

The simulations also substantiate the experimental interpretation of enhanced selectivity in the $K_2C_2O_4$-derived carbons. GCMC maps show preferential occupancy of ultramicropores adjacent to carbonyl groups by CO_2 molecules, where they experience higher fluid–solid interaction energies than N_2. This selective stabilization reproduces the IAST selectivity trends and confirms that the concerted effect of sub-nanometer confinement and carbonyl-induced polarity is the mechanistic origin of the superior separation performance.

3.7.7. Process and sustainability considerations

From a practical perspective, KOH remains a highly efficient activator but requires corrosion-resistant equipment and extensive neutralization of highly caustic effluents, generating concentrated brines and increasing operational entropy. In contrast, $K_2C_2O_4$ decomposes into K_2CO_3, CO, and CO_2, with the latter acting in situ as a mild porogen that contributes to the preservation of ultramicropores. The by-product K_2CO_3 is comparatively benign and easier to wash out, reducing water and acid consumption. Although the purchase price of $K_2C_2O_4$ is higher than KOH, these advantages can offset the raw-material cost at scale by lowering downstream expenditures on effluent treatment and equipment maintenance. The co-activation strategy, in which $K_2C_2O_4$ partially replaces KOH, combines the high reactivity of KOH with the milder environmental profile of $K_2C_2O_4$, providing a favorable compromise between adsorption performance and sustainability. This highlights that evaluating porous carbons for CO_2 capture requires not only adsorption metrics but also consideration of process entropy, environmental footprint, and economic feasibility.

4. Conclusions

This study systematically compared the impact of KOH, $K_2C_2O_4$, and their mixtures on the development of porosity and CO_2 capture performance in pine wood–derived activated carbons produced at 800 °C. KOH activation (1:4 ratio) yielded the highest surface area (2655 m^2/g) and total pore volume (1.34 cm^3/g), but also led to ultramicropore degradation due to over-etching. In contrast, $K_2C_2O_4$ activation (1:4) preserved ultramicroporosity (~0.150 cm^3/g), resulted in higher carbon yield (~18.5 %), and achieved the highest CO_2/N_2 selectivity (>21 at 5 % CO_2, 1 bar), owing to narrower pores and increased surface polarity. The co-activated sample (1:2:2 ratio) achieved a favorable balance: high surface area (2029 m^2/g), accessible microporosity (~0.156 cm^3/g), strong CO_2 uptake (9.22 mmol/g at 0 °C; 5.44 mmol/g at 25 °C), and selectivity comparable to pure $K_2C_2O_4$-ACs. These adsorption values position the synthesized materials among the top-performing biomass-derived activated carbons currently described in the literature. Complementary evidence from isosteric heat analysis (26–36 kJ/mol), Radke–Prausnitz model fitting, and GCMC simulations confirmed that carbonyl rich sub-nanometer pores are key to enhancing CO_2 affinity. Altogether, co-activation with KOH and $K_2C_2O_4$ offers a tunable and less chemically severe route to engineer ultramicroporous carbon sorbents from biomass. This scalable strategy holds promise for practical CO_2 separation technologies and warrants further research into sorbent stability, feedstock variability, and pilot-scale implementation.

CRediT authorship contribution statement

Bartosz Dziejarski: Writing – original draft, Visualization, Validation, Software, Project administration, Methodology, Investigation, Formal analysis, Data curation, Conceptualization. **Jarosław Serafin:** Writing – original draft, Visualization, Methodology, Investigation, Formal analysis, Data curation, Conceptualization. **Diego Felipe Hernández-Barreto:** Writing – original draft, Validation, Investigation, Formal analysis, Data curation. **Elena Naumovska:** Visualization, Investigation. **Joanna Sreńscek-Nazzal:** Resources, Methodology, Investigation, Formal analysis. **Nikom Klomkliang:** Writing – original draft, Validation, Software, Investigation, Formal analysis. **Eric Tam:** Validation, Software, Investigation, Formal analysis. **Renata Krzyżyńska:** Supervision. **Klas Andersson:** Supervision, Funding acquisition, Conceptualization. **Pavleta Knutsson:** Supervision, Resources, Project administration, Methodology, Investigation, Conceptualization.

Declaration of competing interest

The authors declare that they have no known competing financial interests or personal relationships that could have appeared to influence the work reported in this paper.

Acknowledgements

This work was supported by the Area of Advance Energy at Chalmers University of Technology (Project No. C2023-0121-15).

Jarosław Serafin is grateful to the Generalitat of Catalunya for the financial support through the AGAUR grant for project No. 2023 CLIMA 00009 funded by the Department of Research and Universities: of the Department of Climate Action, Food and Rural Agenda; and the Climate Fund of the Generalitat de Catalunya.

Nikom Klomkliang is grateful to Suranaree University of Technology for the financial support.

Appendix A. Supplementary data

Supplementary data to this article can be found online at https://doi.org/10.1016/j.cej.2025.169677.

Data availability

Data will be made available on request.

References

[1] G. Lopez, D. Keiner, M. Fasihi, T. Koiranen, C. Breyer, From fossil to green chemicals: sustainable pathways and new carbon feedstocks for the global chemical industry, Energy Environ. Sci. 16 (7) (2023) 2879–2909, https://doi.org/10.1039/D3EE00478C.

[2] O.S. Olugbenga, P.G. Adeleye, S.B. Oladipupo, A.T. Adeleye, K.I. John, Biomass-derived biochar in wastewater treatment-a circular economy approach, Waste Manag. Bull. 1 (4) (2024) 1–14, https://doi.org/10.1016/j.wmb.2023.07.007.

[3] S. Longo, M. Cellura, L.Q. Luu, T.Q. Nguyen, R. Rincione, F. Guarino, Circular economy and life cycle thinking applied to the biomass supply chain: a review, Renew. Energy 220 (2024) 119598, https://doi.org/10.1016/j.renene.2023.119598.

[4] C.J. Hsiao, J.L. Hu, Biomass and circular economy: now and the future, Biomass 4 (3) (2024) 720–739, https://doi.org/10.3390/biomass4030040.

[5] V. Avitabile, R. Pilli, M. Migliavacca, G. Duveiller, A. Camia, V. Blujdea, S. Mubareka, Harmonised statistics and maps of forest biomass and increment in Europe, Sci. Data 11 (1) (2024) 274, https://doi.org/10.1038/s41597-023-02868-8.

[6] The State of the World''s Forests, Forest-sector Innovations Towards a More Sustainable Future. Rome, 2024, https://doi.org/10.4060/cd1211en.

[7] S. Vambol, L. Markina, V. Vambol, A. Mazur, P. Ziarati, P.A. Martin-Cervantes, O. Vlasenko, Type of industries, waste options, and their potential, in: Advances in Energy from Waste, Woodhead Publishing, 2024, pp. 175–221, https://doi.org/10.1016/B978-0-443-13847-8.00006-3.

[8] C. Zhou, Y. Wang, Recent progress in the conversion of biomass wastes into functional materials for value-added applications, Sci. Technol. Adv. Mater. 21 (1) (2020) 787–804, https://doi.org/10.1080/14686996.2020.1848213.

[9] T.A. Saleh, A review on the technologies for converting biomass into carbon-based materials: sustainability and economy, Bioresour. Technol. Rep. 25 (2024) 101771, https://doi.org/10.1016/j.biteb.2024.101771.

[10] S. Sagadevan, T. Balakrishnan, M.Z. Rahman, T. Soga, H. Randriamahazaka, B. Kakavandi, M.R. Johan, Agricultural biomass-based activated carbons for efficient and sustainable supercapacitors, J. Energy Storage 97 (2024) 112878, https://doi.org/10.1016/j.est.2024.112878.

[11] T. Khandaker, T. Islam, A. Nandi, M.A.A.M. Anik, M.S. Hossain, M.K. Hasan, M. S. Hossain, Biomass-derived carbon materials for sustainable energy applications: a comprehensive review, Sustain. Energy Fuels (2025), https://doi.org/10.1039/D4SE01393J.

[12] S. Kundu, T. Khandaker, M.A.A.M. Anik, M.K. Hasan, P.K. Dhar, S.K. Dutta, M. S. Hossain, A comprehensive review of enhanced CO 2 capture using activated carbon derived from biomass feedstock, RSC Adv. 14 (40) (2024) 29693–29736, https://doi.org/10.1039/D4RA04537H.

[13] J. Serafin, B. Dziejarski, Activated carbons—preparation, characterization and their application in CO2 capture: a review, Environ. Sci. Pollut. Res. 31 (28) (2024) 40008–40062, https://doi.org/10.1007/s11356-023-28023-9.

[14] P. Wu, Y. Wang, Y. Liu, Recent advances in heteroatom-doped porous carbon for adsorption of gaseous pollutants, Chem. Eng. J. (2024) 152142, https://doi.org/10.1016/j.cej.2024.152142.

[15] X. Liu, Q. Li, Y. Zhang, F. Zhong, X. Ding, Z. Yu, Synthesis of micro-mesoporous hierarchical structure of coal-based activated carbon and its effect on methane adsorption, Fuel 365 (2024) 131239, https://doi.org/10.1016/j.fuel.2024.131239.

[16] R. Ganjoo, S. Sharma, A. Kumar, M.M. Daouda, Activated carbon: fundamentals, classification, and properties, The Royal Society of Chemistry, 2023, https://doi.org/10.1039/BK9781839169861-00001.

[17] Y. Liu, C. Hao, Z. Wang, J. Xie, W. Zhao, F. Meng, Y. Han, Micropore distribution and methane adsorption process and mechanism in bituminous coals: a molecular dynamics simulation study, J. Environ. Chem. Eng. 12 (2) (2024) 112139, https://doi.org/10.1016/j.jece.2024.112139.

[18] H.R. Lotfy, H. Roubik, Water purification using activated carbon prepared from agriculture waste—overview of a recent development, Biomass Convers. Biorefinery 13 (17) (2023) 15577–15590, https://doi.org/10.1007/s13399-021-01618-3.

[19] I.K. Tetteh, I. Issahaku, A.Y. Tetteh, Recent advances in synthesis, characterization, and environmental applications of activated carbons and other carbon derivatives, Carbon Trends 14 (2024) 100328, https://doi.org/10.1016/j.cartre.2024.100328.

[20] P. Chaudhary, S. Bansal, B.B. Sharma, S. Saini, A. Joshi, Waste biomass-derived activated carbons for various energy storage device applications: a review, J. Energy Storage 78 (2024) 109996, https://doi.org/10.1016/j.est.2023.109996.
[21] K. Malini, D. Selvakumar, N.S. Kumar, Activated carbon from biomass: preparation, factors improving basicity and surface properties for enhanced CO2 capture capacity–a review, J. CO_2 Util. 67 (2023) 102318, https://doi.org/10.1016/j.jcou.2022.102318.
[22] S. Biti, A. Mccue, D. Dionisi, I. Graça, C.F. Martín, Sustainable microcrystalline cellulose-based activated carbons for a greener carbon capture at post-combustion conditions, Int. J. Greenh. Gas Contr. 125 (2023) 103876, https://doi.org/10.1016/j.ijggc.2023.103876.
[23] S. Chowdhury, Y. Kumar, S. Shrivastava, S.K. Patel, J.S. Sangwai, A review on the recent scientific and commercial progress on the direct air capture technology to manage atmospheric CO2 concentrations and future perspectives, Energy Fuel 37 (15) (2023) 10733–10757, https://doi.org/10.1021/acs.energyfuels.2c03971.
[24] S. Elyasi, S. Saha, N. Hameed, P.J. Mahon, S. Juodkazis, N. Salim, Emerging trends in biomass-derived porous carbon materials for hydrogen storage, Int. J. Hydrog. Energy 62 (2024) 272–306, https://doi.org/10.1016/j.ijhydene.2024.02.337.
[25] R. Wang, Y. Feng, D. Li, K. Li, Y. Yan, Towards the sustainable production of biomass-derived materials with smart functionality: a tutorial review, Green Chem. (2024), https://doi.org/10.1039/D4GC01771D.
[26] J.H. Noh, K.Y. Lee, J.H. Kim, H.M. Lee, S. Radhakrishnan, B.S. Kim, Green synthesis of Kenaf-based activated carbons with excellent rate capability and cycle-life via hydrothermal-co-activation process for high-performance capacitive energy storage, Colloids Surf. A Physicochem. Eng. Asp. 682 (2024) 132874, https://doi.org/10.1016/j.colsurfa.2023.132874.
[27] Z. Bao, V.F. Lotfy, X. Zhou, S. Fu, A.H. Basta, Assessment of porous carbon from rice straw residues with potassium ferrate-assisted activation as cationic and anionic dye adsorbents, Ind. Crop. Prod. 212 (2024) 118298, https://doi.org/10.1016/j.indcrop.2024.118298.
[28] M. Sevilla, N. Díez, A.B. Fuertes, More sustainable chemical activation strategies for the production of porous carbons, ChemSusChem 14 (1) (2021) 94–117, https://doi.org/10.1002/cssc.202001838.
[29] J. Wang, Y. Wang, X. Liu, Q. Xiao, M. Demir, M.K. Almesfer, Y. Liu, The synthesis of B-doped porous carbons via a sodium metaborate tetrahydrate activating agent: a novel approach for CO2 adsorption, Molecules 30 (12) (2025) 2564, https://doi.org/10.3390/molecules30122564.
[30] J. Phiri, H. Ahadian, M. Sandberg, K. Granström, T. Maloney, The influence of physical mixing and impregnation on the physicochemical properties of pine wood activated carbon produced by one-step ZnCl2 activation, Micromachines 14 (3) (2023) 572, https://doi.org/10.3390/mi14030572.
[31] N.E. Williams, O.A. Oba, N.P. Aydinlik, Modification, production, and methods of KOH-activated carbon, ChemBioEng Rev. 9 (2) (2022) 164–189, https://doi.org/10.1002/cben.202100030.
[32] G. Singh, A.M. Ruban, X. Geng, A. Vinu, Recognizing the potential of K-salts, apart from KOH, for generating porous carbons using chemical activation, Chem. Eng. J. 451 (2023) 139045, https://doi.org/10.1016/j.cej.2022.139045.
[33] J. Serafin, B. Dziejarski, Ó.J. Fonseca-Bermúdez, L. Giraldo, R. Sierra-Ramírez, M. G. Bonillo, J.C. Moreno-Piraján, Bioorganic activated carbon from cashew nut shells for H_2 adsorption and H_2/CO_2, H_2/CH_4, CO_2/CH_4, $H_2/CO_2/CH_4$ selectivity in industrial applications, Int. J. Hydrog. Energy 86 (2024) 662–676, https://doi.org/10.1016/j.ijhydene.2024.08.417.
[34] J. Sreńscek-Nazzal, A. Kamińska, J. Serafin, B. Michalkiewicz, Chemical activation of banana peel waste-derived biochar using KOH and urea for CO2 capture, Materials 17 (4) (2024) 872, https://doi.org/10.3390/ma17040872.
[35] J. Serafin, B. Dziejarski, J. Sreńscek-Nazzal, An innovative and environmentally friendly bioorganic synthesis of activated carbon based on olive stones and its potential application for CO2 capture, Sustain. Mater. Technol. 38 (2023) e00717, https://doi.org/10.1016/j.susmat.2023.e00717.
[36] J. Serafin, M.C. Román-Martínez, M. Saidi, A.R. Gallego, S. Atlas, M. Ouzzine, Valorization of argan paste cake waste: enhanced CO2 adsorption on chemically activated carbon, J. Anal. Appl. Pyrolysis 181 (2024) 106637, https://doi.org/10.1016/j.jaap.2024.106637.
[37] R. Zakaria, N.A. Jamalluddin, M.Z.A. Bakar, Effect of impregnation ratio and activation temperature on the yield and adsorption performance of mangrove based activated carbon for methylene blue removal, Res. Mater. 10 (2021) 100183, https://doi.org/10.1016/j.rinma.2021.100183.
[38] J. Gopalan, A. Buthiyappan, A.A.A. Raman, Insight into metal-impregnated biomass based activated carbon for enhanced carbon dioxide adsorption: a review, J. Ind. Eng. Chem. 113 (2022) 72–95, https://doi.org/10.1016/j.jiec.2022.06.026.
[39] J.H. Lee, S.J. Park, Potassium oxalate as an alternative activating reagent of corn starch-derived porous carbons for methane storage, J. Nanosci. Nanotechnol. 20 (11) (2020) 7124–7129, https://doi.org/10.1166/jnn.2020.18844.
[40] A. Altwala, R. Mokaya, Direct and mild non-hydroxide activation of biomass to carbons with enhanced CO2 storage capacity, Energ. Adv. 1 (4) (2022) 216–224, https://doi.org/10.1039/D1YA00085C.
[41] A. Rehman, G. Nazir, K.Y. Rhee, S.J. Park, Valorization of orange peel waste to tunable heteroatom-doped hydrochar-derived microporous carbons for selective CO2 adsorption and separation, Sci. Total Environ. 849 (2022) 157805, https://doi.org/10.1016/j.scitotenv.2022.157805.
[42] F.M.B. Kontchouo, Y. Jiang, J. Liang, M. Fan, Y. Shao, L. Zhang, X. Hu, Activation of biomass (cola nut shell) with KOH and K2C2O4: the distinct influence on evolution of volatiles and pore structures of activated carbon, J. Energy Inst. 109 (2023) 101288, https://doi.org/10.1016/j.joei.2023.101288.
[43] E. Dautzenberg, S. van Hurne, M.M. Smulders, L.C. de Smet, GraphIAST: a graphical user interface software for Ideal Adsorption Solution Theory (IAST) calculations, Comput. Phys. Commun. 280 (2022) 108494, https://doi.org/10.1016/j.cpc.2022.108494.
[44] C.M. Simon, B. Smit, M. Haranczyk, pyIAST: ideal adsorbed solution theory (IAST) Python package, Comput. Phys. Commun. 200 (2016) 364–380, https://doi.org/10.1016/j.cpc.2015.11.016.
[45] J. Rouquerol, F. Rouquerol, Methodology of gas adsorption, in: Adsorption by Powders and Porous Solids: Principles, Methodology and Applications: Second Edition, 2012, pp. 57–104, https://doi.org/10.1016/C2010-0-66232-8.
[46] D. Frenkel, B. Smit, Understanding Molecular Simulation: From Algorithms to Applications 443, Elsevier, San Diego: Academic Press, 2023, https://doi.org/10.1063/1.881812.
[47] J.K. Johnson, J.A. Zollweg, K.E. Gubbins, The Lennard-Jones equation of state revisited, Mol. Phys. 78 (3) (1993) 591–618, https://doi.org/10.1080/00268979300100411.
[48] D. Nicholson, N.G. Parsonage, Computer Simulation and the Statistical Mechanics of Adsorption, Acadamic Press, 1982.
[49] C. Zheng, X. Yang, M. Li, S. Bai, Bridging the adsorption data and adsorption process by introducing a polynomial structure to accurately describe IUPAC isotherms, stepwise isotherms, and stepwise breakthrough curves, Langmuir 40 (8) (2024) 4132–4141, https://doi.org/10.1021/acs.langmuir.3c03075.
[50] M. Thommes, K. Kaneko, A.V. Neimark, J.P. Olivier, F. Rodriguez-Reinoso, J. Rouquerol, K.S. Sing, Physisorption of gases, with special reference to the evaluation of surface area and pore size distribution (IUPAC Technical Report), Pure Appl. Chem. 87 (9–10) (2015) 1051–1069, https://doi.org/10.1515/pac-2014-1117.
[51] Mel'gunov, M. S., Application of the simple Bayesian classifier for the N2 (77 K) adsorption/desorption hysteresis loop recognition, Adsorption 29 (5) (2023) 199–208, https://doi.org/10.1007/s10450-022-00369-5.
[52] S. Kousar, K. Javed, B. Begum, M.M. Naeem, S. Zhang, X. Hu, Simultaneous generation of micropores and macropores via synergistic activation of peach wood with K2C2O4 and sodium salts for enlarging pore diameters, Biomass Bioenergy 194 (2025) 107632, https://doi.org/10.1016/j.biombioe.2025.107632.
[53] S. Manna, S. Puravankara, Hierarchically porous closed-pore hard carbon as a plateau-dominated high-performance anode for sodium-ion batteries, Chem. Commun. 60 (22) (2024) 3071–3074, https://doi.org/10.1039/D4CC00025K.
[54] S.G. Wabo, O. Klepel, Nitrogen release and pore formation through KOH activation of nitrogen-doped carbon materials: an evaluation of the literature, Carbon Lett. 31 (4) (2021) 581–592, https://doi.org/10.1007/s42823-021-00252-3.
[55] C. Lu, Z. Yu, X. Zhang, X. Ma, ZnCl2-KOH modulation of biomass-derived porous carbon for supercapacitors, Energ. Sour. Part A 46 (1) (2024) 2212–2222, https://doi.org/10.1080/15567036.2024.2303390.
[56] Y. Guo, Q. Wang, Exploring the adsorption potential of Na2SiO3-activated porous carbon materials from waste bamboo biomass for ciprofloxacin rapid removal in wastewater, Environ. Technol. Innov. 32 (2023) 103318, https://doi.org/10.1016/j.eti.2023.103318.
[57] A.A. Shiryaev, P. Pré, C. Pardanaud, V. Murzin, A. Averin, J.N. Rouzaud, Microporosity and nanostructure of activated carbons: characterization by X-ray diffraction and scattering, Raman spectroscopy and transmission electron microscopy, Adsorption 29 (5) (2023) 275–289, https://doi.org/10.1007/s10450-023-00406-x.
[58] B.S. Girgis, Y.M. Temerk, M.M. Gadelrab, I.D. Abdullah, X-ray diffraction patterns of activated carbons prepared under various conditions, Carbon Lett. 8 (2) (2007) 95–100, https://doi.org/10.1007/s42823-021-00252-3.
[59] N. Yoshizawa, K. Maruyama, Y. Yamada, E. Ishikawa, M. Kobayashi, Y. Toda, M. Shiraishi, XRD evaluation of KOH activation process and influence of coal rank, Fuel 81 (13) (2002) 1717–1722, https://doi.org/10.1016/S0016-2361(02)00101-1.
[60] A. Altwala, R. Mokaya, Direct and mild non-hydroxide activation of biomass to carbons with enhanced CO 2 storage capacity, Energ. Adv. 1 (4) (2022) 216–224, https://doi.org/10.1039/D1YA00085C.
[61] W. Chen, M. Gong, K. Li, M. Xia, Z. Chen, H. Xiao, H. Chen, Insight into KOH activation mechanism during biomass pyrolysis: chemical reactions between O-containing groups and KOH, Appl. Energy 278 (2020) 115730, https://doi.org/10.1016/j.apenergy.2020.115730.
[62] Y.D. Chen, W.Q. Chen, B. Huang, M.J. Huang, Process optimization of K2C2O4-activated carbon from kenaf core using Box–Behnken design, Chem. Eng. Res. Des. 91 (9) (2013) 1783–1789, https://doi.org/10.1016/j.cherd.2013.02.024.
[63] M. Sevilla, G.A. Ferrero, A.B. Fuertes, Beyond KOH activation for the synthesis of superactivated carbons from hydrochar, Carbon 114 (2017) 50–58, https://doi.org/10.1016/j.carbon.2016.12.010.
[64] B. Dziejarski, R. Faust, J. Serafin, R. Krzyzynska, K. Andersson, P. Knutsson, Insights into activation pathways of recovered carbon black (rCB) from end-of-life tires (ELTs) by potassium-containing agents, ACS Omega 9 (29) (2024) 31814–31831, https://doi.org/10.1021/acsomega.4c03160.
[65] C. Li, Y. Li, Y. Shao, L. Zhang, S. Zhang, S. Wang, X. Hu, Activation of biomass with volatilized KOH, Green Chem. 25 (7) (2023) 2825–2839, https://doi.org/10.1039/D2GC04245B.
[66] O. Oginni, K. Singh, G. Oporto, B. Dawson-Andoh, L. McDonald, E. Sabolsky, Influence of one-step and two-step KOH activation on activated carbon

characteristics, Bioresour. Technol. Rep. 7 (2019) 100266, https://doi.org/10.1016/j.biteb.2019.100266.
[67] A.M. Aljumialy, R. Mokaya, Porous carbons from sustainable sources and mild activation for targeted high-performance CO2 capture and storage, Mater. Adv. 1 (9) (2020) 3267–3280, https://doi.org/10.1039/D0MA00449A.
[68] M. Sevilla, A.S.M. Al-Jumialy, A.B. Fuertes, R. Mokaya, Optimization of the pore structure of biomass-based carbons in relation to their use for CO2 capture under low-and high-pressure regimes, ACS Appl. Mater. Interfaces 10 (2) (2018) 1623–1633, https://doi.org/10.1021/acsami.7b10433.
[69] Q. Jiang, Y. Wang, Y. Gao, Y. Zhang, Fabrication and characterization of a hierarchical porous carbon from corn straw–derived hydrochar for atrazine removal: efficiency and interface mechanisms, Environ. Sci. Pollut. Res. 26 (29) (2019) 30268–30278, https://doi.org/10.1007/s11356-019-06174-y.
[70] S. Foorginezhad, M.M. Zerafat, M. Asadnia, G. Rezvannasab, Activated porous carbon derived from sawdust for CO2 capture, Mater. Chem. Phys. 317 (2024) 129177, https://doi.org/10.1016/j.matchemphys.2024.129177.
[71] R. Manikandan, G. Suresh, S.M. Abbas, S. Selvi, S.S. Begum, R. Vezhavendhan, G. Kumaresan, An investigation on thermo-mechanical characterization of activated carbon/coconut shell powder reinforced natural composites, Proc. Inst. Mech. Eng. Part E: J. Process Mech. Eng. 239 (2) (2025) 542–552, https://doi.org/10.1177/09544089221132721.
[72] A. López-Francés, M. Cabrero-Antonino, F. Bernat-Quesada, B. Ferrer, M. Blanes, R. García, S. Navalón, Valorization of field-spent granular activated carbon as heterogeneous ozonation catalyst for water treatment, ChemSusChem 17 (14) (2024) e202400062, https://doi.org/10.1002/cssc.202400062.
[73] C. Wu, G.W. Tindall, C.L. Fitzgerald, M.C. Thies, M.E. Roberts, Decoupling the role of lignin, cellulose/hemi-cellulose, and ash on ZnCl 2-activated carbon pore structure, Mater. Adv. 6 (4) (2025) 1431–1441, https://doi.org/10.1039/D4MA01234H.
[74] C.L. Waters, R.R. Janupala, R.G. Mallinson, L.L. Lobban, Staged thermal fractionation for segregation of lignin and cellulose pyrolysis products: an experimental study of residence time and temperature effects, J. Anal. Appl. Pyrolysis 126 (2017) 380–389, https://doi.org/10.1016/j.jaap.2017.05.008.
[75] E.H. Al-Ghurabi, M.M. Boumaza, W. Al-Masry, M. Asif, Optimizing the synthesis of nanoporous activated carbon from date-palm waste for enhanced CO2 capture, Sci. Rep. 15 (1) (2025) 17132, https://doi.org/10.1038/s41598-025-00498-1.
[76] E. Picheau, S. Amar, A. Derré, A. Pénicaud, F. Hof, An introduction to the combustion of carbon materials, Chem. Eur. J. 28 (54) (2022) e202200117, https://doi.org/10.1002/chem.202200117.
[77] H.S. Kim, J.C. Hyun, Y. Choi, S. Ha, D.H. Kang, Y.H. Heo, Y.S. Yun, A new perspective for potassium intercalation chemistry in graphitic carbon materials, Energ. Stor. Mater. 70 (2024) 103514, https://doi.org/10.1016/j.ensm.2024.103514.
[78] C. Chen, Z. Luo, C. Yu, T. Wang, H. Zhang, Transformation behavior of potassium during pyrolysis of biomass, RSC Adv. 7 (50) (2017) 31319–31326, https://doi.org/10.1039/C7RA05162J.
[79] F. Karuana, A. Prismantoko, H.P. Putra, A.S. Ruhiyat, A. Darmawan, I.N.A. Adi Saputra, H. Hariana, Experimental investigation of sulfur and nitrogen oxide emissions and corrosion propensity during the combustion of coals and biomass fuels, Combust. Sci. Technol. (2024) 1–23, https://doi.org/10.1016/j.joei.2019.04.009.
[80] R. Singh, L. Wang, K. Ostrikov, J. Huang, Designing carbon-based porous materials for carbon dioxide capture, Adv. Mater. Interfaces 11 (4) (2024) 2202290, https://doi.org/10.1002/admi.202202290.
[81] S. Alam, N. ur Rahman, M. Ilyas, I., A. Gul, M. Zahoor, E.A. Ali, Preparation, characterization and removal of Acid Blue 129 and Erioglaucine dyes from aqueous solution by corn cob based activated carbon, Bull. Environ. Contam. Toxicol. 115 (1) (2025) 4, https://doi.org/10.1007/s00128-025-04076-z.
[82] D.D. Viet, D.T. Thao, K.D. Anh, T. Tsubota, Autohydrolysis treatment of bamboo and potassium oxalate (K2C2O4) activation of bamboo product for CO2 capture utilization, Front. Chem. Sci. Eng. 18 (4) (2024) 41, https://doi.org/10.1007/s11705-024-2402-8.
[83] J. Indujalekshmi, M.S. Arsha, V. Biju, KOH-mediated structural modification of activated charcoal by heat treatment for the efficient adsorption of organic dyes, Appl. Surf. Sci. Adv. 19 (2024) 100566, https://doi.org/10.1016/j.apsadv.2023.100566.
[84] K. Jedynak, B. Charmas, Adsorption properties of biochars obtained by KOH activation, Adsorption 30 (2) (2024) 167–183, https://doi.org/10.1007/s10450-023-00399-7.
[85] S.D. Sarkar, D. Mukherjee, D. Kuila, CO2 capture using activated carbon derived from avocado seeds and sawdust: a comparative study on adsorption performance and surface properties, J. Environ. Chem. Eng. (2025) 117643, https://doi.org/10.1016/j.jece.2025.117643.
[86] J.A. Schott, C.L. Do-Thanh, W. Shan, N.G. Puskar, S. Dai, S.M. Mahurin, FTIR investigation of the interfacial properties and mechanisms of CO2 sorption in porous ionic liquids, Green Chem. Eng. 2 (4) (2021) 392–401, https://doi.org/10.1016/j.gce.2021.09.003.
[87] D.J. Morgan, Comments on the XPS analysis of carbon materials, J. Carb. Res. 7 (3) (2021) 51, https://doi.org/10.3390/c7030051.
[88] E. Stefan-Henningsen, N. Roberts, G. Pereira, A. Kiani, Graphene as an additive in complex lithium grease: a comprehensive analysis of friction, wear and thermal behaviour, Next Mater. 8 (2025) 100754, https://doi.org/10.1016/j.nxmate.2025.100754.
[89] M. Ayyoob, M.S. Hegde, An XPS study of the adsorption of oxygen on silver and platinum surfaces covered with potassium or cesium, Surf. Sci. 133 (2–3) (1983) 516–532, https://doi.org/10.1016/0039-6028(83)90017-1.
[90] X. Chen, D. Menon, X. Wang, M. He, M.R.A. Kiapi, M. Asgari, D. Fairen-Jimenez, Flexibility-frustrated porosity for enhanced selective CO2 adsorption in an ultramicroporous metal-organic framework, Chem 11 (2025) 102382, https://doi.org/10.1016/j.chempr.2024.11.020.
[91] M. Zhang, Z. Wang, J. Pan, H. Chu, W. Liu, D. Lv, Q. Hou, Unveiling differential functional group responses in CO2/CH4/N2 adsorption/desorption of deep Ordos coal via in situ DRIFTS, Energy Fuel 39 (17) (2025) 8034–8048, https://doi.org/10.1021/acs.energyfuels.5c00851.
[92] J. Serafin, B. Dziejarski, Application of isotherms models and error functions in activated carbon CO2 sorption processes, Microporous Mesoporous Mater. 354 (2023) 112513, https://doi.org/10.1016/j.micromeso.2023.112513.
[93] F. Raganati, P. Ammendola, CO2 post-combustion capture: a critical review of current technologies and future directions, Energy Fuel 38 (15) (2024) 13858–13905, https://doi.org/10.1021/acs.energyfuels.4c02513.
[94] J.E. Eichler, H. Leonard, E.K. Yang, L.A. Smith, S.N. Lauro, J.N. Burrow, C. B. Mullins, Dual-cation activation of N-enriched porous carbons improves control of CO2 and N2 adsorption thermodynamics for selective CO2 capture, Adv. Funct. Mater. 34 (51) (2024) 2410171, https://doi.org/10.1002/adfm.202410171.
[95] M. Songolzadeh, M. Soleimani, M. Takht Ravanchi, R. Songolzadeh, Carbon dioxide separation from flue gases: a technological review emphasizing reduction in greenhouse gas emissions, Sci. World J. 2014 (1) (2014) 828131, https://doi.org/10.1155/2014/828131.
[96] M. Ouzzine, J. Serafin, J. Sreńscek-Nazzal, Single step preparation of activated biocarbons derived from pomegranate peels and their CO2 adsorption performance, J. Anal. Appl. Pyrolysis 160 (2021) 105338, https://doi.org/10.1016/j.jaap.2021.105338.
[97] H. Yuan, J. Chen, D. Li, H. Chen, Y. Chen, 5 Ultramicropore-rich renewable porous carbon from biomass tar with excellent adsorption capacity and selectivity for CO2 capture, Chem. Eng. J. 373 (2019) 171–178, https://doi.org/10.1016/j.cej.2019.04.206.
[98] Q. Li, S. Liu, W. Peng, W. Zhu, L. Wang, F. Chen, X. Hu, Preparation of biomass-derived porous carbons by a facile method and application to CO2 adsorption, J. Taiwan Inst. Chem. Eng. 116 (2020) 128–136, https://doi.org/10.1016/j.jtice.2020.11.001.
[99] Z. Zhao, C. Ma, F. Chen, G. Xu, R. Pang, X. Qian, X. Hu, Water caltrop shell-derived nitrogen-doped porous carbons with high CO2 adsorption capacity, Biomass Bioenergy 145 (2021) 105969, https://doi.org/10.1016/j.biombioe.2021.105969.
[100] R. Pang, T. Lu, J. Shao, L. Wang, X. Wu, X. Qian, X. Hu, Highly efficient nitrogen-doped porous carbonaceous CO2 adsorbents derived from biomass, Energy Fuel 35 (2) (2020) 1620–1628, https://doi.org/10.1021/acs.energyfuels.0c03832.
[101] J. Serafin, B. Dziejarski, O.F.C. Junior, J. Sreńscek-Nazzal, Design of highly microporous activated carbons based on walnut shell biomass for H2 and CO2 storage, Carbon 201 (2023) 633–647, https://doi.org/10.1016/j.carbon.2022.09.013.
[102] Y. Luo, J. Gong, Z. Yang, Z. Liu, Y. Chen, S. Huang, W. Yan, The impact of neglected potassium in KOH-activated porous carbon on CO2 capture and CO2/N2 selectivity: experimental and molecular simulation studies, Appl. Surf. Sci. 681 (2025) 161571, https://doi.org/10.1016/j.apsusc.2024.161571.
[103] S. Chen, W. Wu, Z. Niu, D. Kong, W. Li, Z. Tang, D. Zhang, High adsorption selectivity of activated carbon and carbon molecular sieve boosting CO2/N2 and CH4/N2 separation, Chin. J. Chem. Eng. 67 (2024) 282–297, https://doi.org/10.1016/j.cjche.2023.10.015.
[104] K. Zhang, D. Hu, F. Yang, X. Wang, N. He, H. Xie, Z. Chen, Efficient CO2 adsorption and selective CO2/CH4/N2 separation by porous carbon with different N, S sources, Sep. Purif. Technol. 367 (2025) 132853, https://doi.org/10.1016/j.seppur.2025.132853.
[105] J. Shao, Y. Wang, M. Che, Q. Xiao, M. Demir, M.K. Al Mesfer, Y. Liu, N, S Co-doped porous carbons from coconut shell for selective CO2 adsorption, J. Energy Inst. (2025) 102273, https://doi.org/10.1016/j.joei.2025.102273.
[106] Y. Zhi, Y. Yin, Q. Ciren, Q. Xiao, L. Zhao, M. Demir, L. Wang, One-step synthesis of K3PO4-activated phosphorus-enriched carbons for enhanced carbon capture, J. Environ. Chem. Eng. (2025) 116694, https://doi.org/10.1016/j.jece.2025.116694.
[107] J. Serafin, K. Kiełbasa, B. Michalkiewicz, The new tailored nanoporous carbons from the common polypody (Polypodium vulgare): the role of textural properties for enhanced CO2 adsorption, Chem. Eng. J. 429 (2022) 131751, https://doi.org/10.1016/j.cej.2021.131751.
[108] A. Nuhnen, C. Janiak, A practical guide to calculate the isosteric heat/enthalpy of adsorption via adsorption isotherms in metal–organic frameworks, MOFs, Dalton Trans. 49 (30) (2020) 10295–10307, https://doi.org/10.1039/d0dt01784a.
[109] A. Naifar, K. Oueslati, E.C. Lima, F. Aouaini, A. Ben Lamine, In-depth study of captopril adsorption on a biosourced adsorbent: statistical physics approach and pore characterization, with modeling of adsorption isotherms, energetic and steric analysis, Langmuir (2025), https://doi.org/10.1021/acs.langmuir.5c01235.
[110] J. Wang, Y. Yin, X. Liu, Y. Liu, Q. Xiao, L. Zhao, X. Hu, Potassium metaborate-activated boron-doped porous carbons for selective CO2 adsorption, Sep. Purif. Technol. (2025) 134079, https://doi.org/10.1016/j.seppur.2025.134079.
[111] Z. Du, X. Nie, S. Deng, L. Zhao, S. Li, Y. Zhang, J. Zhao, Comparative analysis of calculation method of adsorption isosteric heat: case study of CO2 capture using MOFs, Microporous Mesoporous Mater. 298 (2020) 110053, https://doi.org/10.1016/j.micromeso.2020.110053.
[112] S. Duan, Y. Xie, S. Shen, G. Li, Comparative analysis of CO2 and N2 adsorption on zeolite 4A: thermodynamics parameters and site energy distribution

investigations, J. Environ. Chem. Eng. 12 (3) (2024) 112870, https://doi.org/10.1016/j.jece.2024.112870.
[113] M. Jorge, C. Schumacher, N.A. Seaton, Simulation study of the effect of the chemical heterogeneity of activated carbon on water adsorption, Langmuir 18 (24) (2002) 9296–9306, https://doi.org/10.1021/la025846q.
[114] J.J. Potoff, J.I. Siepmann, Vapor–liquid equilibria of mixtures containing alkanes, carbon dioxide, and nitrogen, AICHE J. 47 (7) (2001) 1676–1682, https://doi.org/10.1002/aic.690470719.
[115] A. Tiyawate, N. Khongtor, J. Serafin, S. Chaemchuen, N. Klomkliang, Combined experimental and grand canonical Monte Carlo simulation study of CO2 capture in nitrogen and sulfur co-doped biochar derived from biowaste: cost analysis, kinetics, and equilibrium, J. Environ. Chem. Eng. 12 (5) (2024) 113991, https://doi.org/10.1016/j.jece.2024.113991.

Paper II

Environmental Research 247 (2024) 118169

Contents lists available at ScienceDirect

Environmental Research

journal homepage: www.elsevier.com/locate/envres

Upgrading recovered carbon black (rCB) from industrial-scale end-of-life tires (ELTs) pyrolysis to activated carbons: Material characterization and CO_2 capture abilities

Bartosz Dziejarski [a,b,c,*], Diego Felipe Hernández-Barreto [d], Juan Carlos Moreno-Piraján [d,*], Liliana Giraldo [e], Jarosław Serafin [f], Pavleta Knutsson [c], Klas Andersson [b,g], Renata Krzyżyńska [a]

[a] Faculty of Environmental Engineering, Wroclaw University of Science and Technology, 50-370, Wroclaw, Poland
[b] Department of Space, Earth and Environment, Division of Energy Technology, Chalmers University of Technology, SE-412 96, Gothenburg, Sweden
[c] Department of Chemistry and Chemical Engineering, Division of Energy and Materials, Chalmers University of Technology, SE-412 96, Gothenburg, Sweden
[d] Departamento de Química, Facultad de Ciencias, Grupo de Investigación en Sólidos Porosos y Calorimetría, Universidad de Los Andes, Cra. 1a No. 18A-10, Bogotá D.C. 11711, Colombia
[e] Departamento de Química, Grupo de Calorimetría, Universidad Nacional de Colombia, Sede Bogotá, Cra. 45, Bogotá D.C. 11711, Colombia
[f] Department of Inorganic and Organic Chemistry, University of Barcelona, Martí I Franquès, 1-11, 08028, Barcelona, Spain
[g] Department of Chemical Engineering, University of Utah, Salt Lake City, UT, USA

ARTICLE INFO

Keywords:
Tire recycling
Circular economy
Sustainable materials
Waste management
CO_2 adsorption
Net-zero emissions

ABSTRACT

The current study presents for the first time how recovered carbon black (rCB) obtained directly from the industrial-scale end-of-life tires (ELTs) pyrolysis sector is applied as a precursor for activated carbons (ACs) with application in CO_2 capture. The rCB shows better physical characteristics, including density and carbon structure, as well as chemical properties, such as a consistent composition and low impurity concentration, in comparison to the pyrolytic char. Potassium hydroxide and air in combination with heat treatment (500–900 °C) were applied as agents for the conventional chemical and physical activation of the material. The ACs were tested for their potential to capture CO_2. Ultimate and proximate analysis, Fourier-transform infrared spectroscopy (FT-IR), scanning electron microscopy with energy dispersive X-ray spectroscopy (SEM-EDS), Raman spectroscopy, thermogravimetric analysis (TGA), and N_2/CO_2 gas adsorption/desorption isotherms were used as material characterization methods. Analysis revealed that KOH-activated carbon at 900 °C (AC-900K) exhibited the highest surface area and a pore volume that increased 6 and 3 times compared to pristine rCB. Moreover, the AC-900K possessed a well-developed dual porosity, corresponding to the 22% and 78% of micropore and mesopore volume, respectively. At 0 °C and 25 °C, AC-900K also showed a CO_2 adsorption capacity equal to 30.90 cm^3/g and 20.53 cm^3/g at 1 bar, along with stable cyclic regeneration after 10 cycles. The high dependence of CO_2 uptake on the micropore volume at width below 0.7–0.8 nm was identified. The selectivity towards CO_2 in relation to N_2 reached high values of 350.91 (CO_2/N_2 binary mixture) and 59.70 (15% CO_2/85% N_2).

1. Introduction

Waste treatment of end-of-life tires (ELTs) flows constitute a crucial challenge due to the rapid development of the automotive and transportation sectors and limited infrastructure for disposal and recycling (Dabic-Miletic et al., 2021; Martínez, 2021; Trudsø et al., 2022). ELTs contribute roughly 2% of the total waste generated around the globe (Karaağaç et al., 2017), with 1.6 billion tires being manufactured and discarded in a single year 2020 and the market demand that continues to rise (Global Tire Recycling Market Analysis, 2020). It is suggested that 75% of ELT waste is deposited in landfills without being subjected to any treatment (Ferdous et al., 2021), which can potentially lead to fire

* Corresponding author at: Faculty of Environmental Engineering, Wrocław University of Science and Technology, 50-370 Wrocław, Poland; Department of Space, Earth and Environment, Division of Energy Technology, Chalmers University of Technology, SE-412 96 Gothenburg, Sweden.
* Corresponding author at: Departamento de Química, Facultad de Ciencias, Grupo de Investigación en Sólidos Porosos y Calorimetría, Universidad de Los Andes, Cra. 1a No. 18A-10, Bogotá D.C. 11711, Colombia
E-mail addresses: bartoszd@chalmers.se (B. Dziejarski), jumoreno@uniandes.edu.co (J.C. Moreno-Piraján).

https://doi.org/10.1016/j.envres.2024.118169
Received 10 November 2023; Received in revised form 14 December 2023; Accepted 9 January 2024
Available online 18 January 2024

hazards, breeding grounds for mosquitoes and other pests, and/or release chemicals that have a negative impact on air, ground, and water (Bulei et al., 2018; Mohajerani et al., 2020). Rubber, which constitutes a significant proportion of tires (approximately 60–65%) (Tian et al., 2021), represents a highly stable material with degradation process in soil that may require 800–2000 years (Basik et al., 2021). Among existing waste treatment methods (reuse of whole tires, feedstock recycling, and energy recovery), pyrolysis has shown to be a promising alternative for waste treatment (Hoang et al., 2022). This process represents the thermal decomposition of organic substances at temperature of 400 °C–650 °C without oxidizing agent (Premchand et al., 2023), which allows the recovery of valuable substances. These substances include gases (H_2, H_2S, or C1–C4 light hydrocarbons), condensable oil, as well as carbonaceous solid residues (Singh et al., 2018; Kandasamy et al., 2015). In the case of ELTs pyrolysis, the solid phase (pyrolytic char) represents a share of about 35% of the overall good (Yang et al., 2022). The obtained pyrolytic char needs to be further refined to gain recovered carbon black (rCB) with the high value of elemental carbon. The main driver behind the growth of the interest in rCB is the escalating demand for sustainable substitutes to virgin carbon black (vCB) which is ranked among the top 50 commercial chemicals on a global scale (Cardona-Uribe et al., 2021). The production of rCB acquired from ELTs renders thus a more environmentally viable option than vCB, which is sourced from fossil fuels and characterized with high CO_2 footprint as well as results pollutant emissions (SO_x, NO_x and PM). Hence, the application of sustainable rCB has successfully transitioned into industrial implementation, playing a significant role in achieving circularity within the tire sector.

One of the possible reuses of recovered black carbon is as activated carbons (ACs). Activated carbons are a unique type of carbon-based materials with a wide range of applications, such as for water purification (Jjagwe et al., 2021), energy storage (Ayinla et al., 2019), and separation of flue gas mixtures (Mukherjee et al., 2019). Additionally, ACs exhibit a wide array of desirable properties, including an extensive network of pores, well-developed microporosity, a high surface area, and significant chemical or thermal characteristics, which can find applications in multiple fields. Activated carbons have also been proposed as a cost-effective and efficient alternative to conventional sorbents, such as amine-based solvents for carbon dioxide capture (Kishibayev et al., 2021; Serafin et al., 2017, 2021, 2023a; Abuelnoor et al., 2021). ACs can be synthesized through two well-known processes: physical and chemical activation (Dziejarski et al., 2023). Physical activation frequently involves carbon dioxide, water vapor, air, or combinations thereof. Air is commonly reported as a favorable activation agent due to its availability, low cost, and eco-friendliness. It is typically used at lower temperatures, ranging from 450 °C to 700 °C (Plaza et al., 2014; Ould-Idriss et al., 2011; Gomez-Serrano et al., 1993; Zabaniotou et al., 2008), depending on the precursor and the desired properties of the resulting AC. On the other hand, chemical activation agents that are most often cover KOH, K_2CO_3, H_3PO_4, and $ZnCl_2$. Potassium hydroxide is considered as the most effective in terms of the development of porosity and surface area, where the optimal temperature range is generally higher and typically between 750 °C and 900 °C (Serafin et al., 2022a; Sangchoom and Mokaya, 2015; Shen et al., 2018; Ogungbenro et al., 2020).

Commonly, ACs are produced from biomass residue, because it is considered an abundant and renewable precursor material. However, biomass waste flows are heterogeneous and have a composition that differs significantly depending on the geographical region. On average, the carbon content in biomass is approximately 45–50% by weight, which may be considered fairly low. Biomass-based ACs are usually developed with the aim of fabricating perspective goods that extend beyond the mitigating of environmental degradation, such as addressing the issue of ELTs disposal. Previous studies have addressed the valorization of discarded waste tires in laboratory conditions. These investigations have also explored the turning of the resulting pyrolytic

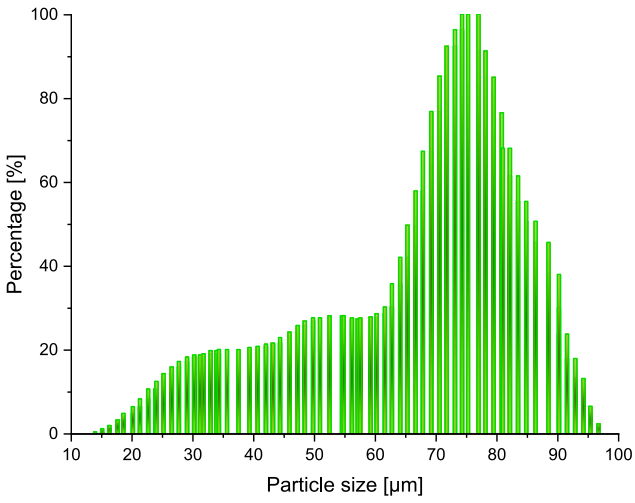

Fig. 1. Histogram of particle size distribution for recovered carbon black.

char into activated carbons. Sun et al. (1997) used scrap tires treated with by both physical and chemical activation methods, such as the use of CO_2 and KOH. The materials were then applied for the storage of natural gas. Teng, Lin, and Hsu (Teng et al., 2000) focused on ACs synthesized by KOH impregnated as a means of exploring the correlation between the devolatilization conditions and their porous structure. Moreover, several other researchers made contributions to this field, including Stavropoulos (2005), Hofman and Pietrzak (2011), López et al. (2013), and Nieto-Márquez et al. (2016). Their works have mostly concentrated on examining the adsorption capacities of the waste tires based ACs for a range of chemicals, such as, e.g., methylene blue, cyclohexane, and major air pollutants (sulphur dioxide, or nitrogen dioxide). Although the outcomes present ACs derived from ELTs pyrolysis as a potentially effective solution for waste management, there is a gap in the literature on the direct conversion of tailor-made rCB transformed from contaminated soot on industrial sector. This gap extends to possible ways for its application when it comes to CO_2 capture, as the most significant greenhouse gas. Research conducted in this specific field has the opportunity to demonstrate rCB/AC production as an industrial ready, economically viable process, and explore their potential utilization for CO_2 capture, which is also the aim of this paper.

The current work shows for the first time rCB conversion from industrial-scale ELTs pyrolysis to ACs for the application of CO_2 emission reduction. By upgrading the rCB to ACs, this approach addresses the ecological concerns related to ELTs at the same time as it makes use of a valuable resource available on the commercial market. Thus, the strategy presented is particularly important in the context of circular economy and resource conservation. The upgraded rCB/ACs are expected to exceed the low boundaries for activated carbons quality derived from waste tire char or various types of biochars. This is closely related to having a standardized original composition, which can result in a repetitive production of high-quality material with improved characteristics, such as a high fixed carbon content and lower impurity and ash levels. As a consequence, while conventional ACs have well-established CO_2 adsorption capabilities, rCB/ACs can exhibit comparable or even higher performance. Additionally, the use of rCB/ACs presents an opportunity to adopt a resource-efficient and responsible method for managing the waste streams generated from the treatment of ELTs. This is particularly advantageous because of the easily accessible rCB. Finally, the results presented in this study contribute to the development of solid adsorbents by simultaneously transforming one of the most widely available global waste into a value-added product. These value-added rCB/ACs can be further improved and potentially applied for CO_2 capture.

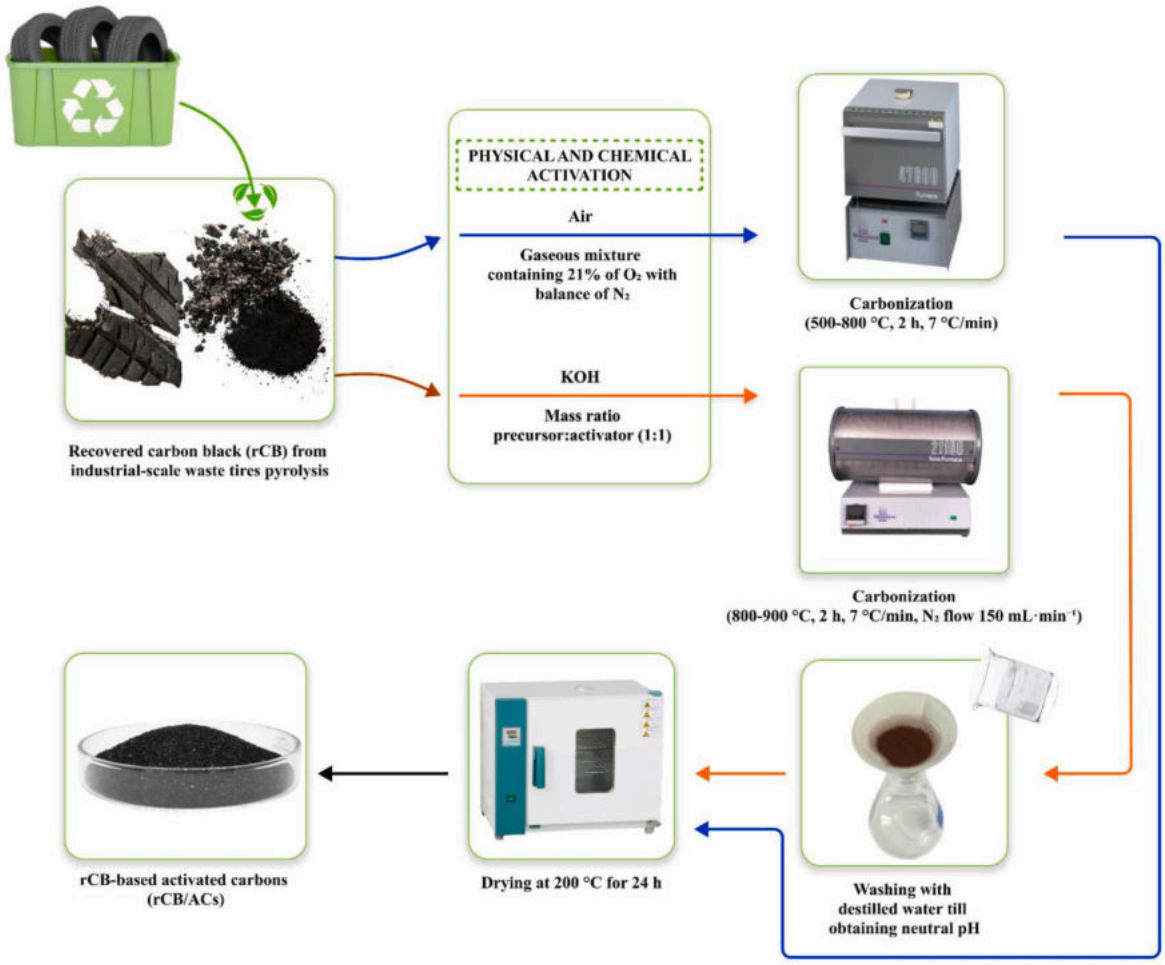

Fig. 2. Schematic representation of the preparation procedures used for activation of rCB/ACs based on recovered carbon black (rCB).

2. Materials and experiment methodology

2.1. Raw material

The recovered carbon black with an average particle size of 30 μm and an ash content equal to 0.5–2% was used as the activated carbon precursor, supplied by Syntoil company located in Poland. To fabricate it, a treatment of char (devolatilization, milling, and optional pelleting) was applied to remove the ash content, metal contaminants, and standardize the particle size variability. As can be observed in Fig. 1, rCB consists mainly of particle sizes of 73–80 μm in the range of 15–100 μm that are the most abundant in its volume. Chemical composition of rCB is variable, depending on composition of tires utilized in pyrolysis, where the main component is carbon in a variety of 92–99.5%. Besides it may also consist of volatile substances with a content of >0.2%, and mineral matter of approximately 0.5–2%, including, among others, silicon, aluminium, zinc, sulphur and calcium.

2.2. Preparation of rCB/AC samples

Activated carbons were prepared from rCB without any additional pre-preparations by physical and chemical activation via air and KOH, as shown in Fig. 2. For physical activation, a Barnstead Thermolyne 47900 muffle was used, and the effect of the activation temperature was studied. The temperature was changed from 500 to 700 °C in atmospheric air (gaseous mixture containing 21% of O_2 with balance of N_2), with a heating rate of 7 °C·min^{-1} and a dwelling time of 2 h. In the case of chemical activation, potassium hydroxide (KOH) was used as the activating agent through a dry mixing method. Equivalent mass quantities of rCB and KOH (mass ratio 1:1) were grounded on a mortar to obtain a homogeneous solid mixture. The 1:1 ratio served as a crucial reference point to establish a baseline and initial assessment of KOH activation behavior stages for the rCB material. The activation was then performed using a Barnstead Thermolyne 21100 tubular horizontal furnace, under an inert atmosphere (N_2) and with a constant flow of 150 mL min^{-1}. The temperatures were set at 800, 850 and 900 °C, holding for 2 h with a heating rate of 7 °C·min^{-1}. The chemically activated carbons obtained were washed several times with deionized water until a constant pH of the washing water was obtained. Finally, all obtained rCB/ACs were dried in oven for 24 h at 200 °C. rCB/ACs samples were labelled AC-XXXZ, where XXX is the activation temperature, and Z corresponds to the activating agent (potassium hydroxide (K) or air (A)).

2.3. Characterization of carbon materials

2.3.1. Textural characterization

In order to analyze the textural properties of the synthesized AC samples, N_2 physisorption isotherms at −196 °C were measured using a Micromeritics ASAP 2020 Plus Adsorption Analyzer. Samples were degassed previous the analysis by two heating steps: the first one (evacuation phase) was carried out at a maximum temperature of 110 °C, under vacuum (10^{-8} bar) and for 1 h. After that the second step (heating phase) reached a temperature of 300 °C for 9h and under vacuum. Then the isotherms were acquired measuring around 40 adsorption points and 20 desorption points from a relative pressure (P/P_0) of $1{\cdot}10^{-6}$. The specific surface area was calculated using the

Table 1
Description of selected adsorption isotherm models.

Isotherm model	Described adsorption phenomenon	Non-linear model equations	Characterization of equation	Ref.
Freundlich-Langmuir	Considering both monolayer and multilayer adsorption effects	$q_e = \frac{q_m \bullet K_{FL} \bullet P^{n_{FL}}}{1 + K_{FL} \bullet P^{n_{FL}}}$	q_m - maximum adsorption capacity (cm^3/g), K_{FL} - Langmuir-Freundlich constant (bar^{-nFL}), n_{FL} - index of heterogeneity [-]	Nuhnen and Janiak (2020)
Redlich–Peterson	Includes the features of both Langmuir and Freundlich isotherm	$q_e = \frac{K_{RP} \bullet P}{1 + a_{RP} \cdot P^{\beta_{RP}}}$	K_{RP} - Redlich-Peterson constant ($cm^3 \cdot g^{-1} \cdot bar^{-1}$), a_{RP} - constant ($bar^{-\beta RP}$) β_{RP} - Redlich–Peterson exponent (−)	Cai et al. (2022)
Toth	Multi-layered sorption on heterogeneous surfaces at both low and high pressure.	$q_e = \frac{q_m \bullet K_T \bullet P}{[1 + (K_T \bullet P)^{n_T}]^{\frac{1}{n_T}}}$	K_T - Toth constant (bar^{-1}), n_T – heterogeneity factor (−)	Aniruddha et al. (2020)
Sips	Combined form of the Langmuir and Freundlich model equations to characterize heterogeneous adsorption systems	$q_e = \frac{q_m \bullet (K_S \bullet P)^{\frac{1}{n_S}}}{1 + (K_S \bullet P)^{\frac{1}{n_S}}}$	K_S - Sips constant (bar^{-1}), n_S – Sips exponent (−)	Mukherjee and Samanta (2019)
Radke–Prausnitz	Adsorption with low concentration of the gas molecules	$q_e = \frac{q_m \bullet K_{RPr} \bullet P}{(1 + K_{RPr} \cdot P)^{e_{RPr}}}$	K_{RPr} - Radke–Prausnitz constant (bar^{-1}), e_{RPr} - Radke–Prausnitz exponent (−)	Khoshraftar and Ghaemi (2023)

Brunauer - Emmett - Teller (B.E.T) equation in the range of relative pressure of 0.05–0.3. The NLDFT model was used to determine the pore size distribution (PSD) and the micropore and mesopore specific volumes. Micropore analysis was complemented by measuring CO_2 adsorption isotherms at 0 °C.

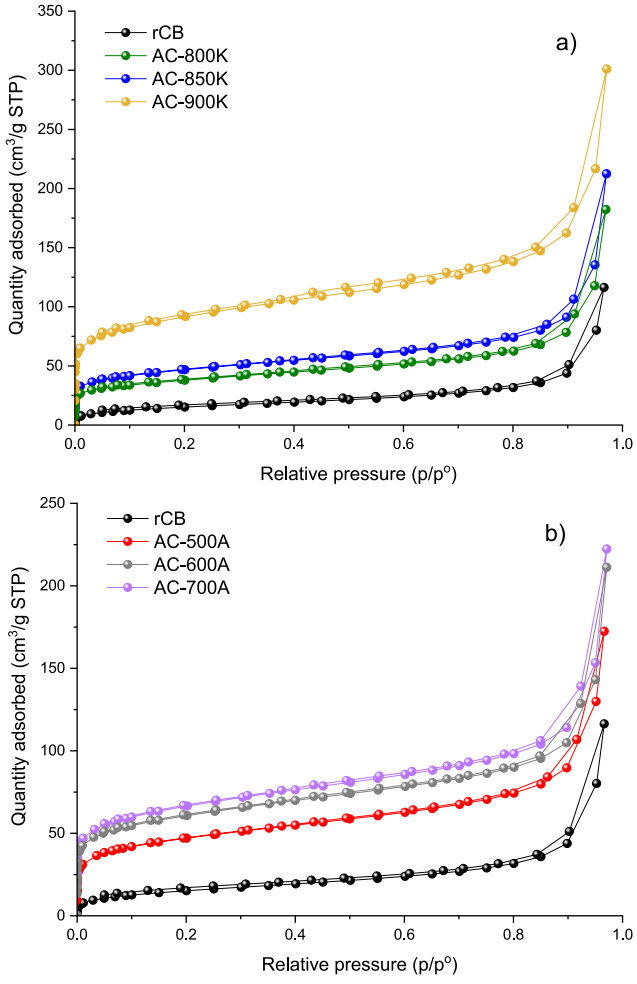

Fig. 3. N_2 adsorption-desorption isotherm curves at −196 °C of the prepared activated carbons samples by (a) chemical activation, (b) physical activation.

2.3.2. Chemical characterization

The ultimate analyses were done using a CHNS Elemental Analyzer FLASH 2000 from Thermo Fisher Scientific. To conduct an analysis of potassium amount, the X-ray fluorescence energy dispersion spectrophotometer (EDXRF) of the Epsilon 3 model, manufactured by PANalytical B, was used. Moreover, the proximate analysis was performed with TGA.

To investigate the interactions and functional groups present on ACs that are relevant to the CO_2 adsorption, Fourier-transform infrared spectroscopy (FT-IR) was applied. FT-IR was performed using a Shimadzu IRTracer-100 spectrometer equipped with the Diffuse Reflectance Accessory, DiffusIR™. The spectra were acquired with 100 scans, a resolution of 1.93 cm^{-1} between 400 and 4000 cm^{-1}, and under nitrogen to avoid absorption of water during the analysis. Carbon-based materials were crushed and mixed with KBr to obtain solid dissolutions with a concentration of 1 % w/w, and each dissolution was analyzed in the spectrometer.

For evaluation of the decomposition and thermal stability of AC materials used for CO_2 capture application, thermogravimetric analysis (TGA) was also utilized. TGA was studied using the thermal analyzer TGA 550 from TA Instruments, with a nitrogen flow of 150 mL min^{-1}, a heating rate of 10 °C·min^{-1} and a temperature range of 20–900 °C.

2.3.3. Morphological characterization

Surface morphologies and differences in the shapes of the activated carbon surfaces were observed through the Scanning-Electron Microscopy (SEM). SEM images were acquired using a TESCAN LYRA3 FIB-SEM microscope coupled to a microanalysis system of Energy-Dispersive X-ray spectroscopy (EDS) and using both, backscattering electrons, and secondary electrons detectors. Samples were previously metal-coated to improve electrical conductivity. To evaluate the structure of the carbon skeleton in the obtained carbon materials, Raman spectroscopy measurements were performed. The measurements were done using a Horiba Xplora Raman microscope via a laser with a wavelength of 523 nm, 100x of magnification, and 70% of the laser power to avoid sample's damage.

2.4. CO_2 adsorption investigation

CO_2 adsorption isotherms were measured using the Micromeritics ASAP 2020 Plus Sorption Analyzer. Analysis temperature was set to 0, 15, 25 and 30 °C using a water bath contained on a Dewar flask. Absolute pressure was changed from 5×10^{-4} to 1 bar and samples were degassed previous the analysis with the same conditions as before, which are 110 °C under vacuum (10^{-8} bar) and for 1 h prior to analysis.

Table 2
Textural parameters of the rCB-based activated carbons.

Sample	BET surface area[a], m^2/g	Total pore volume[b], cm^3/g	Micropore volume [c] (<2 nm), cm^3/g	Supermicropore volume [d] (0.7–2nm), cm^3/g	Ultramicropore volume [d] (<0.7 nm), cm^3/g	Micropore volume(<2 nm)/total pore volume, %	Mesopore volume/ total pore volume, %
rCB	55	0.170	–	–	–	–	–
AC-800K	131	0.275	0.036	0.021	0.015	13	87
AC-850K	165	0.316	0.048	0.028	0.020	15	85
AC-900K	328	0.448	0.100	0.069	0.031	22	78
AC-500A	161	0.253	0.050	0.029	0.021	20	80
AC-600A	218	0.327	0.066	0.042	0.024	20	80
AC-700A	232	0.333	0.072	0.047	0.025	22	78

[a] Brunauer, Emmett & Teller (BET) method using the Rouquerol criteria.
[b] Calculated by N_2 adsorption isotherm at a high relative pressure (~0.99).
[c] DFT method via NLDFT model, assuming slit-shaped pores, based on N_2 adsorption isotherm at −196 °C.
[d] DFT method via NLDFT model, assuming slit-shaped pores, based on CO_2 adsorption isotherm at 0 °C.

Furthermore, the ideal adsorption solution theory (IAST) was employed to determine the CO_2/N_2 adsorption selectivity of the ACs (vital aspect for CO_2 capture application) based on N_2 sorption measurement at a temperature of 25 °C.

2.5. CO_2 adsorption mechanism studies

To identify CO_2 adsorption mechanism, experimental results were fitting the Toth, Freundlich-Langmuir, Sips, Redlich-Peterson, and Radke-Prausnitz isotherm models, using a nonlinear regression method by the quasi-newton algorithm incorporated in the Matlab ® function, fmincon. Table 1 provides a comprehensive presentation of the non-linear form of isotherm equations, along with their theoretical assumptions and parameter description. The adequacy of the chosen theoretical model in relation to the empirical data was assessed by the sum of absolute errors (EABS) that is common modeling tool of adsorption isotherms. The EABS is presented by the below formula:

$$EABS = \sum_{i=1}^{n} \left| q_{e,\exp} - q_{e,mod} \right| \quad (1)$$

Where: $qe_{,mod}$ - predicted amount of adsorbed adsorbate at equilibrium state [cm^3/g], $qe_{,exp}$ - experimental amount of adsorbed adsorbate at equilibrium state [cm^3/g].

Furthermore, the thermodynamic parameters of adsorption were calculated using the van't Hoff equation and Clausius-Clapeyron equations for CO_2 adsorption isotherms at 0, 15, 25 and 30 °C, which are the most widely reported estimation approach for Gibbs free energy, enthalpy, entropy, and isosteric heat of adsorption.

3. Results and discussion

3.1. Studies of textural properties by N_2 adsorption/desorption isotherms at −196 °C and CO_2 adsorption at 0 °C

The textural characteristics of prepared rCB/ACs was examined using N_2 adsorption and desorption measurements at a temperature of −196 °C. Fig. 3 (a,b) schematically illustrates the N_2 isotherms for all samples produced in the temperature range of 800–900 °C and 500–700 °C by applying chemical and physical activation, respectively. Through the examination of isotherms, the crucial adsorption characteristics of materials can be evaluated, simultaneously enabling the design and optimization of adsorbents to effectively adsorb CO_2. Hence, to evaluate the required textural properties for effective CO_2 adsorption, presented methodology focuses on two key factors: the necessity of sufficient surface area with porosity, and the specific range of pore sizes. It is widely reported that materials with high surface areas and tailored pore structures, especially microporosity with pore width below 0.7 nm, are highly beneficial and desirable for CO_2 adsorption (Boujibar et al., 2019; Plaza et al., 2010). The N_2 isotherm data was analyzed to determine the extent of porosity development within the material, assessing the efficiency for CO_2 capture. By examining the shape, steepness, and hysteresis of the isotherms, the valuable insights were gain into the porosity evolution.

The materials were characterized by a rapid increase in adsorption at low relative pressures ($P/P_0 < 0.1$), which is followed by a gradual growth along with P/P_0 values and the appearance of a loop. The shapes of the N_2 sorption isotherm curves correspond to the combination of type I and IV (Baldovino-Medrano et al., 2023; Muttakin et al., 2018). Type I suggests the development of activated carbon with micropore content (<2 nm in diameter) in which a primary filling occurs at very low relative pressure values, as confirmed by a very steep isotherm with a sharp knee below P/Po < 0.15 (Ozpinar et al., 2022). Type IV is a variant of type II but has a discrete multilayer structure that corresponds to mesoporous materials (with pores of 2–50 nm) and gives a characteristic hysteresis loop (Soltani et al., 2019). Consequently, upon achieving a P/Po value of 1.0, indicating a further gradual reduction in pressure, a discernible desorption curve is formed, which is distinguishable from the one that results from the initial adsorption. This phenomenon is highly associated to filling empty mesopores by capillary condensation (Dantas et al., 2019).

Moreover, as can be seen, all isotherms exhibit H3-type hysteresis in an almost complete range of P/P_0 above 0.35, which is especially visible between 0.8 and 1.0 region. These findings strongly indicate that the pore size distributions are nearly analogous to those of combination of micro- and mesopores, including aggregates of plate-like particles forming to slit-shaped pores with non-uniform size and shape (Yousif et al., 2022). Hence, the outcome implies the existence of a dual porosity of the ACs produced from rCB, revealing that the carbon structure is characterized by both well-developed micropores and mesopores.

The textural properties of rCB/ACs are summarized in Table 2. The results of the textural characteristics of activated carbons relative to rCB, as the raw material, confirmed the optimal enhancement of the BET surface area by 83% and the total pore volume by 64%, accordingly. Additionally, all ACs primarily presented a percentage of mesoporosity, ranging from 78 to 87% of the porous structure. As observed, raising the activation temperature led to an increase in BET surface area, total pore volume, and microporosity, which was reported in many other studies (Serafin et al., 2023b; Wang et al., 2020). The augmentation of the

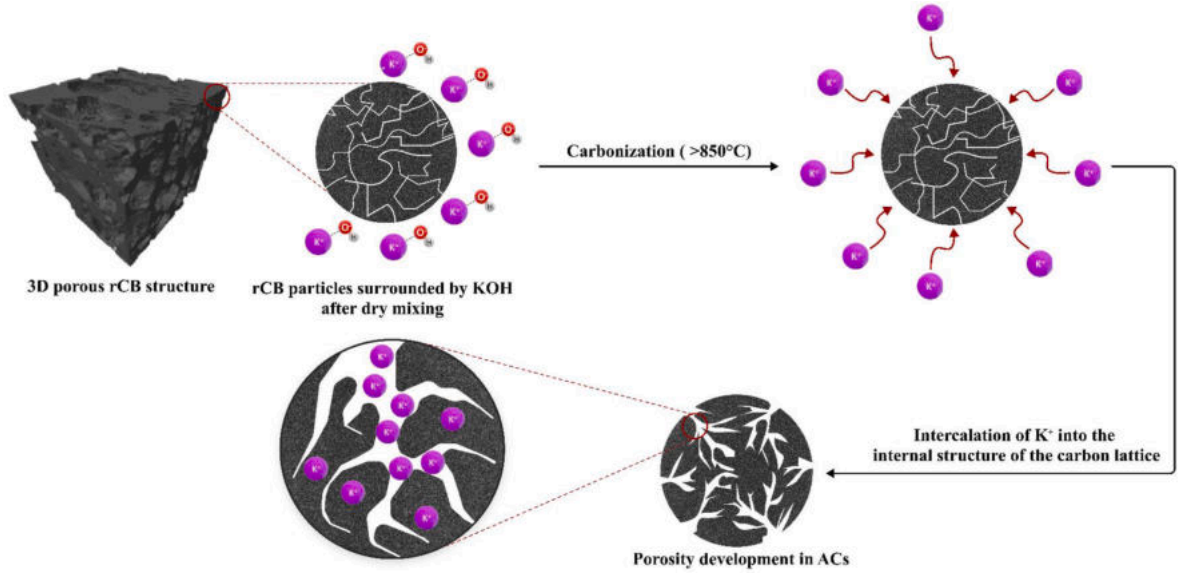

Fig. 4. Schematic Illustration of pore formation mechanism in rCB during chemical activation using KOH.

activation temperature caused a boost in the reactivity of the carbon atoms situated on the surface of the rCB. This, in turn, led to an acceleration of the diffusion rate of activating agent molecules transportation inside the material (Lan et al., 2019).

In the case of physical activation, AC-700A was found to be the best sample due to its the greatest textural parameters, followed by AC-600A and AC-500A. On the other hand, among chemically activated samples with KOH, AC-900K synthesized at 900 °C demonstrated the highest Brunauer-Emmett-Teller surface area, total pore and micropore volume (pores up to 2 nm determined by N_2 adsorption at −196 °C) of 328 m^2/g,

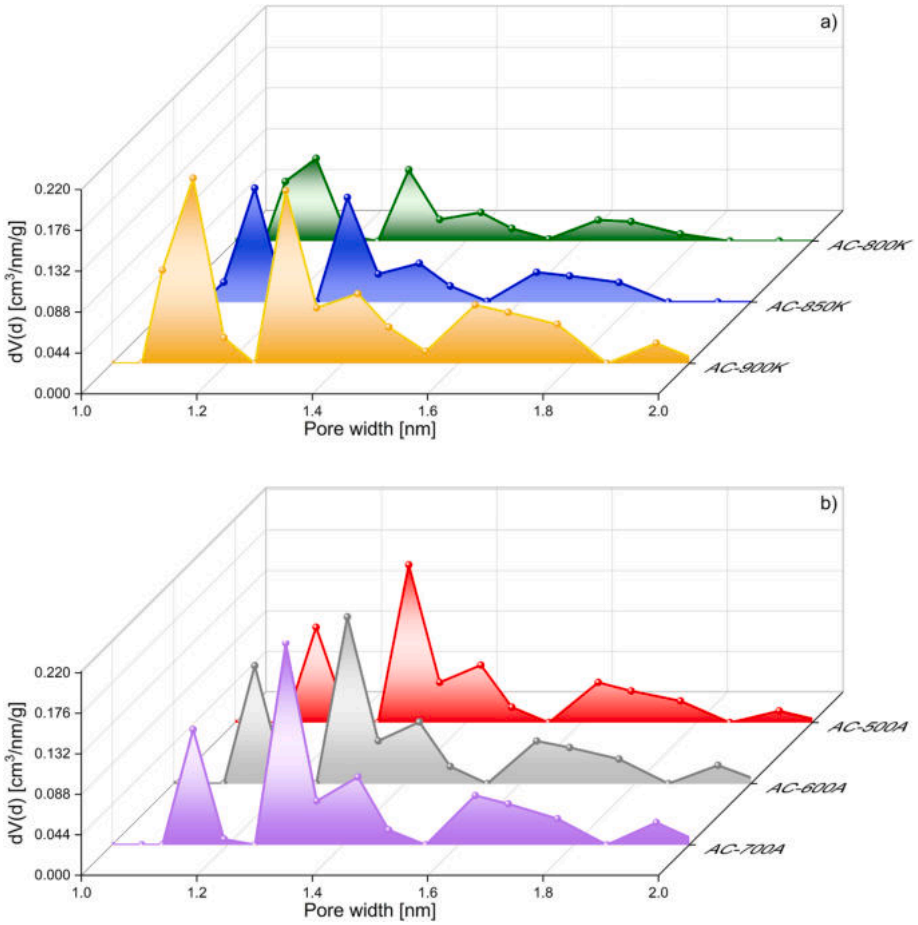

Fig. 5. Pore size distribution within a width of 1–2 nm for activated carbons obtained by (a) chemical activation, (b) physical activation, determined with the NLDFT method based on N_2 sorption at − 196 °C.

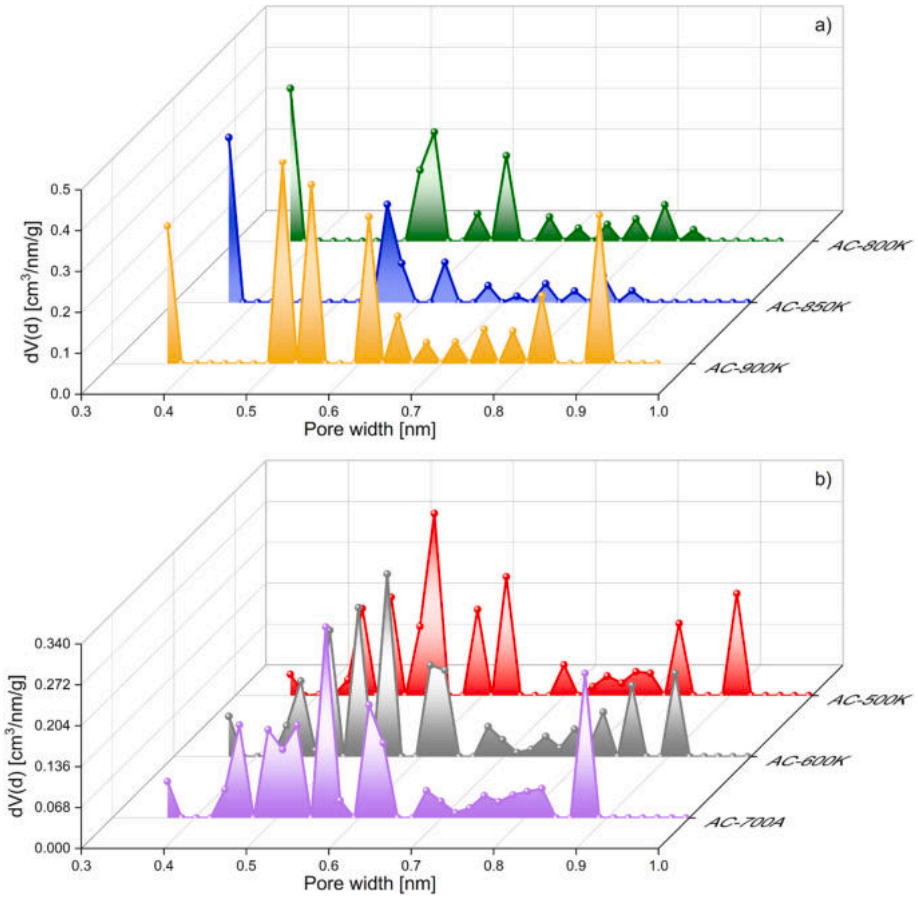

Fig. 6. Pore size distribution within a width below 1 nm for activated carbons obtained by (a) chemical activation, (b) physical activation, determined with the DFT method based on CO_2 sorption at 0 °C.

0.448 cm^3/g, and 0.100 cm^3/g, respectively.

The quite noticeable development of the specific surface area and porosity between 700 and 900 °C according to the literature may be closely related to the formation of metallic potassium (>762 °C) (Arslanoğlu, 2019), which is a significant factor in the generation of the pore framework (Mistar et al., 2020). Exceeding the temperature from 850 to 900 °C improved the micropore content to 22%. This can happen when vapor of metallic K is assimilated and diffused into the internal structure of the carbon particles and predominantly graphitic layers, which eventually leads to the manifestation of new porosities and the stretching of the pores that already exist (Fig. 4). With the generally accepted mechanism, during activation most of KOH is transformed into K_2CO_3 and K_2O, as follows (Gao et al., 2020):

$$2KOH \rightarrow K_2O + H_2O \quad (2)$$

$$K_2O + CO_2 + C \rightarrow K_2CO_3 \quad (3)$$

$$4KOH + C \rightarrow K_2CO_3 + K_2O + 2H_2 \quad (4)$$

Then by their reduction by carbon atoms, potassium is obtained, according to the below equations (Li et al., 2017):

$$K_2O + C \rightarrow 2K + CO \quad (5)$$

$$K_2CO_3 + C \rightarrow 2K + 3CO \quad (6)$$

On the other hand, at 800–900 °C and KOH/AC ratio of 1:1, KOH-ACs should exhibit much higher surface area and micropore volume compared carbons prepared by using air. This suggests that specific ratio between rCB and KOH along with the temperature may need to be further optimized to achieve the right balance between activation and preservation of the desired rCB/ACs porosity characteristics.

3.2. Pore size distribution (PSD) analysis

Further, in order to determine the pore size distributions (PSD) of all AC samples, a non-local density functional theory (NLDFT) model assuming slit pores was also employed. The PSDs obtained from N_2 adsorption measurements at −196 °C are plotted in Fig. 5 and Figure S1 for a pore width range below 2 nm and within 2–35 nm. In line with the graphs, the majority of the pores are nearly completely varied across the spread distribution that is comparatively placed within entire range of 35 nm. The PSD curves indicate that a significant proportion of pores are classified as mesopores in total, while there is a smaller number of micropores, which are relatively large in the combined structure of ACs. The micropore widths are primarily concentrated within the range of 1.05–1.19, and 1.25–1.54 nm, as proven by the two most prominent peaks at 1.14 and 1.30 nm. On the contrary, the mesopore diameters are predominantly situated within the 2.30–3.90, 9.48–10.36, 12.36–13.50 nm, and evidently focused between 16.00 and 34.05 nm spectrum.

PSD determination has conventionally been performed through nitrogen sorption isotherms obtained at −196 °C, as above. However, the diffusion rate of nitrogen molecules into micropores of small size is significantly reduced at low temperatures, and the estimation of pores with width below 1 nm is not feasible. The aforementioned issue can be resolved by performing CO_2 adsorption at a temperature of 0 °C. At elevated temperatures and increased absolute pressures, the accessibility of ultramicropores by CO_2 molecules exceeds that of N_2 at −196 °C, despite the similarity in molecular critical dimensions between the two gases. Therefore, this method provides insight into the characteristics of pores that fall within the diameter range of approximately

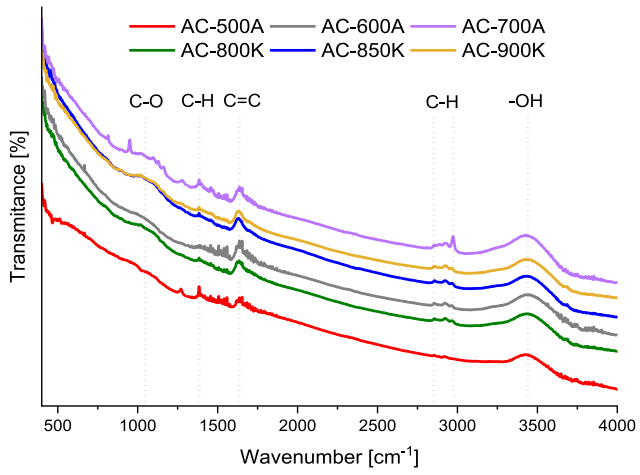

Fig. 7. FT-IR spectra of rCB/AC materials.

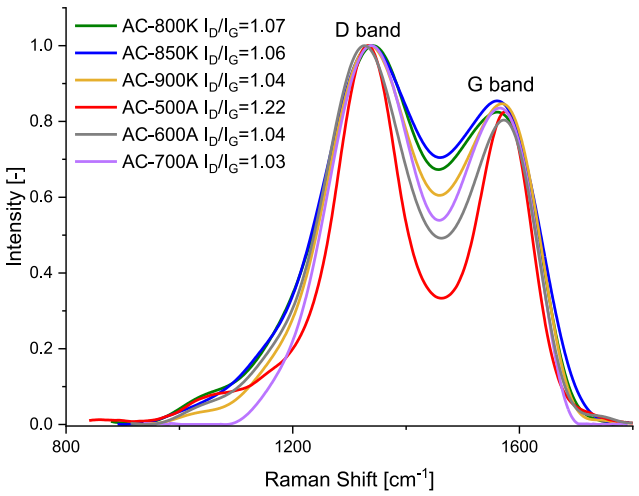

Fig. 8. Raman spectra of rCB/AC materials.

0.3–1 nm. Fig. 6 show PSDs based on CO_2 adsorption at 0 °C determined by using also the DFT method. All rCB/ACs obtained via chemical activation are distinguished by the presence of two distinct peaks that exhibit high intensity at pore diameters measuring approximately from 0.37 to 0.38 nm, and 0.49–0.59 nm. Additionally, AC-900K and AC-850K also exhibited higher pore volume within 0.87–0.91 and 0.61–0.64 nm. For physical activated AC samples, the predominant pore size in the AC-700A was determined to be between 0.44 and 0.64 nm, with a few single distinct peaks above 0.83 nm. The results of the study reveal that the use of potassium hydroxide and air during the activation process is particularly conducive to the formation of supermicropores (0.7–2 nm) and ultramicropores (<0.7 nm), indicating a high content level. In the AC-900K and AC-700A, pores with widths ranging from 0.7 to 2 nm accounted for the majority at 69% and 66% of the microporosity, while pores less than 0.7 nm wide constituted 31% and 34%, respectively. Conversely, they exhibit a relatively lower suitability for the creation of submicropores (<0.4 nm), which manifest a limited number of distinct peaks, however, quite high for the AC-900K.

3.3. Fourier-transform infrared spectroscopy (FT-IR)

Using Fourier transform infrared spectroscopy (FT-IR), the surface functional groups of rCB/ACs were analyzed. Fig. 7 illustrates the FT-IR spectra between 450 and 4000 cm^{-1}, revealing the diverse surface chemistry of the ACs. The FT-IR spectroscopy analysis indicate that the AC samples exhibit similar characteristic absorption peaks, with predominant vibrations observed in the range of 3550-3350 (O–H), 3000-2850 (C–H), 1700-1600 (C=C), 1400-1350 (C–H), 1100-1000 (C–O) cm^{-1}.

The occurrence of a broad band at 3450 cm^{-1} corresponds to the presence of an O–H stretching vibration in free hydroxyl groups on the carbon surface, which can be attributed to the effect of chemical and physical activation (Kajal and Singh, 2019). This vibration is commonly observed as a direct influence of intermolecular hydrogen bonding of chemical compounds, including alcohols, phenols, and carboxylic acids (Gonzalez et al., 2009). Furthermore, the two strong bands observed at within 3000-2850 and at 1380 cm^{-1} are related to the bending vibrations of the C–H bonds of alkanes groups (Talik et al., 2020), simultaneously providing information about the AC structure. Similarly, the band at 1650 cm^{-1} represents C=C stretching vibrations from aromatic rings frequently found in carbonaceous materials (Sricharoenchaikul et al., 2008). The infrared spectra of the ACs also present the occurrence of C–O stretching vibration appearing near the really broad peak region between 1100 and 1000 cm^{-1} (Xuguang, 2005).

The determined absorption bands in all samples were found to be located at comparable wavenumbers, suggesting a high degree of similarity in the functional groups. FTIR spectra indicated the presence of oxygen-containing surface functional groups (OCFG) that are extremely useful for CO_2 adsorption application purposes in flue gas purification. Taking into consideration the fact that OCFG are the most prevalent groups on carbon surfaces, the C–O and O–H bonds should be given a significant amount of focus. Especially, hydroxyl groups can enhance the interaction between CO_2 and the carbon surface through hydrogen bonding and are typically associated with increased CO_2 adsorption capacity (Yue et al., 2008). In overall, the surface reactivity and acidity/basicity of AC can be tremendously influenced by the presence of OCFG, thereby affecting its adsorption towards different gaseous adsorbates.

3.4. Raman spectroscopy

Raman spectroscopy is applied for the insights into the crystal structure of carbon-based materials, such as the degree of graphitization, or the presence of defects. Fig. 8 illustrates the Raman spectra of all activated carbon samples. The Raman spectra investigation of rCB/ACs revealed the existence of two distinct bands, located at approximately 1330 cm^{-1} (D-band) and 1590 cm^{-1} (G-band) wave numbers. These peaks in carbonized structures are referred to as the disordered (D) band and graphitic (G) band, according to the literature that has been widely published (Wang et al., 1990; Bhattacharjya et al., 2014). The D-band is commonly correlated with breaking of symmetry in sp^2 carbon caused by the structural defects and disorders in the carbon framework, leading to a reduction in the crystallographic symmetry of the quasi-infinite lattice (Brown et al., 2001). The precise nature of the vibrational mode responsible for the D-band arise from a breathing mode of the A_{1g} symmetry that involves the out-of-plane vibration of sp^3 carbon atoms (Li et al., 2020a; Irmer and Dorner-Reisel, 2005). While the G-band involves symmetric stretching of the C–C bonds and corresponds to first-order scattering of the stretching vibration mode (E_{2g}) reported for sp^2 hybridized carbon atoms in a hexagonal lattice of graphite layer (Mohan and Manoj, 2012; Han et al., 2012).

The intensity of peak D (I_D) reflects irregular crystal structures, whereas the intensity of peak G (I_G) expresses the regular crystal structures. Calculating the I_D/I_G ratio is essentially indicative of the proportionate number of defects in structure found in the graphene sheets of AC samples that have been synthesized. The I_D/I_G ratio values acquired for the rCB-based activated carbons exhibited a range of 1.037–1.223. Since the ID/IG ratio is more than 1, it indicates that there are a significant number of irregularities in AC crystal structures that can

Table 3
Ultimate analysis of rCB/ACs.

Sample	Yield content [wt.%]	C [wt. %]	H [wt. %]	N [wt. %]	S [wt. %]	O[a] [wt. %]
rCB	–	92.53	1.16	0.42	0.71	5.18
AC-800K	91.6	85.64	0.31	0.34	0.31	13.40
AC-850K	86.3	84.62	0.27	0.72	0.28	14.11
AC-900K	77.9	83.76	0.18	0.90	0.23	14.93
AC-500A	55.8	83.46	0.53	0.43	0.80	14.78
AC-600A	42.4	83.54	0.40	0.40	0.74	14.92
AC-700A	35.9	83.81	0.30	0.34	0.53	15.02

[a] It is obtained by calculation.

affect their physical and chemical properties. In general, higher crystallinity in materials can enhance CO_2 adsorption capacity due to improved stability and ordered arrangements, as well as the presence of well-defined pores or channels for CO_2 interaction (Nandi and Uyama, 2014). However, defects in crystalline materials, such as dislocations or vacancies, can also introduce additional adsorption sites, increasing the surface area available for CO_2 adsorption (Zhang et al., 2020). Both crystallinity and defects can influence CO_2 capture properties, with a balance between the two factors playing a crucial role in determining the overall adsorption performance. The higher increase in I_D/I_G is observed for physical activation, suggesting that it has resulted in the emergence of a greater number of defects in samples than utilizing KOH.

3.5. Ultimate and proximate analysis

The ultimate analysis (CHNS/O) of activated carbons at various activation temperatures is summarized in Table 3. The material in its pristine form showed a significant proportion of carbon (92.53 wt%) and a low content of other elements and ash (7.47 wt%), suggesting an astonishingly pure form of carbon. Chemically, the rCB/ACs produced using KOH generally exhibited a lower O content than those produced physically using air. The observed phenomenon can be attributed to the incorporation of oxygen-containing functional groups onto the surface of carbon. Moreover, the oxygen concentration of the ACs revealed a positive correlation with the activation temperature, whereby AC-900K demonstrates the highest value of 14.93 wt%. The determination of potassium content was also conducted using the XRF method. All samples of activated carbon by KOH contained small amounts of potassium, with concentrations not exceeding 0.09 wt%. The presence of K residues is likely to be attributed to their intercalation into the AC matrix and does not have a direct impact on CO_2 adsorption. On the other hand, physically activated carbons have contents ranging from 11.73 wt% to 33.92 wt%, with AC-700A possessing the highest record, likely due to significant oxidation during the activation process (Ahmadpour and Do, 1997). Additionally, physical activation with air resulted in sample degradation, which is a cause of the lowest carbon content that vaporizes while other minerals remain (Ogungbenro et al., 2018). In terms of other elements examined, AC-900K had the highest nitrogen content of 0.90 wt%. The sulphur content was very low (less than 1%) in all AC samples, indicating that no activation process introduced significant sulphur-containing functional groups, which can negatively impact the sorption performance of the material.

The determination of activated carbon yield typically involves calculating the weight of activated carbon obtained after the activation and washing processes, and then dividing it by the starting weight of the unprocessed raw material. The yield content was in the range of 88.6–77.9%, and 55.8–35.9%, for chemically and physically produced ACs, indicating the high influence of air on burning off carbon. This calculation is performed on a dry basis, as outlined below:

$$\text{Yield content}\,[\%] = \frac{m_P}{m_{RM}} \bullet 100 \quad (7)$$

Where: the variables m_P and m_{RM} represent the dry mass of the resulting AC (in grams) and the dry mass of the AC precursor (in grams).

Lastly, the proximate analysis results of the ACs are presented in Table 4. The volatile matter, fixed carbon, and ash content for all ACs samples varied within the range of 0.90–2.12, 86.50–89.90, and 9.45–12.60 wt%, respectively. The presented data indicates that the AC samples possess a comparatively high concentration of fixed carbon, making it suitable for various adsorption applications.

Table 4
Proximate analysis of rCB/ACs.

Sample	Volatile matter [wt.%]	Fixed carbon [wt.%]	Ash [wt.%]
rCB	0.56	91.12	8.32
AC-800K	1.86	88.34	9.80
AC-850K	2.04	87.07	10.89
AC-900K	2.12	86.64	11.24
AC-500A	0.75	89.80	9.45
AC-600A	0.70	88.94	10.36
AC-700A	0.90	86.50	12.60

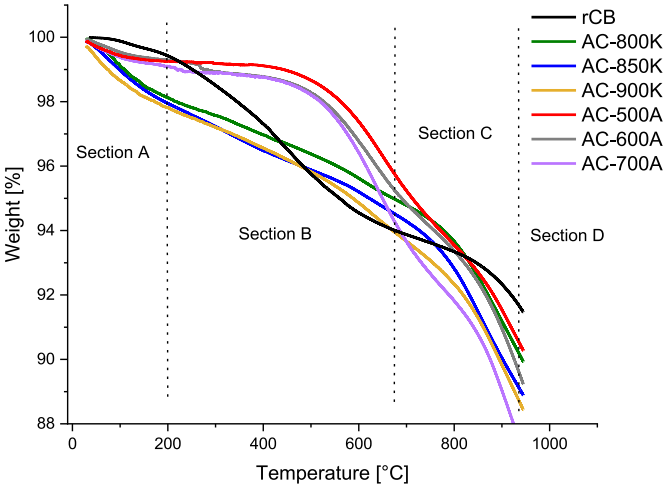

Fig. 9. Thermogravimetric analysis curves of rCB/AC samples.

3.6. Thermogravimetric analysis (TGA)

The thermogravimetric analysis (TGA) curves of activated carbons up to 950 °C are presented in Fig. 9, showing three inflection points defining four distinct ranges for mass loss. Upon activation by air, the samples exhibited a weight loss of 0.71% at temperatures up to 200 °C, 4.46% within the temperature range of 200–700 °C, and 5.60% at temperatures exceeding 700 °C. The activation process utilizing KOH resulted in losses, approximately of 2.05%, 3.66%, and 5.34% wt. for temperatures below 200 °C, ranging from 200 to 700 °C, and higher than 700 °C, respectively.

The shape of the TGA profile is contingent upon the thermal behavior of the precursor, which is intrinsically linked to the chemical composition and chemical bonding present within the material structure. The reduction in mass in Section A can be attributed to the elimination of moisture or highly volatile compounds. Their removal is highly important, as it affects its physical and chemical properties, such as porosity and surface area (Sait et al., 2012). Furthermore, the substantial decrease in weight observed in Section B implies the removing of mineral matters along with the inorganic residues of ACs (Devi and Saroha, 2015), especially for physical activated samples, where the TGA curve

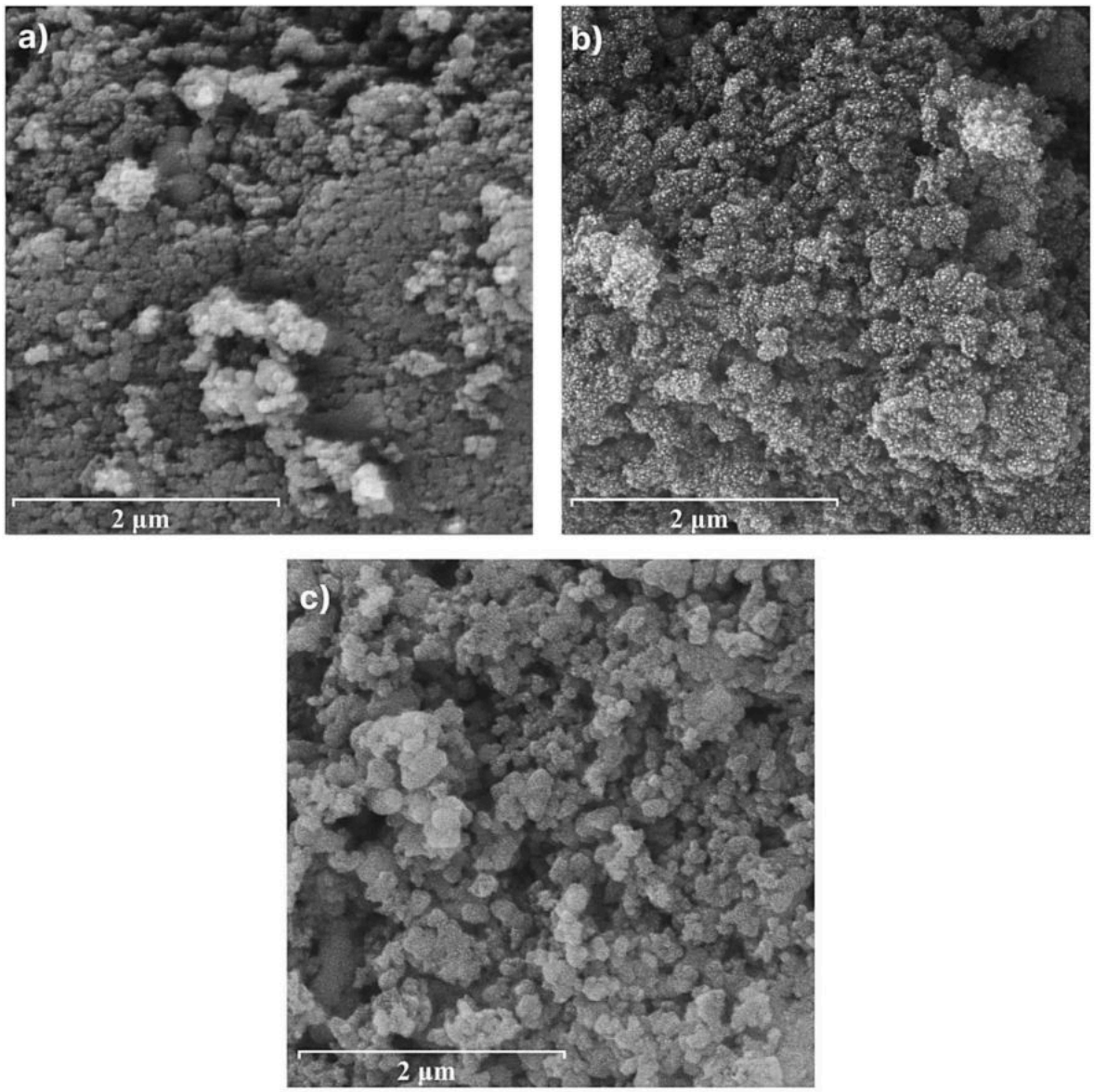

Fig. 10. SEM micrographs with a magnification of 52,000X at a resolution of 2 µm for (a) AC-700A, (b) AC-900K, and (c) recovered carbon black.

drastically decreased between 500 and 700 °C by more than 4.56%. In the third region (Section C), the gradual drop in the TGA curve indicates the combustion of the AC samples (Thonglhueng et al., 2022). The weight loss percentage in this section is relatively low, indicating that ACs have a high degree of purity and thermal stability in higher temperatures. The thermal gravimetric analysis (TGA) curve presented in this section can provide insight into the extent of carbonization of activated carbon and the thermal robustness of the recovered carbon black. Finally, in the fourth region (Section D), a small amount of ash residue (6–7%) was observed, suggesting the presence of inorganic components in samples after complete combustion at 930 °C.

3.7. Scanning electron microscopy (SEM) with energy-dispersive X-ray spectroscopy analysis (EDS)

Scanning electron microscopy with an energy-dispersive X-ray spectroscopy technique was applied to indicate details on the morphology and identify elements present on the surface of ACs along with their relative abundance. Fig. 10 presents the morphology with a magnification of 52,000X at a resolution of 2 µm for AC-700A and AC-900K that showed the most prominent textural properties, compared to the pristine recovered carbon black. In addition, more SEM images with varying magnification levels (ranging from 1000 to 7,000X) obtained at 20 µm and 100 µm, are given in Figure S2.

The complexity of activated carbons, in terms of composition and structure, surpasses that of rCB derived from waste tire pyrolysis. Based on SEM micrographs of synthesized ACs, the presence of porous and highly complex irregular structures differing in size and shape was confirmed, demonstrating a significant surface area beneficial to adsorption. The size, form, and surface attachments of the ACs are highly varied as a direct result of the elevated activation temperature effects. The ACs structure consisted of aggregates and agglomerates characterized by predominantly different-structured particles, while the macropores were dimly observable. Moreover, the observation of aggregates and agglomerates implies that the distribution of AC particles is non-uniform and instead forms clusters or larger groups, which may have an impact on the material's overall porous characteristics (Sun et al., 2016). Whereby, the particles do not possess constant shapes but instead exhibit variations and irregularities in their morphology, spherical or ellipsoidal in appearance (Fig. 11).

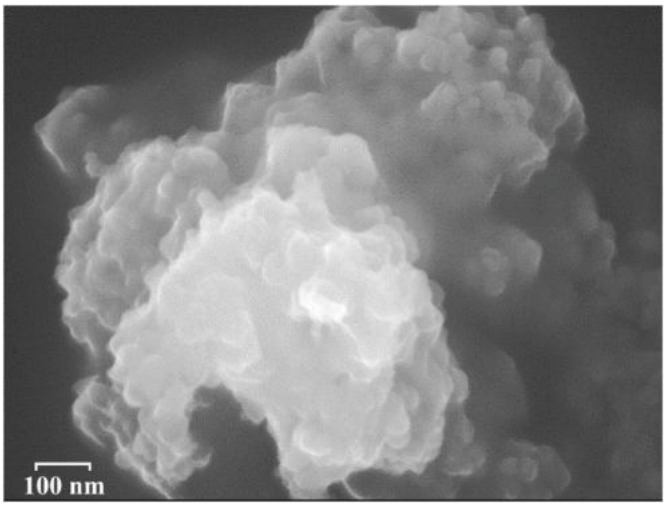

Fig. 11. SEM micrographs with a magnification of 50,000X at a resolution of 100 nm for rCB/ACs clusters.

s. The potential morphological changes occurring during the production of ACs based on recovered carbon black are schematically presented in Fig. 12.

Further, the EDS analysis has verified the atomic percentage of each composition in the sample. The element mapping images for AC-900K micrograph with a magnification of 7,000X at a resolution of 2 μm are depicted in Fig. 13(a–g). They demonstrate that the surface architecture of AC-900K predominantly comprises of carbon (C), oxygen (O) and potassium (K). Additionally, K residue compound refers to leftover potassium compounds from KOH, thus providing further confirmation that it may still be present in the activated carbon product, as was proved in elemental analysis. In contrast, the surface of activated carbon produced by physical activation using air (AC-700A) consists mainly of C, O, given in Fig. 14(a–g). Additionally, the small presence of silicon (Si), aluminum (Al), magnesium (Mg), and sulphur (S) was found, suggesting that additives may have been present in the initial recovered carbon black material, as highlighted in Section 2.1.

3.8. CO_2 adsorption investigation

The most promising samples from each activation type set were measured at four distinct temperatures, 0 °C, 15 °C, 25 °C and 30 °C under a pressure of 1 bar. As can be observed from the empirical data presented in Fig. 15, all curves exhibit an upward convex shape, which aligns with the Type-I (b) classification as defined by the International Union of Pure and Applied Chemistry (IUPAC) (Merin et al., 2021). Furthermore, the isotherm system indicates that the process was facile at low concentrations of CO_2, where a considerable proportion of the adsorption sites remain unoccupied by the gaseous molecules. Therefore, as the pressure increases, serving as the driving force, it led to an increase in the surface coverage of AC by intensifying CO_2 particles accumulation (Raganati et al., 2014). On the other hand, a rise in temperature caused a boost of the diffusion rate due to the heightened energy of gas molecules and also triggers instability of the adsorbed gas on the adsorbent surface, resulting in lower CO_2 adsorption capacities and making the process thermodynamically favorable at reduced temperatures. Gas molecules that are adsorbed possessed adequate energy to surpass the attractive forces present across the surface, thereby disrupting the surface bonds and relocating back into the gas phase, corresponding to the exothermic characteristic of adsorption (David and Kopac, 2014). Hence, it can be concluded that the process of CO_2 adsorption onto carbon-black derived activated carbons was primarily influenced by physisorption, which is driven by weak van der Waals forces that diminish as the temperature elevates. This statement is consistent with the principles outlined by Le Chatelier (Hendricks, 1941).

The AC-900K sample exhibited the highest CO_2 uptake of 30.90 cm^3/g under a pressure of 1 bar at 0 °C, possessing exceptional gas capture attributes comparable to commercial activated carbons. At temperatures of 15 °C, 25 °C and 30 °C, the CO_2 adsorption capacity was measured to

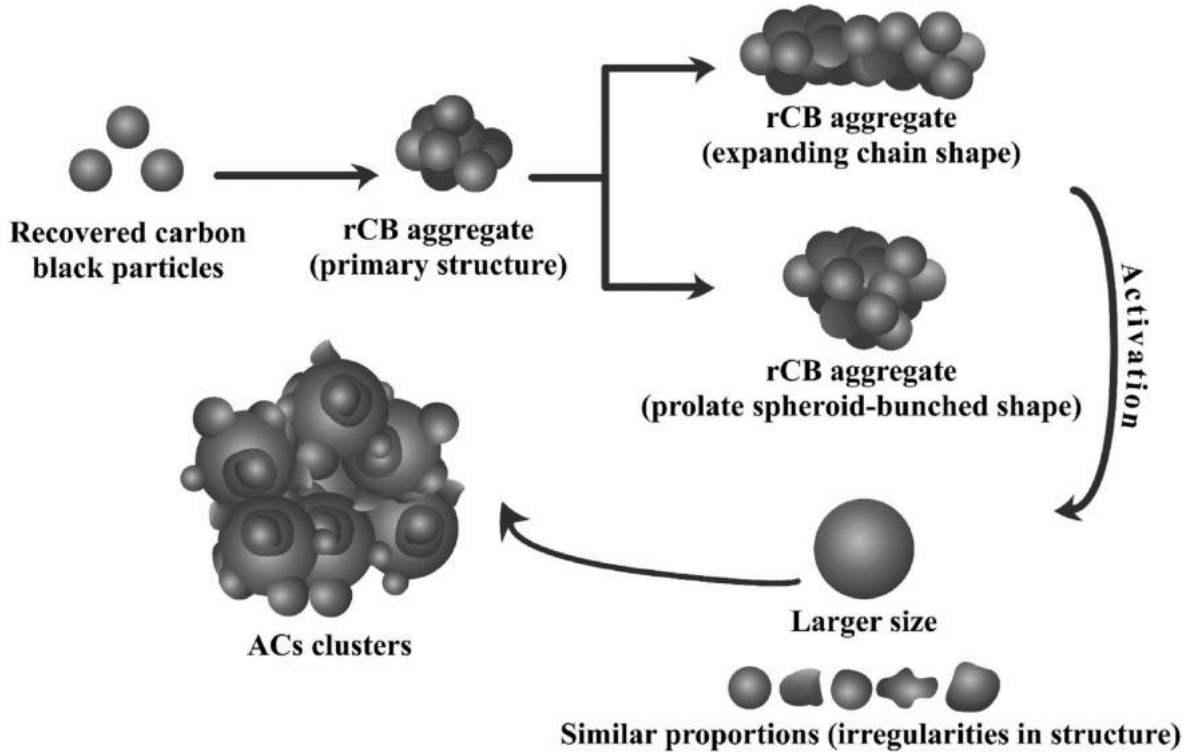

Fig. 12. Morphological changes of particles that occur during the activation process of recovered carbon black to activated carbons.

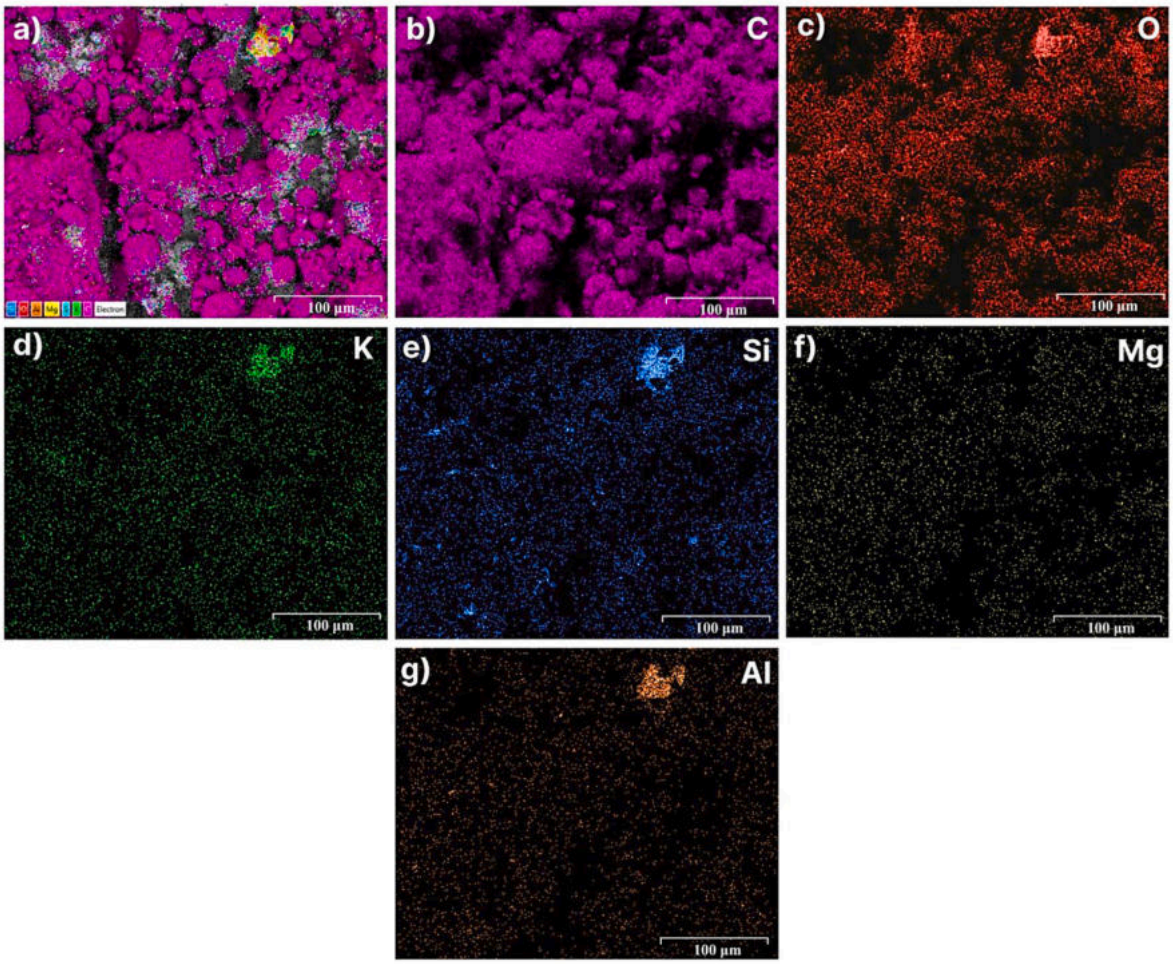

Fig. 13. Energy-dispersive X-ray spectroscopy analysis (EDS) of the AC-900K. (a) representative EDS image, and corresponding elemental mapping analysis: (b) C, (c) O, (d) K, (e) Si, (f) Mg, (g), Al.

be 24.75, 20.53, and 19.73 cm^3/g at the same pressure conditions. On the contrary, the AC-700A demonstrated a CO_2 adsorption capacity ranging from 14.79 to 22.56 cm^3/g at four temperatures under the pressure of 1 bar. Furthermore, for the rest of the samples obtained by chemical and physical activation CO_2 capacities were in the range of 22.39–15.99 cm^3/g at 0 °C, in the following order: AC-700A > AC-600A > AC-850K > AC-800K > AC-500A. It confirms that the optimal temperature for activation, with respect to CO_2 adsorption, was found to be 900 °C and 700 °C for potassium hydroxide and air, as activating agents.

Table 5 presents a summary of the findings obtained from CO_2 adsorption on activated carbons that were previously reported in the literature. The CO_2 uptake of recovered carbon black achieved in this work remain potentially competitive compared to other industrial byproducts, but they may not outperform ACs derived directly from biomass waste. As such, more research needs to focus their efforts and resources on exploring and harnessing the potential of rCB as a valuable resource for developing effective CO_2 adsorption solutions.

3.8.1. *Influence of textural parameters on CO_2 adsorption*

Additionally, to fully examine the correlation of adsorption with regard to textural properties, the dependance of all ACs obtained from rCB for CO_2 capture was evaluated at 0 °C. In order to achieve this objective, we ascertained the correlation between the adsorption of CO_2 and various textural parameters, namely the overall BET surface area (Fig. 16a), the total pore volume (Fig. 16b), the micropore volume with a width of <2 nm determined by the N_2 isotherm (Fig. 16c), and finally the volume of micropores with a width range below 1 nm determined by the CO_2 isotherm (Fig. 16d). The statistical measure known as the coefficient of determination (R^2) serves as a valuable tool to quantify the extent to which the independent variable can forecast the variance in the dependent variable (Wei et al., 2018). By analyzing the R^2 values, conclusions can be drawn about the influence of the texture characteristics on CO_2 adsorption. A high R^2 signifies a robust correlation, implying that the aforementioned factors have a notable impact on forecasting or elucidating the fluctuations in CO_2 adsorption. On the contrary, a diminishing R^2 value signifies a lack of relationship, thereby indicating its marginal impact on the observed variations (Burner et al., 2020).

The unambiguous interpretation of the coefficient of determination values was not readily apparent from the results of the examination due to its high values above 0.9. It may imply that the explication of the R^2 coefficients may not be straightforward. The analysis reveals that the R^2 values for chemical activation were the highest when examining the correlation between CO_2 uptake and the total pore volume or micropore volume determined by using CO_2 at 0 °C, suggesting that CO_2 adsorption mechanism was conditioned by them. Specifically, the R^2 values were equal to 0.946 and 0.940. For physical activation, adsorption mechanism was identified in relation to the specific surface area and micropore volume (determined through nitrogen adsorption) with the most significant values of the R^2 correlation coefficient, reaching 0.995 and 0.999. In summary, the analysis suggests that CO_2 sorption may be influenced by distinct factors associated with different activation methods. However, due to the high R^2 values, further analysis and interpretation may be necessary to fully understand the relationship

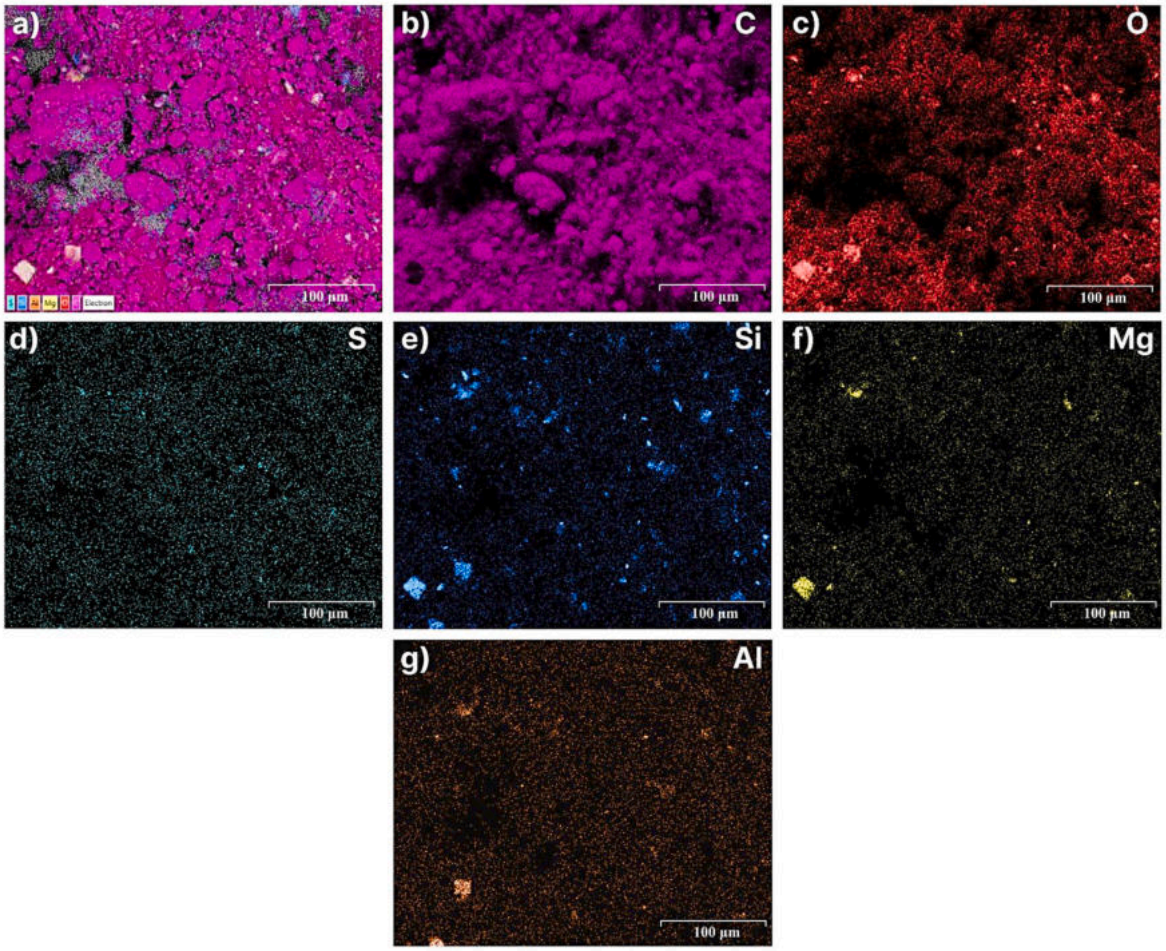

Fig. 14. Energy-dispersive X-ray spectroscopy analysis (EDS) of the AC-700A. (a) representative EDS image, and corresponding elemental mapping analysis: (b) C, (c) O.

between the independent variables and CO_2 capture in this context. Many studies reported similar cases (Serafin et al., 2022a, 2022b; Grundy and Ye, 2014), which would require evaluating especially the dependence of the R^2 on cumulative micropore volumes for particular pore diameter regions.

Fig. 17 illustrates the connection of coefficient of determination (R^2) in relation to the cumulative micropore volume within a specific range of pore width, ranging from 0.3 to 2 nm with a 0.1 nm increment (at 0 °C and up to 1 bar). The obtained results indicate that a pore micropores volumes varying from 0.30 to 0.40 nm exhibit the highest R^2 with an impressive value of 0.999, indicating an exceptionally strong positive correlation between CO_2 adsorption for each activation approach. Additionally, several three distinct pore ranges also demonstrate notable R^2 values (>0.9), specifically 0.6–0.7 nm, 0.7–0.8 nm, and 0.8–0.9 nm, for chemical activation. Regarding physical activation, the coefficient of determination demonstrated a comparable pattern within the corresponding pore range, such as: 0.4–0.5 nm, and 0.6–0.7 nm. The above observations mainly emphasize the significance of submicropores (<0.4 nm), ultramicropores (<0.7 nm) during CO_2 capture, thereby underscoring their vital function in the adsorption mechanism of rCB/ACs, which is schematically presented in Fig. 18.

3.8.2. *Isotherm modeling studies*

The application of mathematical isotherm modeling has been extensively used in order to elucidate the underlying fundamental mechanism involved in CO_2 capture process (Serafin and Dziejarski, 2023; Jagiello and Olivier, 2013; Jagiello et al., 2019a, 2019b). In this instance, five distinct three-parameter isotherms were selected based on their proven ability to accurately predict CO_2 adsorption, namely Toth, combined Freundlich-Langmuir, Sips, Redlich-Peterson, and Radke-Prausnitz.

A non-linear regression analysis was employed to model the CO_2 adsorption isotherms at 0, 5, 25 and 30 °C for the two samples that exhibited the superior CO_2 uptakes (AC-700A and AC-900K). To compare and contrast the precision of various equations, each model has been evaluated with the aim of minimizing an objective error function - the sum of absolute errors (EABS). The statistical procedure facilitated the identification of the isotherm model that displayed the lowest EABS values, indicating the minimized variance of distribution between the empirical and modelled data. The outcomes related to CO_2 adsorption on rCB/ACs are graphically shown in Fig. 19.

The study determined that the Freundlich-Langmuir equation is a dependable method for predicting CO_2 adsorption mechanism at four different temperatures for AC-900K. This conclusion was based on the observation of the smallest EABS obtained for all four CO_2-AC adsorption systems, ranging from 1.3965 to 4.393. Regarding the physically activated sample, specifically AC-700A, the most suitable model that correlated significantly effective with the experimental equilibrium adsorption data was the Redlich-Peterson, with EABS values that varied between 0.419 and 0.613. Furthermore, based on the maximum error functions observed in each dataset, it can be inferred that the Toth (EABS: 2.032–11.728), Sips (EABS: 2.5441–2.9349) equations are inadequate in providing a precise representation of the CO_2 sorption mechanism observed for AC-900K and AC-700A, respectively. To

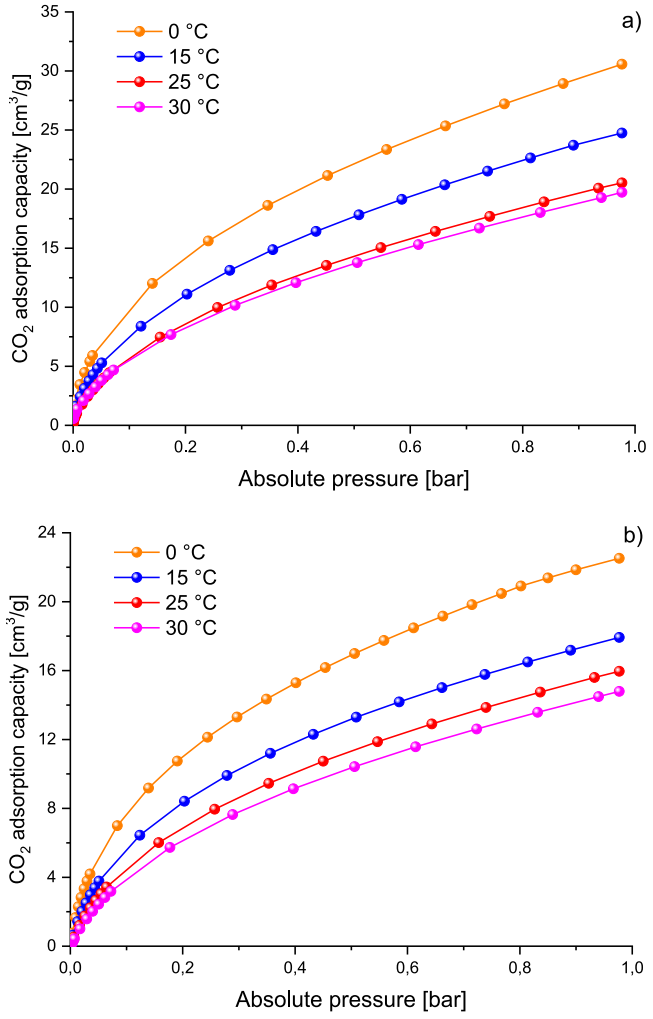

Fig. 15. The CO_2 adsorption isotherms at temperature of 0 °C, 15 °C, 25 °C, and 30 °C on (a) AC-900K and (b) AC-700A.

compare and contrast the fitting of the curves of the chosen isothermal models, their runs are shown for CO_2 adsorption in Figure S3.

The parameters of isotherm models that describe the best fit to the equilibrium CO_2 adsorption data for AC-900K and AC-700A are presented in Table 6. For the rest of the models all data is included in Table S1 and Table S2.

The interpretation of parameters for the most suitable models is another crucial step in accurately understanding the nature of adsorption on rCB/ACs surface. According to the Freundlich-Langmuir equation, it has been observed that an increase in sorption temperature leads to a reduction in the maximum adsorption capacity (q_m). Specifically, the q_m values decline from 418.0 cm^3/g at 0 °C to 114.5 cm^3/g at 30 °C. On the contrary, the K_{FL} constant exhibits a rise along with the temperature, confirming the exothermic nature of the CO_2 capture process. Moreover, for all CO_2-rCB/ACs systems, parameter n_{FL} is consistently lower than 1, which corresponds with the surface heterogeneity characteristic of ACs. With respect to the sample AC-700A, K_{RP} constant and the α_{RP} parameter of the Redlich-Peterson model demonstrate a similar correlation with the temperature as well as for the AC-900K. At 0 °C K_{RP} and α_{RP} are 300.9 $cm^3\ g^{-1}{\cdot}bar^{-1}$ and 12.16 $bar^{-\beta RP}$, while at 30 °C their values are reduced to 86.6 $cm^3\ g^{-1}{\cdot}bar^{-1}$ and 4.8 $bar^{-\beta RP}$, respectively. Finally, the β_{RP} exponent is almost constant throughout the range of 0.59–0.62, also indicating the adsorption on energetically heterogeneous surface.

Table 5
Comparison of CO_2 uptake of ACs derived from various waste at 1 bar and 25 °C for 100 vol% CO_2 feed.

AC precursor	Activation approach	CO_2 uptake (cm^3/g)	Reference
Global industrial waste			
Fly ash	KOH activation	13.44	Alhamed et al. (2015)
Polyacrylonitrile	KOH activation	17.02	Bai et al. (2015)
PET bottles	KOH activation	24.42	Arenillas et al. (2005)
Packaging waste	KOH activation	94.98	Idrees et al. (2018)
Charcoal	–	26.88	Lahuri et al. (2020)
Recovered carbon black	Air activation	16.00	This work
Recovered carbon black	KOH activation	20.53	This work
Biomass waste			
Rice husk	KOH activation	83.10	Li et al. (2015)
Palm shell charcoal	Steam activation	9.16	Khalil et al. (2012)
Rice husk	$ZnCl_2$ activation	29.12	Boonpoke et al. (2011)
Whitewood	Steam activation	30.01	Shahkarami et al. (2015)
Soybean factory waste	$ZnCl_2$ with CO_2 activation	20.83	Thote et al. (2010)
Common polypody	KOH activation	127.01	Serafin et al. (2022a)
Walnut shell	KOH activation	115.81	Serafin et al. (2023b)
Argan fruit shell	KOH activation	126.11	Boujibar et al. (2018)
Bee-collected pollen	KOH activation	72.71	Choi et al. (2019)
Empty fruit bunch	KOH activation	83.10	Parshetti et al. (2015)
Starch	KOH activation	86.02	Alabadi et al. (2015)

3.8.3. Thermodynamic analysis

Besides of the modeling of isotherms, it is crucial to examine the thermodynamic aspects of the interaction between AC and CO_2. The aim of this study was to gain a comprehensive understanding of the thermodynamic processes involved in the adsorption of CO_2 on activated carbon in a state of equilibrium. To verify the assumptions obtained from the analyzed isotherm models, changes in the Gibbs free energy (ΔG°), enthalpy (ΔH°), and entropy (ΔS°) of adsorption were identified. ΔH° and ΔS° were calculated from the van't Hoff equation in the form of a linear relationship ($\ln(K_L)$ vs 1/T), as follows:

$$ln(K_L) = \frac{\Delta S^\circ}{R} - \frac{\Delta H^\circ}{RT} \quad (8)$$

where R is the universal gas constant (8.314 J/mol·K), K_L is the Langmuir adsorption constant that has been utilized as the conventional thermodynamic equilibrium indicator for the computation of thermodynamic parameters [1/bar], and T is absolute temperature [K].

Whereas ΔG° was estimated from the below equation by using Langmuir constant:

$$\Delta G^\circ = -RT\ ln(K_L) \quad (9)$$

Table 7 presents the thermodynamic parameters that were derived from Eq. (7) and Eq. (8). The analysis of their values reveals that changes in standard free entropy and enthalpy remain unaffected by variations in the adsorption temperature. Furthermore, their negative numerical values ($\Delta S^\circ<0$, $\Delta H^\circ<0$) indicate a reduction in disorder and randomness of the CO_2-rCB/AC system and the degree of freedom of CO_2, along with the exothermic nature of adsorption (Abel et al., 2020; Abunowara et al., 2023). This can be attributed to the formation of attractive forces between the rCB/AC surface and CO_2 molecules, leading to their accumulation. In addition, the standard enthalpy change is less than 40 kJ/mol, which suggest physisorption (Ashraf et al., 2022), confirming

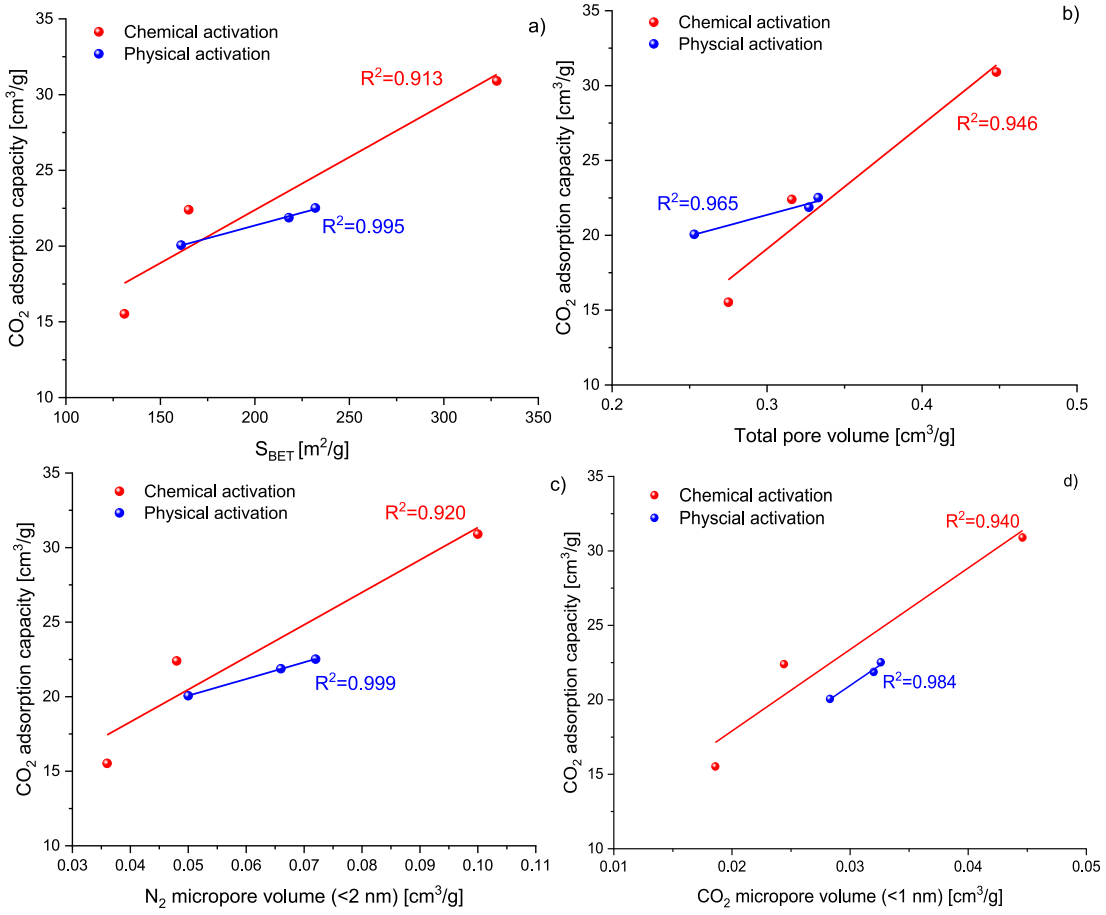

Fig. 16. CO_2 adsorption uptake at 0 °C up to 1 bar as a function of (a) BET surface area (b) total pore volume (c) N_2 micropore volume <2 nm and (d) CO_2 micropore volume <1 nm.

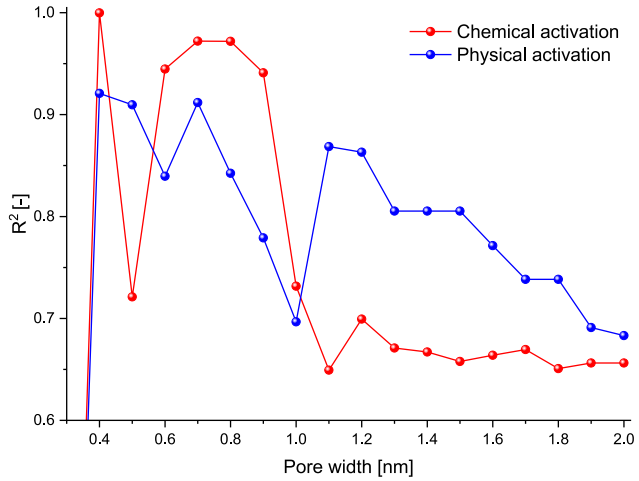

Fig. 17. Relationship between the coefficient of determination and cumulative pore volume within the range of 0.3–2 nm, at 0 °C under a pressure of 1 bar.

the assumptions of the isotherm models. The spontaneous character of the process may also be deduced from the fact that the change in ΔG° exhibits negative values. The estimation of ΔG° via Eq. (8) yields insights into the increased favorable binding of CO_2 molecules at lower temperatures, as a reduction in the negative value of ΔG° is observed as the temperature increases (Du et al., 2021). The performed thermodynamic analysis validated prior findings regarding the characteristics of adsorption. Specifically, it showed that high temperatures lead to a reduction in the strength of the bonds between the adsorbate and the adsorbent, which consequently causes the desorption of the CO_2 molecules. When comparing thermodynamic parameters for physically and chemically activated carbons, the results suggest that the adsorption process is more energetically and entropically favorable for AC-900K than AC-700A.

Furthermore, the fundamental focus of thermodynamic investigation related to surface phenomena involves the mathematical representation of isosteric heat of adsorption. This particular variable serves as a clear indicator of interaction strength between adsorbate and the adsorbent surface, referring to the thermal energy produced during the CO_2 capture process (Serafin et al., 2019), as given by the Clausius-Clapeyron equation:

$$Q_{st} = -R\left(\frac{\partial(\ln(p))}{\partial\left(\frac{1}{T}\right)}\right)_{\theta} \tag{10}$$

where: p is the partial pressure of the CO_2 at equilibrium state [bar], T is absolute temperature [K], R is the ideal gas constant [J/mol·K], Q_{st} denotes isosteric heat of adsorption [J/mol], and θ indicates a specific surface coverage [-].

The pressure values for the specified surface covering degree have been determined using the rearranged Langmuir-Freundlich isotherm equation for AC-900K that efficiently characterized the CO_2 adsorption

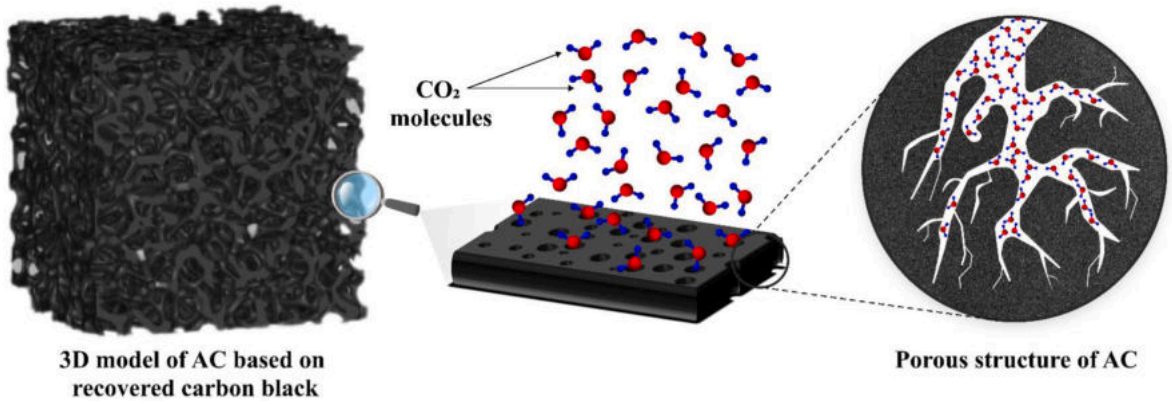

Fig. 18. A schematic representation of the CO_2 adsorption mechanism on AC based on recovered carbon black.

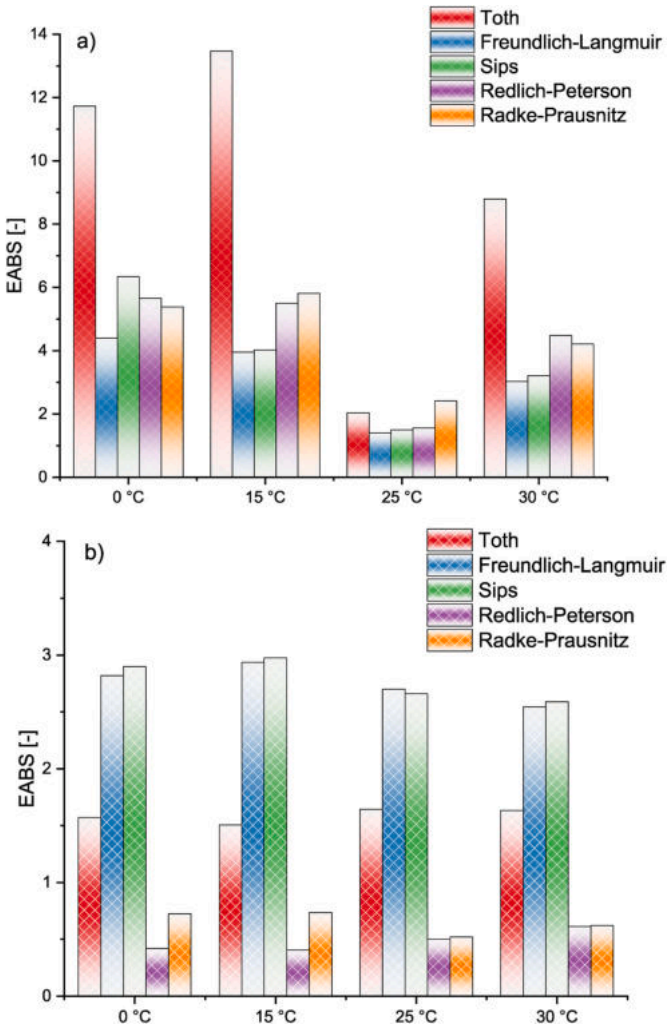

Fig. 19. Summarization of EABS values obtained through data fitting of chosen isotherm models by non-linear regression for (a) AC-900K and (b) AC-700A.

process:

$$p(n) = \sqrt[n_{FL}]{\frac{q_e}{q_m \bullet K_{FL} - q_e \bullet K_{FL}}} \quad (11)$$

The same approach was also applied for AC-700A by implementing the Redlich-Peterson isotherm model.

Finally, thirty points of CO_2 adsorbed amount were used to determine the absolute pressure at each temperature and then to calculate the slope of the straight lines from the data sets of ln(p) versus T^{-1}. The isosteric heat of adsorption as a function of surface coverage (θ) on ACs is presented in Fig. 20.

Table 6
Parameters for the best fitted isotherm model to the experimental data.

Temperature	0 °C	15 °C	25 °C	30 °C
Model	Freundlich-Langmuir[a]			
q_m [cm^3/g]	418.020	232.930	115.947	114.500
K_{FL} [bar $^{-nFL}$]	0.0799	0.121	0.207	0.218
n_{FL} [-]	0.511	0.556	0.630	0.603
Model	**Redlich-Peterson[b]**			
K_{RP} [$cm^3 \cdot g^{-1} \cdot bar^{-1}$]	300.937	172.845	116.110	86.5821
α_{RP} [bar $^{-\beta RP}$]	12.156	8.552	6.194	4.789
β_{RP} [-]	0.622	0.622	0.594	0.596

[a] The best fitted isotherm model for AC-900K.
[b] The best fitted isotherm model for AC-700A.

The range of isosteric heat of adsorption was found to be within the range of 15.19–27.51 kJ/mol and 22.28–36.81 kJ/mol in relation to the total surface coverage for AC-700A and AC-900K, respectively. These data provide solid confirmation that the CO_2 sorption occurring in activated carbons is of a physical nature that is controlled by relatively weak van der Waals forces. Physical adsorption has a modest Q_{st}, which differs from 20 to 40 kJ/mol, while the heat of chemisorption generally falls into the range of 80–200 kJ/mol (Li et al., 2020b). Comparable outcomes have been attained by Tang et al. (2023) and Guo et al. (2020).

Additionally, according to reported research, it has been determined that easily regenerable solid sorbents used for CO_2 capture application must exhibit a preferable heat of adsorption that falls between 26 and 31 kJ/mol for a 20% partial pressure CO_2 flue gas and 22–28 kJ/mol for single-component CO_2 streams (Mert et al., 2023). The present study shows that the isosteric heat of the CO_2 adsorption values of activated carbons meets these specified criteria. Further, the obtained results indicate that there is a significant increase in Qst values at a lower surface coverage, followed by a gradual decline along with a higher degree of surface coverage. There are several possible reasons for this phenomenon, including cooperative effects (Nazir et al., 2021), molecular rearrangement (Guclu et al., 2021), or, especially, the saturation effect. Initially, at lower θ the active adsorption sites are available and it is easier for the CO_2 molecules to interact with these sites, which results in higher adsorbent-adsorbate interactions and thus higher Qst values. Therefore, as the surface coverage of the AC increases, the available strong adsorption sites become progressively occupied, leading to a decrease in the strength of interaction between CO_2 molecules and the remaining vacant sites on the surface.

Table 7
Thermodynamic parameters of CO_2 adsorption.

	AC-900K			AC-700A		
T [°C]	ΔG^0 [kJ/mol]	ΔS^0 [kJ/mol·K]	ΔH^0 [kJ/mol]	ΔG^0 [kJ/mol]	ΔS^0 [kJ/mol·K]	ΔH^0 [kJ/mol]
0	−2.027	−0.0240	−8.626	−2.534	−0.0365	−12.540
15	−1.772			−2.136		
25	−1.601			−1.736		
30	−1.209			−1.387		

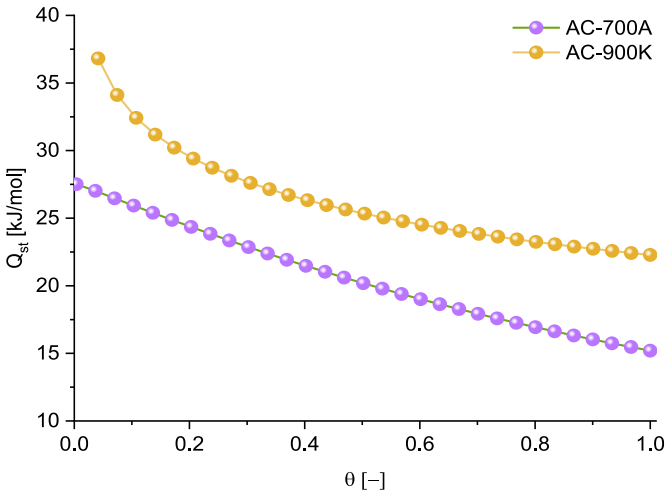

Fig. 20. The isosteric heat of adsorption as a function of surface coverage for AC-900K and AC-700A.

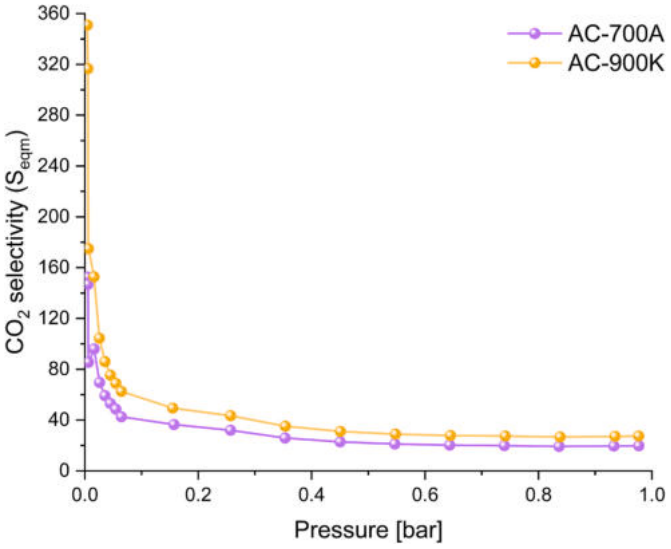

Fig. 21. IAST selectivity for CO_2 over N_2 at 25 °C for a CO_2/N_2 binary mixture.

3.8.4. *Insights into CO_2/N_2 selectivity*

Selectivity adsorption of CO_2 over N_2 is an important factor that should be considered, when assessing adsorbents for the purpose of CO_2 removal from flue gas in carbon capture technologies. Hence, the AC-700A and AC-900K samples, exhibiting the highest CO_2 adsorption capacity, were subjected to nitrogen adsorption measurement at a temperature of 25 °C and a pressure of 1 bar. The results of N_2 adsorption studies are shown in Figure S4.

The Myers and Prausnitz's ideal adsorbed solution theory (IAST) (Gharagheizi and Sholl, 2021) is a commonly employed method for the estimation of adsorption selectivity and mixed-gas adsorption isotherms based on pure-component isotherms. This approach has been found to yield accurate results for a diverse range of systems. The present study utilized IAST to forecast the selectivity of CO_2 over N_2 by relying on the individual adsorption isotherms of these gases

$$S_{IAST} = \frac{q_{CO_2(p)}}{q_{N_2(p)}} \bullet \frac{p_{N_2}}{p_{CO_2}} \tag{12}$$

where: S_{IAST} is the selectivity coefficient, $q_{CO2(p)}$ and $q_{N2(p)}$ refer to the uptake of specific gas [cm^3/g], p_{N2} and p_{CO2} are the partial pressure in the mixture.

Therefore, the selectivity for an equimolar CO_2 and N_2 binary mixture ($S_{IAST(EQM)}$) was analyzed, with equation (11) being expressed as follows:

$$S_{IAST(EQM)} = \frac{q_{CO_{2(p)}}}{q_{N_{2(p)}}} \tag{13}$$

where: $q_{i(p)}$ is the adsorption capacity [cm^3/g] at the same partial pressure p of CO_2 and N_2.

Further, it is of great significance to evaluate the selectivity with regards to flue gas compositions that correspond to those discharged directly from the industrial sector. It is widely acknowledged that the flue gases generated by the most established CO_2 capture technique, namely post-combustion capture, generally comprise approximately 10–15% CO_2 and 75–80% N_2, in addition to other gases including oxygen, carbon monoxide, and sulphur dioxide. Therefore, selectivity for flue gas composition ($S_{IAST(FG)}$) equals 15% CO_2 and 85% N_2 was calculated also based on IAST method using the below equation:

$$S_{IAST(FG)} = \frac{q_{CO_2@0.15\ bar}}{q_{N_2@0.85\ bar}} \bullet \frac{0.85}{0.15} \tag{14}$$

where: $q_{i@jbar}$ is the adsorption capacity [cm^3/g] of CO_2 and N_2 at the partial pressure of 0.15 and 0.85 respectively.

Fig. 21 presents selectivity calculated using single component gas adsorption capacity for equimolar CO_2 and N_2 binary mixture. The selectivity ratio of CO_2 to N_2 was observed to decrease at a pressure of approximately 0.08 bar for the two activated carbon samples. The highest CO_2/N_2 selectivity coefficient at 0.001 bar was 164.80 and 350.91 for AC-700A and AC-900K. Subsequently, as the pressure increased, the selectivity coefficient exhibited a decreasing trend, ultimately attaining values of 19.77 and 27.39 at a pressure of 1 bar. In the case of a gaseous mixture comprising 15% CO_2 and 85% N_2, the CO_2/N_2 selectivity achieved 59.70 and 44.51 at a pressure of 1 bar, for AC-900K and AC-700A. The obtained values are significantly higher than those described in the literature (Serafin et al., 2022a).

3.8.5. *Cyclic regeneration stability*

The regeneration capacity of ACs is a significant aspect in determining the efficacy as an adsorbent material, directly influencing its lifespan and the overall economic feasibility of CO_2 capture process. This characteristic pertains to the inherent capability of ACs to undergo many adsorption-desorption regeneration cycles and regain its initial adsorption capacity subsequent to being fully saturated with adsorbate. Therefore, the stability potential of the AC-900K and AC-700A was evaluated by performing 1 st, 5 th, and 10 th adsorption-desorption runs

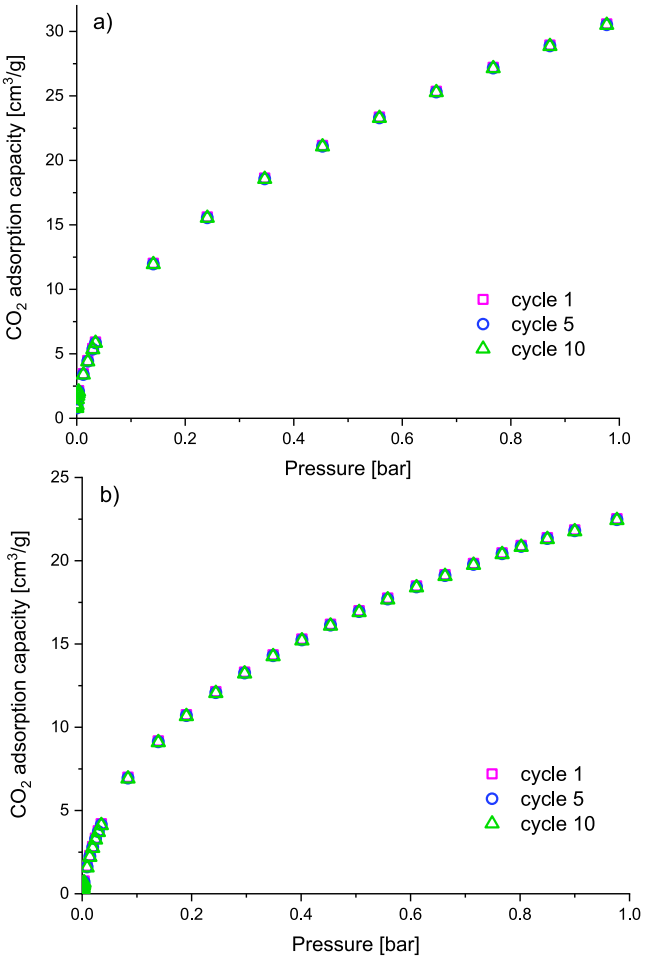

Fig. 22. CO_2 capture performance for (a) AC-900K -and (b) AC-700A at 0 °C in 1st, 5th, and 10th adsorption-desorption cycle.

at a temperature of 0 °C (Fig. 22). After a total of ten cycles, there were no observable differences in the CO_2 uptake performance. The maximum value of the standard deviation equaled 0.09, proving that rCB/ACs exhibits exceptional stability as a solid CO_2 adsorbent.

4. Conclusions

In this work, the high-value-added ACs derived from tailor-made rCB obtained through commercial-scale ELTs pyrolysis for CO_2 capture application have been characterized and reported for the first time in the literature.

The chemically activated carbon material via KOH at 900 °C (AC-900K) among all samples exhibited a notable development in specific surface area, total pore volume, and micropore volume compared to the pristine material that were found to be 328 m^2/g, 0.448 cm^3/g, and 0.100 cm^3/g, respectively. Furthermore, the AC-900K revealed a competitive CO_2 adsorption capacity to other ACs derived from industrial waste, with values of 30.90 cm^3/g at 0 °C and 20.53 cm^3/g at 25 °C under 1 bar, accordingly. The investigation of the CO_2 adsorption mechanism revealed that Freundlich-Langmuir and Redlich-Peterson models demonstrate a high degree of precision in predicting the adsorption behaviors of CO_2 on the AC surface, thus confirming the occurrence of multilayer sorption on the heterogeneous surface. The isosteric heat of adsorption was determined, resulting values suggest favorable application of those materials in CO_2 capture. Additionally, the selectivity of CO_2/N_2 was relatively high, achieving 350.91 and 59.70 for the binary mixture and composition of flue gases commonly encountered in post-combustion capture technology, respectively. Ultimately, rCB/ACs showed the superior cyclic regeneration over 10th cycles.

In general, this study investigates the potential for recycling rCB directly obtained from the industrial-scale pyrolysis of ELTs, which yields a valuable product in the form of ACs. While the CO_2 uptake of the prepared rCB/ACs may be limited to biomass-based ones, they exhibit performance comparable to numerous materials derived from global industrial by-products. On top of that, it is worth noting that the achievement of superior textural characteristics can be further accomplished through the optimization of activation parameters. Consequently, it is strongly advised that additional modification of the activation factors be undertaken to fully exploit the research path of rCB/ACs. Based on the investigations carried out, the final findings proved that the upgraded rCB/ACs developed exhibited further potential CO_2 capture capabilities. In overall, this research contributes to sustainable waste management practices on commercial scale, offering a green solution for repurposing globally discarded ELTs. This highly aligns with the principles of resource efficiency and responsible materials production.

CRediT authorship contribution statement

Bartosz Dziejarski: Conceptualization, Methodology, Experiment, Validation, Data curation, Formal analysis, Software, Investigation, Writing – original draft, Writing – review & editing, Visualization, Project administration. **Diego Felipe Hernández-Barreto:** Conceptualization, Methodology, Experiment, Modeling, Validation, Data curation, Formal analysis, Investigation, Writing – original draft, Writing – review & editing. **Juan Carlos Moreno-Piraján:** Conceptualization, Methodology, Investigation, Supervision, Resources, Funding acquisition. **Liliana Giraldo:** Conceptualization, Investigation, Supervision. **Jarosław Serafin:** Experiment, Formal analysis, Data curation. **Pavleta Knutsson:** Conceptualization, Investigation, Supervision. **Klas Andersson:** Investigation, Supervision. **Renata Krzyżyńska:** Investigation, Supervision.

Declaration of competing interest

The authors declare that they have no known competing financial interests or personal relationships that could have appeared to influence the work reported in this paper.

Data availability

No data was used for the research described in the article.

Acknowledgement

Bartosz Dziejarski extends his gratitude to Prof. Juan Carlos Moreno Piraján (Departamento de Química, Facultad de Ciencias, Grupo de Investigación en Sólidos Porosos y Calorimetría, Universidad de los Andes) and Prof. Liliana Giraldo (Departamento de Química, Grupo de Calorimetría, Universidad Nacional de Colombia) for their exceptional hospitality and for providing the invaluable opportunity to carry out research within their esteemed laboratory. Their collaborative spirit and dedication to fostering a stimulating research environment have been instrumental in presented paper. Prof. Dr. Juan Carlos Moreno-Piraján also acknowledges the Facultad de Ciencias of Universidad de los Andes for the grant (No. INV-2023-162-2735). Diego F. Hernández thanks to "Fondo de Apoyo Financiero para Doctorados" of Universidad de los Andes and to the Ministerio de Ciencia, Tecnología e Innovación for the financial support of the doctorate studies, by the "Convocatoria Nacional para Doctorados 909-2".

Appendix A. Supplementary data

Supplementary data to this article can be found online at https://doi.org/10.1016/j.envres.2024.118169.

References

Abel, U.A., Habor, G.R., Oseribho, O.I., 2020. Adsorption studies of oil spill clean-up using coconut coir activated carbon (CCAC). Am. J. Chem. Eng. 8 (2), 36–47. https://doi.org/10.11648/j.ajche.20200802.11.

Abuelnoor, N., AlHajaj, A., Khaleel, M., Vega, L.F., Abu-Zahra, M.R., 2021. Activated carbons from biomass-based sources for CO_2 capture applications. Chemosphere 282, 131111. https://doi.org/10.1016/j.chemosphere.2021.131111.

Abunowara, M., Bustam, M.A., Sufian, S., Babar, M., Eldemerdash, U., Mukhtar, A., Ullah, S., Assiri, M.A., Al-Sehemi, A.G., Lam, S.S., 2023. High pressure CO_2 adsorption onto Malaysian Mukah-Balingian coals: adsorption isotherms, thermodynamic and kinetic investigations. Environ. Res. 218, 114905 https://doi.org/10.1016/j.envres.2022.114905.

Ahmadpour, A., Do, D.D., 1997. The preparation of activated carbon from macadamia nutshell by chemical activation. Carbon 35 (12), 1723–1732. https://doi.org/10.1016/S0008-6223(97)00127-9.

Alabadi, A., Razzaque, S., Yang, Y., Chen, S., Tan, B., 2015. Highly porous activated carbon materials from carbonized biomass with high CO_2 capturing capacity. Chem. Eng. J. 281, 606–612. https://doi.org/10.1016/j.cej.2015.06.032.

Alhamed, Y.A., Rather, S.U., El-Shazly, A.H., Zaman, S.F., Daous, M.A., Al-Zahrani, A.A., 2015. Preparation of activated carbon from fly ash and its application for CO_2 capture. Kor. J. Chem. Eng. 32, 723–730. https://doi.org/10.1007/s11814-014-0273-2.

Aniruddha, R., Sreedhar, I., Reddy, B.M., 2020. MOFs in carbon capture-past, present and future. J. CO2 Util. 42, 101297 https://doi.org/10.1016/j.jcou.2020.101297.

Arenillas, A., Rubiera, F., Parra, J.B., Ania, C.O., Pis, J.J., 2005. Surface modification of low cost carbons for their application in the environmental protection. Appl. Surf. Sci. 252 (3), 619–624. Surface modification of low cost carbons for their application in the environmental protection. Applied Surface Science, 252(3), 619-624.

Arslanoğlu, H., 2019. Direct and facile synthesis of highly porous low cost carbon from potassium-rich wine stone and their application for high-performance removal. J. Hazard Mater. 374, 238–247. https://doi.org/10.1016/j.jhazmat.2019.04.042.

Ashraf, M.T., AlHammadi, A.A., El-Sherbeeny, A.M., Alhammadi, S., Al Zoubi, W., Ko, Y. G., Abukhadra, M.R., 2022. Synthesis of cellulose fibers/Zeolite-A nanocomposite as an environmental adsorbent for organic and inorganic selenium ions; Characterization and advanced equilibrium studies. J. Mol. Liq. 360, 119573 https://doi.org/10.1016/j.molliq.2022.119573.

Ayinla, R.T., Dennis, J.O., Zaid, H.M., Sanusi, Y.K., Usman, F., Adebayo, L.L., 2019. A review of technical advances of recent palm bio-waste conversion to activated carbon for energy storage. J. Clean. Prod. 229, 1427–1442. https://doi.org/10.1016/j.jclepro.2019.04.116.

Bai, B.C., Kim, E.A., Lee, C.W., Lee, Y.S., Im, J.S., 2015. Effects of surface chemical properties of activated carbon fibers modified by liquid oxidation for CO_2 adsorption. Appl. Surf. Sci. 353, 158–164. https://doi.org/10.1016/j.apsusc.2015.06.046.

Baldovino-Medrano, V.G., Niño-Celis, V., Isaacs Giraldo, R., 2023. Systematic analysis of the nitrogen adsorption–desorption isotherms recorded for a series of materials based on microporous–mesoporous amorphous aluminosilicates using classical methods. J. Chem. Eng. Data. https://doi.org/10.1021/acs.jced.3c00257.

Basik, A.A., Sanglier, J.J., Yeo, C.T., Sudesh, K., 2021. Microbial degradation of rubber: actinobacteria. Polymers 13 (12), 2021. https://doi.org/10.3390/polym13121989.

Bhattacharjya, D., Park, H.Y., Kim, M.S., Choi, H.S., Inamdar, S.N., Yu, J.S., 2014. Nitrogen-doped carbon nanoparticles by flame synthesis as anode material for rechargeable lithium-ion batteries. Langmuir 30 (1), 318–324. https://doi.org/10.1021/la403366e.

Boonpoke, A., Chiarakorn, S., Laosiripojana, N., Towprayoon, S., Chidthaisong, A., 2011. Synthesis of activated carbon and MCM-41 from bagasse and rice husk and their carbon dioxide adsorption capacity. Journal of Sustainable Energy & Environment 2 (2), 77–81.

Boujibar, O., Souikny, A., Ghamouss, F., Achak, O., Dahbi, M., Chafik, T., 2018. CO_2 capture using N-containing nanoporous activated carbon obtained from argan fruit shells. J. Environ. Chem. Eng. 6 (2), 1995–2002. https://doi.org/10.1016/j.jece.2018.03.005.

Boujibar, O., Ghamouss, F., Ghosh, A., Achak, O., Chafik, T., 2019. Activated carbon with exceptionally high surface area and tailored nanoporosity obtained from natural anthracite and its use in supercapacitors. J. Power Sources 436, 226882. https://doi.org/10.1016/j.jpowsour.2019.226882.

Brown, S.D.M., Jorio, A., Dresselhaus, M.S., Dresselhaus, G., 2001. Observations of the D-band feature in the Raman spectra of carbon nanotubes. Phys. Rev. B 64 (7), 073403. https://doi.org/10.1103/PhysRevB.64.073403.

Bulei, C., Todor, M.P., Heput, T., Kiss, I., 2018. Directions for material recovery of used tires and their use in the production of new products intended for the industry of civil construction and pavements. In: IOP Conference Series: Materials Science and Engineering. IOP Publishing, 012064. https://doi.org/10.1088/1757-899X/294/1/012064, 294, No. 1.

Burner, J., Schwiedrzik, L., Krykunov, M., Luo, J., Boyd, P.G., Woo, T.K., 2020. High-performing deep learning regression models for predicting low-pressure CO_2 adsorption properties of metal–organic frameworks. J. Phys. Chem. C 124 (51), 27996–28005. https://doi.org/10.1021/acs.jpcc.0c06334.

Cai, K., Liu, P., Zhao, T., Su, K., Yang, Y., Tao, D.J., 2022. Construction of hyper-crosslinked ionic polymers with high surface areas for effective CO_2 capture and conversion. Microporous Mesoporous Mater. 343, 112135 https://doi.org/10.1016/j.micromeso.2022.112135.

Cardona-Uribe, N., Betancur, M., Martínez, J.D., 2021. Towards the chemical upgrading of the recovered carbon black derived from pyrolysis of end-of-life tires. Sustainable Materials and Technologies 28, e00287. https://doi.org/10.1016/j.susmat.2021.e00287.

Choi, S.W., Tang, J., Pol, V.G., Lee, K.B., 2019. Pollen-derived porous carbon by KOH activation: effect of physicochemical structure on CO_2 adsorption. J. CO2 Util. 29, 146–155. https://doi.org/10.1016/j.jcou.2018.12.005.

Dabic-Miletic, S., Simic, V., Karagoz, S., 2021. End-of-life tire management: a critical review. Environ. Sci. Pollut. Control Ser. 1–18. https://doi.org/10.1007/s11356-021-16263-6.

Dantas, S., Struckhoff, K.C., Thommes, M., Neimark, A.V., 2019. Phase behavior and capillary condensation hysteresis of carbon dioxide in mesopores. Langmuir 35 (35), 11291–11298. https://doi.org/10.1021/acs.langmuir.9b01748.

David, E., Kopac, J., 2014. Activated carbons derived from residual biomass pyrolysis and their CO_2 adsorption capacity. J. Anal. Appl. Pyrol. 110, 322–332. https://doi.org/10.1016/j.jaap.2014.09.021.

Devi, P., Saroha, A.K., 2015. Effect of pyrolysis temperature on polycyclic aromatic hydrocarbons toxicity and sorption behaviour of biochars prepared by pyrolysis of paper mill effluent treatment plant sludge. Bioresour. Technol. 192, 312–320. https://doi.org/10.1016/j.biortech.2015.05.084.

Du, X., Pang, D., Cheng, Y., Zhao, Y., Hou, Z., Liu, Z., Wu, T., Shu, C., 2021. Adsorption of CH_4, N_2, CO_2, and their mixture on montmorillonite with implications for enhanced hydrocarbon extraction by gas injection. Appl. Clay Sci. 210, 106160 https://doi.org/10.1016/j.clay.2021.106160.

Dziejarski, B., Serafin, J., Andersson, K., Krzyżyńska, R., 2023. CO_2 capture materials: a review of current trends and future challenges. Materials Today Sustainability, 100483. https://doi.org/10.1016/j.mtsust.2023.100483.

Ferdous, W., Manalo, A., Siddique, R., Mendis, P., Zhuge, Y., Wong, H.S., Lokuge, W., Aravinthan, T., Schubel, P., 2021. Recycling of landfill wastes (tyres, plastics and glass) in construction–A review on global waste generation, performance, application and future opportunities. Resour. Conserv. Recycl. 173, 105745 https://doi.org/10.1016/j.resconrec.2021.105745.

Gao, Y., Yue, Q., Gao, B., Li, A., 2020. Insight into activated carbon from different kinds of chemical activating agents: a review. Sci. Total Environ. 746, 141094 https://doi.org/10.1016/j.scitotenv.2020.141094.

Gharagheizi, F., Sholl, D.S., 2021. Comprehensive assessment of the accuracy of the ideal adsorbed solution theory for predicting binary adsorption of gas mixtures in porous materials. Ind. Eng. Chem. Res. 61 (1), 727–739. https://doi.org/10.1021/acs.iecr.1c03876.

Global tire recycling market analysis 2025: opportunity, demand, growth and forecast 2017–2025—edition. Available online: https://www.goldsteinresearch.com/report/global-tire-recycling-industry-market-trends-analysis.

Gomez-Serrano, V., Valenzuela-Calahorro, C., Pastor-Villegas, J., 1993. Characterization of rockrose wood, char and activated carbon. Biomass Bioenergy 4 (5), 355–364. https://doi.org/10.1016/0961-9534(93)90052-6.

Gonzalez, J.F., Roman, S., González-García, C.M., Nabais, J.V., Ortiz, A.L., 2009. Porosity development in activated carbons prepared from walnut shells by carbon dioxide or steam activation. Ind. Eng. Chem. Res. 48 (16), 7474–7481. https://doi.org/10.1021/ie801848x.

Grundy, M., Ye, Z., 2014. Cross-linked polymers of diethynylbenzene and phenylacetylene as new polymer precursors for high-yield synthesis of high-performance nanoporous activated carbons for supercapacitors, hydrogen storage, and CO_2 capture. J. Mater. Chem. A 2 (47), 20316–20330. https://doi.org/10.1039/C4TA04038D.

Guclu, Y., Erer, H., Demiral, H., Altintas, C., Keskin, S., Tumanov, N., Su, B.L., Semerci, F., 2021. Oxalamide-functionalized metal organic frameworks for CO_2 adsorption. ACS Appl. Mater. Interfaces 13 (28), 33188–33198. https://doi.org/10.1021/acsami.1c11330.

Guo, Y., Tan, C., Sun, J., Li, W., Zhang, J., Zhao, C., 2020. Porous activated carbons derived from waste sugarcane bagasse for CO_2 adsorption. Chem. Eng. J. 381, 122736 https://doi.org/10.1016/j.cej.2019.122736.

Han, P., Yue, Y., Zhang, L., Xu, H., Liu, Z., Zhang, K., Zhang, C., Dong, S., Ma, W., Cui, G., 2012. Nitrogen-doping of chemically reduced mesocarbon microbead oxide for the improved performance of lithium ion batteries. Carbon 50 (3), 1355–1362. https://doi.org/10.1016/j.carbon.2011.11.007.

Hendricks, S.B., 1941. Base exchange of the clay mineral montmorillonite for organic cations and its dependence upon adsorption due to van der Waals forces. J. Phys. Chem. A 45 (1), 65–81. https://doi.org/10.1021/j150406a006.

Hoang, A.T., Varbanov, P.S., Nižetić, S., Sirohi, R., Pandey, A., Luque, R., Ng, K.H., Pham, V.V., 2022. Perspective review on Municipal Solid Waste-to-energy route: characteristics, management strategy, and role in circular economy. J. Clean. Prod., 131897 https://doi.org/10.1016/j.jclepro.2022.131897.

Hofman, M., Pietrzak, R., 2011. Adsorbents obtained from waste tires for NO_2 removal under dry conditions at room temperature. Chem. Eng. J. 170 (1), 202–208. https://doi.org/10.1016/j.cej.2011.03.054.

Idrees, M., Rangari, V., Jeelani, S., 2018. Sustainable packaging waste-derived activated carbon for carbon dioxide capture. J. CO2 Util. 26, 380–387. https://doi.org/10.1016/j.jcou.2018.05.016.

Irmer, G., Dorner-Reisel, A., 2005. Micro-Raman studies on DLC coatings. Adv. Eng. Mater. 7 (8), 694–705. https://doi.org/10.1002/adem.200500006.

Jagiello, J., Olivier, J.P., 2013. 2D-NLDFT adsorption models for carbon slit-shaped pores with surface energetical heterogeneity and geometrical corrugation. Carbon 55, 70–80. https://doi.org/10.1016/j.carbon.2012.12.011.

Jagiello, J., Kenvin, J., Celzard, A., Fierro, V., 2019a. Enhanced resolution of ultra micropore size determination of biochars and activated carbons by dual gas analysis using N_2 and CO_2 with 2D-NLDFT adsorption models. Carbon N. Y. 144, 206–215. https://doi.org/10.1016/j.carbon.2018.12.028.

Jagiello, J., Kenvin, J., Celzard, A., Fierro, V., 2019b. Enhanced resolution of ultra micropore size determination of biochars and activated carbons by dual gas analysis using N_2 and CO_2 with 2D-NLDFT adsorption models. Carbon 144, 206–215. https://doi.org/10.1016/j.carbon.2018.12.028.

Jjagwe, J., Olupot, P.W., Menya, E., Kalibbala, H.M., 2021. Synthesis and application of Granular activated carbon from biomass waste materials for water treatment: a review. Journal of Bioresources and Bioproducts 6 (4), 292–322. https://doi.org/10.1016/j.jobab.2021.03.003.

Kajal, A., Singh, R., 2019. Coriandrum sativum seeds extract mitigate progression of diabetic nephropathy in experimental rats via AGEs inhibition. PLoS One 14 (3), e0213147. https://doi.org/10.1371/journal.pone.0213147.

Kandasamy, J., Gökalp, I., 2015. Pyrolysis, combustion, and steam gasification of various types of scrap tires for energy recovery. Energy Fuel. 29 (1), 346–354. https://doi.org/10.1021/ef502283s.

Karaağaç, B., Ercan Kalkan, M., Deniz, V., 2017. End of life tyre management: Turkey case. J. Mater. Cycles Waste Manag. 19, 577–584. https://doi.org/10.1007/s10163-015-0427-2.

Khalil, S.H., Aroua, M.K., Daud, W.M.A.W., 2012. Study on the improvement of the capacity of amine-impregnated commercial activated carbon beds for CO_2 adsorbing. Chem. Eng. J. 183, 15–20. https://doi.org/10.1016/j.cej.2011.12.011.

Khoshraftar, Z., Ghaemi, A., 2023. Evaluation of CaO derived from Cerastoderma glaucum of Caspian beach as a natural sorbent for CO_2 capture. Current Research in Green and Sustainable Chemistry 6, 100360. https://doi.org/10.1016/j.crgsc.2023.100360.

Kishibayev, K.K., Serafin, J., Tokpayev, R.R., Khavaza, T.N., Atchabarova, A.A., Abduakhytova, D.A., Ibraimov, Z.T., Sreńscek-Nazzal, J., 2021. Physical and chemical properties of activated carbon synthesized from plant wastes and shungite for CO_2 capture. J. Environ. Chem. Eng. 9 (6), 106798 https://doi.org/10.1016/j.jece.2021.106798.

Lahuri, A.H., Khai, M.L.N., Rahim, A.A., Nordin, N., 2020. Adsorption kinetics for CO2 capture using cerium oxide impregnated on activated carbon. Acta Chim. Slov. 67, 570–580. https://doi.org/10.17344/acsi.2019.5572.

Lan, X., Jiang, X., Song, Y., Jing, X., Xing, X., 2019. The effect of activation temperature on structure and properties of blue coke-based activated carbon by CO_2 activation. Green Process. Synth. 8 (1), 837–845. https://doi.org/10.1515/gps-2019-0054.

Li, D., Ma, T., Zhang, R., Tian, Y., Qiao, Y., 2015. Preparation of porous carbons with high low-pressure CO_2 uptake by KOH activation of rice husk char. Fuel 139, 68–70. https://doi.org/10.1016/j.fuel.2014.08.027.

Li, S., Han, K., Li, J., Li, M., Lu, C., 2017. Preparation and characterization of super activated carbon produced from gulfweed by KOH activation. Microporous Mesoporous Mater. 243, 291–300. https://doi.org/10.1016/j.micromeso.2017.02.052.

Li, W., Li, X., Chang, W., Wu, J., Liu, P., Wang, J., Yao, X., Yu, Z.Z., 2020a. Vertically aligned reduced graphene oxide/Ti 3 C 2 T x MXene hybrid hydrogel for highly efficient solar steam generation. Nano Res. 13, 3048–3056. https://doi.org/10.1007/s12274-020-2970-y.

Li, F., Zhang, Y., Wang, S., Li, G., Yue, X., Zhong, D., Chen, C., Shen, K., 2020b. Insight into ex-situ thermal desorption of soils contaminated with petroleum via carbon number-based fraction approach. Chem. Eng. J. 385, 123946 https://doi.org/10.1016/j.cej.2019.123946.

López, F.A., Centeno, T.A., Rodríguez, O., Alguacil, F.J., 2013. Preparation and characterization of activated carbon from the char produced in the thermolysis of granulated scrap tyres. J. Air Waste Manag. Assoc. 63 (5), 534–544. https://doi.org/10.1080/10962247.2013.763870.

Martínez, J.D., 2021. An overview of the end-of-life tires status in some Latin American countries: proposing pyrolysis for a circular economy. Renew. Sustain. Energy Rev. 144, 111032 https://doi.org/10.1016/j.rser.2021.111032.

Merin, P., Jimmy Joy, P., Muralidharan, M.N., Veena Gopalan, E., Seema, A., 2021. Biomass-derived activated carbon for high-performance supercapacitor electrode applications. Chem. Eng. Technol. 44 (5), 844–851. https://doi.org/10.1002/ceat.202000450.

Mert, H., Deniz, C.U., Baykasoglu, C., 2023. Adsorptive separation of CH_4, H_2, CO_2, and N_2 using fullerene pillared graphene nanocomposites: insights from molecular simulations. J. Mol. Model. 29 (10), 315. https://doi.org/10.1007/s00894-023-05715-0.

Mistar, E.M., Alfatah, T., Supardan, M.D., 2020. Synthesis and characterization of activated carbon from Bambusa vulgaris striata using two-step KOH activation. J. Mater. Res. Technol. 9 (3), 6278–6286. https://doi.org/10.1016/j.jmrt.2020.03.041.

Mohajerani, A., Burnett, L., Smith, J.V., Markovski, S., Rodwell, G., Rahman, M.T., Kurmus, H., Mirzababaei, M., Arulrajah, A., Horpibulsuk, S., Maghool, F., 2020. Recycling waste rubber tyres in construction materials and associated environmental considerations: a review. Resour. Conserv. Recycl. 155, 104679 https://doi.org/10.1016/j.resconrec.2020.104679.

Mohan, A.N., Manoj, B., 2012. Synthesis and characterization of carbon nanospheres from hydrocarbon soot. Int. J. Electrochem. Sci. 7 (10), 9537–9549.

Mukherjee, S., Samanta, A.N., 2019. Amine-impregnated MCM-41 in post-combustion CO_2 capture: synthesis, characterization, isotherm modelling. Adv. Powder Technol. 30 (12), 3231–3240. https://doi.org/10.1016/j.apt.2019.09.032.

Mukherjee, A., Okolie, J.A., Abdelrasoul, A., Niu, C., Dalai, A.K., 2019. Review of post-combustion carbon dioxide capture technologies using activated carbon. J. Environ. Sci. 83, 46–63. https://doi.org/10.1016/j.jes.2019.03.014.

Muttakin, M., Mitra, S., Thu, K., Ito, K., Saha, B.B., 2018. Theoretical framework to evaluate minimum desorption temperature for IUPAC classified adsorption isotherms. Int. J. Heat Mass Tran. 122, 795–805. https://doi.org/10.1016/j.ijheatmasstransfer.2018.01.107.

Nandi, M., Uyama, H., 2014. Exceptional CO_2 adsorbing materials under different conditions. Chem. Rec. 14 (6), 1134–1148. https://doi.org/10.1002/tcr.201402062.

Nazir, G., Rehman, A., Park, S.J., 2021. Role of heteroatoms (nitrogen and sulfur)-dual doped corn-starch based porous carbons for selective CO_2 adsorption and separation. J. CO2 Util. 51, 101641 https://doi.org/10.1016/j.jcou.2021.101641.

Nieto-Márquez, A., Atanes, E., Morena, J., Fernández-Martínez, F., Valverde, J.L., 2016. Upgrading waste tires by chemical activation for the capture of SO_2. Fuel Process. Technol. 144, 274–281. https://doi.org/10.1016/j.fuproc.2016.01.009.

Nuhnen, A., Janiak, C., 2020. A practical guide to calculate the isosteric heat/enthalpy of adsorption via adsorption isotherms in metal–organic frameworks, MOFs. Dalton Trans. 49 (30), 10295–10307. https://doi.org/10.1039/D0DT01784A.

Ogungbenro, A.E., Quang, D.V., Al-Ali, K.A., Vega, L.F., Abu-Zahra, M.R., 2018. Physical synthesis and characterization of activated carbon from date seeds for CO_2 capture. J. Environ. Chem. Eng. 6 (4), 4245–4252.

Ogungbenro, A.E., Quang, D.V., Al-Ali, K.A., Vega, L.F., Abu-Zahra, M.R., 2020. Synthesis and characterization of activated carbon from biomass date seeds for carbon dioxide adsorption. J. Environ. Chem. Eng. 8 (5), 104257 https://doi.org/10.1016/j.jece.2020.104257.

Ould-Idriss, A., Stitou, M., Cuerda-Correa, E.M., Fernandez-Gonzalez, C., Marcias-Garcia, A., Alexandre-Franco, M.F., Gomez-Serrano, V., 2011. Preparation of activated carbons from olive-tree wood revisited. II. Physical activation with air. Fuel Process. Technol. 92, 266–270. https://doi.org/10.1016/j.fuproc.2010.05.018.

Ozpinar, P., Dogan, C., Demiral, H., Morali, U., Erol, S., Samdan, C., Yildiz, D., Demiral, I., 2022. Activated carbons prepared from hazelnut shell waste by phosphoric acid activation for supercapacitor electrode applications and comprehensive electrochemical analysis. Renew. Energy 189, 535–548. https://doi.org/10.1016/j.renene.2022.02.126.

Parshetti, G.K., Chowdhury, S., Balasubramanian, R., 2015. Biomass derived low-cost microporous adsorbents for efficient CO_2 capture. Fuel 148, 246–254. https://doi.org/10.1016/j.fuel.2015.01.032.

Plaza, M.G., Pevida, C., Martín, C.F., Fermoso, J., Pis, J.J., Rubiera, F., 2010. Developing almond shell-derived activated carbons as CO_2 adsorbents. Separ. Purif. Technol. 71 (1), 102–106. https://doi.org/10.1016/j.seppur.2009.11.008.

Plaza, M.G., González, A.S., Pis, J.J., Rubiera, F., Pevida, C., 2014. Production of microporous biochars by single-step oxidation: effect of activation conditions on CO_2 capture. Appl. Energy 114, 551–562. https://doi.org/10.1016/j.apenergy.2013.09.058.

Premchand, P., Demichelis, F., Chiaramonti, D., Bensaid, S., Fino, D., 2023. Biochar production from slow pyrolysis of biomass under CO_2 atmosphere: a review on the effect of CO_2 medium on biochar production, characterisation, and environmental applications. J. Environ. Chem. Eng. 110009 https://doi.org/10.1016/j.jece.2023.110009.

Raganati, F., Ammendola, P., Chirone, R., 2014. CO_2 adsorption on fine activated carbon in a sound assisted fluidized bed: effect of sound intensity and frequency, CO_2 partial pressure and fluidization velocity. Appl. Energy 113, 1269–1282. https://doi.org/10.1016/j.apenergy.2013.08.073.

Sait, H.H., Hussain, A., Salema, A.A., Ani, F.N., 2012. Pyrolysis and combustion kinetics of date palm biomass using thermogravimetric analysis. Bioresour. Technol. 118, 382–389. https://doi.org/10.1016/j.biortech.2012.04.081.

Sangchoom, W., Mokaya, R., 2015. Valorization of lignin waste: carbons from hydrothermal carbonization of renewable lignin as superior sorbents for CO_2 and hydrogen storage. ACS Sustain. Chem. Eng. 3 (7), 1658–1667. https://doi.org/10.1021/acssuschemeng.5b00351.

Serafin, J., Dziejarski, B., 2023. Application of isotherms models and error functions in activated carbon CO_2 sorption processes. Microporous Mesoporous Mater. 354, 112513 https://doi.org/10.1016/j.micromeso.2023.112513.

Serafin, J., Narkiewicz, U., Morawski, A.W., Wróbel, R.J., Michalkiewicz, B., 2017. Highly microporous activated carbons from biomass for CO_2 capture and effective micropores at different conditions. J. CO2 Util. 18, 73–79. https://doi.org/10.1016/j.jcou.2017.01.006.

Serafin, J., Baca, M., Biegun, M., Mijowska, E., Kaleńczuk, R.J., Sreńscek-Nazzal, J., Michalkiewicz, B., 2019. Direct conversion of biomass to nanoporous activated biocarbons for high CO_2 adsorption and supercapacitor applications. Appl. Surf. Sci. 497, 143722 https://doi.org/10.1016/j.apsusc.2019.143722.

Serafin, J., Ouzzine, M., Junior, O.F.C., Sreńscek-Nazzal, J., 2021. Preparation of low-cost activated carbons from amazonian nutshells for CO_2 storage. Biomass Bioenergy 144, 105925. https://doi.org/10.1016/j.biombioe.2020.105925.

Serafin, J., Kiełbasa, K., Michalkiewicz, B., 2022a. The new tailored nanoporous carbons from the common polypody (Polypodium vulgare): the role of textural properties for enhanced CO_2 adsorption. Chem. Eng. J. 429, 131751 https://doi.org/10.1016/j.cej.2021.131751.

Serafin, J., Sreńscek-Nazzal, J., Kamińska, A., Paszkiewicz, O., Michalkiewicz, B., 2022b. Management of surgical mask waste to activated carbons for CO_2 capture. J. CO2 Util. 59, 101970 https://doi.org/10.1016/j.jcou.2022.101970.

Serafin, J., Dziejarski, B., Sreńscek-Nazzal, J., 2023a. An innovative and environmentally friendly bioorganic synthesis of activated carbon based on olive stones and its potential application for CO_2 capture. Sustainable Materials and Technologies 38, e00717. https://doi.org/10.1016/j.susmat.2023.e00717.

Serafin, J., Dziejarski, B., Junior, O.F.C., Sreńscek-Nazzal, J., 2023b. Design of highly microporous activated carbons based on walnut shell biomass for H_2 and CO_2 storage. Carbon 201, 633–647. https://doi.org/10.1016/j.carbon.2022.09.013.

Shahkarami, S., Azargohar, R., Dalai, A.K., Soltan, J., 2015. Breakthrough CO_2 adsorption in bio-based activated carbons. J. Environ. Sci. 34, 68–76. https://doi.org/10.1016/j.jes.2015.03.008.

Shen, F., Wang, Y., Li, L., Zhang, K., Smith, R.L., Qi, X., 2018. Porous carbonaceous materials from hydrothermal carbonization and KOH activation of corn stover for highly efficient CO_2 capture. Chem. Eng. Commun. 205 (4), 423–431. https://doi.org/10.1080/00986445.2017.1367671.

Singh, R.K., Ruj, B., Jana, A., Mondal, S., Jana, B., Sadhukhan, A.K., Gupta, P., 2018. Pyrolysis of three different categories of automotive tyre wastes: product yield analysis and characterization. J. Anal. Appl. Pyrol. 135, 379–389. https://doi.org/10.1016/j.jaap.2018.08.011.

Soltani, R., Marjani, A., Shirazian, S., 2019. Facile one-pot synthesis of thiol-functionalized mesoporous silica submicrospheres for Tl (I) adsorption: isotherm, kinetic and thermodynamic studies. J. Hazard Mater. 371, 146–155. https://doi.org/10.1016/j.jhazmat.2019.02.076.

Sricharoenchaikul, V., Pechyen, C., Aht-ong, D., Atong, D., 2008. Preparation and characterization of activated carbon from the pyrolysis of physic nut (Jatropha curcas L.) waste. Energy Fuel. 22 (1), 31–37. https://doi.org/10.1021/ef700285u.

Stavropoulos, G.G., 2005. Precursor materials suitability for super activated carbons production. Fuel Process. Technol. 86 (11), 1165–1173. https://doi.org/10.1016/j.fuproc.2004.11.011.

Sun, J., Brady, T.A., Rood, M.J., Lehmann, C.M., Rostam-Abadi, M., Lizzio, A.A., 1997. Adsorbed natural gas storage with activated carbons made from Illinois coals and scrap tires. Energy Fuel. 11 (2), 316–322. https://doi.org/10.1021/ef960201h.

Sun, D.L., Wang, F., Hong, R.Y., Xie, C.R., 2016. Preparation of carbon black via arc discharge plasma enhanced by thermal pyrolysis. Diam. Relat. Mater. 61, 21–31. https://doi.org/10.1016/j.diamond.2015.11.004.

Talik, P., Moskal, P., Proniewicz, L.M., Wesełucha-Birczyńska, A., 2020. The Raman spectroscopy approach to the study of Water–Polymer interactions in hydrated hydroxypropyl cellulose (HPC). J. Mol. Struct. 1210, 128062 https://doi.org/10.1016/j.molstruc.2020.128062.

Tang, Z., Gao, J., Zhang, Y., Du, Q., Feng, D., Dong, H., Peng, Y., Zhang, T., Xie, M., 2023. Ultra-microporous biochar-based carbon adsorbents by a facile chemical activation strategy for high-performance CO_2 adsorption. Fuel Process. Technol. 241, 107613 https://doi.org/10.1016/j.fuproc.2022.107613.

Teng, H., Lin, Y.C., Hsu, L.Y., 2000. Production of activated carbons from pyrolysis of waste tires impregnated with potassium hydroxide. J. Air Waste Manag. Assoc. 50 (11), 1940–1946. https://doi.org/10.1080/10473289.2000.10464221.

Thonglhueng, N., Sirisangsawang, R., Sukpancharoen, S., Phetyim, N., 2022. Optimization of iodine number of carbon black obtained from waste tire pyrolysis plant via response surface methodology. Heliyon 8 (12). https://doi.org/10.1016/j.heliyon.2022.e11971.

Thote, J.A., Iyer, K.S., Chatti, R., Labhsetwar, N.K., Biniwale, R.B., Rayalu, S.S., 2010. In situ nitrogen enriched carbon for carbon dioxide capture. Carbon 48 (2), 396–402. https://doi.org/10.1016/j.carbon.2009.09.042.

Tian, X., Zhuang, Q., Han, S., Li, S., Liu, H., Li, L., Zhang, J., Wang, C., Bian, H., 2021. A novel approach of reapplication of carbon black recovered from waste tyre pyrolysis to rubber composites. J. Clean. Prod. 280, 124460 https://doi.org/10.1016/j.jclepro.2020.124460.

Trudsø, L.L., Nielsen, M.B., Hansen, S.F., Syberg, K., Kampmann, K., Khan, F.R., Palmqvist, A., 2022. The need for environmental regulation of tires: challenges and recommendations. Environ. Pollut. 311, 119974 https://doi.org/10.1016/j.envpol.2022.119974.

Wang, Y., Alsmeyer, D.C., McCreery, R.L., 1990. Raman spectroscopy of carbon materials: structural basis of observed spectra. Chem. Mater. 2 (5), 557–563. https://doi.org/10.1021/cm00011a018.

Wang, S., Nam, H., Nam, H., 2020. Preparation of activated carbon from peanut shell with KOH activation and its application for H_2S adsorption in confined space. J. Environ. Chem. Eng. 8 (2), 103683 https://doi.org/10.1016/j.jece.2020.103683.

Wei, P.S., Hsieh, Y.C., Chiu, H.H., Yen, D.L., Lee, C., Tsai, Y.C., Ting, T.C., 2018. Absorption coefficient of carbon dioxide across atmospheric troposphere layer. Heliyon 4 (10). https://doi.org/10.1016/j.heliyon.2018.e00785.

Xuguang, S., 2005. The investigation of chemical structure of coal macerals via transmitted-light FT-IR microspectroscopy. Spectrochim. Acta Mol. Biomol. Spectrosc. 62 (1–3), 557–564. https://doi.org/10.1016/j.saa.2005.01.020.

Yang, F., Liang, S., Wu, H., Yue, C., Yan, H., Wu, H., Chen, X., Zhang, J., Yan, S., Duan, Y., 2022. Upgrading the pyrolysis carbon black from waste tire by hybridization with cellulose. Ind. Eng. Chem. Res. 61 (19), 6512–6520. https://doi.org/10.1021/acs.iecr.2c00601.

Yousif, Q.A., Ranjeh, M., Ghiyasiyan-Arani, M., Al-Nayili, A., Monsef, R., Salavati-Niasari, M., 2022. Morphology engineering of $LiFeO_2$ nanostructures through synthesis controlling for electrochemical hydrogen storage inquiries. Fuel 313, 123025. https://doi.org/10.1016/j.fuel.2021.123025.

Yue, M.B., Sun, L.B., Cao, Y., Wang, Z.J., Wang, Y., Yu, Q., Zhu, J.H., 2008. Promoting the CO_2 adsorption in the amine-containing SBA-15 by hydroxyl group. Microporous Mesoporous Mater. 114 (1–3), 74–81. https://doi.org/10.1016/j.micromeso.2007.12.016.

Zabaniotou, A., Stavropoulos, G., Skoulou, V., 2008. Activated carbon from olive kernels in a two-stage process: industrial improvement. Bioresour. Technol. 99 (2), 320–326. https://doi.org/10.1016/j.biortech.2006.12.020.

Zhang, Y., Tao, L., Xie, C., Wang, D., Zou, Y., Chen, R., Wang, Y., Jia, C., Wang, S., 2020. Defect engineering on electrode materials for rechargeable batteries. Adv. Mater. 32 (7), 1905923 https://doi.org/10.1002/adma.201905923.

Paper III

ACS OMEGA

Open Access

http://pubs.acs.org/journal/acsodf

Article

Insights into Activation Pathways of Recovered Carbon Black (rCB) from End-of-Life Tires (ELTs) by Potassium-Containing Agents

Bartosz Dziejarski,* Robin Faust, Jarosław Serafin, Renata Krzyżyńska, Klas Andersson, and Pavleta Knutsson

Cite This: *ACS Omega* 2024, 9, 31814−31831

Read Online

ACCESS | Metrics & More | Article Recommendations

ABSTRACT: This study explores the conversion of recovered carbon black (rCB) from end-of-life tires (ELTs) into activated carbons (ACs) using potassium-based activators, targeting enhanced textural properties development. The research focuses on the interaction between potassium and rCB, with the aim of understanding the underlying mechanisms of rCB activation. The study investigates several parameters of KOH activation, including the KOH/rCB mass ratio (1:3 to 1:6), activation temperatures (700−900 °C), activation time (1−4 h), and heating rate (5−13 °C/min). It also assesses the effects of different potassium salts (KCl, K_2CO_3, CH_3COOK, and $K_2C_2O_4$) on porosity and surface characteristics of the rCB/ACs. Furthermore, the role of the physical state of KOH as an activator (solid and gas−solid) was examined, alongside a comparative analysis with NaOH to evaluate the distinct effects of potassium and sodium ions. Optimal conditions were identified at an 800 °C activation temperature, a 7 °C/min heating rate, a 1:5 KOH/rCB ratio, and a 4 h activation period. X-ray diffraction analysis showed the formation of several K-phases, such as K_2CO_3, $K_2CO_3{\cdot}1.5H_2O$, $K_4(CO_3)_2{\cdot}(H_2O)_3$, $KHCO_3$, and K_2O. The effectiveness of the potassium salts was ranked as follows: KOH > $K_2C_2O_4$ > CH_3COOK > K_2CO_3 > KCl, with KOH emerging as the most effective. Notably, the gas−solid reaction of KOH/rCB was indicated as a contributor to the activation process. Additionally, it was concluded that the role of KOH in enhancing the textural properties of rCB was primarily due to the interaction of K^+ ions with the graphite-like structure of rCB, compared to the effects observed with NaOH. This research introduces novel insights into the specific roles of different potassium salts and KOH activation conditions in optimizing the textural characteristics of rCB/ACs.

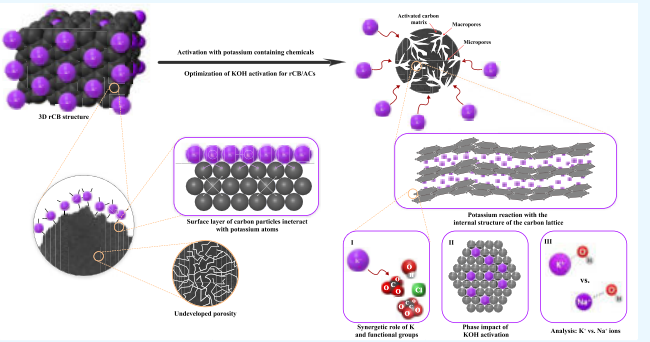

1. INTRODUCTION

Despite the European Union's prohibition on the accumulation of end-of-life tires (ELTs) in landfills since 2009, challenges in enforcement and inadequate infrastructure persist. The number of vehicles increases annually, rising from 1.2 billion since 2014, and it is anticipated that the worldwide count will exceed 1.6 billion by 2024. This growth highlights the escalating challenge of managing the environmental impact of ELTs waste flow. Nowadays, more than 50% of ELTs are disposed of without undergoing any form of treatment, and it is projected that the annual number of discarded tires will reach 1.2 billion by 2030.[1] ELTs can be a source of environmental contamination, which is a result of the release of hazardous substances into soil and water systems during their degradation.[2] Furthermore, tires contain natural (∼14−30%) and synthetic (∼14−27%) rubber, fabric/fillers/accelerators antiozonants (∼10−17%), and a substantial amount of carbon in the form of carbon black (∼20−28%) and steel wire (∼14%).[3] Due to ELTs relatively constant chemical content and their general availability, they are a well-suited resource for the production of activated carbons (ACs) for which the presence of a high carbon content is a prerequisite. The pyrolysis technique has been recognized as the most effective method for recycling ELTs, with no economically viable alternative currently available. Pyrolysis facilitates the breakdown of the organic constituents included in tires, resulting in the formation of pyrolytic char that contains a high proportion of recovered carbon black (rCB) as well as residues of carbonization, as a solid raw material.[4] Therefore, a purification stage for char is essential to obtain high-value rCB with a large carbon content (up to 95%) and to

Received: April 2, 2024
Revised: May 25, 2024
Accepted: May 29, 2024
Published: June 13, 2024

maximize the yield of ACs. In view of this, the conversion of ELTs into rCB/ACs provides a sustainable approach not only to managing waste flows but also for producing value-added products.

Activated carbons are primarily produced by the carbonization and activation of carbon precursors with little ash content, including solid fossil fuels (such as hard coal, brown coal, or peat), biomass (lignin, wood, fruit seeds, nut shells, or bamboo), and polymers (poly(ethylene terephthalate) (PET) bottles, packaging wastes, or epoxy resins).[5−7] The synthesis of ACs from carbon-based materials involves a sequence of crucial procedures referred to as pretreatment and modification. Pretreatment techniques, including washing, drying, and thermal treatment, are essential for purifying carbonaceous precursors and enhancing their reactivity. These steps facilitate the removal of impurities and prepare the surface of the precursor for subsequent activation.[8−10] As a result, ACs are mainly composed of elemental carbon in an amorphous state and fine-crystalline graphite. Currently available commercial ACs remain costly owing to their reliance on nonrenewable precursors, which increases the demand for ACs that can be produced from a wide range of low-cost raw materials. The benefits of ACs are strictly related to their distinct physicochemical properties like a large specific surface area, a well-defined network of pores, significant mechanical strength, and abundant functional groups with various oxygen-containing compounds that can be tailored for the specific application by activation processes.[11,12]

An activation process is necessary for achieving the desired properties of ACs.[13,14] Activation may be accomplished by several methods, including chemical or physical processes. Chemical activation is more favorable since it requires lower temperature, has higher efficiency, and requires shorter processing time compared to a physical one.[15] It involves treatment with oxidizing acids (HNO_3, H_2SO_4, H_3PO_4), salt solutions ($ZnCl_2$, $MgCl_2$), or alkalis (KOH, NaOH, K_2CO_3). Different researchers[16−19] proved that the choice of activating agent such as H_2SO_4, H_3PO_4, HCl, NaOH, and KOH further modulates the properties of the ACs. Each activator operates through distinct mechanisms, impacting pore development and surface chemistry in unique ways. Furthermore, the activation parameters along with the carbonization process play a pivotal role in shaping the structure and characteristics of the resulting activated carbons.[20] Factors such as temperature, heating rate, residence time, mass ratio of precursor:activator, and ambient atmosphere exert significant influence on the final product. While elevated temperatures generally lead to higher carbon content and surface area, they also affect pore size distribution and chemical composition.

Among the various activators, potassium-containing agents such as KOH and K_2CO_3 are particularly favored due to their strong alkalinity, reactivity with carbon, ability to widen pore size distributions, increase total pore volume, and create a highly porous structure, especially enhancing microporosity.[21−26] Furthermore, potassium tends to enhance the activation kinetics, leading to a more efficient thermochemical conversion.[27,28] Previous research on KOH and K_2CO_3 has suggested different chemical reactions to explain potassium effect.[8,29,30] Widely, it is assumed that KOH possesses a tendency to engage with carbon atoms, therefore stimulating the dehydrogenation process (removal of hydrogen atoms from the carbon precursor material) that ultimately results in the formation of a carbon structure characterized by a well-defined porous morphology.[31−33] While the efficacy of KOH and K_2CO_3 is well-documented, the exploration of other potassium-based activators in the production of ACs prompts a closer investigation into the underlying mechanisms.[34−37] This aims to reveal the different interactions of potassium and specific ionic groups and their effects on the AC production process, especially when using diverse precursors. Furthermore, each of these agents interacts with AC precursors in ways that could potentially optimize or enhance specific properties of the resulting ACs, justifying their investigation alongside traditional activators, such as KOH and K_2CO_3.

Initial investigations have explored the viability of ELT char during chemical activation to optimize textural properties (specific surface area, total pore volume, and microporosity).[38−43] The main goal of these investigations has been to examine the effectiveness of potassium hydroxide (KOH), potassium carbonate (K_2CO_3), phosphoric acid (H_3PO_4), zinc chloride ($ZnCl_2$), sodium hydroxide (NaOH), and sodium carbonate (Na_2CO_3). Among the tested activating agents, the application of KOH has shown significant enhancements in specific surface area (180−820 m^2/g), porosity development (0.28−1.32 cm^3/g), and tailored pore size distribution of char/ACs compared to those of other chemicals. Al-Rahbi and Williams[39] claimed that tires char-based ACs produced by the KOH activation with a mass ratio of 1:3 at a temperature of 900 °C had a more prominent porosity compared to those treated with alternative alkali activating agents, including K_2CO_3, NaOH, and Na_2CO_3. Hofman and Pietrzak[40] observed that the KOH has a notable positive influence on the creation of ACs from waste tires char that exhibit a highly developed porous structure, mostly composed of micropores, when activated at a temperature of 800 °C. Furthermore, the research performed by Nieto-Márquez et al.[38] proved that the rise in the proportion of the KOH to waste tires ratio subsequently resulted in a proportional augmentation in surface area, and total pore volume of ACs.

While these findings offer encouraging insights, their scope is limited, focusing solely on examining the dependence of temperature (550−900 °C) and char/activator mass ratio (1:0.5 to 1:4). It did not thoroughly examine how K-containing agents interact with char carbon atoms. Additionally, the studies neglected the impact of other critical activation factors (heating rate or activation time), the formation of specific chemical phases during the thermal process, and the effects of KOH phase transitions. This focus highlights a significant gap, underscoring the need for in-depth research into rCB activation mechanisms. On the other hand, in the field of alkali-enhanced gasification and combustion, the practice of converting solid fuels and waste materials with alkali metals is well-established due to their recognized catalytic role in promoting the efficiency of the overall process.[44−46] Most proposed mechanisms involve the presence of potassium in a metallic state, produced at high temperatures (800−900 °C). Metallic K is capable of intercalating into the carbon framework, creating intercalation compounds that leads to the expansion of graphitic lattice.[47,48]

This work aims to provide insights into the mechanism during the activation of rCB to ACs by potassium-containing activators. The main goal is to improve the textural properties of the rCB/ACs. KOH was selected as the baseline chemical to examine the effect of the KOH/rCB mass ratio, temperature, activation time, and heating rate influence on the characteristics of produced rCB/ACs, as suggested in the literature. It is

https://doi.org/10.1021/acsomega.4c03160
ACS Omega 2024, 9, 31814−31831

recognized that different AC precursors might require tailored activation parameters to optimally develop their porous structures and surface characteristics. The research thoroughly explores these interactions, examining how changes in the KOH activation parameters impact rCB. Then, for the assumed standard parameters, different potassium salts, including KCl, K_2CO_3, CH_3COOK, and $K_2C_2O_4{\cdot}H_2O$, were employed to investigate the potential synergistic role of K^+ with specific functional groups (OH^-, Cl^-, CO_3^{2-}, $COOK^-$, $C_2O_4^{2-}$) in the development of porosity and their effect on the rCB/AC surface. Additionally, the impact of the state of the activating agent (solid-state or gaseous-state reaction) and a comparative analysis with NaOH (Na^+ vs K^+) were explored. Furthermore, it is crucial to test industrially produced material to adapt laboratory findings for industrial-scale production, ensuring that the process is viable and effective on a larger scale.

Herein, the key objectives of this work were to fill this gap in knowledge by (1) revealing the optimal conditions for the rCB activation using K-based activators; (2) establishing the responsible factors in the conversion of rCB to ACs using potassium alkalis for porosity development; and (3) uncovering the generic mechanism driving rCB activation to efficiently convert the ELTs into ACs. Through laboratory experiments and material characterization, we provide potential activation pathways of rCB conversion to ACs with emphasis put on interactions with potassium. Understanding the potassium interaction with the rCB surface and optimizing the activation of potassium-containing agents of rCB has important implications as it can improve the production of ACs, aiding sorption application, and promote sustainability by using waste materials like ELTs.

2. EXPERIMENTAL SECTION

2.1. Chemicals and Materials. The reagents used for the synthesis of rCB/ACs were KOH, K_2CO_3, KCl, CH_3COOK, $K_2C_2O_4{\cdot}H_2O$, and NaOH with a purity of 97%. The activated carbon precursor employed in this study was tailor-made rCB obtained from a company in Poland. The production process involved treating char through devolatilization, milling, and, if necessary, pelleting to reduce the ash content, remove metal impurities, and normalize variations in the particle size. The chemical composition of rCB is notably variable and contingent on the composition of the ELTs subjected to industrial-scale pyrolysis. Carbon stands out as the principal component, ranging from 92% to 99.5 wt %, as shown in Table 1. Additionally, rCB may encompass volatile substances (>0.2 wt % content) and mineral matter (0.5−2 wt % content), including elements like Si, Al, Zn, S, and Ca.

Table 1. Chemical Composition of rCB in wt %

sample	C [wt %]	H [wt %]	N [wt %]	S [wt %]	O [wt %]
rCB	92.53	1.16	0.42	0.71	5.18

2.2. Preparation of rCB-Based Activated Carbons. The methodology employed in this study involves testing several key factors of KOH activation, including the reaction phase, mass ratio, temperature, heating rate, and activation time, as these are known to have a significant impact on the overall process. By systematic examination of these variables, the activation mechanism can be followed and optimized. The materials were exposed to tube furnace conditions. About 8 g of mixture of rCB and activator agent was placed in alumina crucibles and located in the center of the horizontal furnace, as presented in Figure 1. Two types of set rCB activators were tested: gas−solid reactions (activator salt as gas) and solid/liquid−solid (activator salt as solid) reactions. In the case of a gas−solid reaction, the reactants were separated into two crucibles, accordingly. Then, the sample was heated under a continuous flow of N_2 gas at a rate of 200 cm^3/min, based on the previous research related with ELTs[38−40,49] and in accordance with recommendations from the existing literature.[50−52] The temperature, ranging from 700 to 900 °C, depending on the experimental setup was achieved by a heating rate of 5−13 °C/min and then maintained for a duration of 1−4 h (Table 2). Following that, the sample was exposed to a controlled cooling process, gradually reducing its temperature to correspond with 25 °C at a rate of 5 °C/min.

For the solid-state activation reaction, the rCB was dry mixed in a mortar with specific potassium-containing (KOH, K_2CO_3, KCl, CH_3COOK, and $K_2C_2O_4{\cdot}H_2O$) or sodium-containing (NaOH) activating agents in the solid−solid phase. The mass ratios between the precursor and the chosen salts ranged from 1:3 to 1:6. Following the completion of the activation step under the selected reaction conditions, half of the resultant solid material was rinsed with water until achieving a neutral pH of the washing solution in order to eliminate salt leftovers and evaluate the textural characteristics of the obtained activated carbons. Simultaneously, the other half of the material that was left untreated was used for the investigation of the carbon−potassium reaction mechanism through X-ray diffraction (XRD) analysis and scanning electron microscopy coupled with energy-dispersive X-ray spectroscopy (SEM-EDS). Finally, the rCB/ACs were subsequently dried at a temperature of 110 °C for a duration of 12 h. The samples were labeled using coding: activating agent, carbonization temperature, and residence time during activation (Tables 3 and 4). For example, the notation KOH_1:3_700_3_5 represents a rCB/AC sample that has undergone activation with KOH in the mass ratio 1:3 at 700 °C for 3 h with a heating rate of 5 °C/min. In line with the published literature concerning the reutilization of pyrolytic char to produce ACs, the baseline activation parameters for the study objectives were determined to be 800 °C, 1:4, 3 h, and 5 °C/min. It should be noted that these parameters were selected by assuming the ACs were not further manipulated to optimize their textural properties.

2.3. Characterization Techniques of Carbon Materials. The analysis of the chemical composition of recovered carbon black was conducted using a FLASH 2000 CHNS Elemental Analyzer from Thermo Fisher Scientific.

The most important qualities of carbon materials are their textural characteristics, such as the surface area, pore volume, and pore size distribution, as well as their crystallographic structure. Thus, these aspects play a crucial role in defining the activation process and are the first parameters to follow in the rCB in order to evaluate a new activation procedure.

The enhancement of textural properties of prepared rCB/ACs was measured by N_2 adsorption−desorption at 77 K using the fully automated, three-station surface area and porosity analyzer Tristar II 3020 Micromeritics. Prior to conducting adsorption tests, the samples were left in a degassed chamber overnight at a temperature of 250 °C. To calculate the specific surface area of samples (S_{BET}), the experimental data was fitted

https://doi.org/10.1021/acsomega.4c03160
ACS Omega 2024, 9, 31814−31831

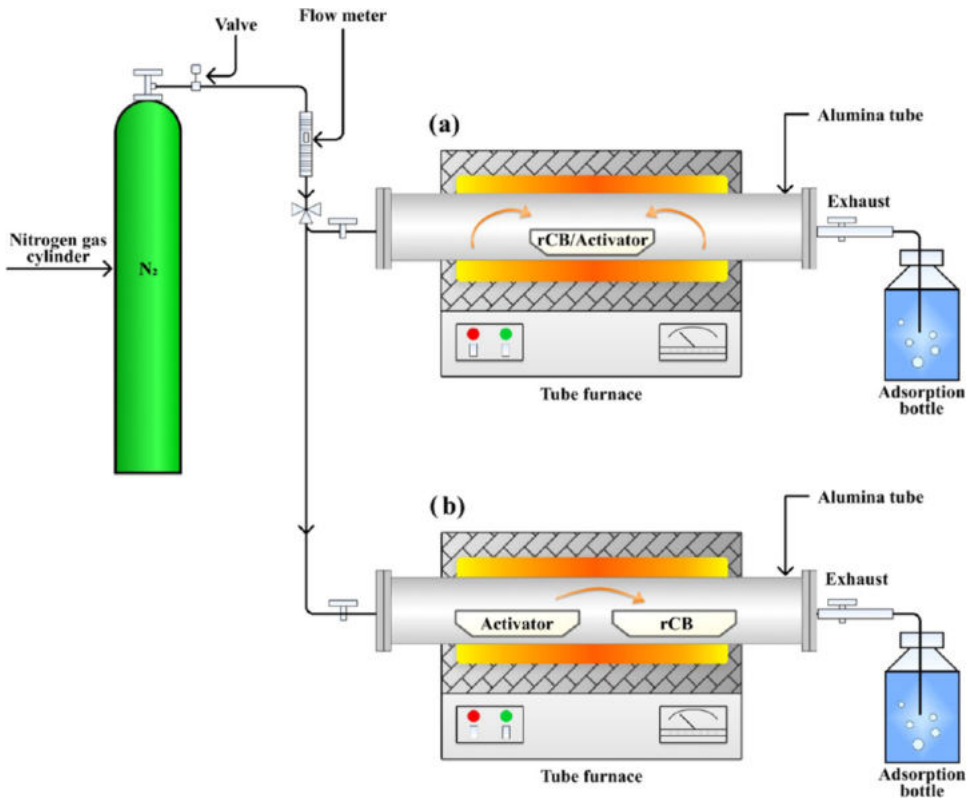

Figure 1. Schematic diagram of the experimental process setup applied for solid/liquid-solid state activation (a) and gas-solid state activation (b).

Table 2. Experimental Conditions for Activation Processes

type of activation	heating rate [°C/min]	temperature [°C]	activation time [h]	flow rate of N_2 [cm^3/min]	cooling rate [°C/min]
chemical activation	5−13	700−900	1−4	200	5

Table 3. Overview of rCB/ACs Sample Symbol Sets for Porosity Development

symbol	mass ratio [-]	temperature [°C]	activation time [h]	heating rate [°C/min]
Effect of KOH Activation Temperature				
KOH_1:4_700_3_5	1:4	700	3	5
KOH_1:4_800_3_5[a]	1:4	800	3	5
KOH_1:4_900_3_5	1:4	900	3	5
KOH Activation Time Influence				
KOH_1:4_800_1_5	1:4	800	1	5
KOH_1:4_800_2_5	1:4	800	2	5
KOH_1:4_800_4_5	1:4	800	4	5
Effect of Mass Ratio Between rCB/KOH				
KOH_1:3_800_3_5	1:3	800	3	5
KOH_1:5_800_3_5	1:5	800	3	5
KOH_1:6_800_3_5	1:6	800	3	5
Effect of Heating Rate				
KOH_1:4_800_3_7	1:4	800	3	7
KOH_1:4_800_3_10	1:4	800	3	10
KOH_1:4_800_3_13	1:4	800	3	13

[a]The study's base activation conditions were set at 1:4 ratio, 800 °C, 3 h, and 5 °C/min.

to the Brunauer−Emmett−Teller (BET) equation in a relative pressure range of P/P_0 from 0.05 to 0.3, as presented below

$$y = \frac{1}{Q \cdot \left(\frac{P}{P_0} - 1\right)} \quad (1)$$

where Q represents the mass of gas adsorbed at a given relative pressure (P/P_0), P is the pressure of the nitrogen gas used in the adsorption experiment [mmHg], and P_0 is the saturation pressure of nitrogen gas [mmHg].

Additionally, the selection of a proper P/P_0 range was based on a modification of the BET theory proposed by Rouquerol et al.[53,54] to obtain the highest linear relationship in regard to the coefficient of determination ($R^2 \sim 1$).

The total pore volume (V_{TOT}) was determined from the N_2 adsorption isotherm at a high relative pressure, typically close to unity (0.99 or higher). The examination of micropore volume (V_{MIC}) within the range of pore diameters from 1.4 to 2 nm and pore size distribution (PSD) was conducted using the density functional theory (DFT) approach, specifically by applying the nonlocal density functional theory (NLDFT) model. Furthermore, the mesopore volume (V_{MES}) was estimated by subtracting the micropore volume from the total pore volume, utilizing the assumption that mesopores (2−50 nm) constitute the difference between these two volumetric measurements.

The crystallographic structure of the rCB/ACs was examined by X-ray diffraction analysis using a Bruker D8 Discover X-ray diffractometer. The particles were finely powdered before the patterns were recorded. Cu Kα radiation was applied (λ = 0.15418 nm) as the radiation source, and the

https://doi.org/10.1021/acsomega.4c03160
ACS Omega 2024, 9, 31814−31831

Table 4. Description of rCB/ACs Sample Symbol Sets for Research Goals

symbol	activating agent	mass ratio [-]	temperature [°C]	activation time [h]	heating rate [°C/min]
Role of Potassium and Functional Groups in Porosity Development					
CH_3COOK_1:4_800_3_5	CH_3CO_2K	1:4	800	3	5
K_2CO_3_1:4_800_3_5	K_2CO_3	1:4	800	3	5
KCl_1:4_800_3_5	KCl	1:4	800	3	5
$K_2C_2O_4$ _1:4_800_3_5	$K_2C_2O_4$	1:4	800	3	5
Phase Impact of KOH Activation					
KOH(vapor)_1:4_800_3_5	KOH	1:4	800	3	5
Potassium Hydroxide (K^+) vs Sodium Hydroxide (Na^+)					
NaOH_1:4_800_3_5	NaOH	1:4	800	3	5

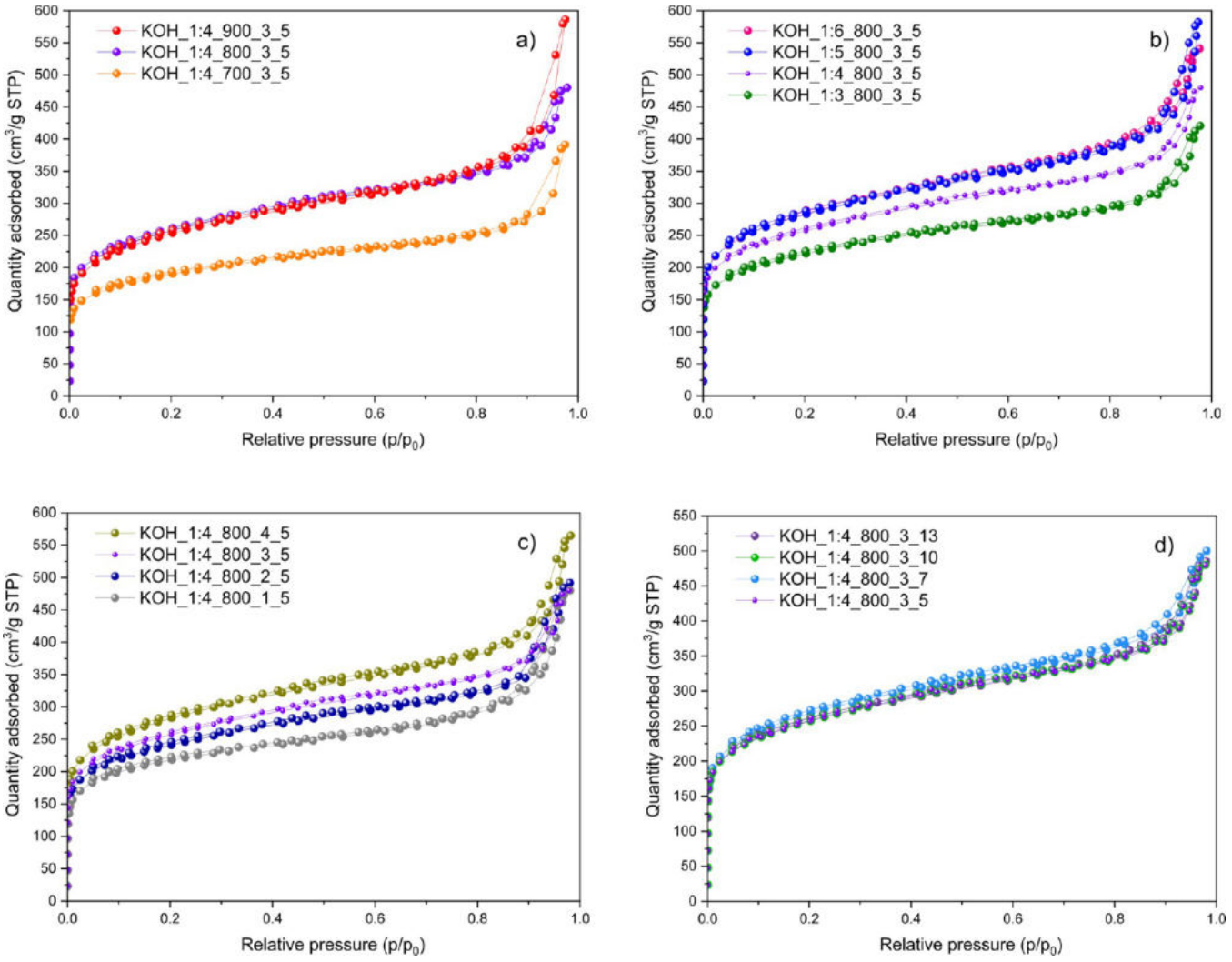

Figure 2. N_2 adsorption−desorption isotherm curves at 77 K of the rCB/ACs in relation to the activation effect of temperature (a), mass ratio (b), time (c), and heating rate (d).

diffraction patterns were recorded at regular 2θ intervals covering 10−85°. The identification of the relevant phases created during activation was performed using the DIFFRAC.EVA software, with reference to the PDF-4 + 2022 database (ICDD), which was also used for semiquantitative analysis.

Scanning electron microscopy with an energy-dispersive X-ray spectroscopy system was used to analyze the distribution of potassium on recycled rCB/ACs processed with different potassium-containing activators. The analysis was conducted using a JEOL 7800F Prime SEM, operating at 20 kV with a solid-state detector (SSD), utilizing backscattered electrons (BSE). The primary objective of the SEM-EDS analysis was to map the spatial distribution of K on the surfaces of rCB/ACs and to quantitatively evaluate the surface elemental composition. This approach provides insights into the effectiveness of the activation process in incorporating potassium into the carbon structure of the materials.

3. RESULTS AND DISCUSSION

3.1. Effect of KOH Activation Parameters on rCB/ACs Textural Properties. The optimization of KOH activation parameters, including the temperature (Figure 2a), mass ratio

https://doi.org/10.1021/acsomega.4c03160
ACS Omega 2024, 9, 31814−31831

Table 5. Textural Properties Associated with the Produced rCB/ACs by Specific Activation Parameters

sample	BET surface area[a] [m^2/g]	total pore volume[b] [cm^3/g]	micropore volume[c] [cm^3/g]	mesopore volume[c] [cm^3/g]	micropore volume/total pore volume [%]
rCB	55 ± 0.8	0.170	-	-	-
		Effect of Temperature			
KOH_1:4_900_3_5	915 ± 2.3	0.854	0.288	0.566	39
KOH_1:4_800_3_5	945 ± 5.6	0.743	0.303	0.440	36
KOH_1:4_700_3_5	688 ± 1.8	0.605	0.225	0.380	37
		Effect of Mass Ratio Between rCB/ACs			
KOH_1:6_800_3_5	1022 ± 3.8	0.837	0.312	0.525	39
KOH_1:5_800_3_5	1025 ± 2.2	0.901	0.327	0.574	35
KOH_1:3_800_3_5	801 ± 1.8	0.651	0.252	0.399	39
		Effect of Activation Time			
KOH_1:4_800_4_5	1028 ± 1.5	0.874	0.332	0.542	38
KOH_1:4_800_2_5	876 ± 3.08	0.727	0.276	0.467	37
KOH_1:4_800_1_5	788 ± 1.3	0.699	0.211	0.488	30
		Effect of Heating Rate			
KOH_1:4_800_3_7	970 ± 1.9	0.884	0.314	0.460	41
KOH_1:4_800_3_10	934 ± 2.0	0.774	0.298	0.452	40
KOH_1:4_800_3_13	900 ± 1.8	0.750	0.289	0.595	32

[a]Brunauer, Emmett, and Teller method using the Rouquerol criteria. [b]V_{TOT} calculated by the N_2 adsorption isotherm at a high relative pressure (~0.99). [c]DFT method by the NLDFT model.

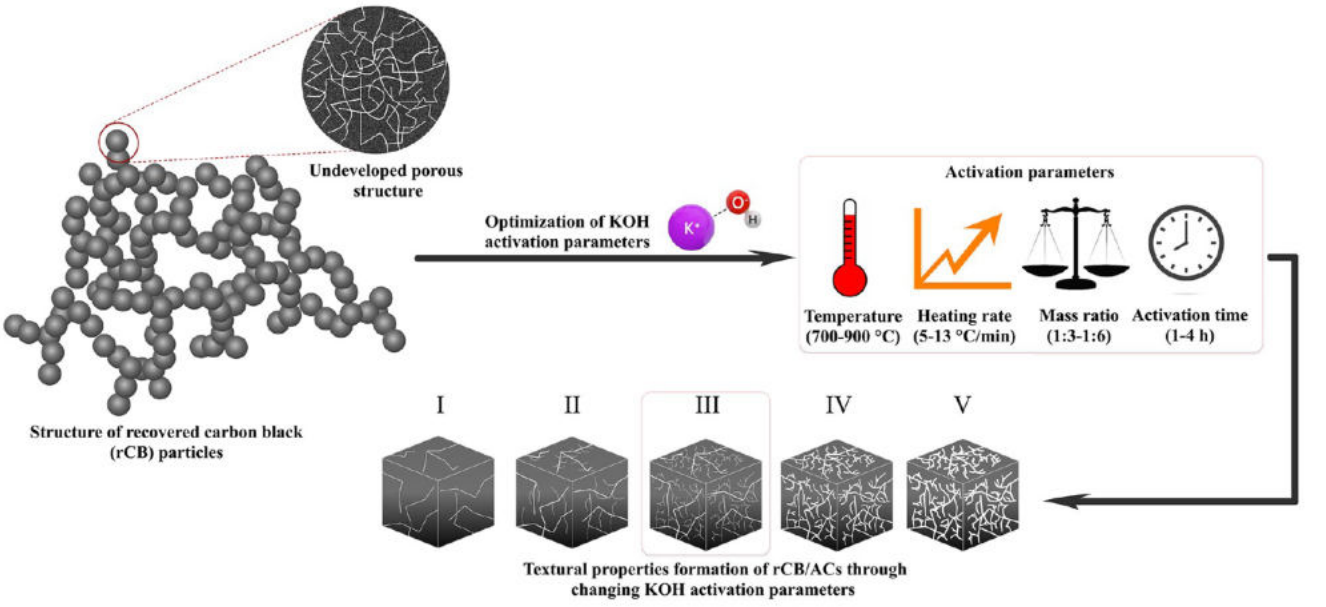

Figure 3. Optimal formation of rCB/ACs textural properties (BET surface area, total pore volume, and microporosity) influenced by KOH activation parameters (III stage, 800 °C, 7 °C/min, 1:5, and 4 h).

(Figure 2b), residence time (Figure 2c), and heating rate (Figure 2d) emerges as a critical aspect of examining the limitations of the rCB precursor. Based on the obtained N_2 isotherms for each parameter, the development of the porosity can be followed, which indicates the type of structure of the material that evolves as a result of activation. According to the IUPAC classification, all curves exhibit a mixture of type I and type IV isotherms, indicating a bimodal pore system in the rCB/ACs. This combination suggests the existence of both micropores (<2 nm) and mesopores (2−50 nm).[55] The presence of micropores was confirmed by the significant N_2 adsorption found at a P/P_0 below 0.05. Furthermore, the hysteresis loops have a nearly narrow, horizontal, and parallel shape throughout a broad range of P/P_0 (up to 0.85) with a pointed end, proving the H3-type of isotherm. The H3-type implies that the main pore morphology in all rCB/ACs samples involves slit-shaped pores with a well-developed mesoporous structure.[56] The desorption isotherm exhibited a hysteresis loop as a result of capillary condensation occurring in mesopores.[57]

The N_2 adsorption−desorption isotherms were further applied for the determination of the textural properties of all rCB/AC samples along with the related impact of the activation parameters on them, including the specific surface area, total volume of the pores, and mesoporosity and microporosity content (Table 5). The rCB had a very low BET surface area of 55 m^2/g, lacking micropores, and possessing a limited total pore volume of 0.170 cm^3/g. The KOH-activated rCB exhibited both micro- and mesoporous characteristics, with the mesopore percentage (determined by

https://doi.org/10.1021/acsomega.4c03160
ACS Omega 2024, 9, 31814−31831

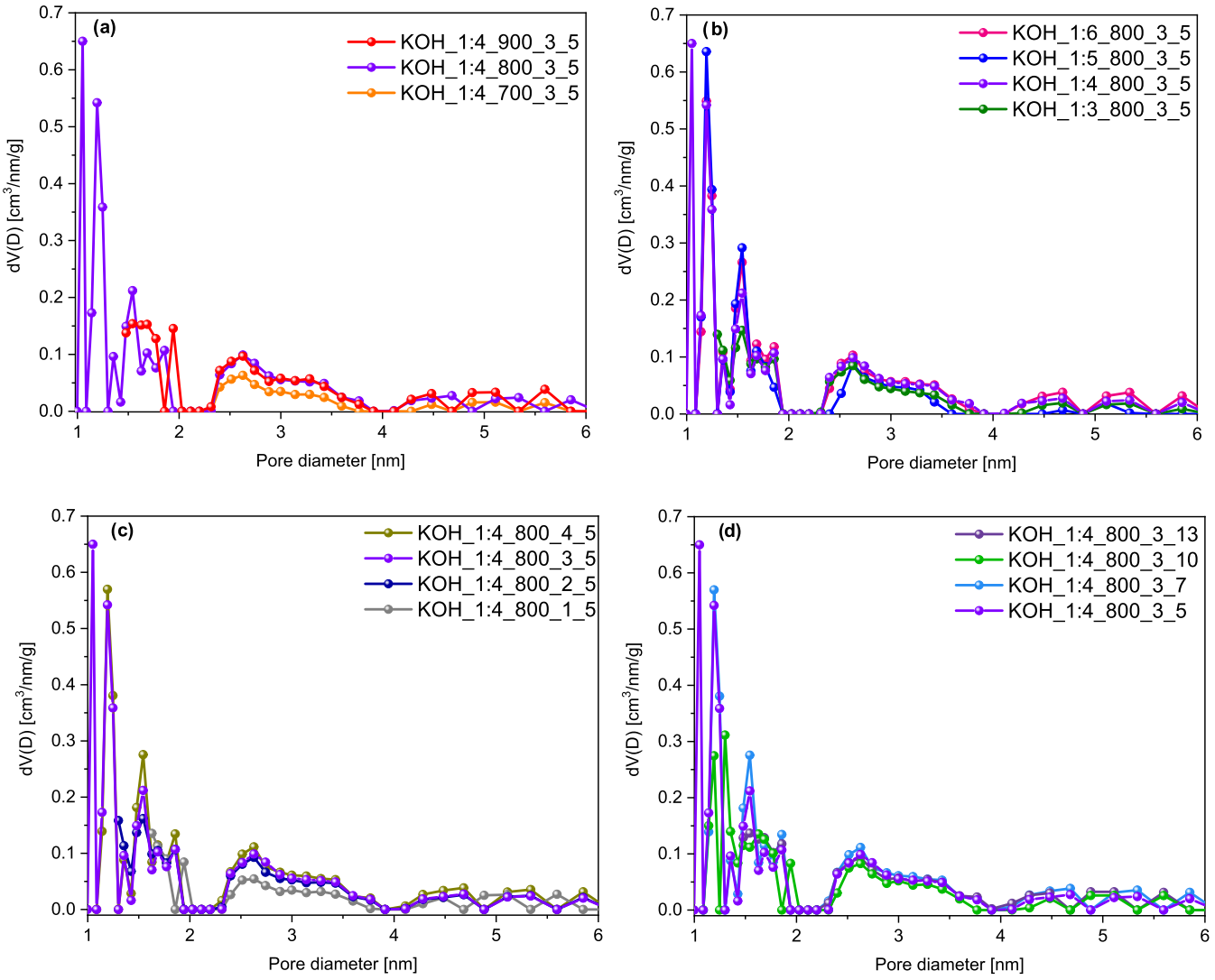

Figure 4. Pore size distribution of the rCB/ACs based on the DFT method of N_2 adsorption at 77 K on carbon slit pores by the NLDFT model in relation to the activation effect of temperature (a), mass ratio (b), time (c), and heating rate (d).

the V_{MES}/V_{TOT} ratio) mostly exceeding 60%. These findings demonstrate that the KOH benefits increased porosity with the BET surface of rCB/ACs. Based on Table 5, each examined activation parameter (temperature, mass ratio, activation time, and heating rate) is expected to fall within a certain range to influence the obtained textural properties of the rCB/ACs optimally. Furthermore, through the experiments performed, one can gain an understanding of how each of the varied parameters influences the overall activation mechanism, as shown in Table 3. Ultimately, the specific surface areas of the rCB/ACs in this study exceed those documented by other researchers who activated char formed from ELTs using KOH with the main focus on temperature (550−900 °C) and mass ratio effect (1:0.5−1:4).[38−40]

As demonstrated previously, the optimal conditions, detailed in Figure 3 highlight the critical role of activation parameters in enhancing the quality and efficiency of rCB/ACs production.

The temperature dependence can be followed when the temperature increased from 700 to 800 °C. As a result of the increased temperature, the KOH activation reaction and diffusion rate with carbon atoms become more intense, leading to the creation of the pore skeleton (0.605−0.743 cm^3/g), the development of microporosity (0.225−0.303 cm^3/g), and increase in the specific surface area (688−945 m^2/g). In the range of 700−800 °C, K^+ ions can penetrate the carbonized surface more effectively, which leads to the growth of micropores. On the other hand, the temperature dependence observed during the activation of rCB between 800 and 900 °C can be related to the intensified activation of carbonaceous rCB that forms wide interconnected mesopores (0.901 cm^3/g), which partially degrades the specific area to 915 m^2/g and decreases the microporous structure to 0.288 cm^3/g. This observation aligns with the conclusions reported by Serafin et al.[58] In addition, Hofman and Pietrzak[40] also proposed that the ideal temperature for the pyrolytic char is 800 °C, with a KOH/rCB ratio of 1:4. Other authors, Al-Rahbi and Williams[39] indicated that a temperature of 900 °C leads to higher effectiveness in achieving the desired S_{BET}, V_{TOT}, and V_{MIC}, despite the use of a lower mass ratio. That fact potentially implies a significant correlation between these two factors.

Further, when considering the impacts of the rCB/KOH mass ratio (1:6, 1:5, 1:4, and 1:3), the optimized values of S_{BET} (1025 m^2/g), V_{TOT} (0.901 cm^3/g), and V_{MIC} (0.901 cm^3/g)

https://doi.org/10.1021/acsomega.4c03160
ACS Omega 2024, 9, 31814−31831

Table 6. Comparison of Textural Characteristics of ACs Prepared from Various Precursors by KOH Activation

precursor	BET surface area [m^2/g]	total pore volume [cm^3/g]	mesopore volume [cm^3/g]	micropore volume [cm^3/g]	refs
recovered carbon black (KOH_1:5_800_3_5)	1025	0.90	0.54	0.33	this work
pristine gelatin	1294	0.63	-	-	62
starch	714	0.40	-	-	62
slash pine	906	0.35	-	-	63
bituminous coal	1089	0.50	0.05	0.45	64
vine shoots	1032	0.49	0.036	0.35	65
garlic peel	947	0.51	0.01	0.50	66
coconut shell	1026	0.58	-	-	67
petroleum coke	990	0.60	0.05	0.55	68
packaging waste	1283	0.69	0.11	0.58	69
PET bottles	1165	0.47	0.01	0.46	70

were found to be 1:5. The 1:4 ratio shows a decrease in all properties compared to 1:5, reinforcing the importance of the correct amount of KOH for achieving optimal activation. The performance decreases further at a 1:3 ratio, indicating insufficient activation, while the 1:6 ratio suggests diminishing returns with excess KOH. At ideal levels, KOH efficiently reacts with rCB, ensuring a balanced reaction and the appropriate quantity of KOH for the formation and stabilization of the desired pore structure. However, beyond a certain threshold (≥1:6), excessive KOH can lead to the blockage of pores due to deposition of potassium compounds within them.[59]

For different activation periods (1−4 h), 4 h was the most effective time interval for producing rCB/ACs, resulting in an enhanced surface area (1028 m^2/g), micropore volume (0.332 cm^3/g), and a more evenly distributed range of pore sizes (0.874 cm^3/g). A longer period of time (3−4 h) allows for the complete realization of chemical processes, such as carbonate formation and gasification, required for opening and expanding pores in rCB/ACs. This is directly connected to the overall reaction rate.[60] Conversely, shorter activation durations (≤3 h) may not provide enough time for these processes to occur fully (788−945 m^2/g, 0.699−0.743 cm^3/g).

Upon comparing the heating rates in the range of 5−13 °C/min, it is evident that the best results for S_{BET} and developed pore structure, of 970 m^2/g and 0.774 cm^3/g, respectively, were attained at 7 °C/min. The consistent trend across different properties indicates a measurable, yet low, impact of the heating rate on rCB/ACs properties. This particular rate achieves an optimal equilibrium between the dispersion of heat and improved kinetics. It is fair to assume that heating rates below 7 °C/min would provide improved contact between the carbon and the molten KOH (>360 °C) before the desired reaction temperature is attained. Moreover, KOH activation leads to the formation of surface oxygen complexes, causing carbon gasification and the release of gases like CO_2 and CO. The use of a particular heating rate threshold contributes to a more regulated release of gas, which might possibly compensate for the enhanced formation of micropores (0.314 cm^3/g), as described by Lozano-Castello et al.[61] Whereas a rate of 5 °C/min may be insufficient, impeding the growth of pores, 10 and 13 °C/min may be excessive, posing a danger of irregular porosity and significant harm to the structure.

The pore size distribution of rCB/ACs for each KOH activation parameter is schematically shown in Figure 4a−d, which proves the previous observations. A comparable PSD has been identified for all carbon samples that were analyzed. The application of KOH as an activator led to an enhancement in microporosity that confirmed previous observations (∼30−40% enhancement). The content of micropores in rCB/AC was significantly improved at a temperature of 800 °C, rCB/KOH ratio of 1:5, heating rate of 7 °C/min, and a time of 4 h, illustrating that the pore size was mainly concentrated in three distinct peaks, situated in the ranges of 0.99−1.09, 1.09−1.30, and 1.43−1.63 nm. Furthermore, it was found that the mesopores had a dominating size located within the range of 2.0−13.49 nm.

In continuation of previous discussions, a comparison of activated carbons synthesized from various precursors via KOH activation is presented in Table 6, showing the textural properties, including BET surface area and porosity, as reported in the literature. It is observed that the synthesized rCB/ACs compare favorably with others in terms of S_{BET}, V_{TOT}, and V_{MIC} values. In the case of V_{MIC}/V_{TOT}, a significant distinction exists, which may be related to the fact that rCB features a rigid, spherical, and aggregated structure.[49] This configuration starkly contrasts with the "model" texture that was earlier identified as optimal for KOH activation, which should ideally develop a high content of micropores.[42] The closed nature of the rCB structure likely restricts potassium accessibility, thereby hindering its penetration and subsequent reactions within the particles. Nevertheless, limited amounts of potassium can still infiltrate the interior of these particles, fostering porosity through both carbon consumption and intercalation.

3.2. Analyzing the Interplay of Factors in the KOH Activation Process. Figure 5a−d displays the XRD patterns of rCB/ACs prior to the washing treatment, providing a thorough examination of the evolution characteristics of KOH throughout activation. The spectra of the rCB/AC products reveal that the primary phases identified in rCB/ACs are K_2CO_3, $K_2CO_3{\cdot}1.5H_2O$, $K_4(CO_3)_2{\cdot}(H_2O)_3$, $KHCO_3$, and K_2O, confirming the presence of carbonates/bicarbonate and oxides as crucial components. According to the existing literature, it is well-acknowledged that carbon elements in precursor materials may initially engage in redox solid−solid interactions, KOH dehydration at 400 °C, and subsequently progress through a solid−liquid state, as detailed in eq 2.[71] Furthermore, the thermal treatment (<700 °C) might result in an excess of compounds from carbonaceous materials, such as carbon monoxide (CO), hydrogen (H_2), carbon dioxide (CO_2), and water vapor (H_2O) as described in eqs 3−5, supporting previous reported findings.[72] Ultimately, the

https://doi.org/10.1021/acsomega.4c03160
ACS Omega 2024, 9, 31814−31831

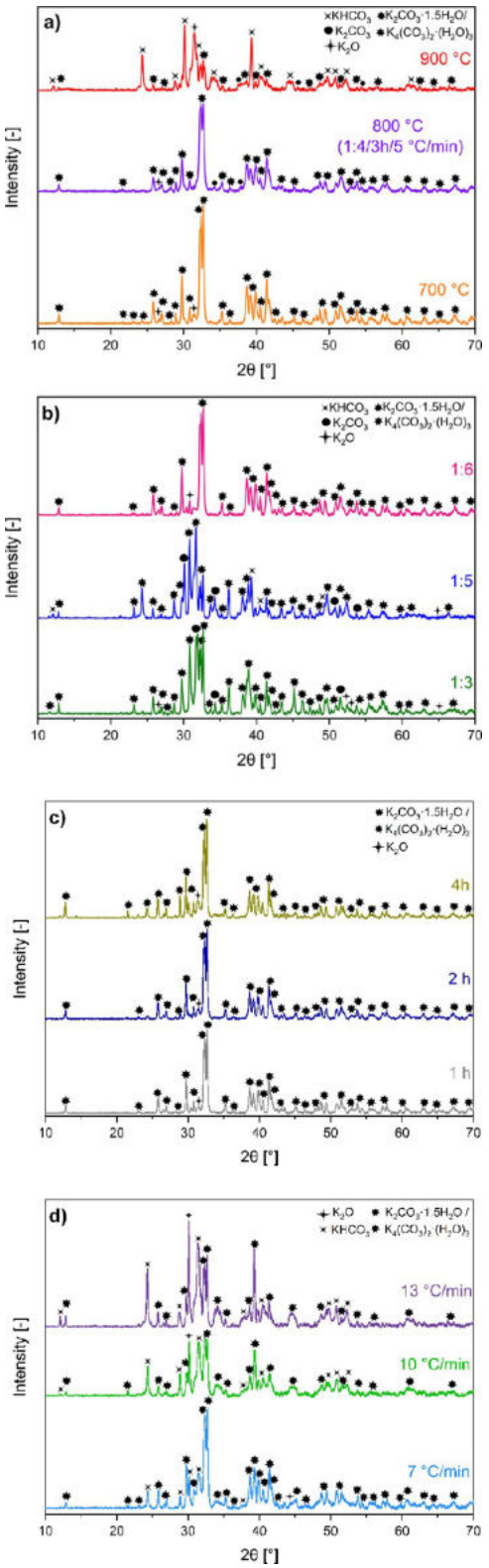

Figure 5. XRD patterns for rCB/ACs before washing treatment related to the effect of KOH activation parameters: temperature (a), mass ratio (b), activation time (c), and heating rate (d).

procedure can involve metallic potassium obtained from decomposed K_2O and K_2CO_3 at temperatures over 750 °C that intercalates into the carbon matrix and is mainly responsible for generating the pore network (eqs 6 and 7). The initial interaction of K with the C-matrix is followed by many supplementary reactions between KOH and carbon, including distinct active intermediates, as proposed by Otowa et al.[73]

$$2KOH \rightarrow K_2O + H_2O \quad (2)$$

$$2KOH + 2C \rightarrow 2CO + 2K + H_2 \quad (3)$$

$$C + H_2O \rightarrow H_2 + CO \quad (4)$$

$$CO + H_2O \rightarrow H_2 + CO_2 \quad (5)$$

$$K_2CO_3 + 2C \rightarrow 2K + 3CO \quad (6)$$

$$C + K_2O \rightarrow 2K + CO \quad (7)$$

To delineate the trajectory of chemical evolution more clearly during the KOH treatment of rCB/ACs, the mechanism of rCB activation is outlined based on the applied experimental setup. This confirms and expands on existing proposals in the field as following.

- Multistage transformation to K_2CO_3, $K_2CO_3{\cdot}1.5H_2O$, and $K_4(CO_3)_3{\cdot}(H_2O)_3$. The resulting peaks of K_2CO_3, $K_2CO_3{\cdot}1.5H_2O$, and $K_4(CO_3)_3{\cdot}(H_2O)_3$ phases for each activation parameters are clearly distinguishable in Figure 5a–d. For all of the examined activation parameters, the reaction might occur at 400 °C with KOH consumption by majority of the carbon atoms in rCB. This leads to a release of H_2, K, while carbon is oxidized to form carbonates, as presented in eq 8. As a second step, pores are generated through the process of carbon gasification in the presence of CO_2, effective at temperatures below 700 °C. Concurrently, this phase facilitates the formation of K_2CO_3, a reaction notably influenced by the textural properties of the raw material. These properties significantly affect CO_2 accessibility, underscoring the importance of physical activation (eq 9).[74] Furthermore, K_2CO_3 can undergo a hydration process in a humid environment, leading to the formation of $K_2CO_3{\cdot}1.5H_2O$ (eq 10). This probably occurs once the rCB/AC samples are taken out from the furnace due to absorption of moisture from the air. The level of hydration is influenced by the surrounding humidity and temperature.

$$6KOH + 2C \rightarrow 2K_2CO_3 + 2K + 3H_2 \quad (8)$$

$$2KOH + CO_2 \rightarrow K_2CO_3 + H_2O \quad (9)$$

$$K_2CO_3 + 1.5H_2O \rightarrow K_2CO_3{\cdot}1.5H_2O \quad (10)$$

$K_4(CO_3)_2{\cdot}(H_2O)_3$, it is most likely produced through a series of reactions involving KOH, CO_2, and water vapor, under the influence of temperature, KOH concentration, and humidity.

- Decomposition of K_2CO_3 to K_2O. The XRD patterns of rCB/ACs in Figure 5a unequivocally prove the detection of K_2O within the rCB/AC samples KOH post-thermal treatment at 800–900 °C. The presence of K_2O, identified in this specific temperature range, provides empirical evidence supporting the breakdown of K_2CO_3 into K_2O and CO/CO_2. This reaction is a thermally driven process that often occurs at temperatures higher than the standard melting point of K_2CO_3 (>700 °C), as shown in eqs 11–13. In addition, the transformation of KOH into K_2O and H_2O occurs at elevated temperatures. The presence of other impurities in the activation

https://doi.org/10.1021/acsomega.4c03160
ACS Omega 2024, 9, 31814–31831

Table 7. Textural Properties Associated to rCB/ACs Produced via Chemical Activation with CH_3COOK, $K_2C_2O_4$, K_2CO_3, and KCl

sample	BET surface area[a] [m^2/g]	total pore volume[b] [cm^3/g]	micropore volume[c] [cm^3/g]	mesopore volume[c] [cm^3/g]	micropore volume/total pore volume [%]
KOH_1:4_800_3_5	945 ± 5.6	0.743	0.303	0.440	36.0
CH_3COOK_1:4_800_3_5	217 ± 2.0	0.240	0.071	0.136	34.3
K_2CO_3_1:4_800_3_5	146 ± 0.3	0.207	0.043	0.197	17.9
$K_2C_2O_4$ _1:4_800_3_5	299 ± 1.1	0.369	0.093	0.276	25.2
KCl_1:4_800_3_5	57 ± 0.08	0.189	0.011	0.178	5.8

[a]Brunauer, Emmett, and Teller method using the Rouquerol criteria. [b]V_{TOT} calculated by N_2 adsorption isotherm at a high relative pressure (~0.99). [c]DFT method by the NLDFT model.

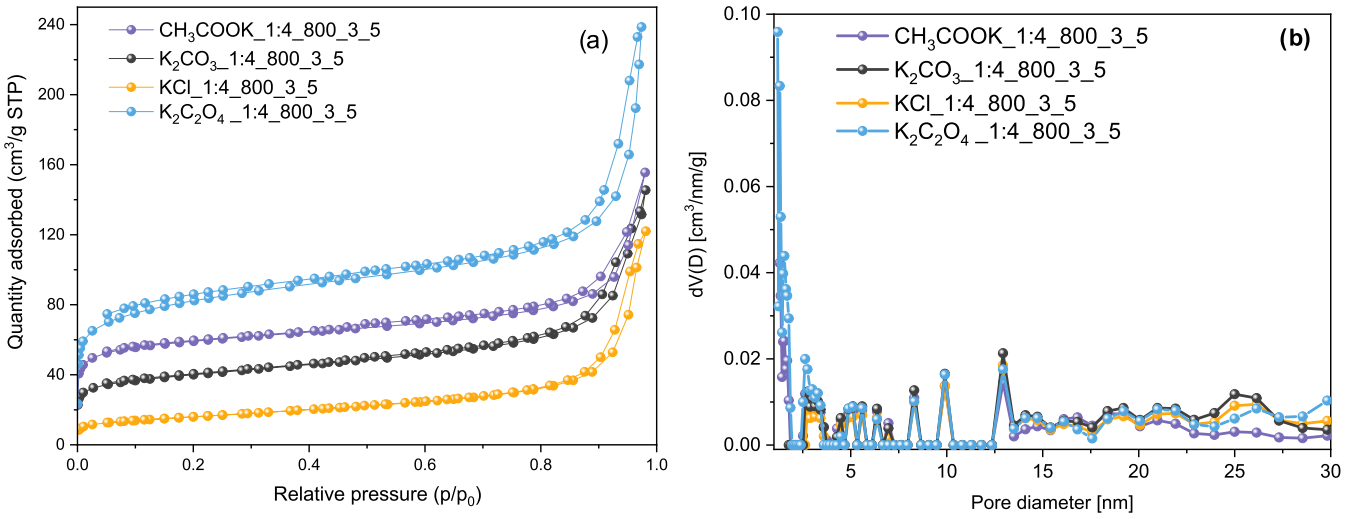

Figure 6. N_2 adsorption−desorption isotherm curves at 77 K (a) and PSD based on the DFT method on carbon slit pores by the NLDFT model (b) of the rCB/ACs obtained through the utilization of CH_3COOK, K_2CO_3, KCl, and $K_2C_2O_4$, as potassium-containing activating agents.

system can influence the overall process as well, potentially altering the temperature required for effective decomposition. K_2O can further react with atmospheric CO_2, leading back to the formation of K_2CO_3.

$$K_2CO_3 \rightarrow K_2O + CO_2 \quad (11)$$

$$K_2CO_3 + C \rightarrow K_2O + 2CO \quad (12)$$

$$2K + CO_2 \rightarrow K_2O + CO \quad (13)$$

- Formation of $KHCO_3$

The presence of the $KHCO_3$ phase is notably indicated in Figure 5a,b,d. Theoretically, its formation in a reversible reaction and stability can be influenced by the partial pressure of CO_2 and the moisture content in the environment. Reversibility mainly refers to the ability of $KHCO_3$ to undergo decomposition into KOH and CO_2 (eq 14), resulting in the establishment of a dynamic equilibrium

$$KOH + CO_2 \Leftrightarrow KHCO_3 \quad (14)$$

3.3. Identification of the Synergetic Role of Potassium and Functional Groups (OH^-, CO_3^{2-}, $COOK^-$, $C_2O_4^{2-}$, Cl^-) in Porosity Development. Table 7 provides an overview of the textural properties of rCB/ACs activated through different K-containing salts, such as CH_3COOK, K_2CO_3, $K_2C_2O_4$, and KCl. Despite the KOH_1:4_800_3 sample, $K_2C_2O_4$_1:4_800_3 stood out with the highest BET surface area (299 m^2/g), total pore volume (0.369 cm^3/g), and micropore volume (0.093 cm^3/g) among the samples. On the other hand, KCl_1:4_800_3 exhibited the lowest values among the tested samples, such as 56.7 m^2/g, 0.189 cm^3/g, and 0.011 cm^3/g, for BET, pore volume, and micropore volume, respectively. Moreover, all rCB/ACs share the same type of N_2 isotherm as KOH, emphasizing uniform adsorption behavior across the studied activators (Figure 6a). It should be noted that their pore size distribution is characterized by a high proportion of mesopores, with clear peaks in size that vary from 2.8 to 13.5 nm, and a broader peak extending up to 30 nm and further to 48 nm (Figure 6b). In addition, rCB/ACs synthesized with potassium oxalate used as an activating agent have exhibited the most developed microporosity among all activators, with the range identified to be between 1.2 and 1.94 nm.

By examining the synergetic role of both potassium ions and its related anions (OH^-, Cl^-, CO_3^{2-}, $C_2O_4^{2-}$, and $COOK^-$) in several chemical compounds, it becomes evident that K-based compounds serve as a powerful activator of rCB/ACs. The effectiveness of potassium-containing agents in generating pore structures within a carbon matrix can be influenced by several factors, the types and amounts of gases released during decomposition, the control over the pore generation step, and the specific chemical reactivity of the compound under the activation conditions. Among the four activators, the development of textural properties can be ranked in the following order: KOH > $K_2C_2O_4$ > CH_3COOK > K_2CO_3 > KCl. The observed findings prove the collaborative specific impact of K and its related anion groups on the formation of a porous

https://doi.org/10.1021/acsomega.4c03160
ACS Omega 2024, 9, 31814−31831

structure and intercalated phases during the overall activation reactions, as given in Figure 7.

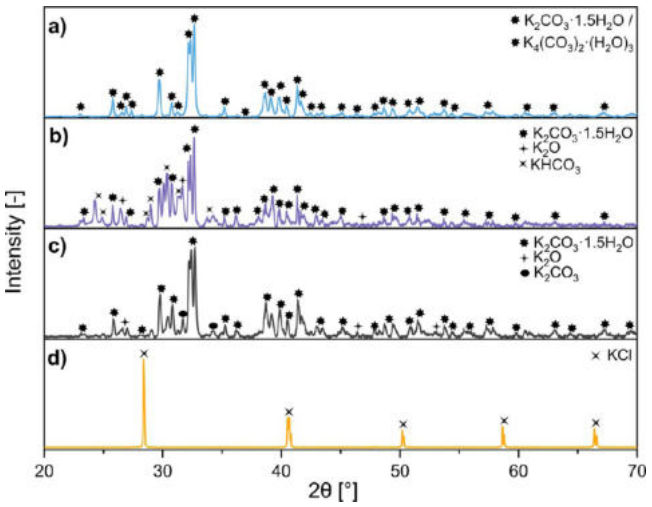

Figure 7. XRD patterns for rCB/ACs before washing treatment produced with CH_3COOK (a), $K_2C_2O_4$ (b), K_2CO_3 (c), and KCl (d) as potassium-containing activating agents.

Upon reviewing the data of rCB/ACs from Table 7, the efficiency of KOH is clearly noticed, as suggested by the existing literature.[75] The high molar content of K and the presence of OH^- groups are likely responsible for the enhancement of textural characteristics, especially microporosity. The potassium hydroxide undergoes dissociation during high-temperature activation, resulting in the formation of potassium cations (K^+) and hydroxide (OH^-) ions. Hydroxyl ions have the ability to chemically attack and weaken the bonds in the carbon substrate, releasing volatile substances, thus efficiently converting the rCB into more porous ACs.[76] This is also consistent with the quantitative energy-dispersive X-ray spectroscopy analysis (Table 8) and the corresponding

Table 8. EDS Semiquantitative Analysis of rCB/AC Samples

sample	K [wt %]	C [wt %]	O [wt %]
KOH_1:4_800_3_5	29.5	31.7	38.8
CH_3COOK_1:4_800_3_5	20.9	49.8	29.3
K_2CO_3_1:4_800_3_5	13.1	62.0	24.9
$K_2C_2O_4$ _1:4_800_3_5	27.5	37.9	34.6
KCl_1:4_800_3_5	19.7	76.0	4.4

SEM-EDS elemental mapping of potassium images (Figure 8). The EDS image of KOH_1:4_800_3_5 shows a high-intensity potassium signal, suggesting a high concentration of K (29.5 wt %) uniformly distributed throughout the rCB/AC sample.

In contrast, CH_3COOK, K_2CO_3, and $K_2C_2O_4$ have lower K/C and K/O ratios. As reported by Yang et al.,[77] this enables the production of a greater amount of CO_2 and H_2O during activation, leading to the formation of larger pores and a decrease in specific surface areas. For K_2CO_3 and CH_3COOK, the EDS mapping of AC/rCB shows a variance in the K distribution, suggesting inhomogeneity due to the local formation of new K-enriched compounds or the dispersal of volatile products. K_2CO_3 has lower reactivity toward carbon materials compared to KOH and a much higher melting point. The pure form of K_2CO_3 melts at 891 °C. At 800 °C, K_2CO_3 is not expected to be completely liquefied but still can soften, releasing a significant amount of CO_2 (above 650 °C) and K_2O (below 650 °C), with possible subsequent formation of salt complexes (~475 °C) on the surface of rCB/ACs (eqs 7−9). On the other hand, the BSE image and EDS map of CH_3COOK_1:4_800_3_5 show a more heterogeneous distribution of potassium with areas of higher and lower K concentration. Smaller particles and some individual bright spots can be identified, suggesting possible agglomeration or coagulation of potassium-rich phases upon thermal decomposition of CH_3COOK to K_2CO_3 (>303 °C), which undergoes a series of reactions with the carbon structure to produce K-species. In the case of $K_2C_2O_4$, the EDS mapping reveals a more intense and patchy spread of potassium, indicative of its higher overall presence (27.5 wt %) than the smoother distributions observed for K_2CO_3 and CH_3COOK. Lastly, KCl has been found to be ineffective as an activator, which is primarily attributed to its melting point (~770 °C), and weak reactivity with rCB, according to the XRD patterns in Figure 7 and SEM-EDS image in Figure 8.

3.4. Examining the Phase Impact of KOH Activation: Solid/Liquid State vs Gas State Reactions. The process of activating rCB with KOH requires a complex combination of chemical reactions, including not only the conventional solid−solid (<380 °C) and solid−liquid (≥406 °C) interactions[78] but also a substantial solid−gas reaction. The use of KOH vapor contributes to the enhancement of the rCB/ACs characteristics, as shown in Table 9 and Figure 9a,b. The gaseous KOH etches the carbon surface and creates pores when the temperature exceeds 600 °C, resulting in the release of gases such as CO_2 and H_2O. This phenomenon induces a substantial modification in the surface and pore morphology of the rCB. The S_{BET} value increased from 55 m^2/g to 118, while the V_{TOT} increased to 0.239 cm^3/g. Although the growth of V_{MIC} was not significant (0.033 cm^3/g), the total change in adsorbed quantity of N_2 and PSD suggests a modification in the texture of the rCB.

The EDS mapping of the rCB sample postreaction with vapor-phase KOH (Figure 10) presents a homogeneous distribution of oxygen, indicating the oxygenation of the carbon structure. Moreover, the rCB/ACs appear to have an irregular K compound distribution from the reaction with vapor-phase KOH. EDS findings directly corroborate with XRD analysis (Figure 11), identifying the formation of $KHCO_3$, K_2O, and K_2CO_3 within the sample, which are the expected products of the gas−solid reaction. The presence of $KHCO_3$ (60 wt %), K_2O (10 wt %), and K_2CO_3 (30 wt %) in the unwashed rCB/ACs samples indicates that they may be involved in the alterations in textural qualities, including specific surface area and porosity. The formation of $KHCO_3$, K_2O, and K_2CO_3 is based on the reaction between gaseous KOH and carbon oxidation. The relative content of C (75 wt %), O (17.8 wt %), and K (7.2 wt %) further supports the impact of the gas−solid reaction on rCB/ACs textural properties.

3.5. Comparative Analysis: Potassium (K^+) vs Sodium (Na^+) Ions. The isotherms and textural characteristics presented in Figure 12a and Table 10 indicate that KOH outperforms NaOH in the chemical activation of rCB/ACs. The utilization of NaOH as an activator led to the development of rCB/ACs that possessed S_{BET}, V_{TOT}, and V_{MIC} of 480 m^2/g, 0.523 cm^3/g, and 0.146 cm^3/g, respectively. Furthermore, the improvement in microporosity (Figure

https://doi.org/10.1021/acsomega.4c03160
ACS Omega 2024, 9, 31814−31831

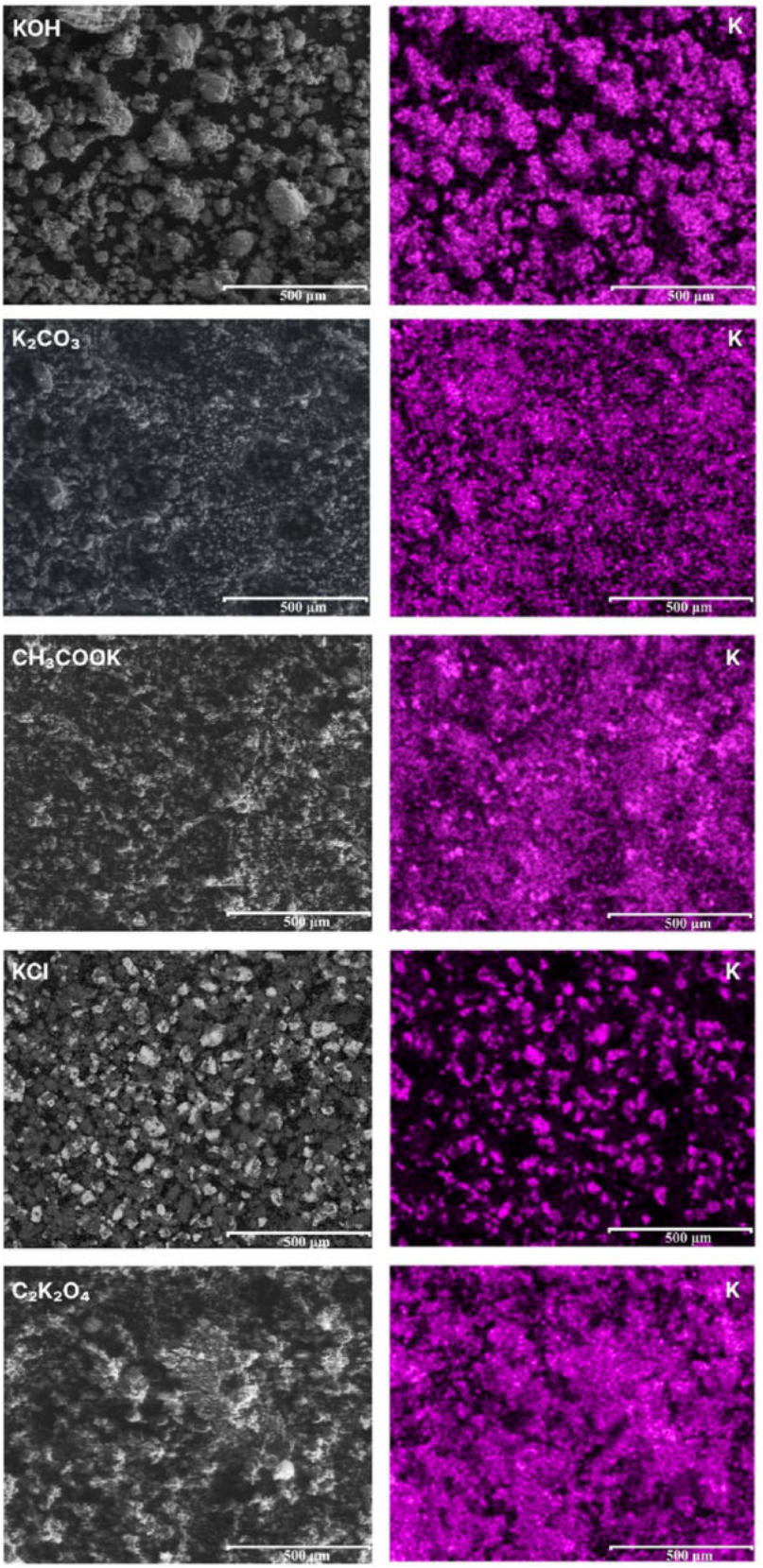

Figure 8. SEM-EDS elemental mapping of potassium for rCB/ACs before washing treatment obtained through KOH, K_2CO_3, CH_3COOK, KCl, and $C_2K_2O_4$ activation.

12b,c) may be attributed to the nature of alkali metal cation (K^+ vs Na^+), as studied by Guo et al.[79] KOH demonstrated a greater propensity to interact with the carbon atoms from rCB, resulting in the formation of micropores in the range of 1.1−1.64 nm and mesopores that vary from 2 to 8.7 nm. On the other hand, NaOH exhibited a greater tendency to generate

https://doi.org/10.1021/acsomega.4c03160
ACS Omega 2024, 9, 31814−31831

Table 9. Textural Properties Associated with rCB/ACs Produced through Gas−Solid Reaction during KOH Activation

sample	BET surface area[a] [m^2/g]	total pore volume[b] [cm^3/g]	micropore volume[c] [cm^3/g]	mesopore volume[c] [cm^3/g]	micropore volume/total pore volume [%]
rCB	55 ± 0.8	0.170			
KOH(vapor) _1:4_800_3_5	118 ± 0.2	0.239	0.033	0.206	13.8

[a]Brunauer, Emmett, and Teller method using the Rouquerol criteria. [b]V_{TOT} calculated by N_2 adsorption isotherm at a high relative pressure (~0.99). [c]DFT method by the NLDFT model.

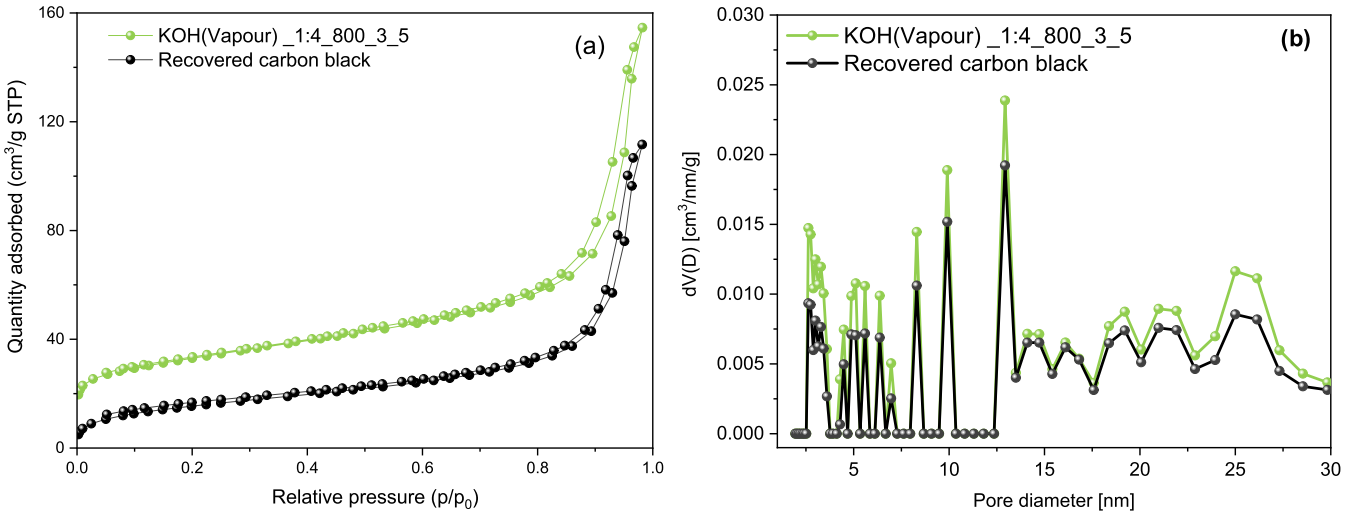

Figure 9. N_2 adsorption−desorption isotherm curves at 77 K (a) and PSD based on the DFT method on carbon slit pores by the NLDFT model (b) of the rCB and rCB/ACs produced through gas−solid reaction during KOH activation.

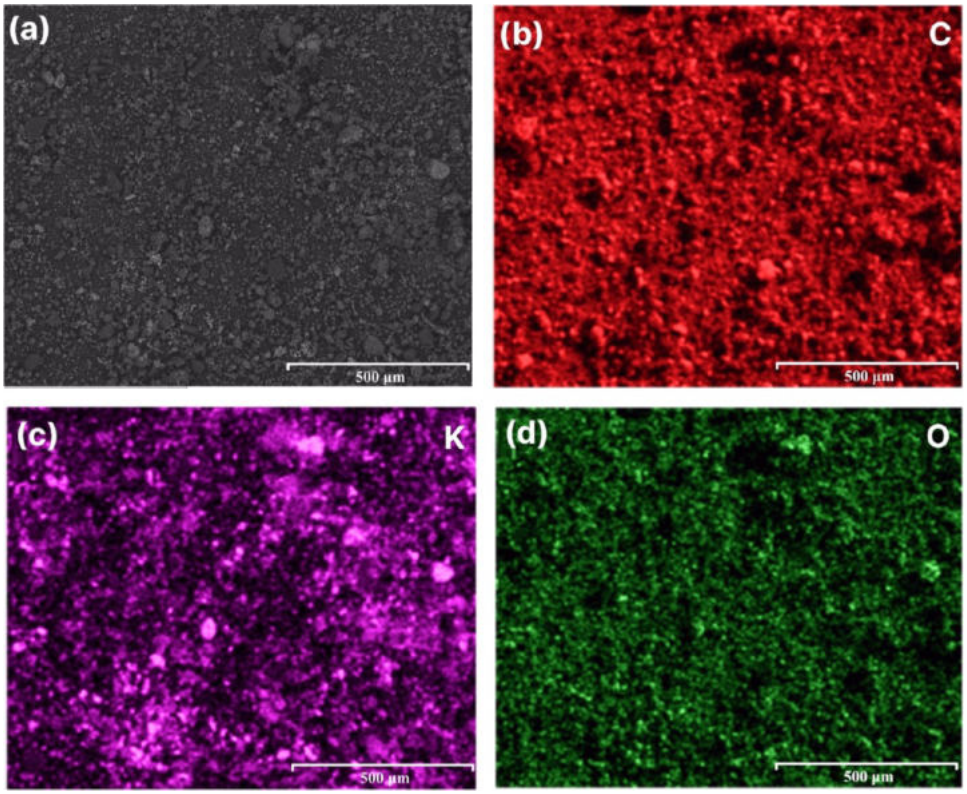

Figure 10. EDS analysis of KOH(vapor)_1:4_800_3_5; (a) representative SEM image and corresponding elemental mapping analysis: C (b), K (c), and O (d).

mesoporosity when the pore width exceeded 9.5 nm. As alkali metal hydroxides intercalate in the carbon network, they function as electron donors during gasification. This property of the hydroxides is most probably responsible for the

https://doi.org/10.1021/acsomega.4c03160
ACS Omega 2024, 9, 31814−31831

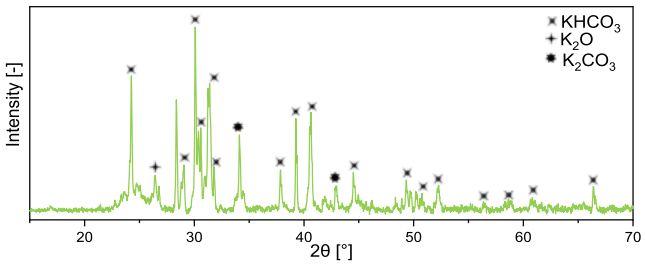

Figure 11. XRD pattern for unwashed rCB/ACs produced through a gas−solid reaction during KOH activation.

activation process. Yahya et al.[80] and Rambabu et al.[81] have both reported similar findings. Additionally, the intercalation of alkali metals (Na or K) depends upon the crystallinity of the precursor used during the activation procedure, since the structural arrangement, which was formerly overlooked, plays a crucial role. Linares-Solano, Lillo-Ródenas, Marco-Lozar et al.[82] stated that NaOH is more suitable for carbons with poor ordered atom arrangement (nongraphitic structure), whereas KOH produces better results for those displaying some organizational regularity (graphite-like structure). Based on this understanding, it can be assumed that rCB/ACs tend to have a more crystalline phase than an amorphous one. This makes KOH a preferred choice as an activator due to its effectiveness in engaging with and enhancing the organized, graphite-like arrangement of atoms.

The comparison of EDS mapping between NaOH-activated rCB (Figure 13) and KOH-activated rCB (Figure 10) and semiquantitative analysis suggest that NaOH activation results in a lower distribution of alkali metal (Na: 19.8 wt %) compared to KOH (K: 29.5 wt %) but similar oxygen content (O: 37.8 wt % vs O: 38.8 wt %). The XRD analysis presented in Figure 14, which detected only Na_2CO_3 as the primary phase in the NaOH-treated rCB/ACs, points to a more limited set of chemical reactions in the case of NaOH compared to that obtained with KOH treatment, where $KHCO_3$, K_2O, and K_2CO_3 were identified. This is likely because K^+, with its larger ionic radius (152 pm) and higher reactivity than Na^+ (116 pm), is more effective at incorporating in the carbon structure of rCB and reacting with CO_2. On the contrary, the stronger ionic bonds and lower polarizing power of Na^+ relative to K^+ might potentially affect the transport and interaction with the carbon matrix. Therefore, potassium not only promotes more reactions but also leads to more pronounced porosity and surface complexity.

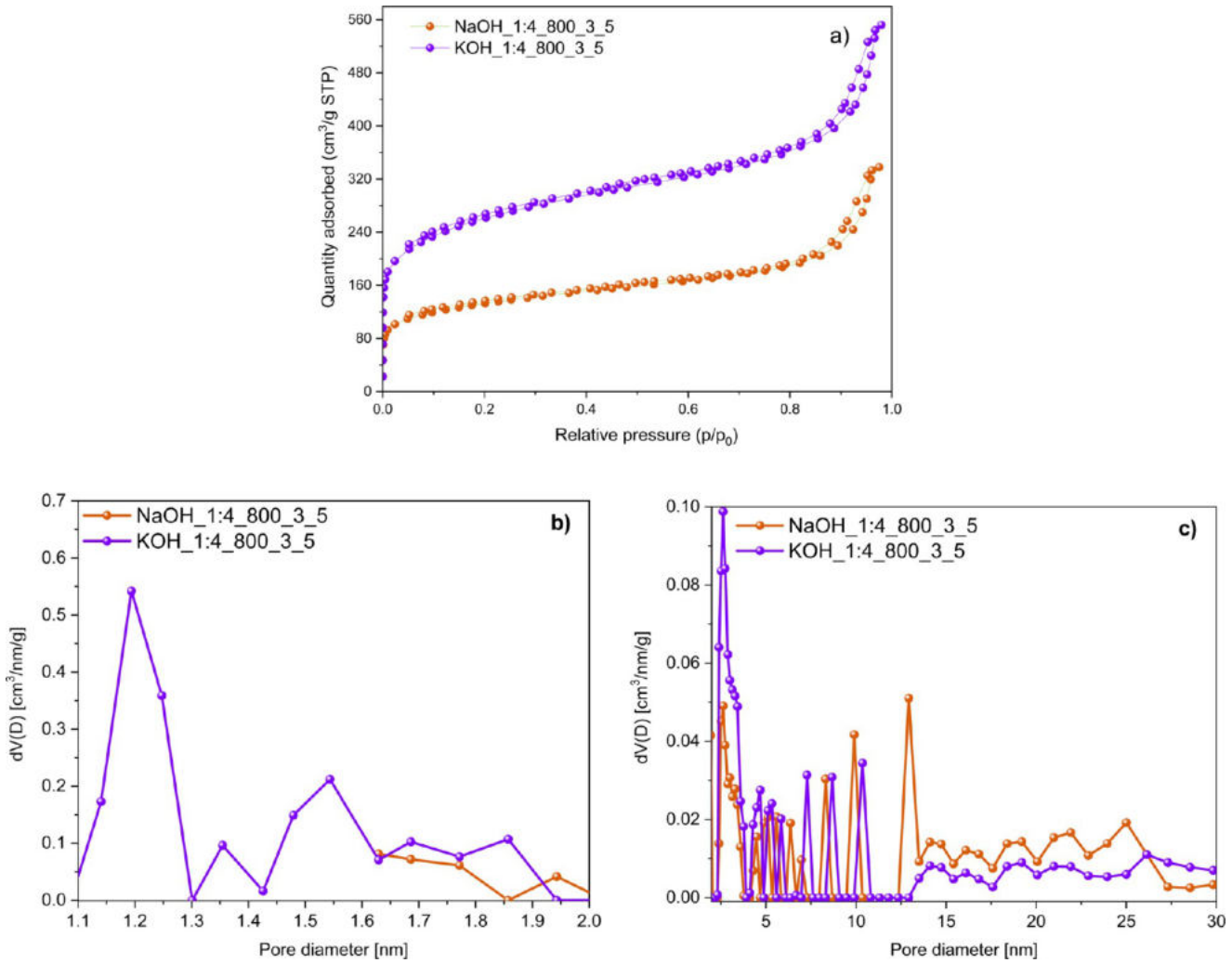

Figure 12. N_2 adsorption−desorption isotherm curves at 77 K (a), PSD based on DFT method on carbon slit pores by the NLDFT model for the pore diameter in the ranges of 1.1−2 nm (b) and 2−30 nm (c) of the rCB/ACs obtained by KOH/NaOH activation.

https://doi.org/10.1021/acsomega.4c03160
ACS Omega 2024, 9, 31814−31831

Table 10. Textural Properties Associated with rCB/ACs Obtained by NaOH Activation[abc]

sample	BET surface area [m^2/g]	total pore volume [cm^3/g]	micropore volume [cm^3/g]	mesopore volume [cm^3/g]	micropore volume/total pore volume [%]
KOH_1:4_800_3_5	945 ± 5.6	0.743	0.303	0.440	36
NaOH_1:4_800_3_5	480 ± 0.9	0.523	0.146	0.377	28

[a]Brunauer, Emmett, and Teller method using the Rouquerol criteria. [b]V_{TOT} calculated by the N_2 adsorption isotherm at a high relative pressure (~0.99). [c]DFT method by the NLDFT model.

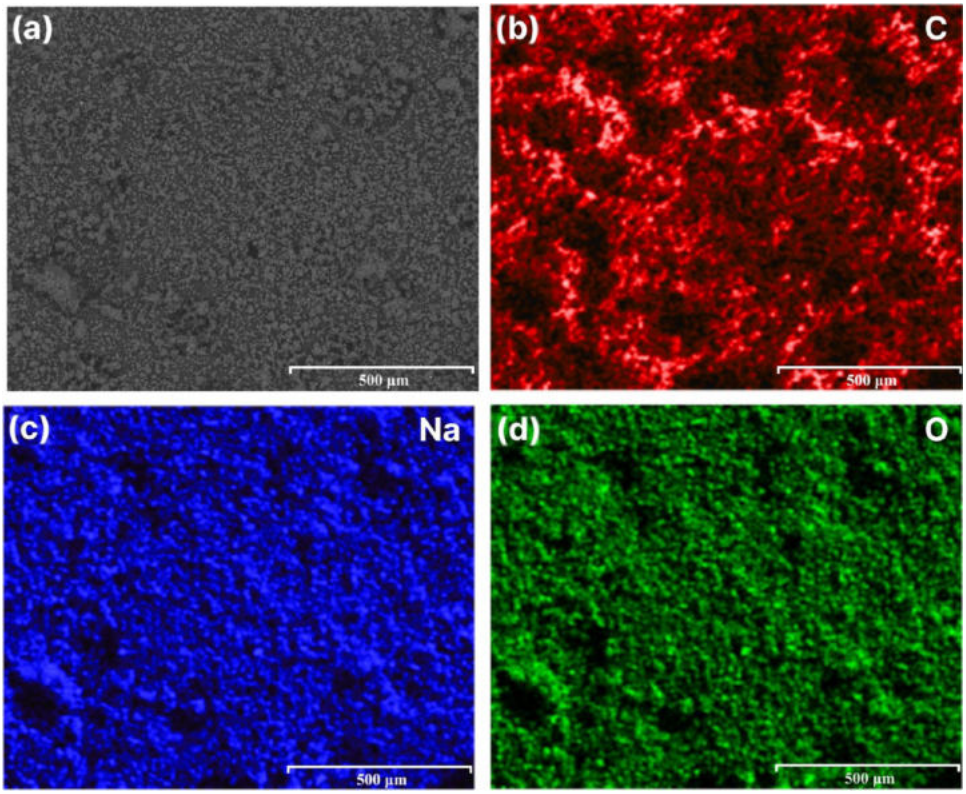

Figure 13. EDS analysis of the NaOH-activated rCB; (a) representative EDS image and corresponding elemental mapping analysis: C (b), Na (c), and O (d).

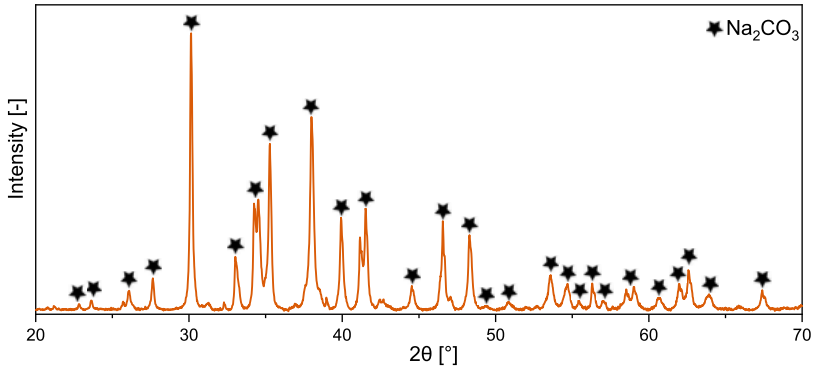

Figure 14. XRD patterns for unwashed rCB/ACs produced through NaOH activation.

4. CONCLUSIONS

In this study, the activation mechanism of rCB using potassium-based activators was explored to efficiently transform ELTs into ACs. The objectives were to determine the optimal activation conditions and analyze textural changes, explore the interactions between rCB and potassium alkalis, and unveil a universal process for efficient rCB activation. Techniques such as N_2 adsorption−desorption at 77 K, XRD, and SEM-EDS were used to investigate the structural and chemical properties of the rCB/ACs. The study identified the below.

- The most effective KOH activation parameters for enhancing the textural properties of ACs were determined, which include an activation temperature of 800 °C, a heating rate of 7 °C/min, a KOH to rCB ratio of 1:5, and a process duration of 4 h. These

https://doi.org/10.1021/acsomega.4c03160
ACS Omega 2024, 9, 31814−31831

conditions were found to be optimal for achieving the desired improvements in specific surface area, total pore volume, and micro/mesoporosity.

- XRD patterns of the rCB/ACs products revealed the presence of key phases such as K_2CO_3, $K_2CO_3 \cdot 1.5H_2O$, $K_4(CO_3)_2 \cdot (H_2O)_3$, $KHCO_3$, and K_2O. This confirmed the significant role of carbonates, bicarbonates, and oxides in the activated products, indicating a complex chemical transformation during the activation process. This order of importance was shown to be correlated with the potassium content and its distribution, as revealed using SEM-EDS analysis. The rank of activation potency, from highest to lowest, was as follows: KOH > $K_2C_2O_4$ > CH_3COOK > K_2CO_3 > KCl.
- The impact of the KOH gas−solid interaction with rCB suggested that improvements are not solely attributed to liquid/solid−solid reactions.
- The KOH activation was primarily attributed to the nature of the alkali metal cation and graphite-like structure of rCB. This emphasizes the importance of the specific chemical characteristics of the activating agent in influencing the final properties of the rCB/ACs.

In essence, the research highlights effective strategies for producing rCB/ACs with superior textural properties, underscoring the significance of carefully chosen activation conditions and the role of potassium-containing activating agents. Moreover, it sets the stage for future studies to explore the potential environmental benefits of utilizing such materials in specific sorption applications, such as water and air purification.

AUTHOR INFORMATION

Corresponding Author

Bartosz Dziejarski − *Department of Chemistry and Chemical Engineering, Division of Energy and Materials, Chalmers University of Technology, SE-412 96 Gothenburg, Sweden; Department of Space, Earth and Environment, Division of Energy Technology, Chalmers University of Technology, SE-412 96 Gothenburg, Sweden; Faculty of Environmental Engineering, Wroclaw University of Science and Technology, 50-370 Wroclaw, Poland;* orcid.org/0000-0001-6631-1985; Email: bartoszd@chalmers.se

Authors

Robin Faust − *Department of Chemistry and Chemical Engineering, Division of Energy and Materials, Chalmers University of Technology, SE-412 96 Gothenburg, Sweden;* orcid.org/0000-0001-5614-3578

Jarosław Serafin − *Department of Inorganic and Organic Chemistry, University of Barcelona, 08028 Barcelona, Spain*

Renata Krzyżyńska − *Faculty of Environmental Engineering, Wroclaw University of Science and Technology, 50-370 Wroclaw, Poland*

Klas Andersson − *Department of Space, Earth and Environment, Division of Energy Technology, Chalmers University of Technology, SE-412 96 Gothenburg, Sweden; Department of Chemical Engineering, University of Utah, Salt Lake City, Utah 84112, United States;* orcid.org/0000-0001-5968-9082

Pavleta Knutsson − *Department of Chemistry and Chemical Engineering, Division of Energy and Materials, Chalmers University of Technology, SE-412 96 Gothenburg, Sweden*

Complete contact information is available at: https://pubs.acs.org/10.1021/acsomega.4c03160

Notes

The authors declare no competing financial interest.

ACKNOWLEDGMENTS

This work was supported by the Area of Advance Energy at Chalmers University of Technology (Project No. C2023-0121-15).

REFERENCES

(1) Abbas-Abadi, M. S.; Kusenberg, M.; Shirazi, H. M.; Goshayeshi, B.; Van Geem, K. M. Towards full recyclability of end-of-life tires: Challenges and opportunities. *J. Cleaner Prod.* **2022**, *374*, No. 134036.

(2) Gomes, F. O.; Rocha, M. R.; Alves, A.; Ratola, N. A review of potentially harmful chemicals in crumb rubber used in synthetic football pitches. *J. Hazard. Mater.* **2021**, *409*, No. 124998.

(3) Arabiourrutia, M.; Lopez, G.; Artetxe, M.; Alvarez, J.; Bilbao, J.; Olazar, M. Waste tyre valorization by catalytic pyrolysis−A review. *Renewable Sustainable Energy Rev.* **2020**, *129*, No. 109932.

(4) Bowles, A. J.; Wilson, A. L.; Fowler, G. D. Synergistic benefits of recovered carbon black demineralisation for tyre recycling. *Resour., Conserv. Recycl.* **2023**, *198*, No. 107124.

(5) Bhattarai, R. M.; Chhetri, K.; Natarajan, S.; Saud, S.; Kim, S. J.; Mok, Y. S. Activated carbon derived from cherry flower biowaste with a self-doped heteroatom and large specific surface area for supercapacitor and sodium-ion battery applications. *Chemosphere* **2022**, *303*, No. 135290.

(6) Acevedo, S.; Giraldo, L.; Moreno-Piraján, J. C. Adsorption of CO_2 on activated carbons prepared by chemical activation with cupric nitrate. *ACS Omega* **2020**, *5* (18), 10423−10432.

(7) Caicedo Salcedo, O. D.; Vargas, D. P.; Giraldo, L.; Moreno-Piraján, J. C. Study of mercury [Hg (II)] adsorption from aqueous solution on functionalized activated carbon. *ACS Omega* **2021**, *6* (18), 11849−11856.

(8) Heidarinejad, Z.; Dehghani, M. H.; Heidari, M.; Javedan, G.; Ali, I.; Sillanpää, M. Methods for preparation and activation of activated carbon: a review. *Environ. Chem. Lett.* **2020**, *18*, 393−415.

(9) González-García, P. Activated carbon from lignocellulosics precursors: A review of the synthesis methods, characterization techniques and applications. *Renewable Sustainable Energy Rev.* **2018**, *82*, 1393−1414.

(10) Reza, M. S.; Yun, C. S.; Afroze, S.; Radenahmad, N.; Bakar, M. S. A.; Saidur, R.; Juntakan, T.; Azad, A. K. Preparation of activated carbon from biomass and its' applications in water and gas purification, a review. *Arab J. Basic Appl. Sci.* **2020**, *27* (1), 208−238.

(11) Zhang, S.; Zheng, M.; Tang, Y.; Zang, R.; Zhang, X.; Huang, X.; Pang, H. Understanding synthesis−structure−performance correlations of nanoarchitectured activated carbons for electrochemical applications and carbon capture. *Adv. Funct. Mater.* **2022**, *32* (40), No. 2204714.

(12) Garcés-Polo, S. I.; Vargas, G. d. J. C.; Estupiñán, P. R.; Hernández-Barreto, D. F.; Giraldo, L.; Moreno-Piraján, J. C. CO_2 adsorption on carbonaceous materials obtained from forestry and urban waste materials: a comparative study. *Environ. Sci. Pollut. Res.* **2023**, 1−16.

(13) Vieira, Y.; Dotto, G. L. Trends and Perspectives Towards Activated Carbon and Activated Carbon-derived Materials in Environmental Catalysis Applications. In *Activated Carbon: Progress and Applications* 2023; pp 206−232.

(14) Feng, P.; Li, J.; Wang, H.; Xu, Z. Biomass-based activated carbon and activators: preparation of activated carbon from corncob by chemical activation with biomass pyrolysis liquids. *ACS Omega* **2020**, *5* (37), 24064−24072.

(15) Zhao, Z.; Sun, L.; Li, Y.; Feng, W. Polymer-derived carbon materials for energy storage devices: A mini review. *Carbon* **2023**, *210*, No. 118066.

(16) Kiełbasa, K.; Bayar, Ş.; Varol, E. A.; Sreńscek-Nazzal, J.; Bosacka, M.; Miądlicki, P.; Michalkiewicz, B.; et al. Carbon dioxide adsorption over activated carbons produced from molasses using H_2SO4, H_3PO_4, HCl, NaOH, and KOH as activating agents. *Molecules* **2022**, *27* (21), No. 7467.
(17) Wang, B.; Lan, J.; Bo, C.; Gong, B.; Ou, J. Adsorption of heavy metal onto biomass-derived activated carbon. *RSC Adv.* **2023**, *13* (7), 4275−4302.
(18) Khoshraftar, Z.; Masoumi, H.; Ghaemi, A. Characterization and evaluation of low-cost biomass-based-AC for CO_2 capture: A review. *Case Stud. Chem. Environ. Eng.* **2023**, No. 100373.
(19) Wang, Q.; Li, T.; Tian, H.; Zou, D.; Zeng, J.; Chen, S.; Xie, H.; Zhou, G. Effect of pore size distribution of biomass activated carbon adsorbents on the adsorption capacity. *J. Chem. Technol. Biotechnol.* **2024**, *99*, 1148.
(20) Zou, R.; Yang, Z.; Zhang, J.; Lei, R.; Zhang, W.; Fnu, F.; Tsan, D.; Heyne, J.; Zhang, X.; Ruan, R.; Lei, H. Machine learning application for predicting key properties of activated carbon produced from lignocellulosic biomass waste with chemical activation. *Bioresour. Technol.* **2024**, *399*, No. 130624.
(21) Nandi, R.; Jha, M. K.; Guchhait, S. K.; Sutradhar, D.; Yadav, S. Impact of KOH activation on rice husk derived porous activated carbon for carbon capture at flue gas alike temperatures with high CO_2/N_2 selectivity. *ACS Omega* **2023**, *8* (5), 4802−4812.
(22) Pimentel, C. H.; Díaz-Fernández, L.; Gómez-Díaz, D.; Freire, M. S.; González-Álvarez, J. Separation of CO_2 using biochar and KOH and ZnCl2 activated carbons derived from pine sawdust. *J. Environ. Chem. Eng.* **2023**, *11* (6), No. 111378.
(23) Mani, D.; Elango, D.; Priyadharsan, A.; Al-Humaid, L. A.; Al-Dahmash, N. D.; Ragupathy, S.; Jayanthi, H.; Ahn, Y. H. Groundnut shell chemically treated with KOH to prepare inexpensive activated carbon: Methylene blue adsorption and equilibrium isotherm studies. *Environ. Res.* **2023**, *231*, No. 116026.
(24) Serafin, J.; Vikram, S.; Dziejarski, B.; Sahoo, S. An environmentally friendly synthesis method of activated carbons based on subabul (Leucaena leucocephala) sawdust waste for CO_2 adsorption. *J. Cleaner Prod.* **2023**, *412*, No. 137406.
(25) Deepak, K. R.; Mohan, S.; Dinesha, P.; Balasubramanian, R. CO_2 uptake by activated hydrochar derived from orange peel (Citrus reticulata): Influence of carbonization temperature. *J. Environ. Manage.* **2023**, *342*, No. 118350.
(26) Mistar, E. M.; Alfatah, T.; Supardan, M. D. Synthesis and characterization of activated carbon from Bambusa vulgaris striata using two-step KOH activation. *J. Mater. Res. Technol.* **2020**, *9* (3), 6278−6286.
(27) Sakhiya, A. K.; Baghel, P.; Anand, A.; Vijay, V. K.; Kaushal, P. A comparative study of physical and chemical activation of rice straw derived biochar to enhance Zn^{+2} adsorption. *Bioresour. Technol. Rep.* **2021**, *15*, No. 100774.
(28) Dahou, T.; Defoort, F.; Jeguirim, M.; Dupont, C. Towards understanding the role of K during biomass steam gasification. *Fuel* **2020**, *282*, No. 118806.
(29) Chen, W.; Gong, M.; Li, K.; Xia, M.; Chen, Z.; Xiao, H.; Fang, Y.; Chen, Y.; Yang, H.; Chen, H. Insight into KOH activation mechanism during biomass pyrolysis: Chemical reactions between O-containing groups and KOH. *Appl. Energy* **2020**, *278*, No. 115730.
(30) Zhang, X.; Gang, D. D.; Zhang, J.; Lei, X.; Lian, Q.; Holmes, W. E.; Zappi, M.; Yao, H. Insight into the activation mechanisms of biochar by boric acid and its application for the removal of sulfamethoxazole. *J. Hazard. Mater.* **2022**, *424*, No. 127333.
(31) Jiménez, V.; Sánchez, P.; Valverde, J. L.; Romero, A. Effect of the nature the carbon precursor on the physico-chemical characteristics of the resulting activated carbon materials. *Mater. Chem. Phys.* **2010**, *124* (1), 223−233.
(32) Borghei, S. A.; Zare, M. H.; Ahmadi, M.; Sadeghi, M. H.; Marjani, A.; Shirazian, S.; Ghadiri, M. Synthesis of multi-application activated carbon from oak seeds by KOH activation for methylene blue adsorption and electrochemical supercapacitor electrode. *Arab. J. Chem.* **2021**, *14* (2), No. 102958.
(33) Guerrera, J. V.; Burrow, J. N.; Eichler, J. E.; Rahman, M. Z.; Namireddy, M. V.; Friedman, K. A.; Mullins, C. B.; et al. Evaluation of two potassium-based activation agents for the production of oxygen- and nitrogen-doped porous carbons. *Energy Fuels* **2020**, *34* (5), 6101−6112.
(34) Gómez, I. C.; Cruz, O. F., Jr; Silvestre-Albero, J.; Rambo, C. R.; Escandell, M. M. Role of KCl in activation mechanisms of KOH-chemically activated high surface area carbons. *J. CO_2 Util.* **2022**, *66*, No. 102258.
(35) Khuong, D. A.; Trinh, K. T.; Nakaoka, Y.; Tsubota, T.; Tashima, D.; Nguyen, H. N.; Tanaka, D. The investigation of activated carbon by K_2CO_3 activation: Micropores-and macropores-dominated structure. *Chemosphere* **2022**, *299*, No. 134365.
(36) Garba, Z. N.; Hussin, M. H.; Galadima, A.; Lawan, I. Potentials of Canarium schweinfurthii seed shell as a novel precursor for CH_3COOK activated carbon: statistical optimization, equilibrium and kinetic studies. *Appl. Water Sci.* **2019**, *9*, 1−13.
(37) Kontchouo, F. M. B.; Jiang, Y.; Liang, J.; Fan, M.; Shao, Y.; Zhang, L.; Zhang, S.; Hu, X. Activation of biomass (cola nut shell) with KOH and $K_2C_2O_4$: The distinct influence on evolution of volatiles and pore structures of activated carbon. *J. Energy Inst.* **2023**, *109*, No. 101288.
(38) Nieto-Márquez, A.; Atanes, E.; Morena, J.; Fernández-Martínez, F.; Valverde, J. L. Upgrading waste tires by chemical activation for the capture of SO_2. *Fuel Process. Technol.* **2016**, *144*, 274−281.
(39) Al-Rahbi, A. S.; Williams, P. T. Production of activated carbons from waste tyres for low temperature NOx control. *Waste Manage.* **2016**, *49*, 188−195.
(40) Hofman, M.; Pietrzak, R. Adsorbents obtained from waste tires for NO_2 removal under dry conditions at room temperature. *Chem. Eng. J.* **2011**, *170* (1), 202−208.
(41) Sun, J.; Brady, T. A.; Rood, M. J.; Lehmann, C. M.; Rostam-Abadi, M.; Lizzio, A. A. Adsorbed natural gas storage with activated carbons made from Illinois coals and scrap tires. *Energy Fuels* **1997**, *11* (2), 316−322.
(42) Stavropoulos, G. G. Precursor materials suitability for super activated carbons production. *Fuel Process. Technol.* **2005**, *86* (11), 1165−1173.
(43) López, F.; Centeno, T. A.; Rodríguez, O.; Alguacil, F. J. Preparation and characterization of activated carbon from the char produced in the thermolysis of granulated scrap tyres. *J. Air Waste Manage. Assoc.* **2013**, *63* (5), 534−544.
(44) Halim, N.; Tajima, A.; Asano, S.; Kudo, S.; Hayashi, J. I. Change in catalytic activity of potassium during CO_2 gasification of char. *Energy Fuels* **2020**, *34* (1), 225−234.
(45) Arnold, R. A.; Hill, J. M. Catalysts for gasification: a review. *Sustainable Energy Fuels* **2019**, *3* (3), 656−672.
(46) Safar, M.; Lin, B. J.; Chen, W. H.; Langauer, D.; Chang, J. S.; Raclavska, H.; Pétrissans, A.; Rousset, P.; Pétrissans, M. Catalytic effects of potassium on biomass pyrolysis, combustion and torrefaction. *Appl. Energy* **2019**, *235*, 346−355.
(47) Miao, Z.; Guo, Z.; Qiu, G.; Zhang, Y.; Wu, J. Synthesis of activated carbon from high-ash coal gasification fine slag and their application to CO_2 capture. *J. CO_2 Util.* **2021**, *50*, No. 101585.
(48) Li, S. Y.; Li, W. H.; Wu, X. L.; Tian, Y.; Yue, J.; Zhu, G. Pore-size dominated electrochemical properties of covalent triazine frameworks as anode materials for K-ion batteries. *Chem. Sci.* **2019**, *10* (33), 7695−7701.
(49) Dziejarski, B.; Hernández-Barreto, D. F.; Moreno-Piraján, J. C.; Giraldo, L.; Serafin, J.; Knutsson, P.; Andersson, K.; Krzyżyńska, R. Upgrading recovered carbon black (rCB) from industrial-scale end-of-life tires (ELTs) pyrolysis to activated carbons: Material characterization and CO_2 capture abilities. *Environ. Res.* **2024**, *247*, No. 118169.
(50) Serafin, J.; Kiełbasa, K.; Michalkiewicz, B. The new tailored nanoporous carbons from the common polypody (Polypodium vulgare): The role of textural properties for enhanced CO_2 adsorption. *Chem. Eng. J.* **2022**, *429*, No. 131751.

https://doi.org/10.1021/acsomega.4c03160
ACS Omega 2024, 9, 31814−31831

(51) Tian, Y.; Liu, P.; Wang, X.; Zhong, G.; Chen, G. Offgas analysis and pyrolysis mechanism of activated carbon from bamboo sawdust by chemical activation with KOH. *J. Wuhan Univ. Technol., Mater. Sci. Ed.*. **2011**, *26* (1), 10−14.
(52) Işıtan, S.; Ceylan, S.; Topcu, Y.; Hintz, C.; Tefft, J.; Chellappa, T.; Guo, J.; Goldfarb, J. L. Product quality optimization in an integrated biorefinery: conversion of pistachio nutshell biomass to biofuels and activated biochars via pyrolysis. *Energy Convers. Manage.* **2016**, *127*, 576−588.
(53) Rouquerol, J.; Baron, G. V.; Denoyel, R.; Giesche, H.; Groen, J.; Klobes, P.; Levitz, P.; Neimark, A.; Rigby, S.; Skudas, R.; Sing, K.; Thommes, M.; Unger, K. The characterization of macroporous solids: An overview of the methodology. *Microporous Mesoporous Mater.* **2012**, *154*, 2−6.
(54) Verma, V.; Choudhury, S. R.; Rathour, V.; Choudhury, S. R.; Ganesan, V. Hollow core mesoporous carbon spheres as catalyst support for improved platinum utilization in phosphoric acid fuel cells. *Microporous Mesoporous Mater.* **2024**, *367*, No. 113005.
(55) Baldovino-Medrano, V. G.; Niño-Celis, V.; Isaacs Giraldo, R. Systematic analysis of the nitrogen adsorption−desorption isotherms recorded for a series of materials based on microporous−mesoporous amorphous aluminosilicates using classical methods. *J. Chem. Eng. Data* **2023**, *68* (9), 2512−2528.
(56) Iqbal, O.; Padmanabhan, E.; Mandal, A.; Dvorkin, J. Characterization of geochemical properties and factors controlling the pore structure development of shale gas reservoirs. *J. Pet. Sci. Eng.* **2021**, *206*, No. 109001.
(57) Yang, H.; Jayaatmaja, K.; Qiu, X.; Fan, M.; Dejam, M.; Tan, S. P.; Adidharma, H. Accurate Measurement of the Isothermal Heat of Capillary Condensation in Nanopores Using Differential Scanning Calorimetry and Adsorption/Desorption Experiments. *J. Phys. Chem. C* **2023**, *127* (45), 21980−21988.
(58) Serafin, J.; Dziejarski, B.; Junior, O. F. C.; Sreńscek-Nazzal, J. Design of highly microporous activated carbons based on walnut shell biomass for H2 and CO2 storage. *Carbon* **2023**, *201*, 633−647.
(59) Aghababaei, M.; Ghoreyshi, A. A.; Esfandiari, K. Optimizing the conditions of multi-walled carbon nanotubes surface activation and loading metal nanoparticles for enhanced hydrogen storage. *Int. J. Hydrogen Energy* **2020**, *45* (43), 23112−23121.
(60) Foo, K. Y.; Hameed, B. H. Coconut husk derived activated carbon via microwave induced activation: effects of activation agents, preparation parameters and adsorption performance. *Chem. Eng. J.* **2012**, *184*, 57−65.
(61) Lozano-Castello, D.; Lillo-Ródenas, M. A.; Cazorla-Amorós, D.; Linares-Solano, A. Preparation of activated carbons from Spanish anthracite: I. Activation by KOH. *Carbon* **2001**, *39* (5), 741−749.
(62) Alabadi, A.; Razzaque, S.; Yang, Y.; Chen, S.; Tan, B. Highly porous activated carbon materials from carbonized biomass with high CO2 capturing capacity. *Chem. Eng. J.* **2015**, *281*, 606−612.
(63) Ahmed, M. B.; Johir, M. A. H.; Zhou, J. L.; Ngo, H. H.; Nghiem, L. D.; Richardson, C.; Moni, M.; Bryant, M. R. Activated carbon preparation from biomass feedstock: clean production and carbon dioxide adsorption. *J. Cleaner Prod.* **2019**, *225*, 405−413.
(64) Toprak, A.; Kopac, T. Carbon dioxide adsorption using high surface area activated carbons from local coals modified by KOH, NaOH and $ZnCl_2$ agents. *Int. J. Chem. React. Eng.* **2017**, *15* (3), No. 20160042.
(65) Manyà, J. J.; González, B.; Azuara, M.; Arner, G. Ultra-microporous adsorbents prepared from vine shoots-derived biochar with high CO2 uptake and CO_2/N_2 selectivity. *Chem. Eng. J.* **2018**, *345*, 631−639.
(66) Huang, G. G.; Liu, Y. F.; Wu, X. X.; Cai, J. J. Activated carbons prepared by the KOH activation of a hydrochar from garlic peel and their CO_2 adsorption performance. *New Carbon Mater.* **2019**, *34* (3), 247−257.
(67) Mohd Din, A. T.; Hameed, B. H.; Ahmad, A. L. Batch adsorption of phenol onto physiochemical-activated coconut shell. *J. Hazard. Mater.* **2009**, *161* (2−3), 1522−1529.
(68) Kawano, T.; Kubota, M.; Onyango, M. S.; Watanabe, F.; Matsuda, H. Preparation of activated carbon from petroleum coke by KOH chemical activation for adsorption heat pump. *Appl. Therm. Eng.* **2008**, *28* (8−9), 865−871.
(69) Idrees, M.; Rangari, V.; Jeelani, S. Sustainable packaging waste-derived activated carbon for carbon dioxide capture. *J. CO_2 Util.* **2018**, *26*, 380−387.
(70) Yuan, X.; Li, S.; Jeon, S.; Deng, S.; Zhao, L.; Lee, K. B. Valorization of waste polyethylene terephthalate plastic into N-doped microporous carbon for CO_2 capture through a one-pot synthesis. *J. Hazard Mater.* **2020**, *399*, No. 399.
(71) Wang, J.; Kaskel, S. KOH activation of carbon-based materials for energy storage. *J. Mater. Chem.* **2012**, *22* (45), 23710−23725.
(72) Williams, N. E.; Oba, O. A.; Aydinlik, N. P. Modification, Production, and Methods of KOH-Activated Carbon. *ChemBioEng Rev.* **2022**, *9* (2), 164−189.
(73) Otowa, T.; Tanibata, R.; Itoh, M. Production and adsorption characteristics of MAXSORB: high-surface-area active carbon. *Gas Sep. Purif.* **1993**, *7* (4), 241−245.
(74) Guizani, C.; Widsten, P.; Siipola, V.; Paalijärvi, R.; Berg, J.; Pasanen, A.; Kalliola, A.; Torvinen, K. New insights into the chemical activation of lignins and tannins using K_2CO_3—a combined thermoanalytical and structural study. *Carbon Lett.* **2023**, 1−16.
(75) Singh, G.; Ruban, A. M.; Geng, X.; Vinu, A. Recognizing the potential of K-salts, apart from KOH, for generating porous carbons using chemical activation. *Chem. Eng. J.* **2023**, *451*, No. 139045.
(76) Chen, S.; Chen, G.; Chen, H.; Sun, Y.; Yu, X.; Su, Y.; Tang, S. Preparation of porous carbon-based material from corn straw via mixed alkali and its application for removal of dye. *Colloids Surf., A* **2019**, *568*, 173−183.
(77) Yang, R.; Zhou, J.; Wu, L.; Zhang, Q.; Song, Y. Understanding effects of potassium activator on the porous structure and adsorption performance of bluecoke-based porous powder during microwave heating. *J. Mol. Liq.* **2022**, *366*, No. 120249.
(78) Wu, Q.; Chen, J.; Li, J.; Wu, Y.; Ran, F. Designing advanced anode materials via regulating accumulation of cobalt ions in polystyrene nanoparticles enriched in Pistia stratiotes. *Mater. Today Nano* **2024**, *25*, No. 100438.
(79) Guo, Y.; Yu, K.; Wang, Z.; Xu, H. Effects of activation conditions on preparation of porous carbon from rice husk. *Carbon* **2003**, *41* (41), 1645−1648.
(80) Yahya, M. A.; Al-Qodah, Z.; Ngah, C. Z. Agricultural bio-waste materials as potential sustainable precursors used for activated carbon production: A review. *Renewable Sustainable Energy Rev.* **2015**, *46*, 218−235.
(81) Rambabu, N.; Rao, B. V. S. K.; Surisetty, V. R.; Das, U.; Dalai, A. K. Production, characterization, and evaluation of activated carbons from de-oiled canola meal for environmental applications. *Ind. Crops Prod.* **2015**, *65*, 572−581.
(82) Linares-Solano, A.; Lillo-Rodenas, M. A.; Marco Lozar, J. P.; Kunowsky, M.; Romero Anaya, A. J. NaOH and KOH for preparing activated carbons used in energy and environmental applications. *Int. J. Energy Environ. Econom.* **2012**, *20* (4), 59−91.

https://doi.org/10.1021/acsomega.4c03160
ACS Omega 2024, 9, 31814−31831

Paper IV

Materials & Design 254 (2025) 114073

Contents lists available at ScienceDirect

Materials & Design

journal homepage: www.elsevier.com/locate/matdes

Valorization of hazardous graphite from black mass (NMC 111) of lithium-ion battery recycling via KOH activation for functional carbon design

Bartosz Dziejarski [a,b,c,*], Jose Eduardo Arevalo Fester [a], Jarosław Serafin [d], Martina Petranikova [a], Eric Tam [e], Anna Martinelli [f], Renata Krzyżyńska [c], Klas Andersson [b], Pavleta Knutsson [a]

[a] Department of Chemistry and Chemical Engineering, Division of Energy and Materials, Chalmers University of Technology, SE-412 96 Gothenburg, Sweden
[b] Department of Space, Earth and Environment, Division of Energy Technology, Chalmers University of Technology, SE-412 96 Gothenburg, Sweden
[c] Faculty of Environmental Engineering, Wroclaw University of Science and Technology, 50-370 Wroclaw, Poland
[d] Department of Inorganic and Organic Chemistry, University of Barcelona, Martí i Franquès, 1-11, 08028 Barcelona, Spain
[e] Department of Industrial and Materials Science, Division of Materials and Manufacture, Chalmers University of Technology, SE-412 96 Gothenburg, Sweden
[f] Department of Chemistry and Chemical Engineering, Division of Applied Chemistry, Chalmers University of Technology, SE-412 96 Gothenburg, Sweden

ARTICLE INFO

Keywords:
LIBs
Graphite recovery
Activated carbon
Carbon-based materials
Circular economy
Resource valorization

ABSTRACT

The rapid adoption of lithium-ion batteries (LiBs) in energy storage has driven research into resource recovery. This study converts hazardous graphite from the black mass (NMC 111) of spent LiBs into functional activated carbons (ACs) via KOH activation. Tailoring the synthesis at 800 °C and a graphite-to-KOH ratio of 1:6 produced AC with a surface area of 678 m^2/g and a total pore volume of 0.442 cm^3/g. The material showed a balanced micropore–mesopore structure, with micropores contributing 53 % of the total pore volume. The material showed a balanced micropore–mesopore structure, with micropores contributing 53 % of the total volume. XRD confirmed preserved graphitic crystallinity with a dominant (002) peak at 26.52°. Raman spectroscopy indicated increased defect density ($I_D/I_G = 1.053$), facilitating porosity formation. SEM and TEM revealed a transition from smooth graphite layers to a porous, defect-rich structure, with TEM highlighting mesopore-like voids and distorted graphitic domains featuring edge defects. XPS identified surface modifications, including a higher proportion of sp^2 carbon and oxygen-containing groups (C–O, C=O, C-OH, CO_3^{2-}). TGA demonstrated stability (~900 °C) under inert conditions and enhanced reactivity in oxidative environments. This work valorizes LiB-derived graphite waste into ACs, supporting circular economy strategies and demonstrating potential for industrial scalability.

1. Introduction

Over the past decade, lithium-ion batteries (LiBs) have been at the forefront of energy storage innovations, driving transformative changes across numerous industries, particularly in transportation and renewable energy integration [1,2]. The extensive integration of Li-ion batteries in electric vehicles (EVs) has positioned them as a key technology in the global transition toward sustainable, low-carbon energy systems [3]. The widespread adoption of electric vehicles was evident in 2023 when nearly 14 million electric cars were sold globally, representing 18 % of the total car sales, a significant increase if compared to the 14 % level in 2022. As the trend continues, electric car sales are projected to climb further, potentially reaching around 17 million in 2024, i.e. more than one in five cars sold worldwide [4]. This transition from internal combustion engines to battery-powered alternatives has led to decreased greenhouse gas emissions (220 Mt in 2023 compared to 80 Mt in 2022) [4], cleaner transportation and improved air quality [5]. Furthermore, the demand for LiBs extends beyond the automotive industry, including larger-scale stationary energy storage systems that support renewable energy integration and grid stability [6,7]. As renewable energy sources

* Corresponding author at: Department of Chemistry and Chemical Engineering, Division of Energy and Materials, Chalmers University of Technology, SE-412 96 Gothenburg, Sweden.
E-mail address: bartoszd@chalmers.se (B. Dziejarski).

https://doi.org/10.1016/j.matdes.2025.114073
Received 16 March 2025; Received in revised form 23 April 2025; Accepted 6 May 2025
Available online 9 May 2025

such as solar and wind power become more prevalent, the need for efficient energy storage to address intermittent energy supply will grow correspondingly [8]. Projections indicate that the demand for LiBs is anticipated to grow by approximately 33 % annually, reaching an estimated 4.7 GWh by 2030 [9].

Even though it contributes to the decrease of environmental impact of the transport and energy sector, the rapid expansion of LiBs introduces new challenges related to their short lifecycle, typically spanning the range of 3–8 years. The main challenge is connected to the end-of-life (EoL) management, where over 2 million tons of spent LiBs are projected to be generated annually [10]. LiBs are complex electrochemical systems containing a mix of valuable secondary resources, such as lithium (Li), cobalt (Co), nickel (Ni), manganese (Mn), and copper (Cu), which are essential for battery performance and can be recovered for reuse [11]. However, they also contribute to hazardous waste generation, encompassing electrolyte residues, fluorinated compounds, and toxic metals such as lead and cadmium, which can pose serious environmental and health hazards if not effectively controlled [12]. A LiB cell comprises approximately 25 wt% casing materials (steel and plastics), ~27 wt% cathode materials (e.g., $LiCoO_2$, $LiFePO_4$, $LiNiCoMnO_2$), 12–17 wt% anode materials (graphite), ~13 wt% current collectors (Cu and Al), 10–15 wt% electrolyte (such as $LiPF_6$ or $LiBF_4$ dissolved in dipolar organic solvents), ~4 wt% separator (polypropylene), and ~ 4 wt% binder (polyvinylidene difluoride) [13,14]. Among the most prominent batteries in production, nickel manganese cobalt (NMC)-based LiBs have cathodes composed of a mixture of Li, Ni, Mn, and Co, such as $LiNi_{0.6}Mn_{0.2}Co_{0.2}O_2$ (NMC 622), $LiNi_{0.8}Mn_{0.1}Co_{0.1}O_2$ (NMC 811), and $LiNi_{1/3}Mn_{1/3}Co_{1/3}O_2$ (NMC 111). Notably, NMC 111 has garnered significant attention as a cathode material for next-generation LiBs due to its numerous advantages, including lower cost compared to $LiCoO_2$, high theoretical capacity, low toxicity, excellent thermal stability, and superior energy density [15].

Lithium, cobalt, and nickel are key elements for enhancing battery performance, longevity, and energy density [16]. The EU Battery Directive anticipates an improvement in Li-ion battery recycling efficiency, increasing from 50 % in 2006 to 65 % by 2025 [17]. This advancement aims to close the material loop by recovering valuable metals, with Ni and Co being the main economic incentives driving LiBs recovery efforts. The recently introduced European Battery Regulation sets ambitious recovery targets: lithium recovery is expected to reach 50 % by 2027 and 80 % by 2031, while Co, Cu, Pb, and Ni are targeted at 90 % by 2027 and 95 % by 2031 [18]. Achieving these goals, however, is challenging due to the complex composition and diverse materials within LiBs, which require multiple preparatory steps before processing. The initial stages involve classification, discharge or inactivation, disassembly, and material separation. These processes prepare the batteries for subsequent treatment using direct recycling, pyrometallurgy, or hydrometallurgy [19]. Due to the legislative requirements, hydrometallurgy is and will be the preferred method for the recycling. This brings the challenges for the recyclers to deal with the significant amount of waste graphite since its application is limited and moreover it is considered to be a hazardous waste. Current EoL strategies typically begin with discharge and mechanical pre-treatment, followed by optional pyrolysis to remove organic components. The subsequent steps, including sorting and pre-processing, result in a sieved mixture of cathode powders and anode graphite, commonly referred to as black mass (BM) [20]. Processing BM focuses on extracting valuable transition metals while isolating and purifying graphite from the anode. Historically overlooked, graphite has only recently been recognized as a recoverable and valuable resource, further enhancing the economic and environmental benefits of LiB recycling [21].

Graphite continues to dominate as the preferred anode material in commercial LiBs, primarily due to its outstanding cycling stability, high electrical conductivity, and mechanical flexibility. With approximately 1 kg of graphite required per kWh of battery capacity, which is 10 to 20 times more than lithium, its demand has driven the market to a value of $29.05 billion by 2022 [22]. Beyond its role in batteries, graphite's unique combination of electrical conductivity, thermal stability and structural versatility also makes it an ideal precursor for advanced material synthesis [23–25]. One promising research path involves using recovered graphite as a precursor for activated carbons (ACs), a class of porous materials with extensive environmental applications due to their high specific surface area, tunable pore structure, low cost, and thermal and chemical stability [26,27]. ACs are widely used in, for example, gas separation and storage [28], water purification [29], energy storage [30], and as catalyst supports in chemical processes [31]. The synthesis of ACs typically involves activation processes applied to precursor materials to optimize their textural and structural properties. Among the commonly used chemical activating agents (including KOH, K_2CO_3, H_3PO_4, and $ZnCl_2$), KOH stands out as the most promising activator resulting in high-quality ACs with a large pore volume, abundant surface oxygen functional groups, and dominant microporosity [32,33]. The effectiveness of KOH, likewise the other activators, is significantly influenced by the chosen activation parameters, which vary depending on the raw material. Among the multiple activation parameters, activation temperature (500–900 °C) and mass ratio between the activator and precursor (1:1–1:7) are reported to have the most substantial impact on the resulting AC properties [34,35].

While traditional precursors such as biomass, coal, or petroleum-derived polymers have been widely explored, they often require intensive energy input and may yield materials with inconsistent properties [36–38]. In contrast, graphite recovered from spent lithium-ion batteries exhibits a high fixed carbon content, partial graphitization, and intrinsic electrical conductivity, which not only facilitates the formation of well-developed porosity during activation but also reduces the activation energy required [39]. These favorable physicochemical properties enable the synthesis of high-performance activated carbons with lower process energy demands. Moreover, the presence of residual metal species and surface defects in the recovered graphite can further promote pore development. From a cost perspective, although the initial collection and purification of black mass involves logistical and technical challenges, the use of this industrial waste stream circumvents the need for virgin raw materials, making it a more economically attractive and sustainable solution in the long term [20]. From a circular economy perspective, valorizing black mass diverts hazardous waste from landfills and simultaneously creates value-added materials suitable for energy and environmental applications. Despite the growing interest in ACs derived from waste materials, the potential of graphite recovered from LiBs as a precursor for AC synthesis has not received significant attention. Nonetheless, a two studies have explored graphite nanofibers (GNFs) as a carbon source for activation. For example, Meng et al. [40] investigated the effect of heat treatment (700–1000 °C) on the activation of GNFs using KOH. Similarly, Yuan et al. [41] prepared porous GNFs (PGNFs) through KOH activation, varying the GNF/KOH weight ratio from 0 to 5 at 900 °C. In view of this, investigating the use of recovered graphite as a precursor for ACs is particularly relevant in the context of sustainable waste management and the transition to a circular economy. Transforming waste graphite into high-value ACs addresses three critical challenges: reducing the environmental impact of LiB disposal, recovering graphite as an essential raw material, and creating functional materials that promote economic sustainability.

This study explores the transformation of graphite recovered from industrial black mass (NMC 111) of spent lithium-ion batteries into ACs through chemical activation using KOH. The research focuses on uncovering the underlying mechanisms that lead to structural, textural, and chemical changes during the activation process. Following the mechanism provides a comprehensive understanding of how waste-derived graphite can be converted into high-performance porous materials. A wide array of advanced characterization techniques was employed to investigate the evolution of properties in the activated carbons. These techniques include nitrogen adsorption/desorption isotherms for textural analysis, Raman spectroscopy and X-ray diffraction

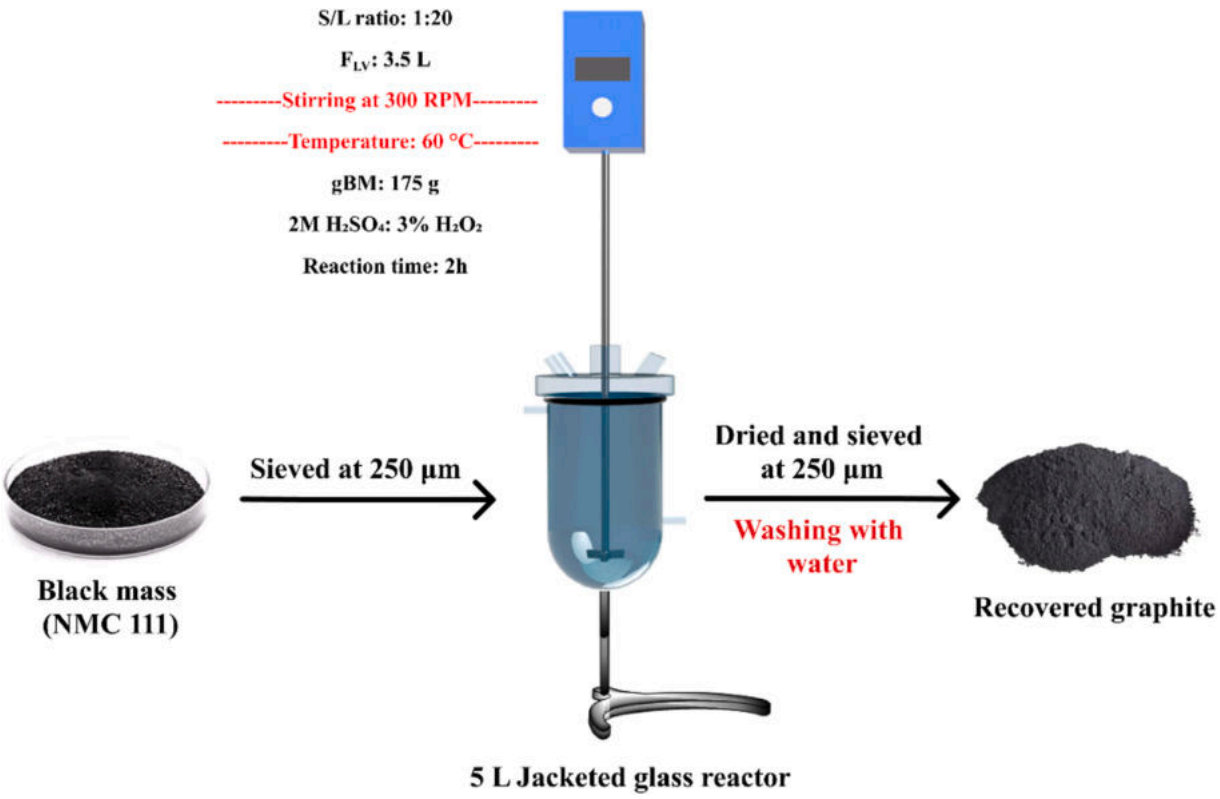

Fig. 1. A schematic representation illustrating the preparation steps utilized for the leaching of industrial black mass (NMC 111) to enable graphite recovery.

(XRD) for structural evaluation, and scanning electron microscopy (SEM), transmission electron microscopy (TEM), and energy-dispersive X-ray spectroscopy (EDS) for morphological and compositional studies. Furthermore, X-ray photoelectron spectroscopy (XPS) was used to examine the chemical modifications, specifically focusing on the introduction of functional groups and the changes in bonding states, while thermogravimetric analysis (TGA) assessed the thermal behavior and stability of the materials. The novelty of this work lies in its detailed investigation of the chemical activation process of recovered graphite, providing the first mechanistic insights into its transformation into activated carbons. The study uniquely addresses the interplay between activation conditions, such as temperature and KOH-to-graphite ratio, and their effects on the resulting material properties. This research not only contributes to advancing resource recovery strategies for spent LiBs but also highlights the potential for developing sustainable, high-value waste materials, thereby supporting the principles of a circular economy.

2. Materials and methods

2.1. Black mass

The black mass was obtained after disassembling 150 kg of battery packs from Volvo Cars AB (Sweden). Packs were discharged by Volvo Cars AB and disassembled by Stena Recycling AB (Sweden). Then, the 120 kg of the cells (NMC 111) were mechanically treated and separated by Akkuser Oy (Finland), at temperatures below 50 °C. Obtained black mass was further sieved to under 500 µm at the Industrial Materials Recycling group at Chalmers University of Technology (Sweden) to achieve a highly concentrated homogeneous powder. Carbon content of the black mass was 32 wt%.

2.2. Leaching of industrial black mass (NMC 111)

The overall procedure, illustrating the preparation steps for the leaching of industrial black mass to enable graphite recovery, is presented in Fig. 1.

In a 5 L glass-jacketed reactor equipped with a mechanical stirrer, 2 L of deionized water and 392.8 mL of 95 % H_2SO_4 were introduced portion-wise, followed by an additional 929.3 mL of deionized water. The reactor temperature was set to 60 °C. While stirring at 300 RPM, 175 g of black mass, previously sieved to 250 µm, was gradually incorporated. Finally, 178 mL of 59 % H_2O_2 was introduced portion-wise to prevent overflow from the formation of black foam. The final concentrations of H_2SO_4 and H_2O_2 were 2 M and 3 %, respectively, maintaining a solid-to-liquid ratio of 1:20 with a final liquid volume of 3.5 L. After 2 h of reaction, stirring was stopped, and the slurry was poured into a 4 L beaker for vacuum filtration. The black solid was washed with deionized water until the pH reached 7. Approximately 80 g of the solid was then transferred to a 4 L beaker, and 2 L of deionized water was added. The mixture was stirred at 300 RPM for 60 min. Subsequently, the slurry was filtered, washed with deionized water, and dried overnight at 60 °C. Finally, the dried solid was crushed in a mortar and sieved again to 250 µm. Recovered graphite was obtained after this sieving process, which effectively reduced the plastic content originating from Li-ion battery separators.

XRF analysis, as shown in **Table S1**, confirmed the removal of most metal impurities after leaching, including complete elimination of P (0.340 wt%.). Trace amounts of Ni (0.118 wt%.), Co (0.261 wt%.), and Mn (0.331 wt%.) remained in the recovered graphite, while Si (0.364 wt %) appeared despite being undetected in the original black mass, likely due to washing-related contamination. The low residual transition metal content suggests minimal catalytic influence during activation. In contrast to conventional graphite, LiB-derived precursors require additional purification due to their complex composition (active material residues, binders, and additives), but they offer potential for tuning the

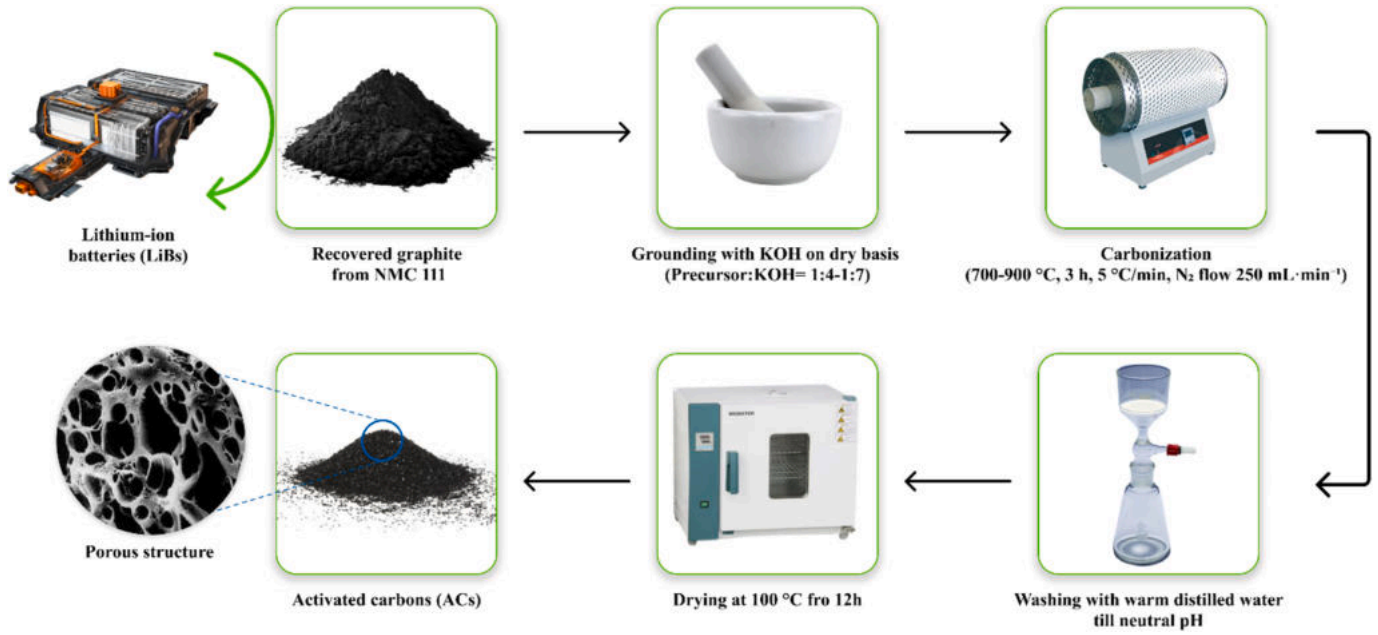

Fig. 2. Methodology for preparation procedures used for KOH activation of recovered graphite from NMC 111.

properties of activated carbon materials.

2.3. Preparation of activated carbons

Activated carbons were synthesized from the recovered graphite through chemical activation using KOH in a dry mixing process, as presented in Fig. 2 and **Table S2**. The specific mass amounts of graphite and KOH were ground together in a mortar to create a uniform solid mixture which was placed in a horizontal furnace.

Activation was performed under an inert nitrogen atmosphere with a constant flow rate of 250 mL·min^{-1}. Two activation parameters were examined: temperature and the graphite to KOH ratio. The temperatures were set at 700 °C, 800 °C, and 900 °C, each maintained for 3 h, based on preliminary studies and reported literature confirming the adequacy of this duration, with a heating rate of 5 °C·min^{-1}. An initial graphite to KOH ratio of 1:4 was used as a baseline to assess the stages of KOH activation behavior. This ratio was further modulated at the optimal temperature (800 °C) to enhance the textural properties, adjusting from ratios of 1:5 up to 1:7. The resulting ACs were washed multiple times with deionized water until the washing water reached a constant pH. Finally, all samples were dried in an oven at 100 °C for 24 h. The activated carbon samples were labeled as AC-X_Z, where X represents the activation temperature, and Z represents the graphite to KOH ratio.

2.4. Characterization of carbon-based materials

2.4.1. Textural characterization

The textural properties of the synthesized ACs were assessed using N_2 adsorption isotherms measured at −196 °C. The analysis was performed using fully automated Tristar II 3020 Micromeritics, a surface area and porosity analyzer with three stations. Before testing, the samples were degassed by sequential heating to 90 °C for 4 h, followed by 250 °C for 16 h. A total of approximately 61 adsorption/desorption points were recorded across a relative pressure (P/P_0) range from $1{\cdot}10^{-4}$ to ~0.98. The maximum volume of nitrogen gas adsorbed during the analysis was 25 cm^3/g STP.

The specific surface area was evaluated using the Brunauer-Emmett-Teller (S_{BET}) method within a P/P_0 range of 0.05 to 0.3, then adjusted according to the modified BET approach by Rouquerol et al. [42], ensuring the highest linear correlation ($R^2 \approx 1$). The total pore volume (V_{TOT}) was evaluated at a high relative pressure, typically around 0.99 or higher. The pore size distribution (PSD), as well as the micropore (V_{MIC}) and mesopore (V_{MES}) volumes, were determined using the non-local density functional theory (NLDFT) model, assuming a slit-shaped pore structure within the density functional theory (DFT) framework.

2.4.2. Structural and surface characterization

The lattice structural changes during the transformation from NM 111 to ACs were investigated using XRD analysis with a Bruker D8 Discover diffractometer. Prior to analysis, the samples were ground to a fine powder and mounted on a zero-background sample holder to minimize interference. The measurements were conducted using the Cu Kα radiation (λ = 1.5406 Å). The recorded spectra were analyzed using the DIFFRAC.EVA and PDF 4 + databases. Additionally, based on the XRD data, graphitic structural parameters were calculated for the recovered graphite and the synthesized ACs [43–45]. The mean crystallite thickness (L_c) and the mean graphene sheet diameter (L_a) were calculated using the Scherrer equation [46]:

$$L_{c,a} = K\lambda/(\beta cos\theta) \quad (1)$$

where:

L_c is the average crystallite thickness [nm], where the (002) signal was used with K = 0.89,

L_a is the average graphene sheet diameter [nm], where (110) signal was applied with K = 1.84.

K is a constant specific to the reflection plane,

λ is the X-ray wavelength (0.154 nm for Cu),

β is the peak width at half maximum intensity (110 or 002), corrected for instrumental broadening (0.07121 rad) using the Warren method [47] and assuming Gaussian peak shapes [rad].

θ is the diffraction angle [rad].

The average interlayer spacing between the graphitic layers (d_{002}) was calculated using Bragg's law [48]:

$$d_{002} = n\lambda/(2sin\theta) \quad (2)$$

where n is the diffraction order (typically n = 1).

Finally, the number of graphene sheets (N) was estimated as [49]:

$$N = L_c/d \quad (3)$$

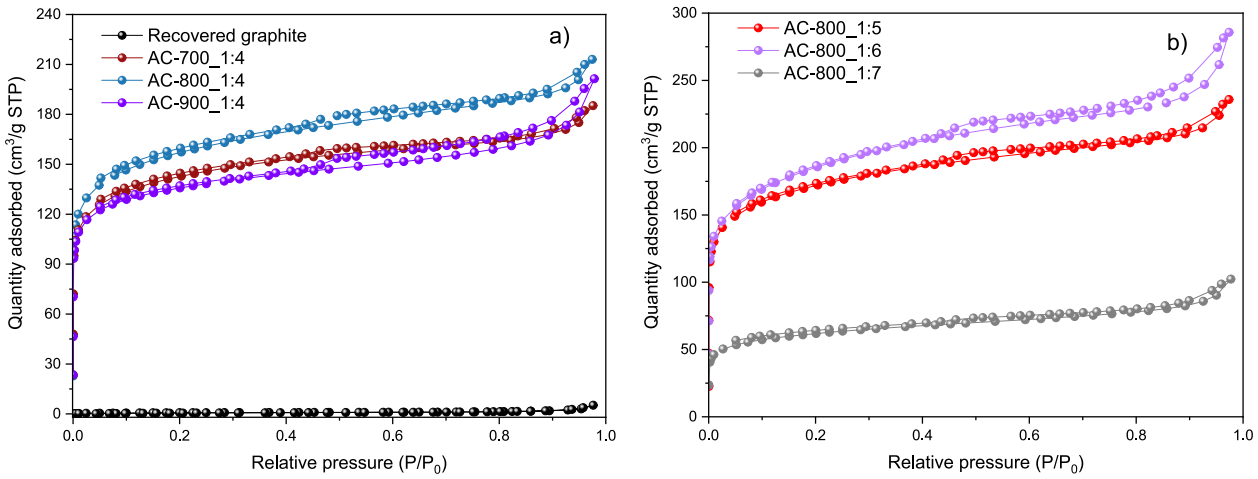

Fig. 3. N_2 adsorption–desorption isotherms at −196 °C for the prepared ACs illustrating the effects of (a) varying temperatures (700–900 °C) and (b) different mass ratios between recovered graphite and KOH (1:5–1:7).

Surface chemical composition and the chemical states of the determined elements were analyzed using an X-ray photoelectron spectroscopy (PHI5000 VersaProbe III – Scanning XPS Microprobe™). To handle non-conductive samples, dual charge compensation was employed by running both Ar ion gun (+ve) and electron neutralizer (−ve) during measurements. Survey scan in an energy range between 0 and 1300 eV with the step size of 1.0 eV was first carried out to assess the overall elemental composition. With the elements identified, narrow scans (0.1 eV step size) were conducted at the selected regions to determine the chemical states of the elements of interest. The spectral peak's energy resolution was determined to be 0.673 eV (full width at half maximum, FWHM) based on the Ag $3d_5/_2$ peak measurement from a sputter-cleaned silver (Ag) foil. The energy scale was calibrated following the ISO 15472 standard, aligning the core-level spectra of sputter-cleaned gold (Au $4f_7/_2$), silver (Ag $3d_5/_2$), and copper (Cu $2p_3/_2$) at 83.96 eV, 368.21 eV, and 932.62 eV, respectively.

Raman spectra were collected using a InVia Raman spectrometer from Renishaw. An Ar-ion laser, 532 nm and 100 mW of maximum power at the source, was used as the excitation source coupled with a Peltier-cooled CCD detector and a grating with 2400 l/mm. The spectral resolution was better than 2 cm^{-1} and the spectral range 100–4000 cm^{-1} was covered. Before any measurement, the spectrometer was calibrated to the first order line of a Si wafer at 520.6 cm^{-1}. Raman spectra were recorded on different spots using 1 % of the nominal power (to avoid overheating and hence damage of the sample), accumulating for 10 s during 10 accumulations. The spectra were presented in their original. Background subtraction was applied to enhance the clarity of the spectral features, and cosmic ray artifacts were removed during data processing to ensure the reliability of the results. The analysis aimed to evaluate the structure of the carbon skeleton in the obtained carbon materials, such as the degree of graphitization or the presence of defects.

Elemental composition was determined using an energy-dispersive X-ray fluorescence spectrometer (EDXRF, Epsilon 3 type, PANalytical B.V.) to assess the removal of metal impurities before and after leaching.

2.4.3. Thermogravimetric characterization

Thermogravimetric analysis was performed using a Mettler Toledo TGA-DSC 3 + thermal analyzer to evaluate the thermal stability and decomposition behavior of the materials. The samples were heated from 30 °C to 900 °C at a rate of 10 K/min under both N_2 and air atmospheres. The influence of oxidative and inert conditions on material degradation was monitored through the mass loss profile during continuous heating.

2.4.4. Morphological characterization

A scanning electron microscopy (FEI ESEM Quanta 200) equipped with energy-dispersive X-ray spectroscopy was used to determine the morphological changes of the samples. Imaging was conducted using the backscattered electron (BSE) signal. To prevent surface charging, the microscope was operated in low vacuum mode at a pressure of 20 Pa, with an electron beam acceleration voltage of 10 kV.

Transmission electron microscopy was used to examine the microstructure of the samples, focusing on lattice ordering, pore formation, and edge morphology. Imaging was carried out using a Titan 80–300 microscope (FEI) equipped with a field emission gun, a monochromator (0.11 eV energy resolution for EELS), and a Gatan 866 GIF Tridiem energy filter. A spherical aberration corrector enabled high-resolution TEM imaging with a spatial resolution down to 70 pm, and fast Fourier transform (FFT) analysis was applied to assess structural disorder and lattice features.

3. Results and discussion

3.1. Effect of KOH activation on the textural properties of recovered graphite

Fig. 3**(a, b)** presents the N_2 adsorption/desorption isotherms of activated carbons produced at temperatures ranging from 700 to 900 °C and with mass ratios of graphite to KOH between 1:5 and 1:7. The isotherms show a rapid uptake at low relative pressures ($P/P_0 < 0.1$), confirming that the ACs are predominantly microporous, while the hysteresis loops indicate the presence of secondary mesoporosity. This result aligns with expectations, as KOH activation is well known to produce micropores due to its chemical etching and widening effects on the carbon matrix. Additionally, it was noticed that the amount of N_2 adsorbed increased with the rise in thermal treatment temperature and the recovered graphite:KOH ratio during carbon sample preparation, reaching its maximum at 800 °C with a ratio of 1:6.

According to the International Union of Pure and Applied Chemistry (IUPAC) classification, the N_2 sorption isotherms shown in Fig. 3**(a, b)** display Type Ib at low P/P_0 values and Type IVa behavior at medium and higher relative pressures [50]. Type Ib is typical for microporous materials with a broader pore size distribution, encompassing wider micropores and possibly narrow mesopores (< ~2.5 nm). The sharp uptake at very low P/P_0 values (<0.015) is attributed to strong N_2-ACs interactions and is linked to the progressive filling of micropores [51]. Conversely, the Type IVa isotherm is characteristic of mesoporous materials. It begins with monolayer-multilayer adsorption on the mesopore walls, following a similar path to the corresponding portion of a Type II isotherm, and is then followed by capillary condensation [52]. In the case of a Type IVa isotherm, capillary condensation occurring in wider

Table 1
The textural properties of ACs produced at different temperatures and different graphite:KOH ratios and using recovered graphite from NMC 111.

Sample	BET surface area[a,] [m^2/g]	Total pore volume[b,] [cm^3/g]	Micropore volume[c,] [cm^3/g]	Mesopore volume[c,] [cm^3/g]	Micropore volume/total pore volume, [%]	Mesopore volume/total pore volume, [%]	Yield, [%]	Burn off, [%]
Recovered graphite	3 ± 0.06	0.008	–	–	–	–	–	–
AC-700_1:4	531 ± 1.95	0.286	0.191	0.095	67	33	58.6	41.4
AC-800_1:4	583 ± 2.37	0.329	0.200	0.129	61	39	54.8	45.2
AC-900_1:4	514 ± 1.14	0.312	0.182	0.130	58	42	48.1	51.9
AC-800_1:5	633 ± 3.13	0.364	0.222	0.142	61	39	53.5	46.5
AC-800_1:6	678 ± 1.09	0.442	0.233	0.209	53	47	51.2	48.8
AC-800_1:7	228 ± 0.64	0.158	0.083	0.075	53	47	45.3	54.7

[a] BET method using the Rouquerol criteria.
[b] V_{TOT} was determined from the N_2 adsorption isotherm at a high relative pressure (~0.98–0.99).
[c] DFT method by the NLDFT model.

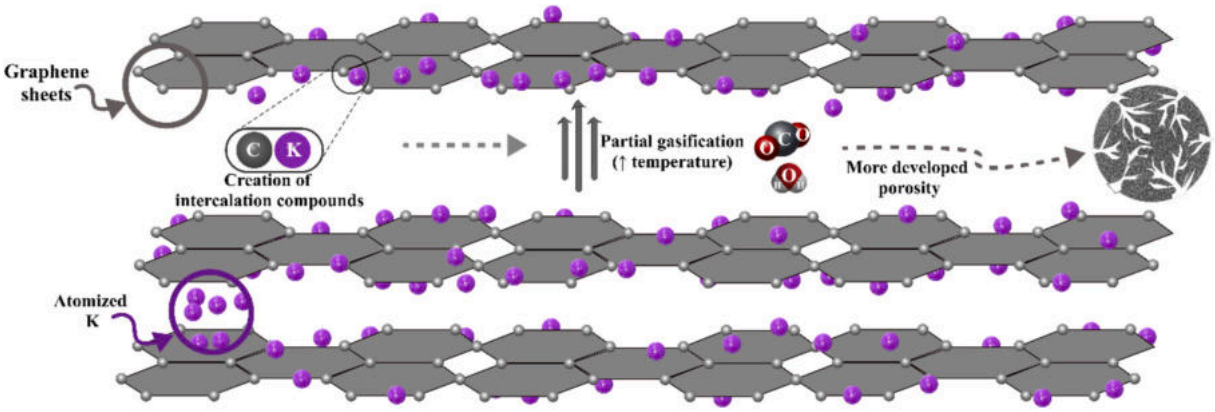

Fig. 4. Schematic illustration of the sequence of potassium intercalation into graphitic layers and the formation of porosity.

mesopores (> 4 nm) results in hysteresis. The observed Type H4 hysteresis suggests the presence of slit-shaped pores, consistent with structures containing limited amounts of mesopores constrained by surrounding micropores [53].

The textural properties of all ACs and recovered graphite from NMC 111, including BET surface area, total pore volume, and micropore and mesopore volumes, as determined by N_2 sorption measurements, are summarized in Table 1. From the different activation temperatures, the sample prepared at 800 °C (AC-800_1:4) demonstrated the most favorable textural characteristics: specific surface area of 583 m^2/g, total pore volume of 0.329 cm^3/g, and a balanced distribution between micropores and mesopores. The micropore volume reached 0.200 cm^3/g, while the mesopore volume measured 0.129 cm^3/g, accounting for 61 % and 39 % of the total pore volume, respectively. When the mass ratio between recovered graphite and KOH was varied at 800 °C, the AC-800_1:6 sample showed superior textural properties, combining a high surface area with a balanced micro- and mesopore structure. This sample achieved the S_{BET} of 678 m^2/g and the largest V_{TOT} of 0.442 cm^3/g, with mesopores contributing with 47 %. The increase in V_{MES} is particularly notable, suggesting that adjusting by increasing to a certain degree the graphite-to-KOH ratio enhances mesopore development, which is beneficial for applications involving larger molecule adsorption or faster diffusion rates. However, the AC-800_1:7 produced with a higher KOH dosage, exhibited significantly lower S_{BET} (228 m^2/g) and V_{TOT} (0.158 cm^3/g), highlighting the detrimental effect of over-etching. Although higher KOH ratios enhance chemical etching via redox and gasification reactions, excessive activation as observed for the 1:7 ratio leads to pore wall thinning, shrinkage, and partial collapse of the carbon framework [54]. This over-etching effect results in a paradoxical reduction in both specific surface area and mesopore volume, as reflected further in the broadening of the PSD and the decrease in cumulative pore volume (Fig. S1) [55]. Additionally, the narrowing of mesopores is indicated by the shift and weakening of the hysteresis loop in the desorption branch of the N_2 isotherm. Finally, the yield of AC samples varies depending on the activation conditions, with values ranging from 45.3 % to 58.6 %, indicating that a higher KOH ratio and temperature lead to greater mass loss during activation. This trend suggests that increasing the temperature and KOH ratio enhances the etching effect, leading to more extensive removal of carbonaceous material and consequently lower yield.

The efficiency of KOH activation of recovered graphite at 800 °C can be attributed to the formation of metallic potassium. At temperatures above 760 °C, metallic K forms during heat treatment, intercalates into the graphitic layers, and diffuses into the internal structure of the carbon particles [56]. This process generates new porosity or expanding existing pores within the graphite structure (Fig. 4) [33]. At higher temperatures, these changes intensify due to the increased activity and mobility of K atoms. Consequently, KOH activation can be described in three main stages, with the final stage being the formation of metallic K. The first stage involves the partial gasification of carbon, where reactive gases such as CO_2 and H_2O are generated, contributing to the development of porosity. The second stage occurs at temperatures exceeding 700 °C, where the formation of K-species promotes etching of the carbon skeleton, thereby creating the pore framework through redox reactions [57]. These species contribute to the breakdown of the carbon matrix, promoting the formation of porosity during the thermal activation process [58,59]. Further XRD analysis of unwashed AC-800_1:6 confirmed the presence of various K-containing species formed during KOH activation, supporting the proposed multi-step activation mechanism and highlighting the role of in situ-generated K species in pore development. Finally, between 800 °C and 900 °C, the S_{BET}, V_{TOT}, and V_{MIC} decreased, while the V_{MES} remained similar to that at 800 °C.

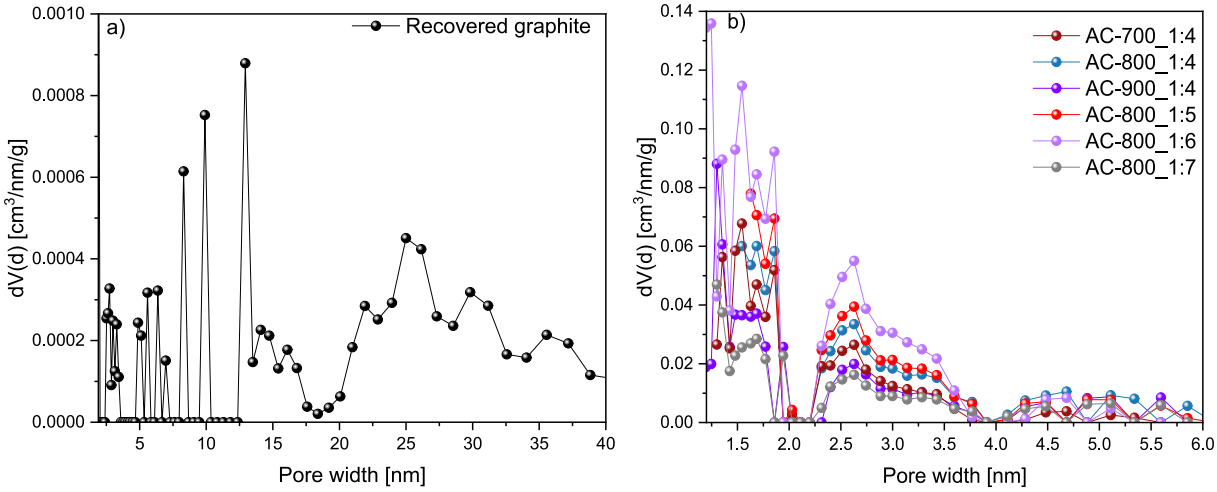

Fig. 5. Pore size distribution of (a) recovered graphite and (b) activated carbons at different temperatures and graphite:KOH ratios, calculated on the basis of N_2 adsorption by using DFT method.

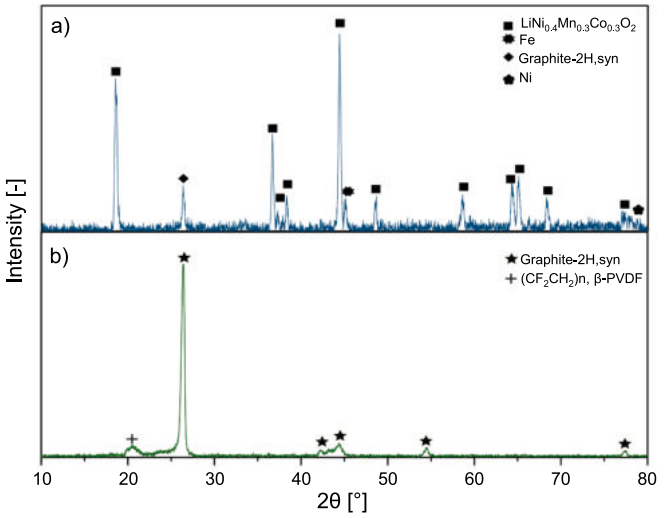

Fig. 6. XRD patterns of (a) NMC 111 and (b) unwashed graphite after leaching.

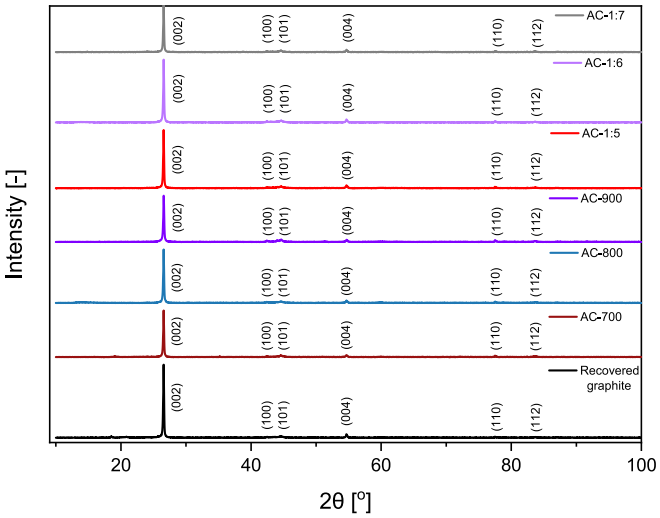

Fig. 7. XRD patterns of recovered graphite after washing and synthesized ACs at different temperatures and various graphite:KOH ratios. The crystallographic planes corresponding to the peaks are also indicated.

Although mesopore formation still occurs at higher temperatures, prolonged exposure can lead to partial collapse or damage of the porous network, thereby reducing the overall surface area and limiting pore accessibility [60,61].

Fig. 5**(a, b)** illustrates the pore size distribution of recovered graphite and ACs. The porosity of graphite was found to be very low, consisting mainly of mesopores, with primary peaks concentrated between 5 nm and 15 nm, and sharp, distinct spikes around 6 nm, 8 nm, and 10 nm. In contrast, the PSD analysis reveals that the ACs obtained were predominantly microporous and mesoporous, with higher content of pore sizes up to 2 nm. It should be noted that significant peaks were observed between 1.2 and 2 nm, with a particular concentration below 1 nm, reflecting the presence of developed narrow micropores. Due to their kinetic diameter, nitrogen molecules are unsuitable for accurately determining the pore volume of pores smaller than 1 nm; however, the cumulative pore volume curve indicates their presence [62]. Additionally, mesopores up to 6 nm were identified, with the majority concentrated between 2.2 and 4 nm, as indicated by a pronounced peak at 2.6 nm. A secondary distribution was also evident in the 4 to 6 nm range.

3.2. Structural transformations: From NMC 111 to activated carbons

Fig. 6 presents the XRD diffractograms of (a) NMC 111 and (b) unwashed graphite after leaching of NMC 111. The XRD pattern of the pristine NMC 111 reveals peaks corresponding to an intermediary mixture of active components from Li-ion battery wastes. The peaks attributed to $LiNi_{0.4}Mn_{0.3}Co_{0.3}O_2$ reflect the layered structure of the cathode active material, while additional peaks for crystalline graphite confirm the presence of anode material [63,64]. Minor peaks corresponding to metallic Fe and Ni are also observed, which likely originate as impurities or secondary phases inherent to the black mass composition [65].

By comparing Fig. 6**(a)** and **(b)**, it becomes evident that the leaching process effectively dissolves a portion of the metallic content while retaining the graphite. The XRD pattern of unwashed recovered graphite after the leaching of NMC 111 exhibits a dominant peak at 2 theta of 26.52°, indicating the retention of its highly crystalline structure during the leaching process. Additionally, a minor peak at 21°, associated with polyvinylidene fluoride (PVDF), a polymeric binder material used to attach the cathode materials to aluminum, is also observed [66]. These observations suggest that while the leaching process was effective in

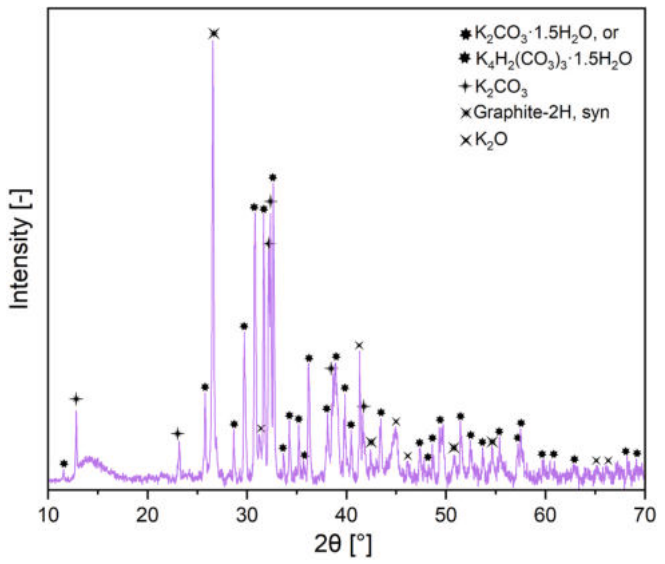

Fig. 8. XRD diffractogram of AC-800_1:6 before washing treatment.

recovering the graphite, some semicrystalline plastic phases remain. However, subsequent water washing further reduced these residues, indicating the effectiveness of this additional purification step, as shown in Fig. 7.

Fig. 7 presents the XRD patterns of the recovered graphite after washing with water, as well as the prepared AC samples. The recovered graphite washed with water and synthesized activated carbons exhibit characteristic peaks at 26.52°, 42.38°, 44.62°, 54.66°, 77.52°, and 83.64°, corresponding to the (002), (100), (101), (004), (110), and (112) crystal planes, respectively. These findings are consistent with values reported in the literature (ICDD card No. 41–1487) [67]. The preservation of characteristic peaks in recovered graphite and ACs confirms that KOH activation does not alter the graphite crystal structure. The sharp diffraction peaks show that the long-range order of the hexagonal layers remains intact, with no changes in interlayer spacing or stacking. This demonstrates that KOH activation improves textural properties while maintaining structural integrity during thermochemical conversion.

Moreover, based on the XRD pattern of the unwashed activated carbon sample (AC-1:6) after KOH activation of recovered graphite, several crystalline phases have been identified, including potassium carbonate hydrates ($K_2CO_3 \cdot 1.5H_2O$, $K_4H_2(CO_3)_3 \cdot 1.5H_2O$), potassium carbonate ($K_2CO_3$), graphite (Graphite-2H), and potassium oxide (K_2O). Fig. 8 provides insight into the potential reactions occurring during the activation process, highlighting the formation of K-based residues and the incomplete removal of activation by-products [68].

- Reaction of recovered graphite with KOH

During high-temperature activation, potassium hydroxide reacts with graphite (C), leading to the formation of potassium compounds and gaseous by-products (H_2, H_2O, CO, CO_2). This process consists of several simultaneous reactions that introduce porosity into the carbon structure while depositing K_2CO_3 and K_2O as residues. These reactions can be described in two generic ways, as outlined below:

$$6KOH + 2C \rightarrow 2K_2CO_3 + 2K + 3H_2 \quad (4)$$

$$4KOH + C \rightarrow K_2CO_3 + K_2O + 2H_2 \quad (5)$$

K_2CO_3 may mainly form via the direct interaction of K_2O with CO_2:

$$K_2O + CO_2 \rightarrow K_2CO_3 \quad (6)$$

Table 2
The average values of d_{002}, L_c, L_a, and N.

Sample	d_{002} [nm]	L_c [nm]	L_a [nm]	N [-]
Recovered graphite	0.335	50.401	154.391	145
AC-700_1:4		49.630	212.2	148
AC-800_1:4		48.660	249.359	145
AC-900_1:4		45.074	174.491	135
AC-800_1:5		49.447	189.587	148
AC-800_1:6		49.045	253.286	146
AC-800_1:7		51.153	194.041	153

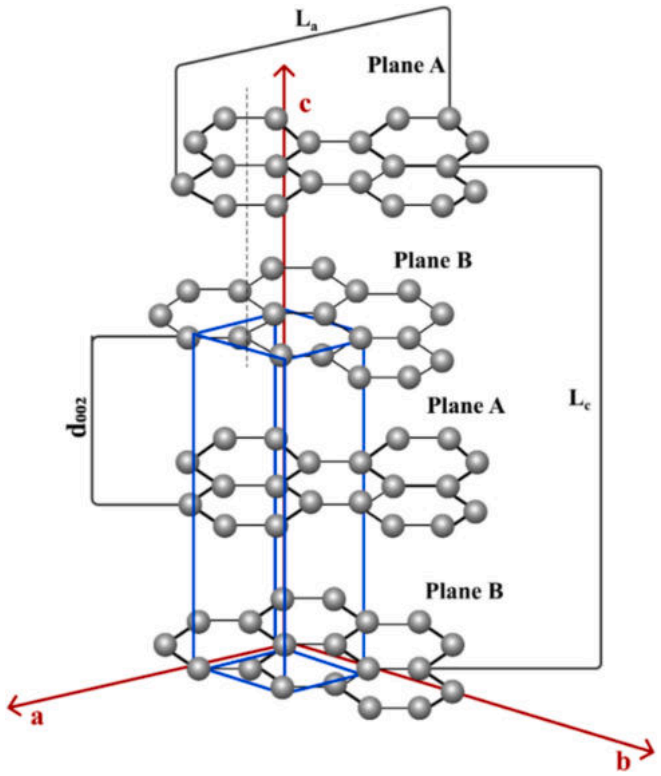

Fig. 9. Visualization of graphitic structural parameters (La, Lc, d_{002}) for recovered graphite and synthesized ACs.

K_2O arises independently, primarily due to the thermal decomposition of KOH and K_2CO_3 or the reaction of K with CO_2:

$$2KOH \rightarrow K_2O + H_2O \quad (7)$$

$$K_2CO_3 \rightarrow K_2O + CO_2 \quad (8)$$

$$K_2CO_3 + C \rightarrow K_2O + 2CO \quad (9)$$

- Formation of potassium carbonate hydrates

During cooling and exposure to ambient moisture, K_2CO_3 can absorb water, leading to the formation of hydrated potassium carbonate phases:

$$K_2CO_3 + 1.5H_2O \rightarrow K_2CO_3 \bullet 1.5H_2O \quad (10)$$

$$2K_2CO_3 + H_2CO_3 + 1.5H_2O \rightarrow K_4H_2(CO_3)_3 \bullet 1.5H_2O \quad (11)$$

These phases suggest that moisture absorption occurred post-activation, possibly during handling.

- Presence of graphite

Despite the activation process, some graphite (Graphite-2H) is still

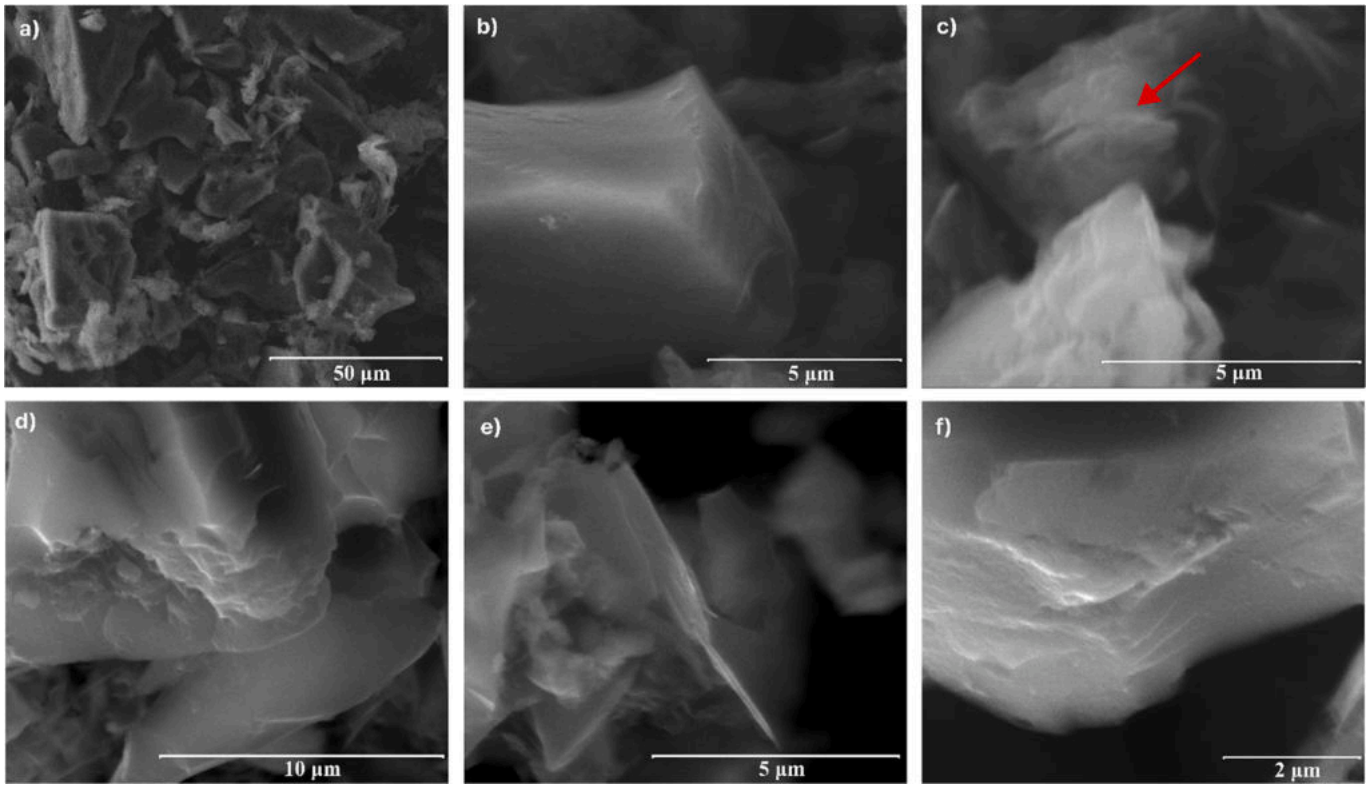

Fig. 10. SEM micrographs of (a–c) recovered graphite from NMC 111, showing the overall structure with distinct, plate-like particles (a), smooth and well-defined edges (b), and stacked graphitic layers within a single particle (c, red arrow); and (d–f) AC-800_1:6, displaying an irregular and porous structure with voids and cavities (d), a fragmented structure (e), and a rough surface (f). (For interpretation of the references to colour in this figure legend, the reader is referred to the web version of this article.)

visible in the XRD pattern, suggesting retention of graphitic layers within the AC structure.

Table 2 presents the structural parameters of recovered graphite and synthesized ACs, including d_{002}, L_c, L_a, and N, respectively. These parameters are further visualized in Fig. 9**.** The d_{002} value remains constant at 0.335 nm across all samples, indicating that the KOH treatment does not alter the fundamental spacing between graphene sheets, as discussed before. In contrast, L_c decreases with increasing temperatures (49.630–45.074 nm), suggesting a progressive reduction in the vertical alignment of graphene layers within the graphite structure. Notably, samples with higher KOH ratios, such as AC-800_1:6 and AC-800_1:7, tend to exhibit stable or slightly increased L_c, reflecting variations in the degree of structural preservation under these conditions. To further support the interpretation of structural changes, the FWHM of the (002) peak was calculated and is summarized in **Table S3**, offering a quantitative measure of peak broadening and structural disorder. Slight variations in FWHM align with the observed trends in L_c, where broader peaks generally correspond to reduced stacking heights along the c-axis.

L_a values show significant variability, with the highest values observed for AC-800_1:4 ($L_a = 249.359$) and AC-800_1:6 ($L_a = 253.286$). These increases suggest that, under certain conditions, the process supports the expansion of lateral crystallite dimensions, corresponding to the in-plane domains of graphene. Conversely, at elevated temperatures, such as for AC-900_1:4 ($L_a = 174.491$), L_a decreases, likely due to fragmentation and structural breakdown. However, no clear dependence on temperature or KOH ratio is observed, as L_a fluctuates probably due to variations in the treatment process affecting graphene sheet dimensions. Finally, the number of graphene layers decreases with rising activation temperatures, as observed in AC-900_1:4 ($N = 135$), reflecting the thinning of graphite stacks at higher temperatures. For samples with varying KOH proportions, the ratio itself does not significantly affect the stacking order or layer thickness.

3.3. Role of KOH activation in morphological changes

Fig. 10**(a, b, c)** depicts SEM images of the recovered graphite from NMC 111. The micrographs reveal distinct, plate-like particles with well-defined edges, characteristic of graphite's layered, crystalline structure. The smooth surfaces and sharp boundaries indicate the orderly stacking of graphene sheets, with minimal porosity, surface roughness, or voids. Additionally, the integrity of the layered arrangement of graphitic layers is prominently visible, which contributes to the high structural order of material [69]. In contrast, the SEM micrographs of the AC sample (AC-800_1:6), as shown in Fig. 10**(d, e, f)**, reveal a substantial morphological transformation compared to the pristine recovered graphite precursor. The structure appears irregular and porous, as a result of the KOH activation process. During this process, carbon atoms are removed from the graphite structure, introducing defects and irregularities [70]. The surface roughness of the particles has noticeably increased, with the formation of voids and cavities throughout the material. This porous morphology, marked by irregular shapes and uneven surfaces, is characteristic of ACs and is key to its high surface area [71]. Furthermore, the edges of the particles are less defined, reflecting the partial breakdown of the stacked layer structure observed in the original graphite. Overall, the results indicate that KOH activation of recovered graphite simultaneously preserves the graphitic structure while introducing structural imperfections that contribute to porosity development. This can be attributed to selective etching, where ordered graphitic domains remain intact, while defects such as vacancies are introduced at the edges, grain boundaries, or amorphous regions. Similar observations were reported by Tai et al. [72], who found that increasing KOH concentrations led to surface roughening, particle fragmentation, and enhanced K^+ ions transmission, while XRD confirmed the retention of characteristic graphite peaks.

To examine the interaction of potassium species with the carbon

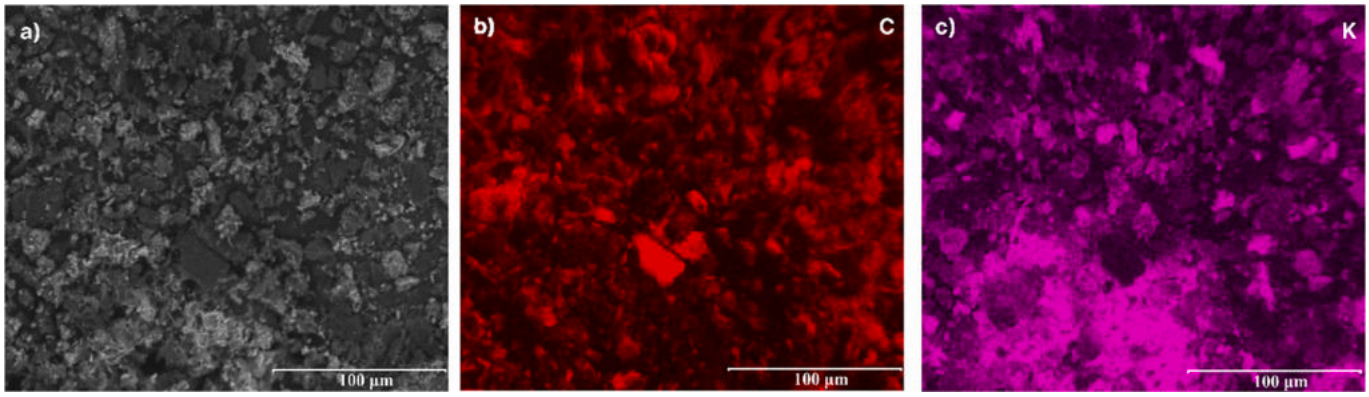

Fig. 11. EDS analysis of the unwashed, recovered graphite-based AC sample (AC-800_1:6): (a) representative SEM micrograph and corresponding elemental intensity maps for (b) C and (c) K.

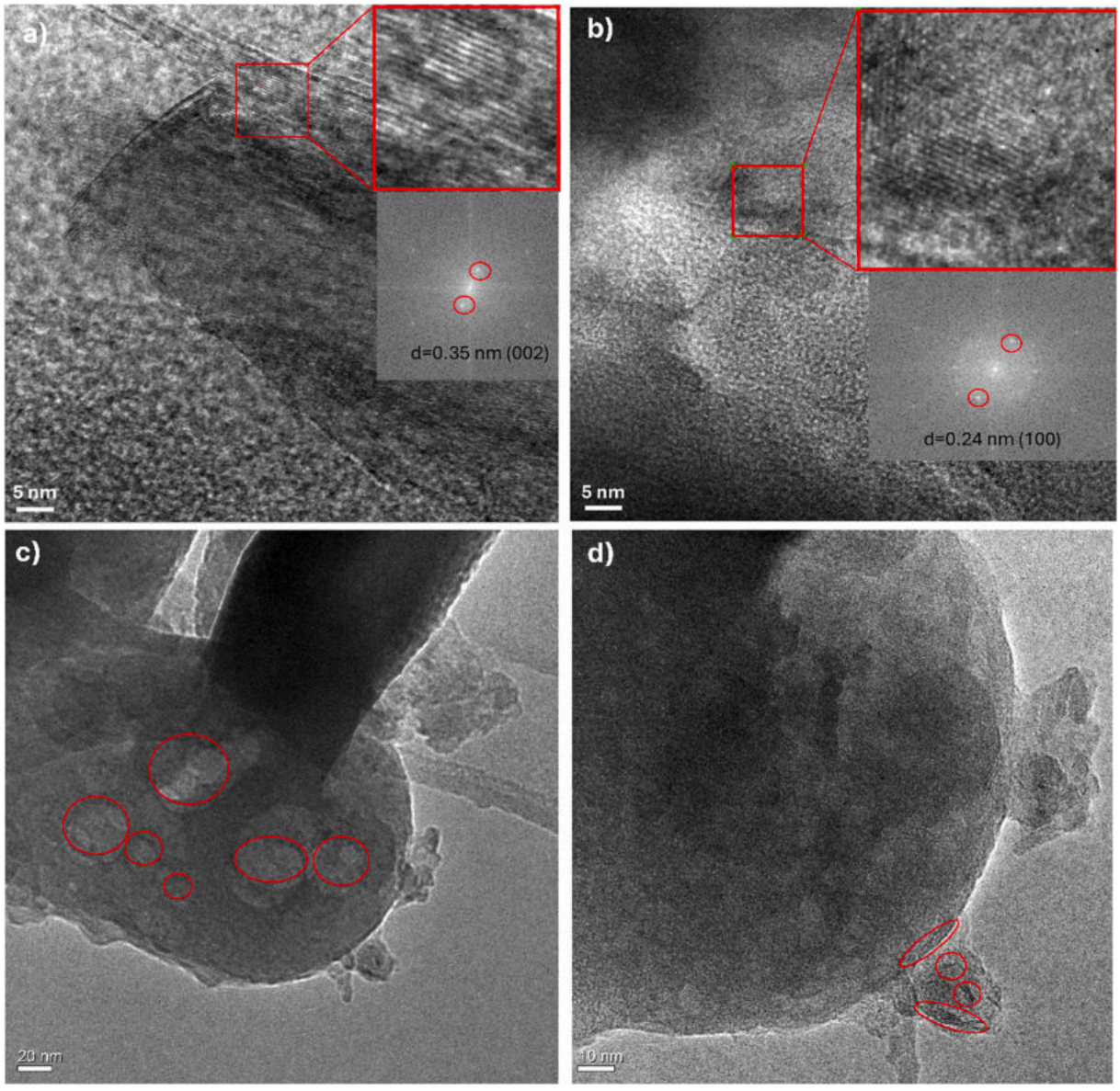

Fig. 12. HRTEM images and FFT patterns of recovered graphite (a) and AC-800_1:6 (b), and TEM images of AC-800_1:6 showing (c) mesopore-like voids formation and (d) structural defects with partially delaminated graphitic layers at the particle edge.

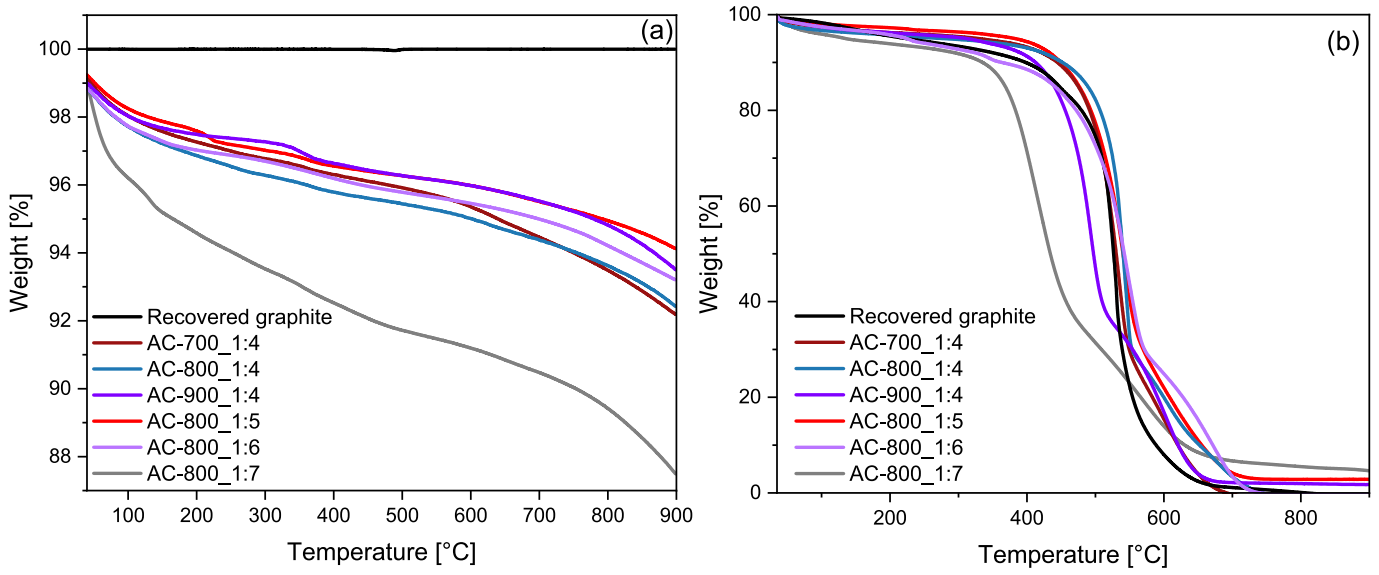

Fig. 13. TGA curves of the samples subjected to a heating rate of 10 K/min from 30 to 900 °C: (a) in a nitrogen atmosphere; (b) in an air atmosphere for activated carbon samples synthesized at different temperatures and graphite:KOH ratios.

matrix of recovered graphite during high-temperature KOH activation, and the retention of potassium-rich compounds, EDS analysis of the unwashed sample is presented in Fig. 11**.** C mapping shows a relatively uniform distribution, consistent with the graphitic structure of the material. In contrast, K mapping reveals a non-uniform distribution, with localized regions exhibiting high potassium concentrations (13.3 wt%). This uneven distribution arises from the retention of K-containing compounds, such as $KHCO_3$, K_2CO_3, and K_2O, formed during thermochemical conversion at 800 °C, along with other volatile by-products [73]. The localized potassium-rich regions likely result from the agglomeration or incomplete dispersion of these K species, contributing to the observed inhomogeneity [32].

To gain deeper insight into the microstructural differences between the recovered graphite and AC-800_1:6, HRTEM combined with FFT analysis was performed. Fig. 12 shows representative HRTEM images and the corresponding FFT patterns for both samples. The recovered graphite (Fig. 12**(a)**) presents well-ordered and extended lattice fringes, with an interlayer distance of approximately 0.35 nm. This spacing corresponds to the (002) planes of graphitic carbon and is slightly larger than the ideal value (0.335 nm) obtained from XRD analysis, which can be attributed to minor turbostratic disorder. The sharp and symmetric reflections observed in the FFT pattern confirm the presence of long-range stacking along the c-axis, characteristic of layered graphite [74,75]. In contrast, the AC-800_1:6 (Fig. 12**(b)**) exhibits a significantly more disordered microstructure. The HRTEM image reveals no evidence of long-range stacking, but short, curved fringes can still be observed locally. The dominant lattice spacing in this region is approximately 0.24 nm, which aligns with the (1 0 0) in-plane lattice of hexagonal carbon, rather than the interlayer (002) spacing. The FFT pattern is diffuse and lacks the symmetry seen in the recovered graphite sample, indicating that structural coherence is lost during activation [76]. This localized disruption of (002) stacking is further supported by XRD analysis, which reveals broadening and reduced intensity of the (002) peak, along with a moderate decrease in L_c. However, the presence of (1 0 0) lattice fringes in the TEM-FFT, together with the stable d_{002} and high L_a values from XRD, confirms that while vertical order is partially degraded, the planar graphitic structure and in-plane crystallinity are largely preserved (Table 2). This disruption of graphitic stacking is consistent with KOH activation pathways involving selective removal of less ordered carbon and partial gasification of graphene layers. These processes fragment the structure into nanoscale domains with edge defects, promoting porosity [77]. As shown in Fig. 12**(c)**, circular low-contrast features within the carbon matrix suggest the formation of mesopore-like voids, while Fig. 12**(d)** shows structural defects and partially delaminated graphitic layers at the particle edge, indicating a disordered framework consistent with hierarchical porosity, including regions near the surface. Combined with BET surface area and porosity data, the observed loss of (002) features alongside preserved in-plane order confirms a transition to a defect-rich carbon network. This direct structural evidence supports the view that KOH activation not only increases disorder, but specifically disrupts interlayer stacking, forming short-range graphene-like domains with enhanced surface accessibility.

3.4. Thermal performance of recovered graphite-based ACs in inert and oxidative conditions

The TGA curves, illustrating the thermal stability and decomposition behavior of the samples under a N_2 atmosphere up to 900 °C, are presented in Fig. 13**(a)**. Recovered graphite exhibited minimal weight loss (<0.5 % wt.) throughout the entire temperature range, reflecting its high thermal stability and crystalline structure. ACs demonstrated a generally similar shape across all activation temperatures and KOH-to-graphite mass ratios. This similarity indicates comparable thermal events, such as moisture release, decomposition of oxygen-containing functional groups (OCFGs) and structural degradation, occurring in distinct temperature regions [78]. Despite the uniformity in curve shape, the extent of weight loss varies depending on the activation temperature and chemical ratio, reflecting differences in structural integrity and OCFGs. ACs prepared at activation temperatures of 700 °C, 800 °C, and 900 °C showed an initial weight loss below 200 °C, consistent across all samples (~2–3 wt%), that can be attributed to the removal of water, physisorbed or adsorbed volatiles [79]. Between 200 °C and 600 °C, the most pronounced decomposition was observed for AC-800 (~5 wt%), indicating the highest concentration of oxygen-containing functional groups, which degrade at intermediate temperatures [80]. However, above 600 °C, AC-700_1:4 exhibited the greatest weight loss (~8% wt.), which may indicate a higher proportion of thermally less stable components within the carbon framework. Among ACs synthesized with graphite-to-KOH ratios of 1:5, 1:6, and 1:7, the AC-800_1:5 and AC-800_1:6 demonstrated moderate thermal stability, with approximately 6 wt% and 7 wt% loss by 900 °C, suggesting stable porous structure. The

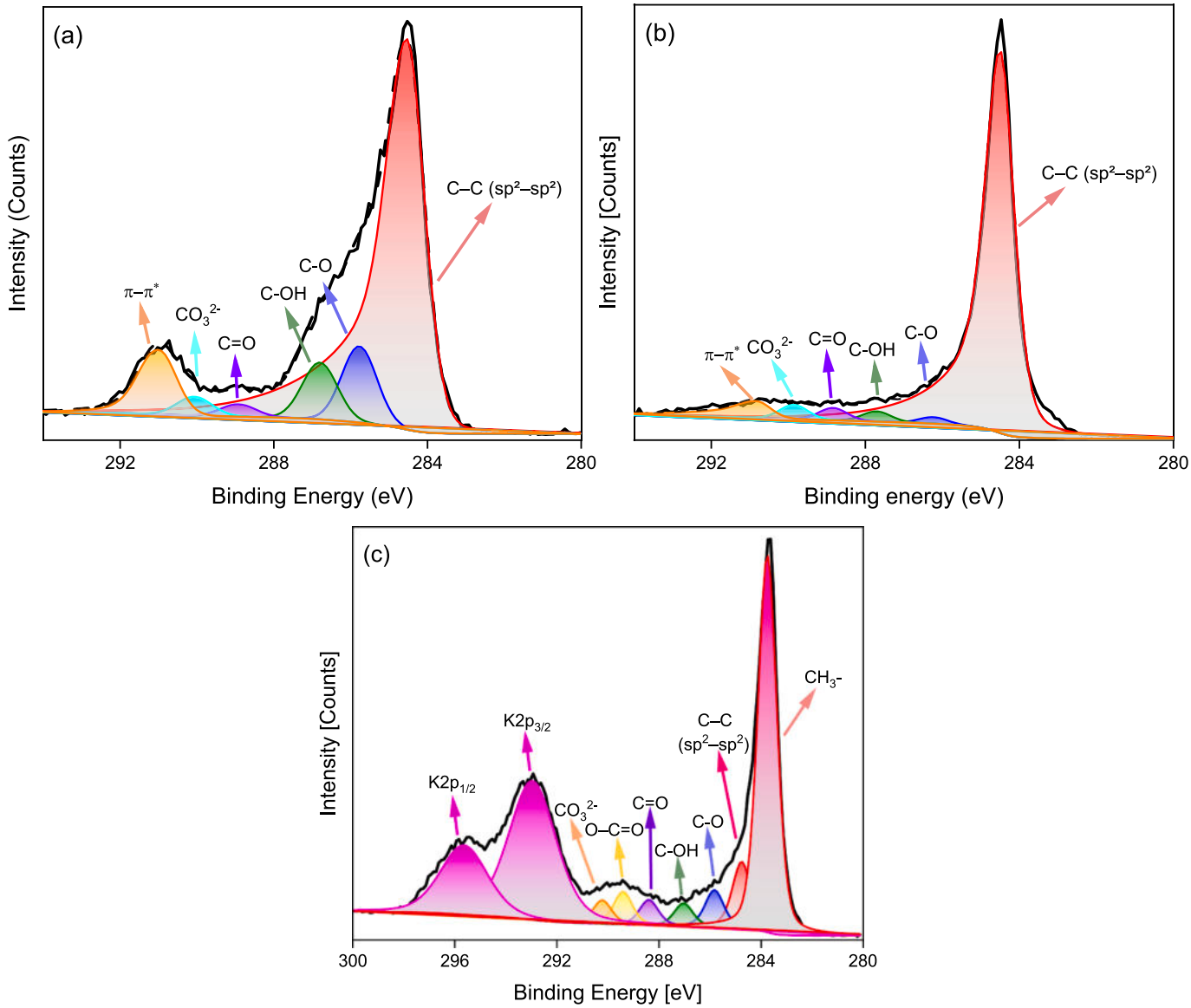

Fig. 14. XPS spectra in the C1s region for (a) recovered graphite, (b) the recovered graphite-based AC sample (AC-800_1:6), and in the C1s–K2p region for (c) unwashed AC-800_1:6.

AC-800_1:7 showed the lowest stability (~13 wt%), likely resulting from excessive activation, which may have caused structural densification or potential pore collapse, as observed previously, despite the higher chemical loading. Notably, the overall standard deviation was very low, around 0.5 %, indicating consistent results across measurements.

The weight change observed during the oxidation of the samples in an air atmosphere is illustrated in the TGA curves shown in Fig. 13**(b)**. A general trend in thermal degradation is observed, characterized by an initial gradual change in sample weight, followed by a sharp decline as the temperature rises [81]. Weight loss initiates around 450 °C for most materials, marking the onset of carbon structure oxidation. It intensifies significantly between 500 °C and 650 °C, signifying the full oxidation of the more resilient carbon frameworks. The rate and onset of degradation seems to vary depending on the activation conditions, with some samples exhibiting a more gradual weight loss, while others degrading more rapidly. Among the ACs, the AC-800_1:7 has a weight loss that begins earlier, at approximately 350 °C, and accelerates rapidly above 400 °C. The activation conditions for AC-800_1:7 appear to have resulted in a framework that lacks the robust 3D carbon network characteristic of graphite. This network, composed of numerous graphene-stacked layers held together by van der Waals forces, is known for providing exceptional stability under oxidative conditions [82]. As a result, the AC-800_1:7 material may exhibit fewer thermally resistant carbon bonds or an alternative structural configuration, which could influence its stability compared to other ACs.

3.5. *Surface chemistry and carbon framework evolution through KOH activation*

Fig. 14**(a, b)** illustrates the C1s spectra for the recovered graphite and the AC-800_1:6 after the KOH treatment, respectively. The asymmetric C1s peaks at a binding energy of 284.6 eV, coupled with a π-π* shake-up at approximately 291.0 eV, are the characteristic features of sp^2-hybridized carbon, confirming the graphitic nature of the samples. This graphitic carbon is the dominant chemical state in both samples [83]. Besides that, the other oxidized states including C–O (285.8 eV), C-OH (287.0 eV), C=O (288.8 eV), and CO_3^{2-} (290.0 eV) are determined. After KOH activation, the intensity of the graphitic carbon (C–C, sp^2-sp^2) peak increases, reflecting graphitization or the development of a more ordered graphitic structure. However, K intercalation during activation

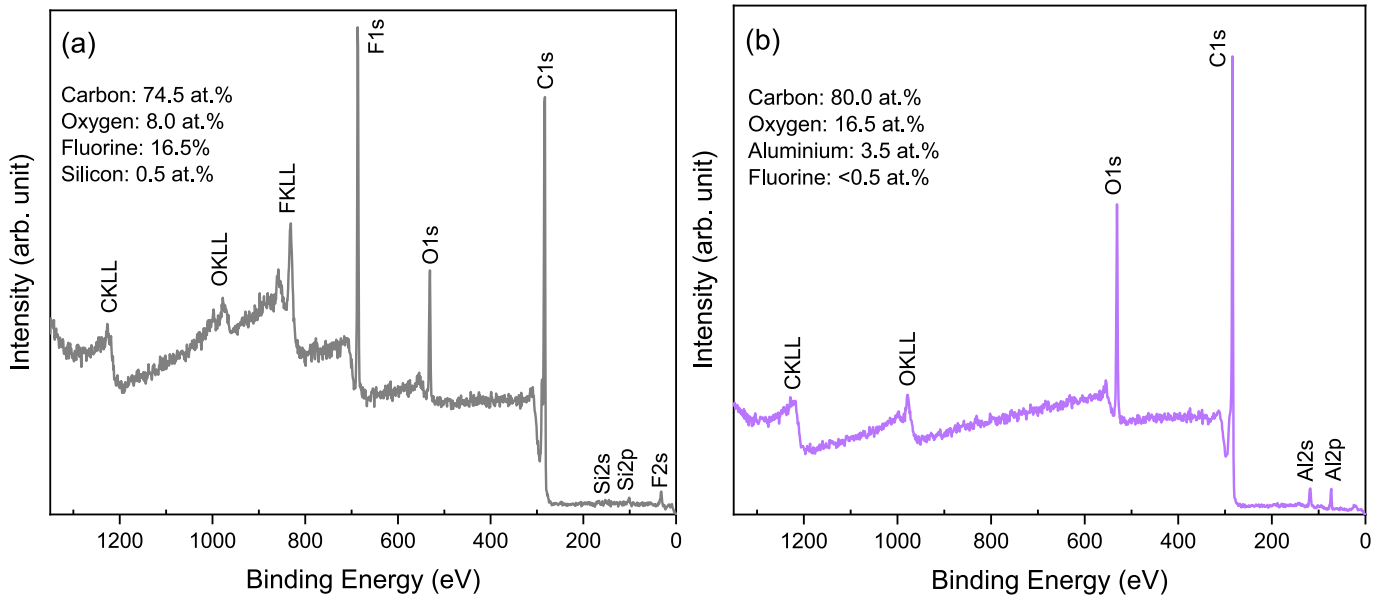

Fig. 15. Survey spectra of (a) recovered graphite, and (b) recovered graphite-based AC sample (AC-800_1:6).

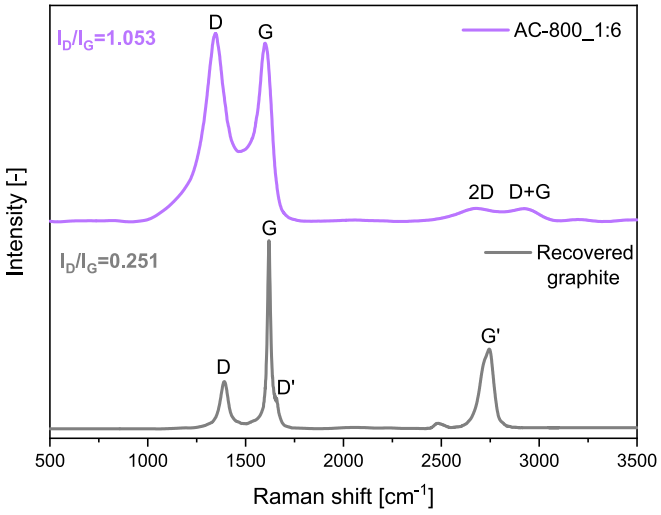

Fig. 16. Raman spectra of the recovered graphite and recovered graphite-based AC sample (AC-800_1:6).

can also cause local structural distortions, as confirmed later by Raman spectroscopy, which shows some disorder alongside the overall graphitization trend. Simultaneously, the oxidized states decrease non-uniformly, potentially due to high-temperature reactions with KOH that remove pre-existing OCFGs from the surface. This process may also involve redox reactions, where metallic potassium, formed during activation at temperatures above 762 °C, interacts with surface oxygen groups, altering their arrangement and promoting their removal [84,85].

In Fig. 14**(c)**, the XPS spectrum in the C1s–K2p region of unwashed AC-800_1:6 reveals both C–C (sp^2–sp^2) and CH_3-related peaks. While the sp^2–sp^2 bonding is consistent with the expected graphitic structure, the appearance of CH_3-associated signals is atypical, which is likely due to surface contamination, residual potassium compounds, or hydrocarbon fragments introduced during activation or handling. Additionally, the presence of the O–C=O group (289.2 eV) suggests carbonate-like phases formed via surface oxidation or interactions with residual potassium-containing compounds, as confirmed by XRD analysis. The $K2p_{3/2}$ and $K2p_{1/2}$ peaks further support the presence of these K-based species, which may influence the local carbon bonding environment.

In view of the quantitative analysis of the surface composition via survey scan (Fig. 15), the overall carbon content increases from 74.5 at.% in the recovered graphite to 80.0 at.% after activation. This increase is attributed to the removal of surface contaminants, including fluorine, which decreases significantly from 16.5 at.% to below 0.5 at.%, therewith enriching the surface carbon proportion. Conversely, the oxygen content rises from 8.0 at.% to 16.5 at.% due to the introduction of OCFGs during the KOH activation process, consistent with expected surface oxidation. However, high-resolution C1s spectra shows a reduction in the intensities of oxidized carbon states after activation (Fig. 14). This apparent contradiction most probably arises from the redistribution or transformation of oxygen-containing species [86]. While specific oxidized carbon states decrease, the overall oxygen content likely increases due to the formation of other OCFGs. These groups are not directly detected in the C1s spectra but contribute to the higher oxygen signal in the survey scan without significantly influencing the C1s peaks. Finally, aluminium (~9.0 at.% Al_2O_3) that observed in the sample originates from the alumina crucible used during the thermochemical process. To facilitate clearer interpretation, the XPS analysis results are summarized in comparative form in **Table S4**.

The Raman spectra of the recovered graphite and the AC-800_1:6 (Fig. 16) provide insight into the structural changes induced by KOH activation, complementing the observations from the XPS analysis. In Raman spectroscopy, the D mode corresponds to the breathing modes of sp^2 atoms in rings and is indicative of defects or disorder in the carbon structure, while the G mode arises from the in-plane vibration of sp^2-bonded carbon atoms, representing the graphitic domains. The intensity ratio I_D/I_G, derived from the integrated areas under the D and G peaks, serves as a measure of structural disorder. For the recovered graphite sample, the I_D/I_G ratio is 0.251, indicating a low level of structural disorder and a relatively high graphitic content. After activation, this ratio increases significantly to 1.053, reflecting the introduction of defects and greater disorder in the carbon structure [87]. These structural modifications, such as edge sites and functionalized pores, are likely a result of KOH etching and are consistent with the higher defect density observed in the Raman spectroscopy analysis. At the same time, the XPS spectra at the C1s regions (Fig. 14) reveal a notable increase in the relative intensity of the sp^2-hybridized carbon peak in the AC-800_1-6, suggesting enhanced graphitization at the surface level, likely due to the removal of oxidized states during activation [88]. Together, the

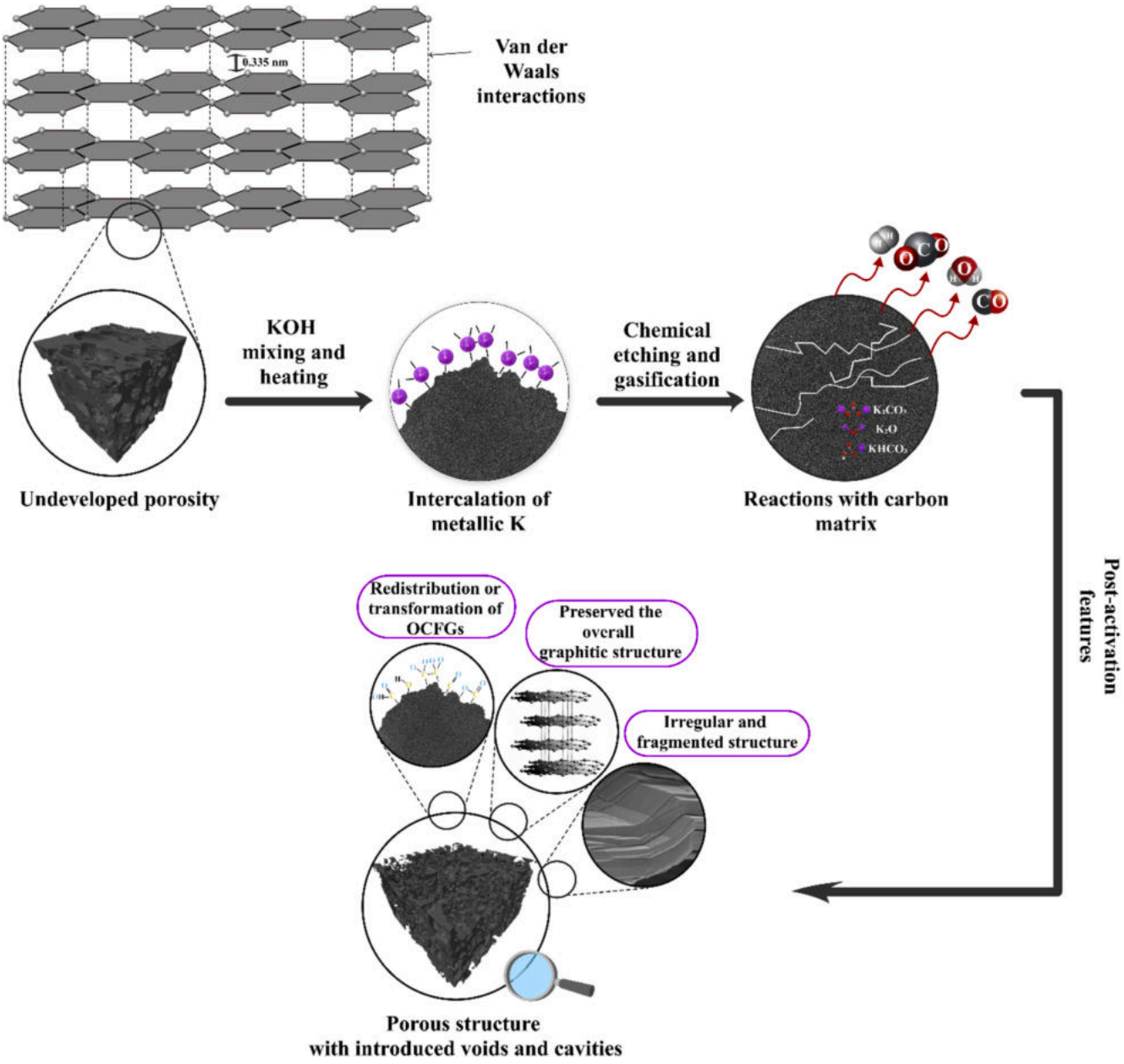

Fig. 17. Mechanistic pathway of KOH activation for converting unused hazardous graphite from NMC 111 into ACs.

Raman and XPS spectroscopic analyses highlight a complex interplay: while Raman spectroscopy indicates increased disorder within the carbon lattice, XPS reveals improved structural ordering in the surface carbon domains.

4. Conclusions

This study provides a comprehensive assessment of the transformation of graphite recovered from NMC 111 black mass of spent lithium-ion batteries into activated carbons via KOH activation (Fig. 17). The findings explore the changes in the textural, structural, morphological, and surface chemistry properties of the material throughout the KOH activation process.

KOH activation involves the selective removal of carbon from recovered graphite, leading to defect formation, disorder, and pore development, resulting in a microporous and mesoporous structure. Tailored activation conditions (800 °C, 1:6 graphite-to-KOH ratio) yielded ACs with a specific surface area of 678 m^2/g, a total pore volume of 0.442 cm^3/g, and a balanced micropore (53 %) and mesopore (47 %) distribution, contributing to the material's hierarchical porosity. Structural analysis confirmed the preservation of the graphitic framework. XRD revealed characteristic crystallographic planes, including (002), (100), (101), (104), (110), and (112), with an unchanged interlayer spacing of 0.335 nm. However, the broadening and reduction in intensity of the (002) peak indicated that activation predominantly affected the less ordered regions, leading to some loss of long-range order in the graphitic structure. The increased I_D/I_G ratio (0.251 to 1.053) in Raman spectroscopy indicated enhanced defect density and disorder.

SEM revealed a transition from smooth graphite layers to a fragmented, rough surface, while TEM showed a complex nanoscale architecture with mesopore-like voids and structural defects at the particle edge. FFT analysis of the recovered graphite showed well-ordered lattice fringes with an interlayer distance of ~0.35 nm, corresponding to the (002) planes. This spacing, slightly larger than the ideal 0.335 nm from XRD, suggests minor turbostratic disorder. In contrast, FFT of the AC

revealed a dominant lattice spacing of ~0.24 nm, highlighting the exposure of the (1 0 0) in-plane lattice and disruption of the interlayer stacking.

EDS mapping confirmed a predominantly carbon-rich composition with localized potassium residues. XPS analysis identified oxygen-containing functional groups (C–O, C-OH, C=O, and CO_3^{2-}), contributing to chemical reactivity. Thermal stability tests demonstrated high stability under inert conditions and increased reactivity in oxidative environments, reflecting structural defects and oxygen functionalities introduced during activation.

These results underscore the potential of chemical activation for converting unused hazardous graphite waste from NMC 111 into functional materials for applications such as CO_2 capture, gas separation, energy storage, water treatment, and catalysis. Future research should evaluate the application-specific performance of these ACs in industrial gas sorption systems and energy storage devices. Expanding the methodology to diverse black mass compositions and LiB chemistries will enhance scalability. Additionally, optimizing energy efficiency, reducing chemical consumption, and conducting life cycle assessments will be crucial for industrial adoption. To further highlight the benefits of the strong alkali-assisted process, comparative studies with commercial graphite and activated carbons are recommended to emphasize the unique characteristics and performance advantages of the recycled graphite-derived porous carbon from LiBs.

CRediT authorship contribution statement

Bartosz Dziejarski: Writing – original draft, Visualization, Validation, Software, Methodology, Investigation, Formal analysis, Data curation, Conceptualization, Writing – review & editing. **Jose Eduardo Arevalo Fester:** Formal analysis, Data curation, Conceptualization, Writing – review & editing. **Jarosław Serafin:** Validation, Investigation, Formal analysis, Conceptualization, Data curation, Software, Writing – review & editing, Methodology. **Martina Petranikova:** Writing – original draft, Supervision, Resources, Investigation, Funding acquisition, Conceptualization. **Eric Tam:** Writing – original draft, Validation, Software, Investigation, Formal analysis, Data curation. **Anna Martinelli:** Validation, Supervision, Software, Resources, Investigation, Formal analysis. **Renata Krzyżyńska:** Supervision, Investigation. **Klas Andersson:** Supervision, Methodology, Investigation, Conceptualization. **Pavleta Knutsson:** Supervision, Resources, Project administration, Methodology, Investigation, Funding acquisition, Formal analysis, Conceptualization.

Declaration of competing interest

The authors declare that they have no known competing financial interests or personal relationships that could have appeared to influence the work reported in this paper. This work was supported by the Swedish Energy Agency (Project Nos. P2021-90022 and P2023-00146).

Appendix A. Supplementary data

Supplementary data to this article can be found online at https://doi.org/10.1016/j.matdes.2025.114073.

Data availability

Data will be made available on request.

References

[1] M. Slattery, J. Dunn, A. Kendall, Transportation of electric vehicle lithium-ion batteries at end-of-life: a literature review, Resour. Conserv. Recycl. 174 (2021) 105755.
[2] C.D. Quilty, D. Wu, W. Li, D.C. Bock, L. Wang, L.M. Housel, E.S. Takeuchi, Electron and ion transport in lithium and lithium-ion battery negative and positive composite electrodes, Chem. Rev. 123 (4) (2023) 1327–1363.
[3] X. Zhang, Z. Li, L. Luo, Y. Fan, Z. Du, A review on thermal management of lithium-ion batteries for electric vehicles, Energy 238 (2022) 121652, https://doi.org/10.1016/j.energy.2021.121652.
[4] IEA (2024), Global EV Outlook 2024, IEA, Paris https://www.iea.org/reports/global-ev-outlook-2024, Licence: CC BY 4.0.
[5] J. Jayaprabakar, J.A. Kumar, J. Parthipan, A. Karthikeyan, M. Anish, N. Joy, Review on hybrid electro chemical energy storage techniques for electrical vehicles: technical insights on design, performance, energy management, operating issues & challenges, J. Storage Mater. 72 (2023) 108689.
[6] M.M. Rana, M. Uddin, M.R. Sarkar, S.T. Meraj, G.M. Shafiullah, S.M. Muyeen, T. Jamal, Applications of energy storage systems in power grids with and without renewable energy integration—A comprehensive review, J. Storage Mater. 68 (2023) 107811.
[7] W. Wang, B. Yuan, Q. Sun, R. Wennersten, Application of energy storage in integrated energy systems—A solution to fluctuation and uncertainty of renewable energy, J. Storage Mater. 52 (2022) 104812.
[8] S.B. Wali, M.A. Hannan, P.J. Ker, S.A. Rahman, K.N. Le, R.A. Begum, T.I. Mahlia, Grid-connected lithium-ion battery energy storage system towards sustainable energy: a patent landscape analysis and technology updates, J. Storage Mater. 77 (2024) 109986.
[9] J. Fleischmann, M. Hanicke, E. Horetsky, D. Ibrahim, S. Jautelat, M. Linder, ... A. van de Rijt.Battery 2030: Resilient, sustainable, and circular. McKinsey & Company, 2-18. 2023. https://www.mckinsey.com/industries/automotive-and-assembly/our-insights/battery-2030-resilient-sustainable-and-circular#/.
[10] X. Gu, H. Bai, X. Cui, J. Zhu, W. Zhuang, Z. Li, Z. Song, Challenges and opportunities for second-life batteries: key technologies and economy, Renew. Sustain. Energy Rev. 192 (2024) 114191.
[11] V. Srivastava, V. Rantala, P. Mehdipour, T. Kauppinen, S. Tuomikoski, A. Heponiemi, U. Lassi, A comprehensive review of the reclamation of resources from spent lithium-ion batteries, Chem. Eng. J. (2023) 145822.
[12] B. Niu, Z. Xu, J. Xiao, Y. Qin, Recycling hazardous and valuable electrolyte in spent lithium-ion batteries: urgency, progress, challenge, and viable approach, Chem. Rev. 123 (13) (2023) 8718–8735.
[13] B. Niu, J. Xiao, Z. Xu, Utilizing spent Li-ion batteries to regulate the π-conjugated structure of gC_3N_4: a win–win approach for waste recycling and highly active photocatalyst construction, J. Mater. Chem. A 9 (1) (2021) 472–481.
[14] X. Zhang, L. Li, E. Fan, Q. Xue, Y. Bian, F. Wu, R. Chen, Toward sustainable and systematic recycling of spent rechargeable batteries, Chem. Soc. Rev. 47 (19) (2018) 7239–7302.
[15] K. Elong, M.F. Kasim, A. Azahidi, Z. Osman, LiNi0. 3Mn0. 3Co0. 3O2(NMC 111) cathode material synthesize via combustion method: effect of combustion fuel on structure, morphology and their electrochemical performances, Mater. Today Proc. (2023).
[16] F.N.U. Khan, M.G. Rasul, A.S.M. Sayem, N. Mandal, Maximizing energy density of lithium-ion batteries for electric vehicles: a critical review, Energy Rep. 9 (2023) 11–21.
[17] E. Kastanaki, A. Giannis, Dynamic estimation of end-of-life electric vehicle batteries in the EU-27 considering reuse, remanufacturing and recycling options, J. Clean. Prod. 393 (2023) 136349.
[18] A. Tankou, G. Bieker, D. Hall, February). Scaling up reuse and recycling of electric vehicle batteries: Assessing challenges and policy approaches, in: In Proc. ICCT, 2023, pp. 1–138.
[19] A.M. Abdalla, M.F. Abdullah, M.K. Dawood, B. Wei, Y. Subramanian, A.T. Azad, A. K. Azad, Innovative lithium-ion battery recycling: sustainable process for recovery of critical materials from lithium-ion batteries, J. Storage Mater. 67 (2023) 107551.
[20] Y. Zou, A. Chernyaev, M. Ossama, S. Seisko, M. Lundström, Leaching of NMC industrial black mass in the presence of LFP, Sci. Rep. 14 (1) (2024) 10818.
[21] M. Olutogun, A. Vanderbruggen, C. Frey, M. Rudolph, D. Bresser, S. Passerini, Recycled graphite for more sustainable lithium-ion batteries, Carbon Energy e483 (2024).
[22] S. Natarajan, V. Aravindan, An urgent call to spent LIB recycling: whys and wherefores for graphite recovery, Adv. Energy Mater. 10 (37) (2020) 2002238.
[23] K. Bilisik, M. Akter, Polymer nanocomposites based on graphite nanoplatelets (GNPs): a review on thermal-electrical conductivity, mechanical and barrier properties, J. Mater. Sci. 57 (15) (2022) 7425–7480.
[24] Y.A. Kumar, J.K. Alagarasan, T. Ramachandran, M.D. Rezeq, M.A. Bajaber, A. A. Alalwiat, M. Lee, The landscape of energy storage: insights into carbon electrode materials and future directions, J. Storage Mater. 86 (2024) 111119.
[25] K. Yang, Z. Ling, X. Fang, Z. Zhang, Introducing a flexible insulation network to the expanded graphite-based composite phase change material to enhance dielectric and mechanical properties for battery thermal management, J. Storage Mater. 66 (2023) 107486.
[26] I.K. Tetteh, I. Issahaku, A.Y. Tetteh, Recent advances in synthesis, characterization, and environmental applications of activated carbons and other carbon derivatives, Carbon Trends (2024) 100328.
[27] F. Nawaz, M. Ali, S. Ahmad, Y. Yong, S. Rahman, M. Naseem, N. Ali, Carbon based nanocomposites, surface functionalization as a promising material for VOCs (volatile organic compounds) treatment, Chemosphere (2024) 143014.
[28] L.A. Xing, F. Yang, X. Zhong, Y. Liu, H. Lu, Z. Guo, J. Pan, Ultra-microporous cotton fiber-derived activated carbon by a facile one-step chemical activation strategy for efficient CO_2 adsorption, Sep. Purif. Technol. 324 (2023) 124470.

[29] C. Madhusha, T. Jayasundara, I. Munaweera, C. Perera, G. Wijesinghe, M. Weerasekera, N. Kottegoda, Synthesis and structural characterization of copper nanoparticles doped activated carbon derived from coconut coir for drinking water purification, Mater. Today Chem. 27 (2023) 101312.
[30] S. Mandal, J. Hu, S.Q. Shi, A comprehensive review of hybrid supercapacitor from transition metal and industrial crop based activated carbon for energy storage applications, Mater. Today Commun. 34 (2023) 105207.
[31] J.H. Wee, S. Shin, D.W. Kim, C. Lee, Y.A. Kim, M.W. Shin, S.Y. Yeo, Boron-doped activated carbon supports for cobalt-catalyzed oxygen evolution in alkaline electrolyte, ACS Appl. Mater. Interfaces 15 (15) (2023) 18771–18780.
[32] B. Dziejarski, R. Faust, J. Serafin, R. Krzyżyńska, K. Andersson, P. Knutsson, Insights into activation pathways of recovered carbon black (rCB) from end-of-life tires (ELTs) by potassium-containing agents, ACS Omega 9 (29) (2024) 31814–31831.
[33] G. Singh, A.M. Ruban, X. Geng, A. Vinu, Recognizing the potential of K-salts, apart from KOH, for generating porous carbons using chemical activation, Chem. Eng. J. 451 (2023) 139045.
[34] J. Singh, H. Bhunia, S. Basu, Adsorption of CO_2 on KOH activated carbon adsorbents: effect of different mass ratios, J. Environ. Manage. 250 (2019) 109457.
[35] M. Gayathiri, T. Pulingam, K.T. Lee, K. Sudesh, Activated carbon from biomass waste precursors: factors affecting production and adsorption mechanism, Chemosphere 294 (2022) 133764.
[36] M.M. Amin, L.S. Mohamed, M.M. Hossain, S.A. Razzak, M.N. Siddiquee, Prospects and challenges of carbon fiber production from heavy petroleum fractions, Ind. Eng. Chem. Res. 63 (36) (2024) 15613–15636.
[37] I. Skoczko, R. Guminski, Tests on the application of various types of biomass for activated carbon production, J. Ecol. Eng. 25 (1) (2024).
[38] M. Tesfaye Gari, B. Tessema Asfaw, S.K. Arumugasamy, L. Deso Abo, M. Jayakumar, Natural resources-based activated carbon synthesis, in: Encyclopedia of Green Materials, Springer Nature Singapore, Singapore, 2024, pp. 1520–1530.
[39] Z. Shang, W. Yu, J. Zhou, X. Zhou, Z. Zeng, R. Tursun, S. Xu, Recycling of spent lithium-ion batteries in view of graphite recovery: a review, ETransportation (2024) 100320.
[40] L.Y. Meng, S.J. Park, Effect of heat treatment on CO_2 adsorption of KOH-activated graphite nanofibers, J. Colloid Interface Sci. 352 (2) (2010) 498–503.
[41] H. Yuan, L.Y. Meng, S.J. Park, KOH-activated graphite nanofibers as CO_2 adsorbents, Carbon Lett. 19 (1) (2016) 99–103.
[42] J. Rouquerol, G.V. Baron, R. Denoyel, H. Giesche, J. Groen, P. Klobes, K. Unger, The characterization of macroporous solids: an overview of the methodology, Microporous Mesoporous Mater. 154 (2012) 2–6.
[43] J. Serafin, M. Ouzzine, O.F. Cruz Jr, J. Sreńscek-Nazzal, I.C. Gómez, F.Z. Azar, C. R. Rambo, Conversion of fruit waste-derived biomass to highly microporous activated carbon for enhanced CO_2 capture, Waste Manag. 136 (2021) 273–282.
[44] K.R. Hallam, J.E. Darnbrough, C. Paraskevoulakos, P.J. Heard, T.J. Marrow, P. E. Flewitt, Measurements by x-ray diffraction of the temperature dependence of lattice parameter and crystallite size for isostatically-pressed graphite, Carbon Trends 4 (2021) 100071.
[45] P. Puech, M. Jeanningros, D. Neumeyer, M. Monthioux, Addressing the effect of stacking faults in X-ray diffractograms of graphite through atom-scale simulations, Carbon Trends 13 (2023) 100311.
[46] F.T.L. Muniz, M.R. Miranda, C. Morilla dos Santos, J.M. Sasaki, The Scherrer equation and the dynamical theory of X-ray diffraction, Found. Crystallogr. 72 (3) (2016) 385–390.
[47] S. Basak, R. Das, Confirmation of the presence of edge dislocations in the prepared FCC ZnTe nanocrystals from the study of structural analysis through the MWH method with added Fourier analysis (WA method) of diffraction peaks, Mater. Sci. Semicond. Process. 179 (2024) 108477.
[48] R. Sharma, D.P. Bisen, U. Shukla, B.G. Sharma, X-ray diffraction: a powerful method of characterizing nanomaterials, Recent Res. Sci. Technol. 4 (8) (2012) 77–79.
[49] V. Kumar, A. Kumar, D.J. Lee, S.S. Park, Estimation of number of graphene layers using different methods: a focused review, Materials 14 (16) (2021) 4590.
[50] S. Shimizu, N. Matubayasi, Understanding sorption mechanisms directly from isotherms, Langmuir 39 (17) (2023) 6113–6125.
[51] V.G. Baldovino-Medrano, V. Niño-Celis, R. Isaacs Giraldo, Systematic analysis of the nitrogen adsorption–desorption isotherms recorded for a series of materials based on microporous–mesoporous amorphous aluminosilicates using classical methods, J. Chem. Eng. Data 68 (9) (2023) 2512–2528.
[52] G. Chen, Z. Liu, G. Yang, Q. Zhang, T. Lan, C. Zhang, S. He, Synthesis of chain-like nitrogen-doped carbon for high-performance supercapacitors, Colloids Surf. A Physicochem. Eng. Asp. 687 (2024) 133498.
[53] Z. Song, J. Zhang, S. Jin, C. Liu, A. Abula, J. Hou, L. Ma, The occurrences and mobility of shale oil in the pore space of terrestrial shale, Fuel 374 (2024) 132377.
[54] T. Manimekala, R. Sivasubramanian, M.A. Dar, G. Dharmalingam, Crafting the architecture of biomass-derived activated carbon via electrochemical insights for supercapacitors: a review, RSC Adv. 15 (4) (2025) 2490–2522.
[55] N. Boonraksa, E. Swatsitang, K. Wongsaprom, Electrochemical performance of KOH-activated lotus seedpods carbon, Mater. Sci. Eng. B 301 (2024) 117151.
[56] T. Ji, X. Liu, T. Zhang, Y. Shi, D. Sheng, H. Yin, D. Chao, Potassium metal underpotential deposition in crystalline carbon of potassium-ion batteries, Adv. Energy Mater. 14 (40) (2024) 2401908.
[57] G. Wang, Yu. Minghao, X. Feng, Carbon materials for ion-intercalation involved rechargeable battery technologies, Chem. Soc. Rev. 50 (4) (2021) 2388–2443.
[58] A.A. Papaderakis, A. Ejigu, J. Yang, A. Elgendy, B. Radha, A. Keerthi, R.A. Dryfe, Anion intercalation into graphite drives surface wetting, J. Am. Chem. Soc. 145 (14) (2023) 8007–8020.
[59] R. Yang, L. Mei, Z. Lin, Y. Fan, J. Lim, J. Guo, Z. Zeng, Intercalation in 2D materials and in situ studies, Nat. Rev. Chem. (2024) 1–23.
[60] Y. Luo, Q. Jiang, J. Liu, H. Yang, X. Liao, F. Huang, J. He, Mesoporous collapsing encapsulated carbon dots: direct evidence for the effect of multiple-confined interactions of silica on efficient long-lived phosphorescence, Chem. Eng. J. 486 (2024) 150436.
[61] T. Yin, Z. Zhang, L. Xu, C. Li, D. Han, Preparation of green high-performance biomass-derived hard carbon materials from bamboo powder waste, ChemistryOpen 13 (5) (2024) e202300178.
[62] J. Serafin, M. Baca, M. Biegun, E. Mijowska, R.J. Kaleńczuk, J. Sreńscek-Nazzal, B. Michalkiewicz, Direct conversion of biomass to nanoporous activated biocarbons for high CO_2 adsorption and supercapacitor applications, Appl. Surf. Sci. 497 (2019) 143722.
[63] J. Kafle, J. Harris, J. Chang, J. Koshina, D. Boone, D. Qu, Development of wide temperature electrolyte for graphite/LiNiMnCoO2 Li-ion cells: high throughput screening, J. Power Sources 392 (2018) 60–68.
[64] H. Zhang, Y. Yang, D. Ren, L. Wang, X. He, Graphite as anode materials: fundamental mechanism, recent progress and advances, Energy Storage Mater. 36 (2021) 147–170.
[65] D. Kaiser, S. Pavón, M. Bertau, Recovery of Al, Co, Cu, Fe, Mn, and Ni from Spent LIBs after Li selective separation by the COOL-Process. Part 1: leaching of solid residue from COOL-process, Chem. Ing. Tech. 93 (11) (2021) 1833–1839.
[66] M. Wang, Q. Tan, L. Liu, J. Li, A facile, environmentally friendly, and low-temperature approach for decomposition of polyvinylidene fluoride from the cathode electrode of spent lithium-ion batteries, ACS Sustain. Chem. Eng. 7 (15) (2019) 12799–12806.
[67] B. Zheng, W. Zhou, H. Liu, S. Chen, P. Gao, Z. Wang, J. Liu, Surface chemistry induced robust SEI on graphite surface via soft carbon coating enables fast lithium storage, Carbon 218 (2024) 118729.
[68] T. Otowa, R. Tanibata, M. Itoh, Production and adsorption characteristics of MAXSORB: high-surface-area active carbon, Gas Sep. Purif. 7 (4) (1993) 241–245.
[69] F. Boi, C.Y. Lee, S. Wang, H. Wu, L. Li, L. Zhang, S. Grasso, Rhombohedral stacking-faults in exfoliated highly oriented pyrolytic graphite, Carbon Trends 15 (2024) 100345.
[70] T. Cheng, S. Qi, Y. Jiang, L. Wang, Q. Zhu, J. Zhu, Z. He, Carbon structure regulation strategy for the electrode of vanadium redox flow battery, Small 20 (37) (2024) 2400496.
[71] Y. Zhu, H. Liu, T. Wang, Y. Wang, H. Liu, Evolution of pore structures and fractal characteristics of coal-based activated carbon in steam activation based on nitrogen adsorption method, Powder Technol. 424 (2023) 118522.
[72] Z. Tai, Q. Zhang, Y. Liu, H. Liu, S. Dou, Activated carbon from the graphite with increased rate capability for the potassium ion battery, Carbon 123 (2017) 54–61.
[73] J. Serafin, B. Dziejarski, Ó.J. Fonseca-Bermúdez, L. Giraldo, R. Sierra-Ramírez, M. G. Bonillo, J.C. Moreno-Piraján, Bioorganic activated carbon from cashew nut shells for H_2 adsorption and H_2/CO_2, H_2/CH_4, CO_2/CH_4, $H_2/CO_2/CH_4$ selectivity in industrial applications, Int. J. Hydrogen Energy 86 (2024) 662–676.
[74] J. Serafin, K. Kiełbasa, B. Michalkiewicz, The new tailored nanoporous carbons from the common polypody (Polypodium vulgare): the role of textural properties for enhanced CO_2 adsorption, *Chem. Eng. J.* 429 (2022) 131751.
[75] A.M. Haggar, A.A. Aboul-Enein, A.E. Awadallah, M.A. Azab, Novel concept for synthesizing carbon nano-onion, graphene layers, and graphene nano-ribbons from polypropylene waste over Fe_2O_3 nanoparticles, *Carbon Lett.* (2025) 1–13.
[76] D.W. Boukhvalov, V.Y. Osipov, D. Murzalinov, A. Serikkanov, H. Bi, A comprehensive model of carbon nanodots with 0.21 nm lattice fringes patterns, *Carbon* 225 (2024) 119101.
[77] D.W. Kim, H.S. Kil, J. Kim, I. Mochida, K. Nakabayashi, C.K. Rhee, S.H. Yoon, Highly graphitized carbon from non-graphitizable raw material and its formation mechanism based on domain theory, Carbon 121 (2017) 301–308.
[78] V.R. Magri, C.S. de Matos, M.A. Rocha, C. Taviot-Gueho, V.R. Constantino, Pyrolysis of folic acid: Identification of gaseous/volatile products and structural evolution of N-doped graphitic carbon, Thermochim. Acta 739 (2024) 179813.
[79] A. Marcilla, D. Berenguer, TGA/FTIR study of the decomposition of Heet tobacco in presence of zeolites and silicate compounds, Mater. Sci. Eng. B 295 (2023) 116593.
[80] M. Feizbakhshan, Z. Hashisho, D. Crompton, J.E. Anderson, M. Nichols, Effect of activated carbon's pore size distribution on oxygen induced heel build-up, J. Hazard. Mater. 457 (2023) 126905.
[81] I. Karnis, F. Krasanakis, L. Sygellou, A.N. Rissanou, K. Karatasos, K. Chrissopoulou, Varying the degree of oxidation of graphite: effect of oxidation time and oxidant mass, PCCP 26 (13) (2024) 10054–10068.
[82] S. Gadipelli, Z.X. Guo, Graphene-based materials: synthesis and gas sorption, storage and separation, Prog. Mater. Sci. 69 (2015) 1–60.
[83] D.J. Morgan. Comments on the XPS analysis of carbon materials. C, 7(3) 2021 51.
[84] H. Arslanoğlu, Direct and facile synthesis of highly porous low cost carbon from potassium-rich wine stone and their application for high-performance removal, J. Hazard. Mater. 374 (2019) 238–247.
[85] J. Wang, S. Kaskel, KOH activation of carbon-based materials for energy storage, J. Mater. Chem. 22 (45) (2012) 23710–23725.

[86] M. Hu, Z. Ye, Q. Zhang, Q. Xue, Z. Li, J. Wang, Z. Pan, Towards understanding the chemical reactions between KOH and oxygen-containing groups during KOH-catalyzed pyrolysis of biomass, Energy 245 (2022) 123286.
[87] R. Arunpandian, M. Kumar, P.Y. Yang, C.H. Chiang, J.H. Chang, Enhancing graphitization with desirable porosity for CO_2 adsorption through a one-step strategy and a novel stepwise pyrolysis method from Terminalia boivinii tul tree dead leaves, Surf. Interfaces 44 (2024) 103696.
[88] S. Hu, S. Lin, D. Wen, Regulation of reactive oxygen species generation by graphitization and defect degree of Co-loaded carbon in peroxymonosulfate activation, Sep. Purif. Technol. 354 (2025) 129195.